Universidade de Lisboa
Instituto Superior Técnico

Fracture behaviour of pultruded GFRP profiles: application to web-crippling phenomena

Lourenço Rocheta de Almeida Fernandes

Supervisor: Doctor Nuno Miguel Rosa Pereira Silvestre

Co-Supervisor: Doctor João Pedro Ramôa Ribeiro Correia

Thesis approved in public session to obtain the PhD Degree in
Civil Engineering

Jury final classification:

Pass with Distinction and Honour

December 2020

Universidade de Lisboa
Instituto Superior Técnico

Fracture behaviour of pultruded GFRP profiles: application to web-crippling phenomena

Lourenço Rocheta de Almeida Fernandes

Supervisor: Doctor Nuno Miguel Rosa Pereira Silvestre

Co-Supervisor: Doctor João Pedro Ramôa Ribeiro Correia

Thesis approved in public session to obtain the PhD Degree in Civil Engineering

Jury final classification:

Pass with Distinction and Honour

Jury

Chairperson: Doctor Eduardo Nuno Brito Santos Júlio, Instituto Superior Técnico, Universidade de Lisboa

Members of the Committee:

Doctor Thomas Keller, School of Architecture, Civil and Environmental Engineering, École Polytechnique Fédérale de Lausanne, Switzerland

Doctor Pedro Manuel Ponces Rodrigues de Castro Camanho, Faculdade de Engenharia, Universidade do Porto

Doctor Hélder Carriço Rodrigues, Instituto Superior Técnico, Universidade de Lisboa

Doctor Nuno Miguel Rosa Pereira Silvestre, Instituto Superior Técnico, Universidade de Lisboa

Doctor José Joaquim Costa Branco de Oliveira Pedro, Instituto Superior Técnico, Universidade de Lisboa

December 2020

Abstract

This thesis addresses two main research topics, both of which are applied to pultruded glass fibre reinforced polymer (GFRP) materials and profiles: (i) fracture toughness; and (ii) web-crippling of structural beams. These are considerably different topics, as fracture toughness is a topic that can be implemented in a wide variety of frameworks, whereas web-crippling is a well-known and specific structural case, involving concentrated transverse loads. However, these two topics closely intersect in this thesis, as fracture toughness properties can be implemented in finite element (FE) numerical models to simulate damage evolution of brittle materials, such as GFRP composites. This numerical methodology was thus selected to simulate the web-crippling failure of pultruded GFRP profiles, a topic that currently has significant research needs.

In an initial stage, several pultruded GFRP materials, produced by different manufacturers and comprising different fibre contents and layups, were subjected to a comprehensive mechanical characterization campaign, focusing on determining the elastic and strength properties in tension, compression and shear. In addition, these materials were subjected to calcination tests to assess the fibre layup of each material and the fibre content in each direction. Through this experimental programme, the transverse mechanical properties of each test material were fully characterized and assessed in respect to the fibre layup.

Having characterized the mechanical behaviour of each material, the initial part of the study on fracture toughness characterization consisted of developing experimental methodologies to determine the fracture properties in the in-plane transverse direction of several pultruded GFRP materials. To this end, compact tension tests (CT) were initially carried out to assess the transverse tensile fracture properties (G_2^+) of the various tested materials. However, significant specimen geometry dependency was found in the results and thus the test configuration had to be reconfigured. The specimen geometry dependency found in the results was attributed to the short width of the specimens, which hindered the development of the fracture process. As an alternative, the wide compact tension test (WCT) was implemented. The WCT specimen geometry consists of CT specimens with doubled width, providing additional room for crack growth. By combining WCT tests with data reduction methods based on visual observations of crack growth, accurate estimates of G_2^+ were determined for most tested materials. G_2^+ was found to present an exponential trend in regard to the transverse reinforcement fibre content (fibres oriented at 45° or 90°).

In a subsequent step, the transverse compressive fracture toughness (G_2^-) of the tested materials was assessed through compact compression tests (CCT) coupled with an inverse numerical methodology. This methodology consisted of calibrating FE numerical models in respect to their fracture properties and residual strength, in order to provide the best fit between numerical and experimental load *vs*. displacement curves. Through this procedure, the transverse compressive fracture properties of all materials were assessed and a different trend was found in these results, when compared to G_2^+ results, as higher transverse reinforcement fibre content did not lead to increasing G_2^- values.

Having characterized the transverse fracture properties of these different pultruded GFRP materials, a web-crippling experimental programme was developed, based on end two flange (ETF) and interior two flange (ITF) configurations, and focusing on acquiring comprehensive experimental data, including the local transverse compressive and shear strain fields, as well as the failure mode of each specimen. This experimental programme was developed with two main goals: (i) to provide extensive data to validate fracture toughness-based FE models; and (ii) to provide the basis for the development of novel and more accurate design expressions for web-crippling.

The numerical study on web-crippling consisted of developing relatively simple simulation models, based on commercial FE software. The numerical methodology consisted of using standard shell elements and homogenized mechanical properties through the thickness of the GFRP materials. The numerical models were found to present a good agreement in respect to most of the generated experimental data. The shear strain distributions were found to present higher discrepancies, which were attributed to the simplified simulation of the web-flange junction. The good agreement found between numerical and experimental failure loads further validated the experimentally based fracture toughness properties.

Finally, based on the experimental and numerical web-crippling results, an analytical study was performed, with the goal of generating novel design expressions. The direct strength method (DSM) was implemented to simultaneously address web buckling and web crushing failure modes. Both experimental and numerical results were very well approximated by unified DSM expressions, that fitted both ETF and ITF configurations simultaneously, for a significant variety of materials and section dimensions.

Keywords: pultruded GFRP profiles, fracture toughness, damage evolution, web-crippling, design, DSM.

Resumo

Esta tese aborda dois temas distintos, aplicados a perfis pultrudidos de polímeros reforçados com fibra de vidro (GFRP): (i) a caracterização experimental da energia de fratura; e (ii) o esmagamento da alma de vigas estruturais. Estes temas apresentam âmbitos consideravelmente distintos, pois a energia de fratura é um tema vasto, que pode ser implementado numa grande variedade de aplicações, enquanto o esmagamento da alma é um caso estrutural bem conhecido e específico, envolvendo a aplicação de forças concentradas na direção transversal de um perfil. Contudo, estes dois temas intersetam-se nesta tese, devido ao potencial de implementação da energia de fratura em modelos numéricos de elementos finitos (EF) para simular a evolução do dano em materiais de rotura frágil, como materiais compósitos de GFRP. Esta metodologia numérica foi selecionada para simular a rotura por esmagamento da alma de perfis pultrudidos de GFRP, um tópico que ainda carece significativamente de investigação.

Numa primeira fase, vários perfis pultrudidos de GFRP, produzidos por diferentes fabricantes e contendo diferentes teores e arquiteturas de fibras, foram submetidos a uma campanha de caracterização mecânica, orientada para determinar as suas propriedades elásticas e resistentes à tração, compressão e corte. Adicionalmente, estes materiais foram submetidos a ensaios de calcinação, com o objetivo de avaliar a arquitetura de fibras de cada material, assim como o teor de fibras para diversas orientações. Através deste programa experimental, as propriedades mecânicas transversais de cada material foram totalmente caracterizadas e avaliadas em relação à arquitetura de fibras.

Tendo caracterizado o comportamento mecânico de cada material, o estudo da caracterização da energia de fratura consistiu, numa primeira fase, no desenvolvimento de metodologias experimentais para determinar as propriedades de fratura na direção transversal de vários materiais pultrudidos de GFRP. Nesse sentido, foram realizados ensaios de tração compacta (CT) com o objetivo de avaliar a energia de fratura transversal em tração (G_2^+) dos vários materiais. No entanto, verificou-se existir uma dependência significativa dos resultados em relação à geometria dos provetes e, portanto, esta configuração de ensaio teve de ser modificada. A dependência dos resultados em relação à geometria dos provetes foi atribuída à curta largura dos mesmos, que impediu o desenvolvimento do processo de fratura. Como alternativa, foi implementado o ensaio de tração compacta alargado (WCT). A geometria de um provete WCT resume-se a um provete CT com o dobro da largura, proporcionando espaço adicional para o crescimento da fenda. Ao combinar ensaios WCT e métodos de processamento de dados baseados em observações visuais do crescimento de fendas, foram determinadas estimativas satisfatórias de G_2^+ para a maioria dos provetes ensaiados. Verificou-se ainda que o valor de G_2^+ apresenta uma tendência exponencial em relação ao teor de fibras de reforço transversal (fibras orientadas a 45° ou 90°).

De seguida, a energia de fratura em compressão transversal (G_2^-) foi avaliada através de ensaios de compressão compacta (CCT), associados a uma metodologia numérica inversa. Esta metodologia consistiu em calibrar as energias de fratura e a tensão residual de modelos numéricos de EF, para se atingir um ajuste adequado entre as curvas força *vs*. deslocamento experimentais e numéricas. Desta forma, os valores de G_2^- foram determinados para todos os materiais, tendo-se encontrado uma tendência diferente nestes resultados, quando comparados aos resultados de G_2^+, pois teores de fibra mais elevados na direção transversal não originaram um aumento significativo dos valores de G_2^-.

Após caracterizar as propriedades transversais de fratura destes materiais, foi desenvolvido um programa experimental de esmagamento da alma, com base em configurações de ensaio com carregamento simultâneo dos dois banzos numa extremidade (ETF) e numa secção interior (ITF). Este programa experimental foi desenvolvido com dois objetivos principais: (i) fornecer dados extensos para validar modelos de EF baseados na energia de fratura; e (ii) contribuir para o desenvolvimento de novas e mais precisas expressões de dimensionamento para o esmagamento da alma. Neste sentido, o estudo incluiu a obtenção de dados experimentais adicionais, como os campos locais de deformação por compressão transversal e corte, para além dos modos de rotura.

O estudo numérico sobre esmagamento da alma consistiu no desenvolvimento de modelos simplificados de EF, baseados em software comercial de fácil implementação. Esta metodologia utilizou elementos de casca e propriedades mecânicas homogeneizadas através da espessura dos materiais GFRP. Os modelos numéricos simularam de forma precisa a maioria dos dados experimentais obtidos no programa experimental. As distribuições de deformação por corte apresentaram as discrepâncias mais relevantes, as quais foram atribuídas à simulação simplificada da ligação banzo-alma. A boa concordância encontrada entre forças últimas numéricas e experimentais reforçou a validação das propriedades de energia de fratura determinadas experimentalmente.

Por fim, com base nos resultados experimentais e numéricos de esmagamento da alma, foi realizado um estudo analítico, com o objetivo de desenvolver novas expressões de dimensionamento. Para este efeito, recorreu-se ao método da resistência direta (*direct strength method*, DSM), que permite ter em conta, simultaneamente, os modos de rotura de instabilidade local e esmagamento. As fórmulas propostas apresentaram uma boa concordância com os resultados experimentais e numéricos, para uma amostra abrangente de materiais e geometrias de secção. Verificou-se ainda que as configurações ETF e ITF podem ser estimadas por uma expressão única.

Palavras-chave: perfis pultrudidos de GFRP, energia de fratura, propagação de dano, esmagamento da alma, dimensionamento, DSM.

Acknowledgements

The last 365 days have brought one of the most hectic years of my life, as I got married and a global pandemic broke loose. To top it all off, I am now finally writing the acknowledgements for the PhD thesis that has been my pursuit for the last four and a half years…

I start by thanking my Supervisors, Professors Nuno Silvestre and João Ramôa Correia, who have supported and mentored me throughout this entire time, aside from my MSc dissertation. By working with and learning from them, this PhD gave me both scientific and personal growth. It has been an amazing experience to learn from them the art of researching.

I would also like to thank my colleagues in Core Group, who have shared in a lot of my trials and were always ready to lend a hand. My thanks to Francisco Nunes, João Firmo, João Sousa, José Gonilha, Luís Valarinho, Mário Garrido and Mário Sá. There is not room enough to fully thank all my PhD colleagues, but I could not go without expressing my thanks for their good company: Adriana, Eloísa, Inês, António, Miguel, David, Chao, Mateus, Wallace, Bruno, Shahid, and Pietro. Special thanks also to Mário Arruda, without his cooperation this thesis would not have the same quality, especially in regard to the performed numerical studies.

In the experimental front, I must leave special thanks to Fernando Alves, who always had the best idea on how to manufacture specimens and test setups. I would also like to thank the staff of the Laboratório de Construção and Núcleo de Oficinas, who were always ready to help. In addition, I am thankful for the help of Professor Virgínia Infante and Laboratory Technician Pedro Teixeira, in performing my first CT test in the Mechanics Lab. Finally, I would like to thank MSc student Vítor Bergamaschi for his help in performing web-crippling tests.

I would also like to thank the contributions of my non-FRP PhD colleagues, André Biscaya, João Pacheco, Luís Vieira and Sérgio Nascimento. In addition, I would like to thank the support staff at IST, namely Elaine Gregório and Filipe Aparício, who are enablers of research.

My research had also significant inputs from outside IST. I would like to thank Professors Pedro Camanho and Albertino Arteiro, for their support during my stay at FEUP. In addition, I would like to thank Professors Brian Bak and Esben Lindgaard - their course on fracture mechanics and their cooperation at AAU helped pave the way for my research.

In both my journeys to Porto and Aalborg I was fortunate to also find colleagues who made my stay more comfortable, in particular Carolina Furtado in Porto and Christian Krogh and Jacob Oest in Aalborg.

I would naturally like to thank FCT for sponsoring my PhD. In addition, I would like to thank the companies that provided materials for the studies performed in this thesis: Alto Perfis Pultrudidos Lda., Creative Pultrusions, Fiberline Composites and STEP.

Throughout these four and a half years I focused on a very narrow set of topics, fracture toughness and web-crippling. However, I was fortunate to engage in significantly different activities, from straight eight hour days in the laboratory, cutting, drilling, measuring, painting, marking and testing experimental specimens, to learning a bit of Fortran and implementing UMATs in Abaqus, while fighting over Abaqus licenses so that I could run my numerical models, and, finally, to the time of sitting down and writing it all into papers and a thesis.

My experience would not have been the same without the amazing office partners that I got in office 2.45. Acting as emotional co-supervisors, André Castelo and Tiago Morgado were there for a lot of my experimental and numerical trials.

Outside IST I also have a lot of people to thank, starting with my family who always provided examples to follow and continued support. I am fortunate to have both parents with amazing careers in research, who understand that the day of a researcher is not measured in hours but in results, ideas and breakthroughs. My thanks also to my brother Pedro, for his continued guidance and support, as well as his beautiful family, Vanda, Martim and Carminho.

Aside from my two big families in the Almeida Fernandes and Rocheta, I would like to thank my late grandparents, Maria Amélia and Afonso Almeida Fernandes, Maria Luísa and Daniel Rocheta: their examples continue to inspire me to this day.

To all my friends, who helped shape me into who I am today, thank you very much! This includes the fine people I met along the way in Externato Luso-Britânico, Colégio Valsassina, Ilustres Caderninhos, IST, Sogencivil and CINCLUS. I especially thank my best men, Bernardo Costa, Filipe Nogueira and Luís Oliveira. Finally, special thanks to my younger brother in life, João Sérgio, who is simultaneously a great example of things to follow and to avoid.

My thanks also to all who journeyed with me at Campo Grande Parish, it made a big part of who I am today. In particular, I am thankful for the patience of Rui, Frederico and Gonçalo. And I would also like to give thanks for the teachings and examples of Rocío and Teresa.

This last year has been rough on everyone, but I still have a lot to be thankful for. I am thankful that my new family, Abela and Fernando, have accepted me so well. And, finally, I am truly thankful to have found someone unique in this world to make a life with me, someone whose inner child matches mine in such a perfect way. Someone who is always there to support me when I doubt myself. Thank you Joana!

And for the blessing of everything written above, I thank God.

Para os meus Pais,

os melhores exemplos que poderia pedir.

Obrigado.

Table of contents

List of figures

List of tables

Notation

Roman lower case

a – notch length (equal to $a_0+\Delta a$)

a_0 – initial notch length

d_f^c – damage variable for longitudinal compression

d_f^t – damage variable for longitudinal tension

d_m^c – damage variable for transverse compression

d_m^t – damage variable for transverse tension

d_s – shear damage variable

d_u – applied displacement at ultimate load of WCT test

f_s – interlaminar shear strength

h – height of the profile section

h_w – height of the web of a profile

k_{eq} – undamaged stiffness

k_r – damaged stiffness in residual stress plateau

k_F – calibrated buckling factor

l_b – bearing length

$l_{b,eff}$ – effective bearing length

r – web-flange junction radius

t_w – thickness of the web of a profile

w – distance between the centre of the bearing holes and the back face of CT, CCT and WCT specimens

Roman capital

E_{11} – longitudinal elastic modulus (alternatively E_x)

E_{22} – in-plane transverse elastic modulus (alternatively E_y)

F – Load

F_f^c – Hashin criterion for longitudinal compression

F_f^t – Hashin criterion for longitudinal tension

F_i – numerical damage initiation load

F_m^c – Hashin criterion for transverse compression

F_m^t – Hashin criterion for transverse tension

F_u – ultimate load

G – energy release rate

G_{12} – shear elastic modulus (alternatively, G_{xy})

G_1^+ – longitudinal tensile fracture toughness

G_1^- – longitudinal compressive fracture toughness

G_2^+ – transverse tensile fracture toughness

G_2^- – transverse tensile fracture toughness

G_c – fracture toughness (also referred to as critical energy release rate)

K_I – stress intensity factor for mode I fracture phenomena

P_{buck} – web buckling load

P_{crush} – web crushing load

P_u – web-crippling ultimate load

Greek symbols

χ – buckling reduction factor

δ_{eq} – equivalent applied displacement to a given finite element

Δa – crack growth length

ε_{11} – longitudinal strains

ε_{22} – transverse strains

γ_{12} – shear strains

λ – slenderness

λ_t – transitional slenderness in direct strength method

ν_{12} – Poisson coefficient (alternatively ν_{xy})

σ_{11} – longitudinal stress

σ_{22} – in-plane transverse stress

σ_c – maximum cohesive stress measured through G *vs*. CTOD curves

σ_r – residual stress in compression

σ_{u11} – ultimate longitudinal stress (for tension (+) and compression (-))

σ_{u22} - ultimate transverse stress (for tension (+) and compression (-))

$\hat{\sigma}$ – effective stress, computed as a function of numerical damage

τ_{12} – shear stress

τ_{u12} – ultimate shear stress

Acronyms

C – compliance

CC – compliance calibration

CCT – compact compression test

CFM – continuous filament mats

CFRP – carbon fibre reinforced polymer

CLC – combined load in compression

CMCD – crack mouth closing displacement

CMOD – crack mouth opening displacement

CoV – coefficient of variation

CT – compact tension test

CTCD – crack mouth closing displacement

CTOD – crack tip opening displacement

DCB – double cantilever beam

DEN – double edge notched

DIC – digital image correlation

DSM – direct strength method

ECT – extended compact tension test

EG – end ground configuration

EOF – end one flange configuration

ETF – end two flange configuration

FE – finite element

GFRP – glass fibre reinforced polymer

IG – interior ground configuration

IOF – interior one flange configuration

ITF – interior two flange configuration

LEFM – linear elastic fracture mechanics

LG – linear geometrical analysis

MCC – modified compliance calibration

NLG – non-linear geometrical analysis

OCT – over-height compact tension test

UMAT – user-defined material subroutine

WCT – wide compact tension test

Part I
Introduction

Preamble

Pultruded GFRP profiles have shown great potential for the construction industry; their low weight, non-corrodibility and high strength are significant advantages compared to traditional materials. However, their brittle behaviour poses a significant drawback to their implementation; moreover, there are still significant challenges in the numerical simulation of failure in these composite materials.

Web-crippling failure of pultruded GFRP profiles is a complex and less understood phenomenon that highlights the research need for advanced numerical tools to predict the ultimate loads.

Considering these challenges, fracture toughness has been implemented in numerical models with the goal of simulating damage evolution in composite materials. However, the determination of fracture properties of composite materials remains a challenging topic.

Part I sheds light into the topics of fracture toughness characterization of pultruded GFRP materials and web-crippling failure of pultruded GFRP profiles, summarizing previous research performed on these topics and the most significant challenges and research needs that justified the present thesis.

Chapter 1. Introduction

1.1. Context and motivation

Pultruded glass fibre reinforced polymer (GFRP) profiles have been increasingly implemented in the construction sector [1.1]. These materials are known for their high strength, non-corrodibility and lightweight, which make them an attractive alternative solution to traditional construction materials [1.2]. However, significant research needs still exist regarding the structural behaviour of pultruded GFRP materials; therefore, in spite of their advantages, these materials have been significantly hindered due to the lack of well-established design guidelines [1.3, 1.4].

The study presented in this thesis pursues the research conducted by the author [1.5-1.7] in his Master Dissertation, which addressed the web-crippling behaviour of pultruded GFRP beams, under end two flange (ETF) and interior two flange (ITF) load configurations. This previous research was motivated by the fact that the web-crippling of pultruded GFRP profiles had been poorly characterized [1.3], unlike steel structures for which well-established design formulae had long been developed [1.8-1.10]. In such previous research, experimental web-crippling tests were successfully conducted [1.5]; however, the corresponding numerical simulations fell short in accurately capturing the experimental failure loads [1.6]. These finite element (FE) numerical models used a stress-based failure initiation criterion, the Tsai-Hill criterion [1.11], to establish numerical failure; however, these predictions were found to range between 34% and 70% of the experimental failure loads.

In a subsequent numerical study, Nunes *et al*. [1.4] found out that using the Hashin failure initiation criterion [1.12], coupled with Abaqus [1.13] built-in damage evolution tools, the numerical estimates of the failure load reached a range of ≈80% of experimental results. However, Nunes *et al*. [1.4] implemented values for the fracture toughness properties (needed as input for the damage formulations implemented in Abaqus [1.13]) that lacked experimental basis; in fact, at that stage there was no knowledge about the actual values of the fracture properties of pultruded GFRP materials. The results reported in [1.4, 1.6] highlight the research needs regarding the numerical simulation of web-crippling phenomena, namely the need for more accurate and validated models. Such validation also depends on obtaining more comprehensive test data from web-crippling tests, namely local strain distributions. In spite of the above-mentioned experimental and numerical research efforts, the available design guidelines for FRP structures still do not provide any reliable formulae for the verification of web crippling, despite the relevance of this failure mode.

Based on these previous studies and the research needs that they highlighted, an experimental study was conducted within the present thesis to determine the fracture properties of pultruded GFRP materials, enabling the development of accurate non-linear numerical models able to accurately simulate web-crippling tests and other structural load cases. This was a challenging task, as very little research was performed on this topic for pultruded GFRP materials [1.14, 1.15]. In an initial stage, the study of fracture properties was intended to be a small part of the thesis, with its main focus lying on web-crippling studies, addressing a significant number of section geometries and test configurations. However, the wide application scope of these fracture properties, as well as the complexity and lack of information regarding their characterization, motivated a shift in the scope of the thesis. Therefore, comprehensive research was developed regarding a narrower range of materials, focusing on the characterization of the transverse fracture properties in tension and compression of different pultruded GFRP profiles and on web-crippling studies of a narrower set of test configurations. Web-crippling tests focused on acquiring additional and more detailed experimental data, in order (i) to validate fracture toughness-based models, and (ii) to provide the basis for novel design expressions.

1.2. Objectives and methodology

The research reported in this thesis had two main objectives: (i) to investigate the transverse fracture behaviour of various pultruded GFRP profiles, covering a wide range of fibre layups; and (ii) to better understand the web-crippling phenomenon and provide accurate formulae for the web-crippling design of pultruded GFRP profiles.

The accomplishment of the first objective, which focuses on **investigating the fracture behaviour in the transverse (in-plane) direction of pultruded GFRP materials**, entailed the following steps: (i) to establish a valid methodology to determine the fracture toughness in pultruded GFRP materials; (ii) to test a wide sample of materials, with different mechanical properties and fibre layups; and (iii) to develop FE numerical models to implement and validate the experimentally based fracture properties.

The first step consisted of analysing several methodologies, as no well-established standard test method was available to determine the fracture properties of composite materials [1.16, 1.17]. Furthermore, most research in this topic has focused in carbon fibre reinforced polymer (CFRP) materials for aerospace and automotive industries [1.18]. These materials, despite sharing several features with construction grade pultruded GFRP profiles, present higher levels of quality control, lower thicknesses and more complex fibre layups [1.14]. These are all relevant features when selecting a test configuration for fracture toughness assessment. Wide compact tension tests (WCT), depicted in Figure 1.1 (a), were found to provide accurate fracture toughness results, when coupled with visually based data reduction methods. In a different perspective, compressive fracture properties were assessed through an inverse methodology applied to scaled-up compact compression tests (CCT), illustrated in Figure 1.1 (b).

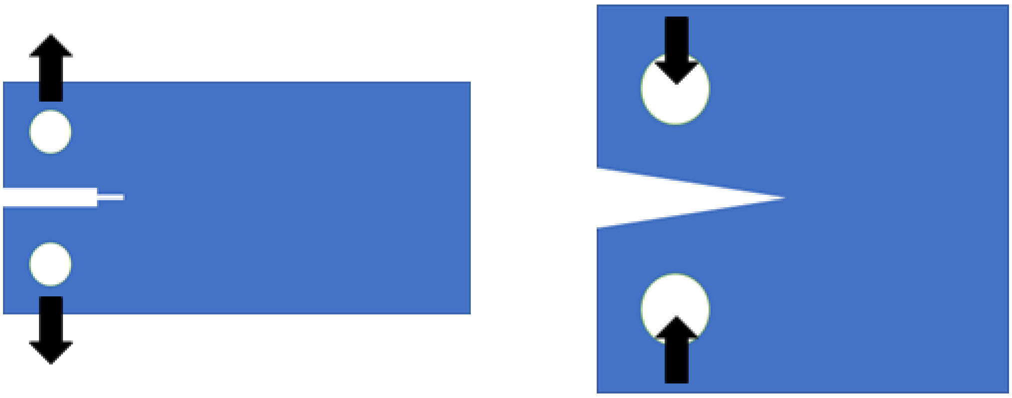

(a) (b)

Figure 1.1: Selected fracture test configurations: (a) WCT; (b) CCT.

Having established valid test methodologies, the second step consisted of applying this methodology to a wide variety of pultruded GFRP materials, including different manufacturers, laminate thicknesses, material properties and fibre layups. This step was of great importance, as fracture toughness has been reported to present significant levels of variability with respect to different thicknesses and fibre layups [1.19, 1.20]. These materials were also subjected to an extensive experimental mechanical characterization programme, in order to enable data-reduction methods for fracture toughness estimation, as well as to provide data for FE numerical models.

Finally, having tested a wide sample of materials, the development of FE models was found to be an efficient method to validate the experimentally determined fracture properties. To this end, FE numerical models were developed to simulate the fracture tests for all tested materials.

Regarding the second major objective of the thesis, to **develop accurate design formulae for web-crippling of pultruded GFRP profiles**, three research axes were defined: (i) experimental web-crippling tests were performed, for a wide range of fibre layups; (ii) FE numerical models were developed, based on the Hashin damage initiation criterion and the previously determined fracture properties; and (iii) an analytical study was performed based on experimental and numerical results, in order to establish new design formulae for web-crippling of pultruded GFRP profiles.

The first research axis consisted of upgrading previously performed web-crippling tests [1.5], by using a video-extensometry system, which enabled an analysis on the compressive and shear strains of each specimen. The experimental study addressed end-two-flange (ETF) and interior-two-flange (ITF) configurations, illustrated in Figure 1.2, similarly to the experimental study detailed in [1.5]. Moreover, the experimental study encompassed a significant variety with respect to cross-section geometries, fibre layups and manufacturers.

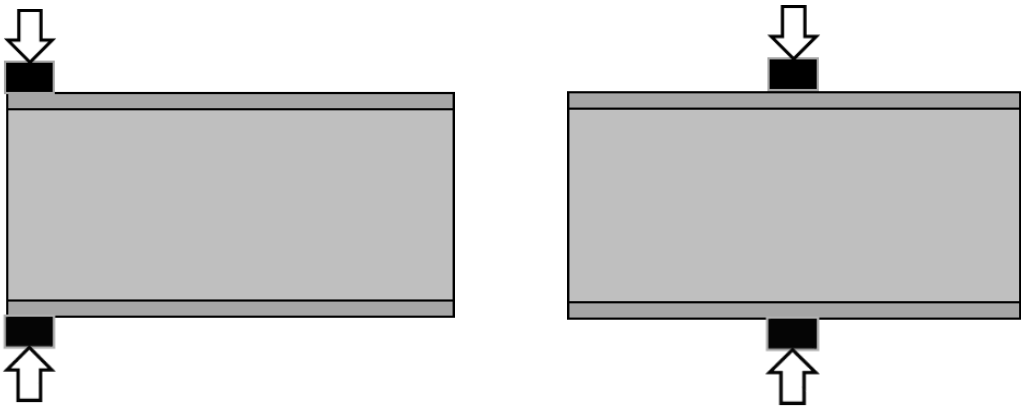

(a) (b)

Figure 1.2: Selected web-crippling test configurations: (a) ETF; (b) ITF.

The second axis consisted of modelling the performed experimental web-crippling tests, to compare experimental failure loads and numerical failure predictions, based on the Hashin criterion [1.12] and the fracture properties determined for each material. These models also included a geometrically non-linear analysis, in order to compare experimental and numerical failure modes, which are typically defined as either web-crushing (near the web-flange junction) or web-buckling (damage at the centre of the web, which buckles).

Finally, the third research axis consisted of developing new design formulae, implementing the direct strength method (DSM) [1.21], based on the previously determined experimental and numerical results. To this end, numerical models were used to determine web buckling and crushing loads, for a wider range of geometries and bearing lengths. These results were then used to define approximate analytical expressions for both failure modes, as well the ultimate loads corresponding to the interactive modes, as depicted schematically in Figure 1.3. Finally, the DSM curve was determined as a function of these approximate expressions and experimental results.

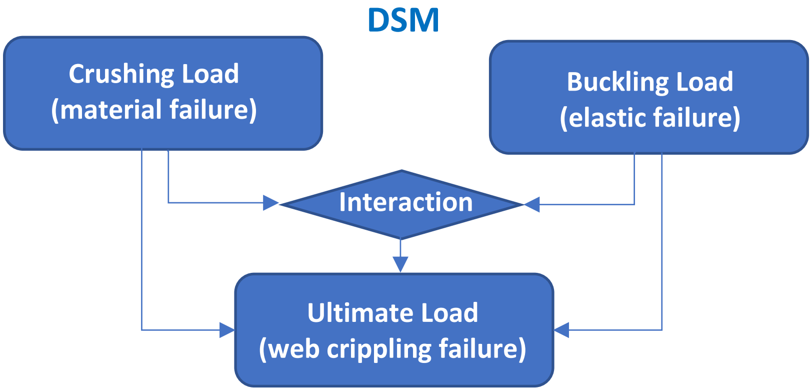

Figure 1.3: DSM flowchart for the design against web-crippling failure.

1.3. Main scientific contributions

The main scientific contributions of this thesis can be defined as follows:

- Experimental characterization of transverse fracture toughness of pultruded GFRP materials in tension, with varied thicknesses and fibre layups;
- Development of accurate FE numerical models of fracture tests;
- Experimental characterization of transverse fracture toughness of pultruded GFRP materials in compression, with varied thicknesses and fibre layups;
- Experimental characterization of web-crippling phenomenon in ETF and ITF configurations;
- Accurate numerical simulation of web-crippling tests in ETF and ITF configurations;
- Development of accurate guidelines for web-crippling design of pultruded GFRP profiles (ETF and ITF configurations).

The transverse fracture properties in tension were a steppingstone for the determination of the fracture properties in compression, which are more relevant for web-crippling load cases. This stems from the significant research found for tensile fracture tests [1.18], whereas compressive fracture tests have been the object of much less research [1.22-1.24]. The developed fracture tests were able not only to estimate the fracture toughness, but also provided additional information into the shape of the cohesive law of each material. These results were disseminated in the following two journal papers:

> Almeida-Fernandes, L., Silvestre, N., Correia, J. R., Characterization of transverse fracture properties of pultruded GFRP material in tension, *Composites Part B: Engineering*, 175, 107095, 2019.
>
> Almeida-Fernandes, L., Correia, J. R., Silvestre, N., Transverse fracture behaviour of pultruded GFRP materials in tension: Effect of fibre layup, *Journal of Composites for Construction*, 24(4), 04020019, 2020.

The FE numerical models developed to simulate the experimental fracture tests were an important step to validate the experimentally based fracture properties. The Hashin criterion was used to establish damage initiation and the fracture properties were used to control damage propagation. This part of the research resulted in the following two publications:

> Almeida-Fernandes, L., Silvestre, N., Correia, J. R., Arruda, M. R. T., Fracture toughness-based models for damage simulation of pultruded GFRP materials, *Composites Part B: Engineering*, 186, 107818, 2020.

Lopes, B., Arruda, M.R.T., Almeida-Fernandes, L., Castro, L., Silvestre, N., and Correia, J.R., Assessment of Mesh Dependency in the Numerical Simulation of Compact Tension Tests for Orthotropic Materials, *Composites Part C: Open Access*, ISSN: 2666-6820, submitted.

After a comprehensive study of tensile fracture properties, an experimental study was performed into the compressive fracture properties of pultruded GFRP materials. Several test configurations were tested, as most led to several unintended failure modes, hindering accurate results to be obtained by most of them. Ultimately, an inverse methodology was implemented, using FE models to help estimating the compressive fracture properties. The results obtained in this part of the thesis are presented in:

Almeida-Fernandes, L., Silvestre, N., Correia, J. R., Arruda, M. R. T., Compressive transverse fracture behaviour of pultruded GFRP materials: experimental study and numerical calibration, *Composite Structures*, 247, 112453, 2020.

After characterizing the fracture properties of these pultruded GFRP materials, an experimental study was performed for web-crippling test configurations ETF and ITF. These experimental tests led to a better understanding of web-crushing and web-buckling failure phenomena, also providing additional information on the strain fields of each specimen through a video-extensometry system. The most relevant results obtained in this part of the research are presented in:

Almeida-Fernandes, L., Correia, J. R., Silvestre, N., Effect of fibre layup in web-crippling of pultruded GFRP profiles, *Composite Structures*, submitted, 2020.

Having performed the experimental tests, numerical FE models were developed, also based on the Hashin criterion for damage initiation assessment and fracture toughness for damage evolution. The stiffness, strain results, experimental failure modes and failure loads were then compared to numerical results. These numerical results led to the following publication:

Almeida-Fernandes, L., Silvestre, N., Correia, J. R., Fracture toughness-based models for web-crippling of pultruded GFRP profiles, *Composites Part B: Engineering*, submitted, 2020.

Finally, based on previous experimental and numerical results for web-crippling loading cases, new design formulae were proposed. Approximate analytical expressions were proposed for web buckling and web crushing failure modes, which were then addressed simultaneously through the DSM. These results are presented in:

Almeida-Fernandes, L., Silvestre, N., Correia, J. R., Direct strength method for web-crippling design of pultruded GFRP beams, *Journal of Composites for Construction*, submitted, 2020.

In addition to the previous publications in international journals, the following conference papers and presentations were prepared:

Almeida-Fernandes, L., Correia, J.R., Silvestre, N., "Web-crippling of pultruded GFRP profiles: experimental, numerical and analytical study", *International Conference on Thin-Walled Structures*, N. 21, 19 p., July 2018, Lisbon.

Almeida-Fernandes, L., Silvestre, N., Correia, J.R., "Assessment of fracture toughness of pultruded GFRP composites", *International Conference on Thin-Walled Structures*, N. 115, 20 p., July 2018, Lisbon.

Almeida-Fernandes, L., Silvestre, N., Correia, J.R., "Characterization of the transverse fracture properties of pultruded GFRP materials in tension", *VI International Conference on Computational Modelling of Fracture and Failure of Materials and Structures*, June 2019, Braunschweig.

1.4. Document outline

This thesis is divided into the following four parts:

- Part I – introduction and state of the art review (Chapters 1 and 2);
- Part II – fracture toughness experimental assessment (Chapters 3 to 5);
- Part III – web-crippling analysis (Chapters 6 to 8);
- Part IV – conclusions and future developments (Chapter 9).

Chapter 1 introduces the context in which this research is framed, as well as the main objectives and the methodologies that were used to pursue them. Finally, the document structure is detailed herein.

Chapter 2 presents a review of the state of the art, focused on the two main topics of the document: (i) fracture toughness of composite materials; and (ii) web-crippling of pultruded GFRP profiles.

Chapter 3 presents the experimental characterization tests that were performed, as well as the experimental methodologies considered for fracture toughness estimations. Various strength and elastic properties were characterized and the fibre layups were assessed through calcination tests. The selected methodology for fracture testing is further detailed, including the data reduction methodologies, which are required for determining the fracture toughness and the cohesive law shape.

Chapter 4 presents the tensile fracture tests performed for various pultruded GFRP materials, including the experimental programme, specimen geometries and experimental results. In addition, the fracture toughness results are analysed as a function of fibre layups, in order to assess the impact of transverse reinforcement layers in these results. Finally, FE numerical models that simulate the performed fracture tests are presented and a comparison is performed between experimental and numerical results.

Chapter 5 presents an experimental and numerical study regarding the transverse fracture toughness in compression. In this respect, an inverse methodology was implemented, by using FE numerical models to estimate the fracture toughness, validated by comparing experimental and numerical load *vs*. displacement curves. These results were also analysed in what concerns the influence of different fibre layups in the compressive fracture response.

Chapter 6 presents the experimental study on web-crippling. A significant amount of test data was obtained, resulting from a total of 87 experimental tests, which provided failure modes, stiffness, ultimate loads and compressive and shear strains.

Chapter 7 presents a numerical study that consisted of simulating the previous experimental web-crippling tests. The numerical models were calibrated with the mechanical and fracture properties determined in Chapters 3 to 5. The comprehensive web-crippling experimental data were used to further validate the numerical models.

Chapter 8 presents an analytical study on the design against web-crippling failure of pultruded GFRP profiles, grounded on the results reported in Chapters 6 and 7. The DSM was implemented in this respect, in order to address simultaneously web buckling and web crushing failure modes.

Chapter 9 summarizes the main conclusions of this document, organized in the two aforementioned main topics. In addition, a summary is provided of the main future developments that should be considered in furthering the current knowledge on fracture toughness and web-crippling of pultruded GFRP profiles.

1.5. References

[1.1] Correia J. R., Branco F. A., Silva N. M. F., Camotim D., Silvestre N., First-order, buckling and post buckling behaviour of GFRP pultruded beams. Part 1: Experimental study, *Computers and Structures*, 89, pp. 2052-2064, 2011.

[1.2] Wu, C., Bai, Y., & Zhao, X. L., Improved bearing capacities of pultruded glass fibre reinforced polymer square hollow sections strengthened by thin-walled steel or CFRP, *Thin-Walled Structures*, 89, pp. 67-75, 2014.

[1.3] Borowicz, D. T., Bank, L. C., Behavior of Pultruded Fiber-Reinforced Polymer Beams Subjected to Concentrated Loads in the Plane of the Web, *Composites for Construction*, 15(2), pp. 2-9, 2011.

[1.4] Nunes F., Silvestre N., Correia JR., Progressive damage analysis of web crippling of GFRP pultruded I-sections, *Composites for Construction*, 21(3), pp. 1-13, 2016.

[1.5] Almeida-Fernandes, L., Gonilha, J., Correia, J. R., Silvestre, N., Nunes, F., Web-crippling of GFRP pultruded profiles. Part 1: Experimental study, *Composite Structures*, 120, pp. 565-577, 2015.

[1.6] Almeida-Fernandes, L., Nunes, F., Silvestre, N., Correia, J. R., Gonilha, J., Web-crippling of GFRP pultruded profiles. Part 2: Numerical analysis and design, *Composite Structures*, 120, pp. 578-590, 2015.

[1.7] Almeida-Fernandes, L., Structural behaviour of GFRP beams subjected to concentrated loads: experimental tests, numerical modeling and analytical study, MSc dissertation in Civil Engineering, Instituto Superior Técnico, Lisbon, Portugal, 2014 [In Portuguese].

[1.8] AISI S100-2007, "North American Cold-Formed Steel Specification", American Iron and Steel Institute (AISI), Washington D.C., 2007.

[1.9] EN 1993-1-3:2006, "Eurocode 3 – Part 1-3: General rules – Supplementary rules for cold-formed members and sheeting", European Committee for Standardization (CEN), Brussels, 2004.

[1.10] EN 1993-1-5:2004, "Eurocode 3 – Part 1-5: Plated Structural elements", European Committee for Standardization (CEN), draft 49, Brussels, 2004.

[1.11] Tsai, S.W., *Strength characterisation of composite materials*, Tech. Rep. NASA CR-224, National Aeronautics and Space Agency (1965).

[1.12] Hashin, Z., and Rotem, A., A fatigue criterion for fiber-reinforced materials, *Journal of Composite Materials*, 7, pp. 448-464, 1973.

[1.13] Simulia, "Abaqus/CAE 2018", 2018.

[1.14] El-Hajjar, R., Haj-Ali, R., Mode-I fracture toughness testing of thick section FRP composites using the ESE(T) specimen, *Engineering Fracture Mechanics*, 72, pp. 631-643, 2005.

[1.15] Liu, W., Feng, P., Huang, J., Bilinear softening model and double K fracture criterion for quasi-brittle fracture of pultruded FRP composites, *Composite Structures*, 160, pp. 1119-1125, 2016.

[1.16] A. Bergan, A., Dávila, C., Leone, F., Awerbuch, J., Tan, T.M., A Mode I cohesive law characterization procedure for through-the-thickness crack propagation in composite laminates, *Composites Part B; Engineering*, 94, pp. 338-349, 2016.

[1.17] Ortega, A., Maimí, P., González, E.V., Trias, D., Specimen geometry and specimen size dependence of the R-curve and the size effect law from a cohesive model point of view, *International Journal of Fracture*, 205, pp. 239-254, 2017.

[1.18] Laffan, M.J., Pinho, S.T., Robinson, P., Mcmillan, A.J., Translaminar fracture toughness testing of composites: a review, *Polymer Testing*, 31, pp. 481-489, 2012.

[1.19] Li, X., Hallett, S.R., Wisnom, M.R., Zobeiry, N., Vaziri, R., Poursartip, A., Experimental study of damage propagation in Over-height Compact Tension tests, *Composites Part A: Applied Science and Manufacturing*, 40, pp. 1891-1899, 2009.

[1.20] Laffan, M.J., Pinho, S.T., Robinson, P., Iannucci, L., Measurement of the in situ ply fracture toughness associated with mode I fibre tensile failure in FRP. Part II: size and lay-up effects, *Composites Science and Technology*, 70, pp. 614-621, 2010.

[1.21] Schafer, B. W., Peköz, T., *Direct strength prediction of cold-formed steel members using numerical elastic buckling solutions*, Fourteenth International Specialty Conference on Cold-Formed Steel Structures, St. Louis, Missouri, October 15-16, 1998.

[1.22] Ratcliffe, J., Jackson, W., & Schaff, J., “Predicting the compression strength of impact-damaged sandwich panels”, American Helicopter Society 60th Annual Forum, Baltimore, 2004.

[1.23] Pinho, S. T., Robinson, P., & Iannucci, L., Fracture toughness of the tensile and compressive fibre failure modes in laminated composites, *Composites Science and Technology*, 66(13), pp. 2069-2079, 2006.

[1.24] Pinho, S. T., Gutkin, R., Pimenta, S., De Carvalho, N. V., & Robinson, P., On longitudinal compressive failure of carbon-fibre-reinforced polymer: from unidirectional to woven, and from virgin to recycled. *Phil. Trans. R. Soc. A, Physical and Engineering Sciences*, 370, pp. 1871-1895, 2012.

Chapter 2. State of the art

2.1. Introduction

The study presented in this thesis addresses two different but interconnected main topics, fracture toughness and web-crippling of pultruded GFRP materials. These are significantly different topics, as fracture toughness is a concept with a wide range of applicability, whereas web-crippling is a structural case with a narrower research scope. These two topics are brought together in this thesis, as fracture toughness may be used as a damage evolution input parameter in finite element numerical models, a tool that was found to be necessary in order to accurately simulate the complex failure of pultruded GFRP profiles subjected to web-crippling tests [2.1, 2.2].

In the following sections, these topics are further detailed, with particular focus on their application to pultruded GFRP materials. It should be noted that both these topics have been initially developed and implemented in the scope metallic materials, which are easier to characterize than FRP materials, given their homogenous and isotropic nature.

Fracture toughness characterization of composite materials has been the topic of several experimental studies, spanning a considerable period of time, as summarized in [2.3, 2.4], whereas web-crippling of pultruded GFRP materials has been addressed by a reduced number of more recent experimental studies, which are summarized in [2.1]. This discrepancy justifies the significant amount of research presented ahead for fracture toughness experimental characterization and the fewer number of references regarding web-crippling of composite materials.

2.2. Fracture toughness

2.2.1. Concept and background

Fracture toughness, also known as critical energy release rate (G_c), was initially defined as a measure of energy required to propagate an initial crack further. This measure established that, if an applied load would provide less elastic energy than this threshold to a given cracked specimen, then the crack would not develop further. On the other hand, if a higher amount of energy would be provided, then the crack would develop in an unstable rate. Finally, if an equivalent amount of energy would be provided, in comparison to G_c, then the crack would be expected to propagate in a stable fashion [2.5]. In many studies, the fracture toughness has been quantified through the stress intensity factor K_I. Fracture toughness may be determined as a function of K_I [2.6], through the following expression,

$$G_c = \frac{{K_I}^2}{\sqrt{2E_xE_y}} * \sqrt{\sqrt{\frac{E_x}{E_y}} + \frac{E_x}{2G_{xy}} - \upsilon_{xy}} \tag{2.1}$$

where, for a crack developing in parallel to the longitudinal direction of a material, E stands for the elastic modulus in the longitudinal (x) and in-plane transverse (y) directions, G_{xy} is the shear elastic modulus and ν_{xy} is the Poisson coefficient.

In a broader and numerical perspective, this parameter has been implemented to represent the elastic energy that must be applied to a finite element in order to fully damage it [2.7]. A typical representation of this parameter is depicted in Figure 2.1, showing a reducing stress for increasing applied displacements, after an initial stage with elastic behaviour.

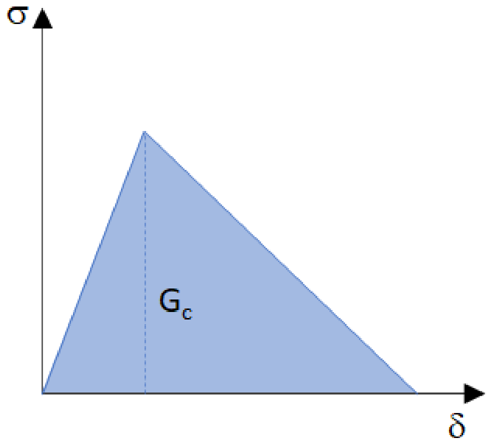

Figure 2.1: Representation of fracture toughness (critical energy release rate G_c), as a function of equivalent stress (σ) and displacement (δ).

This concept has since been applied to a wider scope of cases, as fracture toughness has been implemented as a damage evolution parameter for a broad range of structural cases [2.2, 2.8-2.10]. This property has significant impact for composite materials, as despite their brittle behaviour, some loading configurations have been shown to present significant damage propagation, with significant load increase beyond the damage initiation threshold [2.1, 2.2, 2.11]. This is a broad topic, as different crack opening modes may be considered, typically decomposed into three categories: (i) mode I, which consists of an opening failure mode; (ii) mode II, consisting of a shearing failure mode; and (iii) mode III, consisting of a torsional fracture process. These categories are illustrated in Figure 2.2.

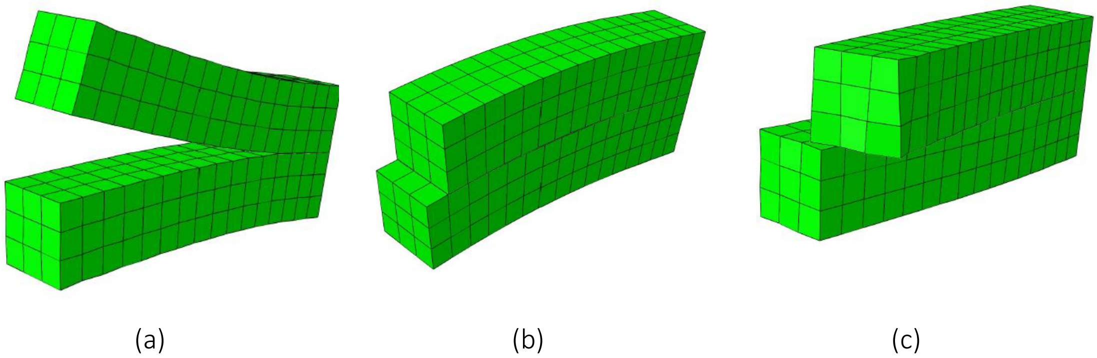

Figure 2.2: Different crack opening modes: (a) Mode I; (b) Mode II; (c) Mode III.

Fracture toughness has been thoroughly characterized for metallic materials, through standards, such as the ASTM E399 [2.12], which defines the test setup for compact tension (CT) tests, regarding metallic materials. However, and despite significant research having been performed on composite materials since the mid-twentieth century [2.3], there are still no well-established test standards for a comprehensive characterization of their fracture properties [2.13, 2.14].

Earlier studies in this topic showed a significant experimental and analytical variability [2.3], as the implementation of fracture toughness was still unclear and numerical solutions were hindered by technological limitations [2.4]. In the last decades, however, numerical implementation of damage evolution in numerical models has become common place, as exemplified by the built-in tools provided by Abaqus [2.15], coupled with the Hashin damage initiation criterion [2.16]. More recent studies still present a wide range of experimental methodologies; however, the goal of implementing fracture toughness in damage evolution [2.17, 2.18] or cohesive zone [2.19, 2.20] models has become a clear trend for research [2.21].

2.2.2. Fracture toughness of composite materials

2.2.2.1. Crack orientation

One major difference between studying fracture toughness in metallic and composite materials pertains to the internal heterogeneous structure of composite materials [2.22], in contrast with the homogeneous one of metallic materials. This internal structure of composites, which typically consists of a stacking of different plies, presenting potentially different fibre orientations, leads to significantly different mechanical behaviours, as a function of crack orientation. The various crack orientations are typically listed as: (i) interlaminar cracks, which develop between fibre layers in the material; (ii) intralaminar cracks, which develop between the fibres of a layer, developing perpendicularly to the layers plane; and (iii) translaminar cracks, which develop perpendicularly to the fibres and the layers plane. These various crack orientations are depicted in Figure 2.3.

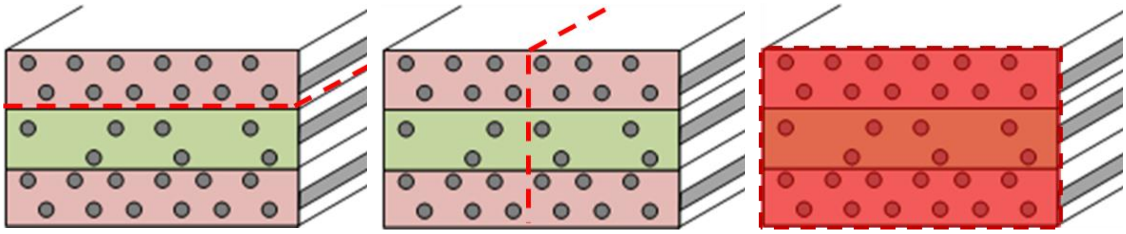
(a) (b) (c)

Figure 2.3: Different crack orientations in composite materials: (a) interlaminar; (b) intralaminar; (c) translaminar.

The characterization of intralaminar and translaminar fracture properties has been shown to present significant levels of variability [2.23, 2.24]. In addition, these phenomena have been shown to present a significant dependency not only on the global fibre layup of a material, but also on the stacking sequence of the layers of a given material [2.24, 2.25], as illustrated in Figure 2.4. Therefore, two materials with equivalent mechanical properties may show considerably different fracture behaviours.

Translaminar fracture processes have been shown to lead to significantly higher fracture toughness results, when compared to intralaminar or interlaminar fracture processes [2.6]. This stems from the fact that the fibres present much stronger mechanical properties than the resin matrixes that bind them together [2.6]. Intralaminar and interlaminar fracture processes are expected to yield similar fracture toughness results [2.26, 2.27].

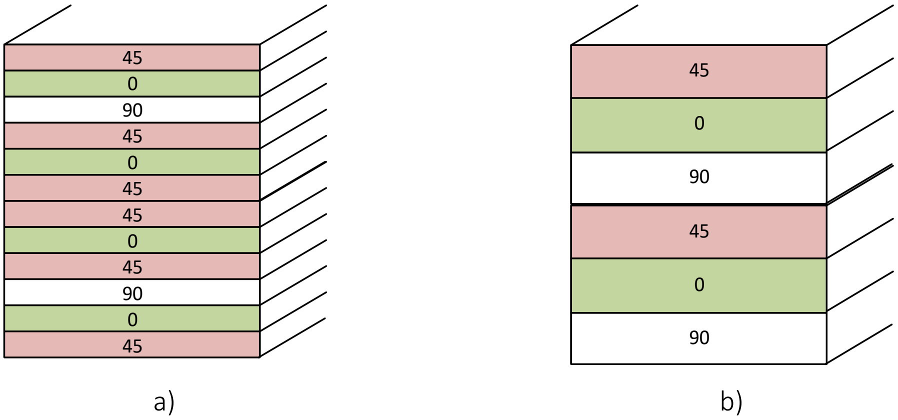

Figure 2.4: Angle-ply laminates: a) symmetrical and dispersed layup; b) asymmetrical and blocked layup.

Interlaminar phenomena have been thoroughly researched [2.4], as it is a typical phenomenon in automotive and aerospace structures. On the contrary, intralaminar and translaminar phenomena have received much less attention from the scientific community, which mainly addressed automotive or aerospace composite materials [2.28-2.30], typically CFRPs, with higher mechanical properties, quality control and more complex layups than pultruded GFRP materials typically used in construction [2.31]. To the best of the author's knowledge, construction grade pultruded GFRP materials have been experimentally characterized in respect to either intralaminar or translaminar fracture toughness in very few experimental studies [2.31, 2.32], which are further detailed in Section 2.2.3.4.

Pultruded GFRP materials typically present several layers with randomly oriented fibres, therefore the translaminar fracture process should be considered for these materials, regardless of the orientation of the crack. This conclusion is supported by the few available results in the literature (≈10 N/mm) [2.31, 2.32], which are significantly higher than the typical results found for interlaminar fracture toughness (typically ≈0.1 N/mm) [2.26, 2.27]. Therefore, translaminar test configurations should be more adequately applicable to pultruded GFRP materials, when compared to intralaminar test configurations.

2.2.2.2. R-curve behaviour and size effects

Another specific complexity of studying fracture toughness in composite materials pertains to the fibre bridging phenomenon, which causes an increasing R-curve behaviour, consisting of an increasing trend for the energy release rate (G) as a function of crack growth [2.6]. Fibre bridging consists of fibres interpenetrating the crack, behind the progressing crack tip [2.33]. As the crack length increases, more fibres interpenetrate the crack and the required energy to promote further crack growth increases – resulting in an increasing trend for G. When the crack propagation length reaches a certain limit, which depends on geometrical and mechanical properties, the initial bridging fibres no longer constrain the crack opening displacement and a stable energy release rate plateau is reached, as illustrated in Figure 2.5. The energy release rate reached at this plateau is considered to be the fracture toughness (critical energy release rate G_c) of the material [2.33]. This material behaviour may limit the experimental specimen geometries, as sufficient room for crack propagation is required, in order to reach the G_c plateau.

Furthermore, smaller specimens may lead to overestimations of fracture toughness, as the fracture toughness process zone is not allowed to develop completely. Ortega *et al.* [2.34] have proposed a ratio between the initial crack of a specimen and its other dimensions, in order to ensure that the fracture toughness determined through the test is accurate.

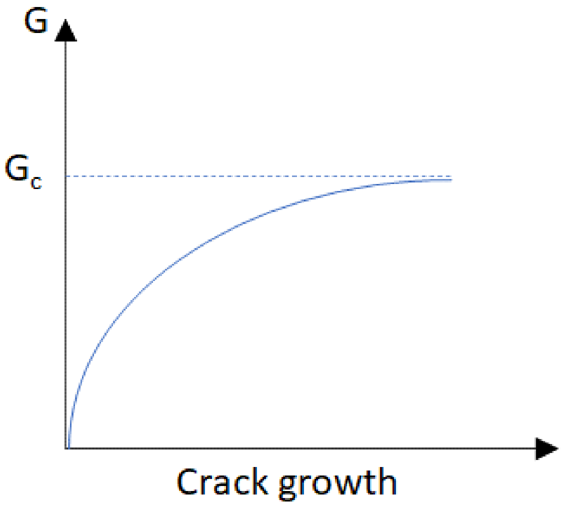

Figure 2.5: Representation of R-curve behaviour, in respect to crack propagation length.

2.2.2.3. Orthotropic behaviour

In addition to the different fracture orientations that may be considered, composite materials typically present an orthotropic behaviour, which leads to different elastic and strength properties in the longitudinal and transverse in-plane directions. This is also expectable for the longitudinal and transverse fracture behaviours. Furthermore, the compressive and tensile properties may also diverge significantly in the longitudinal and transverse directions. This has led to the development of failure criteria which take into account different material orientations, such as the Hashin criterion [2.16], as detailed below:

Fibre tensile failure
$$F_f^t = \frac{\sigma_1^2}{S_{t,1}^2} + \alpha \frac{\sigma_{12}^2}{S_{12}^2} < 1.0 \tag{2.2}$$

Fibre compressive failure
$$F_f^c = \frac{\sigma_1^2}{S_{c,1}^2} < 1.0 \tag{2.3}$$

Matrix tensile failure
$$F_m^t = \frac{\sigma_2^2}{S_{t,2}^2} + \frac{\sigma_{12}^2}{S_{12}^2} < 1.0 \tag{2.4}$$

Matrix compressive failure
$$F_m^c = \frac{\sigma_2^2}{4S_{23}^2} + \left(\frac{S_{c,2}^2}{4S_{23}^2} - 1\right) . \frac{\sigma_2^2}{S_{c,2}^2} + \frac{\sigma_{12}^2}{S_{12}^2} < 1.0 \tag{2.5}$$

Where 1, 2 and 3 represent the longitudinal, in-plane transverse and out-of-plane transverse directions of the material, *c* and *t* stand for compression and tension, *f* and *m* stand for fibre and matrix, σ stands for applied stress, *S* stands for ultimate stress and *F* represents the Hashin criterion ratio.

This failure initiation criterion has been coupled with damage evolution tools in Abaqus software [2.15], in order to simulate damage propagation in composite materials. However, as four different criteria are considered, there is also the need for four different fracture toughness parameters, to address damage in the longitudinal and transverse directions, for compressive and tensile loading [2.7]. This naturally poses an added complexity for studying fracture toughness in composite materials, when compared to more traditional and isotropic materials, as steel and concrete.

2.2.3. Experimental fracture tests

2.2.3.1. Tensile fracture tests

Given the significant array of fracture opening modes and crack orientations in composite materials, it should be highlighted that the research detailed below was sourced in respect to fracture opening mode I (see Figure 2.2), within the scope of intralaminar and translaminar studies (see Figure 2.3).

Several test configurations have been considered to address the translaminar fracture properties of composite materials, as summarized by Laffan *et al.* [2.4]. Significant research has been conducted on compact tension (CT) tests for a wide range of composite materials [2.3, 2.6, 2.13, 2.14, 2.23, 2.24, 2.27, 2.28, 2.30, 2.33-2.35]. The CT test configuration consists of square shaped specimens, as illustrated in Figure 2.6, with the load being applied through two bearing holes. Typical CT specimen dimensions consist of a squared specimen with ≈60 mm of height and width; however, several studies have used variants and different geometric scales for this test configuration [2.23, 2.24].

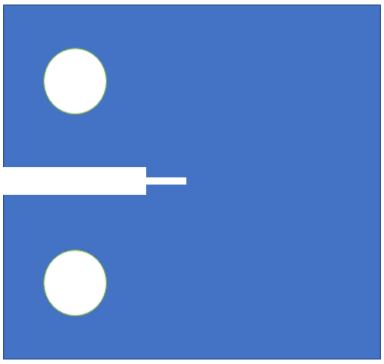

Figure 2.6: CT test specimen geometry.

The CT test configuration also paved the way for some similar configurations, such as the extended compact tension (ECT) [2.31, 2.36], over-height compact tension (OCT) [2.25, 2.37, 2.38] and the wide compact tension (WCT) [2.28]. These variants were meant to surpass unintended failure modes that occurred for the CT test. These various test configurations are illustrated in Figure 2.7.

The ECT test configuration involves using a specimen with a height equivalent to three to four times its width. Underwood *et al.* [2.36] considered this specimen geometry in order to circumvent unintended failure near the bearing holes, which occurred in previous CT tests. The OCT test was proposed by Kongshavn *et al.* [2.37] with a similar goal. The OCT specimen consists of a CT specimen with doubled height and may be considered as an intermediate solution between CT and ECT test configurations. In a different trend, the WCT specimen geometry consists of doubling the CT specimen width, providing additional room for damage propagation. The WCT test geometry has been applied to very few experimental studies on CFRP materials, as this geometry potentiates unintended buckling failure of the test specimens [2.28].

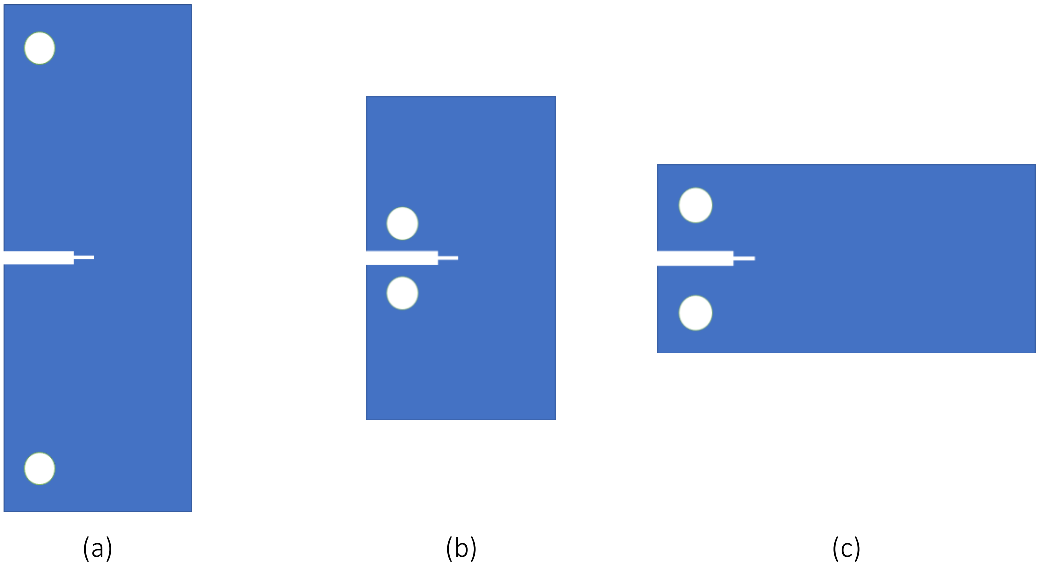

Figure 2.7: Different CT-based test configurations: (a) ECT; (b) OCT; (c) WCT.

In spite of the wide use of CT tests, some research [2.13, 2.34] has found that this test configuration may lead to overestimations of fracture toughness, due to the small dimensions of the specimen in respect to the initial notch. Ortega *et al.* [2.34] have proposed analytical expressions to derive the objectivity of a fracture test, in respect to its geometry. Of the previous CT-based geometries, only the WCT test would contribute to reducing this specimen geometry dependency issue.

An alternative to these CT-based tests consisted of using notched flexural tests [2.32, 2.36, 2.39]. The three-point-bending test has been implemented by different authors [2.32, 2.36]; however, Underwood *et al.* [2.36] reported that this configuration may be problematic, as the load is applied near the notch tip area (see Figure 2.8 (a)), promoting potential stress interactions between the loaded area and the notch tip area. A natural alternative is the notched four-point-bending test [2.39], which circumvents the aforementioned issue of the load application point. These flexural tests are illustrated in Figure 2.8.

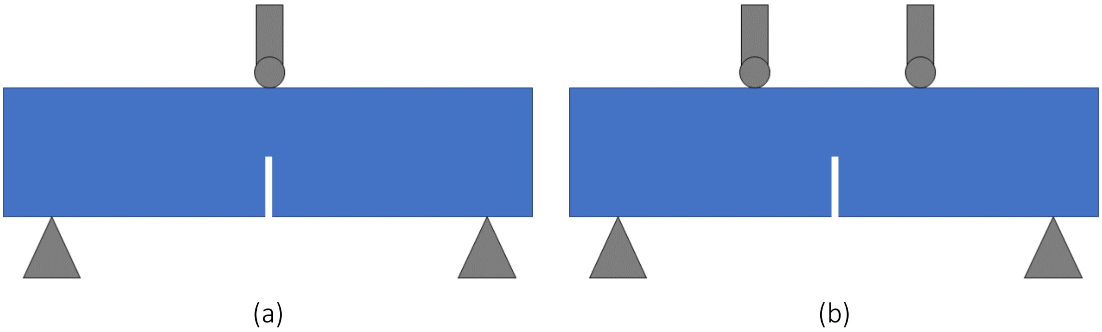

Figure 2.8: Fracture test configurations in bending: (a) 3-point bending; (b) 4-point bending.

Double-cantilever beam (DCB) test configurations were originally implemented for interlaminar fracture tests [2.27]; however, these have also been successfully applied to intralaminar fracture tests [2.22, 2.26, 2.40]. This test configuration, consisting of significantly longer specimens than previous CT based configurations, has the benefit of enabling longer and more stable crack propagation lengths. Unlike the CT and CT-based test configurations, DCB tests were not implemented in cases where the crack developed perpendicularly to fibre layers (translaminar fracture). Figure 2.9 illustrates a DCB test specimen.

The DCB test configuration has also been modified so that the load is introduced as applied moments at both specimen arms [2.41]. This methodology has been reported to present significant analytical advantages, as the fracture toughness results can be determined without the need to monitor crack growth lengths.

Figure 2.9: DCB test specimen geometry.

One complexity that is shared by all the above-mentioned test configurations is that the notch tip shape can severely impact damage initiation [2.6, 2.39]. In this respect, several methodologies have been implemented in order to minimize the notch tip radius, typically including two to three step procedures [2.6, 2.39]. Laffan *et al.* [2.42] have reported that the notch tip radius significantly influences damage initiation, but that damage propagation is not influenced by this parameter and thus, the determination of G_c should not be affected.

In a different perspective, Catalanotti *et al.* [2.43] have successfully implemented double edge notched (DEN) tests to determine the R-curve of composite materials. The authors implemented a methodology which consisted of deriving the R-curve shape based on the measurement of size-effects. To this end, several scaled specimens were tested to measure the size-effects, using this information to derive the R-curve. Scaled DEN specimens are displayed in Figure 2.10. One significant advantage of this methodology is that the notch tip shape has been reported to be irrelevant to the test accuracy, thus simplifying the test preparation process.

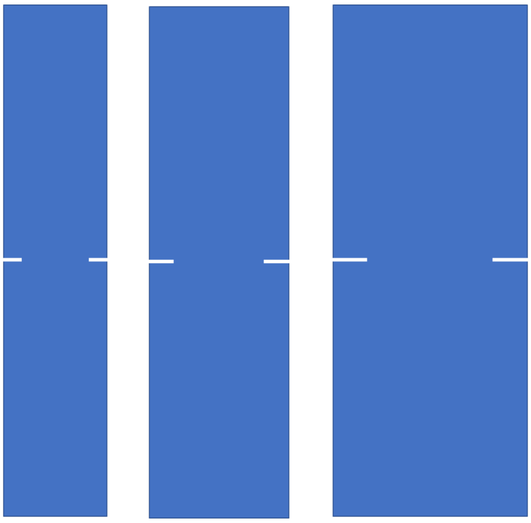

Figure 2.10: Scaled DEN specimens.

2.2.3.2. Compressive fracture tests

Compared to the above reported configurations for tensile fracture tests, compressive fracture tests have received much less attention from the research community. This can be attributed to the higher complexity of compressive fracture tests, which derives from: (i) the higher complexity of monitoring compressive kink bands in the test specimens [2.6]; (ii) compressive damage leads to non-zero strength in the damaged area (unlike an opening crack), leading to overestimations of fracture toughness, when tensile-based data reduction methodologies are implemented [2.6]; and (iii) compressive damage is significantly prone to combine different damage processes, as fibre kinking, delamination and local buckling of layers [2.44].

A CT-based configuration has been implemented in various experimental programmes [2.6, 2.35, 2.45], known as compact compression test (CCT)[1]. This test configuration is illustrated in Figure 2.11, with the main difference to CT tests being the V-shaped initial notch, which is intended to delay contact between the notch faces. However, as stated above, previous research found that using data reduction methods valid for tensile tests did not provide accurate measurements of fracture toughness for compressive tests, due to the aforementioned contact in the crushed area [2.6].

The four-point bending test has also been implemented for compressive analysis of fracture toughness. To this end, the specimen geometry presented in Figure 2.8 (b) simply needs to be inverted, with the initial notch developing from the top edge of the specimen. Laffan *et al.* [2.46] implemented this methodology to study translaminar fracture of unidirectional laminates. In order to better assess damage initiation, the authors implemented acoustic emission sensors, which showed that damage initiation occurred well before visual observation was possible. This is an interesting methodology, however, it remains unclear whether the four-point bending tests provide sufficient room for damage propagation in order to fully characterize fracture toughness.

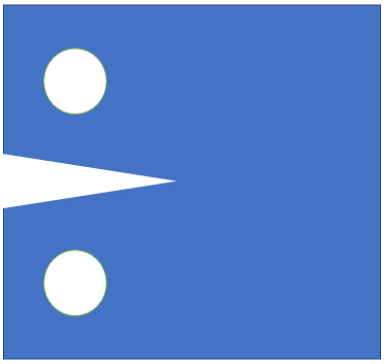

Figure 2.11: CCT test specimen geometry.

Catalanotti *et al.* [2.47] were successful in implementing the aforementioned size-effect methodology to compressive tests. This methodology requires a simplified experimental test setup and the preparation of specimens is also straightforward.

2.2.3.3. Data reduction methods

A significant complexity associated to performing fracture tests is the need to implement data reduction methods. Furthermore, these methods often require the measurement of the crack length throughout the test, a task that is complex, even more so in materials which are heterogeneous through the specimen thickness. These methods assemble different parameters from the experimental data, providing energy release rate estimates.

---

[1] This nomenclature was used to avoid the overlap between the typical abbreviations of compliance calibration and compact compression tests.

Despite the lack of well-established standards, there is a wide variety of methodologies to determine the fracture toughness of composite materials [2.13, 2.14]. These methods range from (i) inverse methodologies, which calibrate fracture properties as a function of experimental load *vs*. displacement curves; (ii) R-curve methods, which consist of measuring the energy release rate throughout crack propagation; and (iii) J-integral methods, which consist of using digital image correlation (DIC) to monitor the strain fields of the specimen, through which the J-integral can be estimated. For each of the above categories there are several variant methodologies.

The J-integral became a commonplace tool to assess fracture toughness, as it is straightforward to determine either in finite element numerical models or by processing the strain fields measured through DIC. If the framework of linear elastic fracture mechanics (LEFM) is applicable (considering that the specimen behaves mostly in an elastic fashion, aside from the crack tip area), the J-integral around the crack tip of a specimen may be considered equivalent to the energy release rate [2.13]. The J-integral consists of measuring the elastic strain energy density within a closed loop, as detailed below,

$$J = \int_{\Gamma_0} \left(w n_1 - \frac{\partial u}{\partial x_1} . t \right) dS \tag{2.6}$$

where, *J* stands for J-integral, n_1 is a unit vector, normal to the contour (Γ_0) of the integral, *t* is the traction vector, *u* stands for the displacement field, x_1 represents an axis aligned with the crack growth direction, *w* is the strain energy density, Γ_0 is a closed contour (encompassing a region around the crack tip, in fracture tests).

Several inverse methodologies may be considered, including performing numerical simulation of structural tests, in order to calibrate fracture properties [2.2, 2.10]. This is a cumbersome approach, especially when various damage phenomena are interacting. This process may also be implemented for fracture tests, which typically focus on a single type of damage. For instance, Ortega *et al.* [2.35] have developed an automatic inverse methodology which was found to provide good results for both CT and CCT configurations.

Focusing on R-curve methods, which have been implemented in a significant number of experimental studies, there are several variants that may be considered: (i) closed-form solutions have been developed for several test configurations, as exemplified by the ASTM E399 standard [2.12] for the CT test configuration in regard to metallic materials; (ii) FE-based J-integral estimates of energy release rate [2.6, 2.48]; (iii) compliance calibration (CC) methods have also been widely implemented [2.24, 2.48, 2.49], including a variant, typically known as modified compliance calibration (MCC) [2.24, 2.48], which consists of determining the crack growth as a function of specimen compliance, circumventing the need for crack growth measurements; and (iv) size-effect methodologies, as the aforementioned research of Catalanotti *et al.* [2.43, 2.47].

The above methodologies are focused on determining the fracture toughness of a material; however, these methodologies may also be used to determine the cohesive law shape of a material, based on measurements of the energy release rate and the crack tip opening displacement, throughout each test [2.41]. This would provide more complete information for numerical models aiming to simulate damage evolution in composite materials. Li *et al.* [2.33] have reported that determining the cohesive law shape is required to simulate damage evolution in smaller specimens. The authors determined fracture properties through CT tests and attempted to model DEN tests, reporting that only when the cohesive law of the material was included in the model it provided accurate estimates for the DEN tests [2.33].

2.2.3.4. Research on pultruded GFRP materials

As mentioned above the research of El-Hajjar and Haj-Ali [2.31] and Liu *et al.* [2.32] stand out as the only previous experimental studies on the fracture behaviour of construction grade pultruded GFRP materials. El-Hajjar and Haj-Ali [2.31] performed ECT tests for the longitudinal and transverse in-plane directions. Through these tests, the authors determined estimates of K_I, which can be extrapolated to G_c results through expression (2.1). The transverse direction of the material was found to present an average G_c value of 8.9 N/mm, whereas in the longitudinal direction the G_c value was 23.7 N/mm.

Regarding data reduction, El-Hajjar and Haj-Ali [2.31] used a closed-form solution presented in the ASTM 1922 standard [2.50]. The experimental programme of El-Hajjar and Haj-Ali [2.31] led to the recommendation of ASTM 1922 for pultruded materials. However, some doubts arise regarding this research work, as the specimens presented little room for crack propagation, and thus the R-curve behaviour of the material may not have been fully assessed.

In a more recent study, Liu *et al.* [2.32] performed three-point bending tests to determine the fracture properties of pultruded GFRP materials, in the transverse direction. The authors considered a bi-linear cohesive law to approximate the exponential behaviour of the material, decomposing the fracture toughness results into two stages, micro-cracking and fibre bridging, in order to determine the intersection point of the bi-linear cohesive law. The overall G_c reported for the material was 7.8 N/mm.

The lack of additional results highlights the stringent research need for accurately determining the fracture toughness of pultruded GFRP materials. In fact, in previous numerical studies, these properties are taken from sources in the literature [2.8], which do not necessarily address the same material used in the tests that are modelled, or are simply calibrated through FE numerical models [2.2, 2.9, 2.10].

2.3. Web-crippling

2.3.1. Concept and background

Web-crippling is a phenomenon that results from the application of concentrated loads in structural beams in their in-plane transverse direction, i.e. parallel to their webs. This loading case typically occurs, as an example, when secondary beams unload on primary beams near the supports, as illustrated in Figure 2.12.

Web-crippling has been thoroughly investigated for steel structures, as attested by the wide variety of well-established design formulae that can be found in different design codes [2.51-2.53]. On the contrary, for pultruded GFRP profiles, this loading case has been addressed by a reduced number of experimental programmes [2.54-2.59]. This lack of research is particularly concerning given the orthotropic nature of pultruded GFRP materials, where the weakest in-plane direction (transverse direction) is parallel to the load application direction of web-crippling cases. Some design expressions have been developed for pultruded GFRP profiles; however, these design guidelines typically present a narrow range of application, in terms of profile section geometries and dimensions [2.54, 2.56, 2.59].

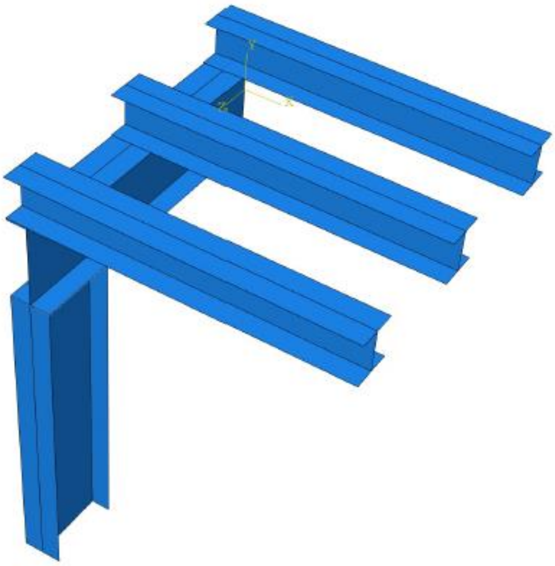

Figure 2.12: Design case for potential web-crippling failure.

This test configuration typically leads to two major failure modes: (i) web-crushing, which consists of material damage developing near one or both web-flange junctions, typically occurring for stockier profiles; and (ii) web-buckling, which consists of local-buckling with damage developing near the centre of the web, typically occurring for more slender profiles. Figure 2.13 illustrates these two failure modes.

(a) (b)

Figure 2.13: Typical web-crippling failure modes in pultruded GFRP profiles: (a) web-crushing; (b) web-buckling.

Web-crippling has been addressed in regard to a wide variety of test configurations: (i) end one flange (EOF), which consists of a short three-point bending test, with narrow supports at both beam extremities; (ii) interior one flange (IOF), similar to EOF, but loaded with a narrower bearing plate in the mid-span section; (iii) end two flange (ETF), consisting of loading both flanges simultaneously in an end section; and (iv) interior two flange (ITF), similar to ETF, but loaded in an interior section. In addition, two configurations have been considered for ground supports: (i) end bearing with solid ground (EG), where one flange is loaded with a narrow bearing plate in an extremity, whereas the other is continuously supported; and (ii) interior bearing with solid ground (IG) similar to EG, but loaded in an interior section. These six web-crippling test configurations are illustrated in Figure 2.14.

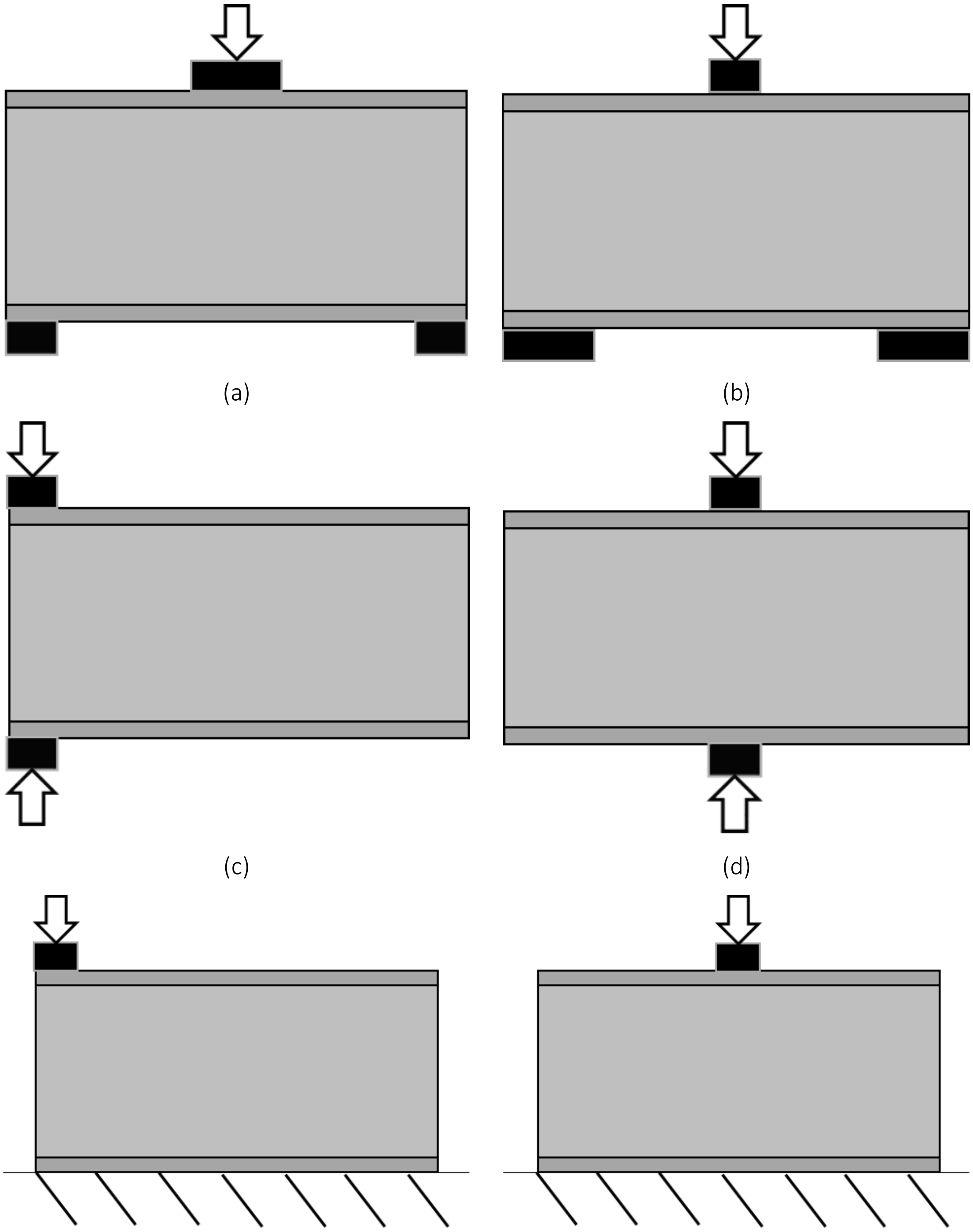
(a) (b) (c) (d) (e) (f)

Figure 2.14: Web-crippling test configurations: (a) EOF; (b) IOF; (c) ETF; (d) ITF; (e) EG; (f) IG.

2.3.2. Web-crippling of pultruded GFRP profiles

Borowicz and Bank [2.54] performed experimental tests on I-section profiles and wide flange profiles, through an IOF-based test configuration. Several modifications were implemented in the load application method, by introducing (i) concentrated loads without bearing plates; (ii) FRP bearing plates; and (iii) steel bearing plates. The authors concluded that the implementation of bearing plates could promote a significant increase of bearing capacity, especially when steel bearing plates were implemented. Following this study, Borowicz and Bank [2.55] investigated the use of different strengthening methods, for pultruded profiles under transverse concentrated loads, with I-section and wide flange sections. The authors concluded that strengthening systems that reinforced the web-flange junction area led to higher increases of bearing capacity, when compared to strengthening systems that reinforced only the web of the profile.

Wu and Bai [2.56] performed EG, IG, ETF and ITF tests on pultruded GFRP profiles with squared hollow sections. A consistent failure mode was reported for all tests, consisting of web-crushing near the web-flange junction area. The authors considered the same bearing length for all tests. In a following study, Wu *et al.* [2.57] studied strengthening solutions for pultruded profiles with squared hollow sections, consisting of CFRP laminates bonded to the webs of the profiles and steel channel sections embracing the GFRP profile. Web-crushing failure near the web-flange junction area was also reported for all tests and the strengthening systems were reported to provide significant increases of bearing capacity, in particular when steel channel reinforcements were implemented [2.57]. In a more recent study, Wu *et al.* [2.58] studied the behaviour of pultruded GFRP profiles, with channel sections, in ETF and ITF test configurations. Four profiles were tested, with a fixed bearing length; however, different specimen lengths were considered. The failure modes were reported to vary between web-crushing near the web-flange junction and web-buckling at the centre of the web. The authors associated a more brittle failure to specimens with a lower length and web-buckling failure to specimens with slender webs [2.58], as expected.

The author of this thesis has also performed a previous experimental study, during the course of his MSc dissertation [2.59]. The experimental programme addressed various I-section profiles, with heights ranging from 100 to 400 mm, tested in the ETF and ITF test configurations, for three different bearing lengths. The bearing length was found to significantly impact the stiffness and ultimate loads of all materials.

Some additional studies have been performed in connection with the topic of web-crippling. In particular, a few experimental and numerical studies have been performed regarding the mechanical characterization of the web-flange junction [2.60-2.63], which may lead to a better understanding of web-crushing failure in web-crippling tests.

The experimental studies detailed above [2.54-2.63] have focused on different aspects of web-crippling test configurations and strengthening methods; however, despite its potential relevance, none of the previous studies has analysed the influence of the fibre layup of the FRP cross-section walls (namely of the transverse reinforcement of the webs) on the resistance to web-crippling.

2.4. Conclusions

This chapter summarized the main findings from previous studies and the research needs on two main topics regarding pultruded GFRP profiles: (i) experimental characterization of fracture toughness; and (ii) experimental assessment of web-crippling behaviour. Both these topics require further research, despite their different stages of development.

A significant amount of research has been conducted on the experimental characterization of fracture toughness in composite materials, however, very little research has been found regarding intralaminar and translaminar fracture in pultruded GFRP materials. Most research on fracture toughness of composite materials has been focused on CFRP laminates, typically designed for the automotive and aerospace industries.

Several test configurations have been implemented to characterize intralaminar and translaminar fracture toughness of composite materials. The CT test configuration has been implemented in a greater number of experimental studies, addressing a wider range of materials, and has been used with several data reduction methods. This test configuration has the added benefit of being versatile, as can be perceived by the large number of successful CT-based test configurations that have been implemented in the past (ECT, OCT and WCT).

The determination of compressive fracture properties of pultruded GFRP materials poses an added challenge, due to the complexity of the damage propagation mechanisms. Some test configurations have been proposed in the past, as the CCT and four-point bending configurations; however, there are significant doubts regarding the data reduction methodology that should be implemented in parallel with these test configurations.

Web-crippling of pultruded GFRP materials has been experimentally assessed in a reduced number of studies. This is a complex phenomenon, with several different variables, being particularly relevant for pultruded GFRP materials, as the load application direction is parallel to the weakest in-plane material orientation. Previous research is sparse, addressing different test configurations and profile sections. This context highlights the need for additional results, so that accurate design guidelines may be developed.

Both these topics are addressed in this thesis, with the goal of implementing experimentally based fracture toughness properties in FE numerical models, as damage evolution control parameters. Successfully modelling the failure of web-crippling tests will be an important step towards establishing a solid basis for the development of design guidelines.

2.5. References

[2.1] Almeida-Fernandes, L., Nunes, F., Silvestre, N., Correia, J.R., Gonilha, J., Web-crippling of GFRP pultruded profiles. Part 2: Numerical analysis and design, *Composite Structures*, 120, pp. 578-590, 2015.

[2.2] Nunes F., Silvestre N., Correia J.R., Progressive damage analysis of web crippling of GFRP pultruded I-sections, *Composites for Construction*, 21(3), pp. 1-13, 2016.

[2.3] Harris, C.E., Morris, D.H., *NASA contractor report 3784: Fracture Behavior of Thick, Laminated Graphite/Epoxy Composites*, National Aeronautics and Space Administration, Washington DC, 1984.

[2.4] Laffan, M. J., Pinho, S. T., Robinson, P., Mcmillan, A. J., Translaminar fracture toughness testing of composites: A review. *Polymer Testing*, 31(3), pp. 481-489, 2012.

[2.5] Griffith A.A., The Phenomena of Ruture and Flow in Solids, *Philosophical Transactions of the Royal Society of London*, A221, pp. 163-198, 1921.

[2.6] Pinho, S.T., Robinson, P., Iannucci, L., Fracture toughness of the tensile and compressive fibre failure modes in laminated composites, *Composites Science and Technology*, 66(13), pp. 2069-2079, 2006.

[2.7] Barbero, E.J., Cosso, F.A., Roman, R., Weadon, T.L., Determination of material parameters for Abaqus progressive damage analysis of E-glass epoxy laminates, *Composites Part B: Engineering*, 46, pp. 211-220, 2013.

[2.8] Girão Coelho, A. M., Toby Mottram, J., Harries, K. A., Finite element guidelines for simulation of fibre-tension dominated failures in composite materials validated by case studies, *Composite Structures*, 126, pp. 299-313, 2015.

[2.9] Nunes, F., Silvestre, N., Correia, J.R., Structural behaviour of hybrid FRP pultruded columns. Part 2: Numerical study. *Composite Structures*, 139, pp. 304-319, 2016.

[2.10] Li, Z., Khennane, A., Hazell, P.J., Brown, A.D., Impact behaviour of pultruded GFRP composites under low-velocity impact loading, *Composite Structures*, 168, pp. 360-371, 2017.

[2.11] Martins, D., Proença, M., Correia, J.R., Gonilha, J., Arruda, M., Silvestre, N., Development of a novel beam-to-column connection system for pultruded GFRP tubular profiles, *Composite Structures*, 171, pp. 263-276, 2017.

[2.12] ASTM E399-90, “Standard test method for plane-strain fracture toughness of metallic materials”, ASTM, Annual Book of ASTM Standards, 1993.

[2.13] Bergan, A., Dávila, C., Leone, F., Awerbuch, J., Tan, T.M., A mode I cohesive law characterization procedure for through-the-thickness crack propagation in composite laminates, *Composites Part B: Engineering*, 94, pp. 338-349, 2016.

[2.14] Ortega, A., Maimí, P., González, E. V., Trias, D., Characterization of the translaminar fracture Cohesive Law. *Composites Part A: Applied Science and Manufacturing*, 91, pp. 501-509, 2016.

[2.15] Simulia, “Abaqus/CAE 2018”, 2018.

[2.16] Hashin, Z., Rotem, A., A fatigue criterion for fiber-reinforced materials, *Journal of Composite Materials*, 7, pp. 448-464, 1973.

[2.17] Maimí, P., Camanho, P.P., Mayugo, J.A., Dávila, C.G., A continuum damage model for composite laminates: Part I - Constitutive model, *Mechanics of Materials*, 39(10), pp. 897-908, 2007.

[2.18] Maimí, P., Camanho, P.P., Mayugo, J.A., Dávila, C.G., A continuum damage model for composite laminates: Part II - Computational implementation and validation, *Mechanics of Materials*, 39(10), 909–919, 2007.

[2.19] Lindgaard, E., Bak, B.L.V., Glud, J.A., Sjølund, J., Christensen, E.T., A user programmed cohesive zone finite element for ANSYS Mechanical. *Engineering Fracture Mechanics*, 180, pp. 229-239, 2017.

[2.20] Jensen, S.M., Martos, M.J., Bak, B.L.V., Lindgaard, E., Formulation of a mixed-mode multilinear cohesive zone law in an interface finite element for modelling delamination with R-curve effects. *Composite Structures*, 216, pp. 477-486, 2019.

[2.21] Liu, P.F., Zheng, J.Y., Recent developments on damage modeling and finite element analysis for composite laminates: A review, *Materials and Design*, 31(8), pp. 3825-3834, 2010.

[2.22] Sato, N., Hojo, M., Nishikawa, M., Intralaminar fatigue crack growth properties of conventional and interlayer toughened CFRP laminate under mode I loading. *Composites Part A: Applied Science and Manufacturing*, 68, pp. 202-211, 2015.

[2.23] Gonzáles, L., Knauss, W.G., Scaling global fracture behavior of structures-sized laminated composites. *International Journal of Fracture*, 118(4), pp. 363-394, 2002.

[2.24] Laffan, M.J., Pinho, S.T., Robinson, P., Iannucci, L., Measurement of the in-situ ply fracture toughness associated with mode I fibre tensile failure in FRP. Part II: Size and lay-up effects, *Composites Science and Technology*, 70(4), pp. 614-621, 2010.

[2.25] Li, X., Hallett, S.R., Wisnom, M.R., Zobeiry, N., Vaziri, R., Poursartip, A., Experimental study of damage propagation in Over-height Compact Tension tests, *Composites Part A: Applied Science and Manufacturing*, 40(12), pp. 1891-1899, 2009.

[2.26] de Moura, M.F.S.F., Campilho, R.D.S.G., Amaro, A.M., Reis, P.N.B., Interlaminar and intralaminar fracture characterization of composites under mode I loading, *Composite Structures*, 92(1), pp. 144-149, 2010.

[2.27] Czabaj, M.W., Ratcliffe, J.G., Comparison of intralaminar and interlaminar mode I fracture toughnesses of a unidirectional IM7/8552 carbon/epoxy composite, *Composites Science and Technology*, 89, pp. 15-23, 2013.

[2.28] Blanco, N., Trias, D., Pinho, S.T., Robinson, P., Intralaminar fracture toughness characterisation of woven composite laminates. Part I: Design and analysis of a compact tension (CT) specimen, *Engineering Fracture Mechanics*, 131, pp. 349-360, 2014.

[2.29] Blanco, N., Trias, D., Pinho, S.T., Robinson, P. Intralaminar fracture toughness characterisation of woven composite laminates. Part II: Experimental characterisation. *Engineering Fracture Mechanics*, 131, pp. 361-370, 2014.

[2.30] Gigliotti, L., Pinho, S. T., Translaminar fracture toughness of NCF composites with multiaxial blankets. *Materials & Design*, 94, pp. 410-416, 2015.

[2.31] El-Hajjar R., Haj-Ali R., Mode-I fracture toughness testing of thick section FRP composites using the ESE(T) specimen, *Engineering Fracture Mechanics*, 72, pp. 631-643, 2005.

[2.32] Liu W., Feng P., Huang J., Bilinear softening model and double K fracture criterion for quasi-brittle fracture of pultruded FRP composites, *Composite Structures*, 160, pp. 1119-1125, 2016.

[2.33] Li, S., Thouless, M.D., Waas, A.M., Schroeder, J.A., Zavattieri, P.D., Use of a cohesive-zone model to analyze the fracture of a fiber-reinforced polymer-matrix composite, *Composites Science and Technology*, 65, pp. 537-549, 2005.

[2.34] Ortega, A., Maimí, P., González, E. V, Trias, D., Specimen geometry and specimen size dependence of the R-curve and the size effect law from a cohesive model point of view, *International Journal of Fracture*, 205, pp. 239-254, 2017.

[2.35] Ortega, A., Maimí, P., Gonz, E.V., Sainz de Aja, J.R., de la Escalera, F.M., Cruz, P., Translaminar fracture toughness of interply hybrid laminates under tensile and compressive loads, *Composites Science and Technology*, 143, pp. 1-12, 2017.

[2.36] Underwood, J.H., Eidinoff, H.L., Kortschot, M.T., Wilson, D.A., Lloyd, W.R., Ashbaugh, N., *Technical Report ARCCB-TR-95013: Methods and results from Interlaboratory tests of carbon / epoxy laminates*, US army armament research, development and engineering center, 1995.

[2.37] Kongshavn, I., Poursartip, A., Experimental investigation of a strain-softening approach to predicting failure in notched fibre-reinforced composite laminates, *Composites Science and Technology*, 59(1), pp. 29-40, 1999.

[2.38] Zobeiry, N., Vaziri, R., Poursartip, A., Characterization of strain-softening behavior and failure mechanisms of composites under tension and compression. *Composites Part A: Applied Science and Manufacturing*, 68, pp. 29-41, 2015.

[2.39] Pinho, S.T., Robinson, P., Iannucci, L., Developing a four point bend specimen to measure the mode I intralaminar fracture toughness of unidirectional laminated composites, *Composites Science and Technology*, 69, pp. 1303-1309, 2009.

[2.40] Iwamoto, M., Ni, Q.Q., Fujiwara, T., Kurashiki, K., Intralaminar fracture mechanism in unidirectional CFRP composites - part I: Intralaminar toughness and AE characteristics, *Engineering Fracture Mechanics*, 64(6), pp. 747-764, 1999.

[2.41] Sørensen, B.F., Jacobsen, T.K., Determination of cohesive laws by the J integral approach, *Engineering Fracture Mechanics*, 70(14), pp. 1841-1858, 2003.

[2.42] Laffan, M.J., Pinho, S.T., Robinson, P., Mcmillan, A.J., Translaminar fracture toughness: The critical notch tip radius of 0 ° plies in CFRP, *Composites Science and Technology*, 72(1), pp. 97-102, 2011.

[2.43] Catalanotti, G., Arteiro, A., Hayati, M., Camanho, P. P., Determination of the mode I crack resistance curve of polymer composites using the size-effect law, *Engineering Fracture Mechanics*, 118, pp. 49-65, 2014.

[2.44] Pinho, S.T., Gutkin, R., Pimenta, S., De Carvalho, N.V., Robinson, P., On longitudinal compressive failure of carbon-fibre-reinforced polymer: from unidirectional to woven, and from virgin to recycled. *Philosophical Transactions of the Royal Society A: Mathematical, Physical and Engineering Sciences*, *370*(1965), pp. 1871-1895, 2012.

[2.45] Catalanotti, G., Camanho, P.P., Xavier, J., Dávila, C. G., Marques, A.T., Measurement of resistance curves in the longitudinal failure of composites using digital image correlation, *Composites Science and Technology*, 70(13), pp. 1986-1993, 2010.

[2.46] Laffan, M.J., Pinho, S.T., Robinson, P., Iannucci, L., Mcmillan, A.J., Measurement of the fracture toughness associated with the longitudinal fibre compressive failure mode of laminated composites, *Composites Part A: Applied Science and Manufacturing*, 43(11), pp. 1930-1938, 2012.

[2.47] Catalanotti, G., Xavier, J., Camanho, P. P., Measurement of the compressive crack resistance curve of composites using the size effect law, *Composites Part A: Applied Science and Manufacturing*, 56, pp. 300-307, 2014.

[2.48] Laffan, M. J., Pinho, S. T., Robinson, P., Iannucci, L., Measurement of the in-situ ply fracture toughness associated with mode I fibre tensile failure in FRP. Part I: Data reduction, *Composites Science and Technology*, 70(4), pp. 606-613, 2010.

[2.49] Pappas, G., Botsis, J., Intralaminar fracture of unidirectional carbon/epoxy composite: experimental results and numerical analysis. *International Journal of Solids and Structures*, 85-86, pp. 114-124, 2016.

[2.50] ASTM E-1922, “Standard Test Method for Translaminar Fracture Toughness of Laminated and Pultruded Polymer Matrix Composite Materials”, ASTM, Annual Book of ASTM Standards, 1997.

[2.51] AISI S100-2007, “North American Cold-Formed Steel Specification”, American Iron and Steel Institute (AISI), Washington D.C., 2007.

[2.52] EN 1993-1-3:2006, “Eurocode 3 – Part 1-3: General rules – Supplementary rules for cold-formed members and sheeting”, European Committee for Standardization (CEN), Brussels, 2004.

[2.53] EN 1993-1-5:2004, “Eurocode 3 – Part 1-5: Plated Structural elements”, European Committee for Standardization (CEN), draft 49, Brussels, 2004.

[2.54] Borowicz, D.T., Bank, L.C., Behavior of Pultruded Fiber-Reinforced Polymer Beams Subjected to Concentrated Loads in the Plane of the Web, *Composites for Construction*, 15, pp. 2-9, 2011.

[2.55] Borowicz, D.T., Bank, L.C., Effect of web reinforcement on the behavior of pultruded fiber-reinforced polymer beams subjected to concentrated loads. *Construction and Building Materials*, 47, pp. 347-357, 2013.

[2.56] Wu, C., Bai, Y., Web crippling behaviour of pultruded glass fibre reinforced polymer sections, *Composite Structures*, 108, pp. 789-800, 2014.

[2.57] Wu, C., Bai, Y., Zhao, X.L., Improved bearing capacities of pultruded glass fibre reinforced polymer square hollow sections strengthened by thin-walled steel or CFRP, *Thin-Walled Structures*, 89, pp. 67-75, 2014.

[2.58] Wu, C., Zhang, L., Bai, Y., Zhao, X. L., Web crippling behavior of pultruded GFRP channel sections under transverse bearing load, *Composite Structures*, 209, pp. 129-142, 2019.

[2.59] Almeida-Fernandes, L., Gonilha, J., Correia, J. R., Silvestre, N., Nunes, F., Web-crippling of GFRP pultruded profiles. Part 1: Experimental study. *Composite Structures*, 120, pp. 565-577, 2015.

[2.60] Yanes-Armas, S., de Castro, J., Keller, T., Energy dissipation and recovery in web-flange junctions of pultruded GFRP decks. *Composite Structures*, *148*, pp. 168-180, 2016.

[2.61] Fascetti, A., Feo, L., Nisticò, N., Penna, R., Web-flange behavior of pultruded GFRP I-beams: A lattice model for the interpretation of experimental results. *Composites Part B: Engineering*, 100, pp. 257-269, 2016.

[2.62] Yanes-Armas, S., de Castro, J., Keller, T., Rotational stiffness of web-flange junctions of pultruded GFRP decks. *Engineering Structures*, *140*, pp. 373-389, 2017.

[2.63] Liu, T.Q., Yang, J.Q., Feng, P., Harries, K.A., Determining rotational stiffness of flange-web junction of pultruded GFRP I-sections. *Composite Structures*, 236, 111843, 2020.

Part II

Fracture toughness characterization

Preamble

The experimental characterization of fracture toughness of composite materials has been the subject of significant research for a long period of time. However, there are still no well-established standardized methods available for this purpose, regarding pultruded GFRP materials. This is a complex topic, as several different fracture phenomena may occur within composite materials and their fracture properties have been reported to vary significantly for different in-plane directions.

Part II presents an experimental and numerical study which aimed to characterize the in-plane transverse tensile and compressive fracture properties of pultruded GFRP materials. Materials with significantly different properties and fibre layups were sourced, to assess and quantify the influence of those parameters on the aforementioned fracture properties.

Chapter 3. Experimental methodology and material characterization

3.1. Introduction

This chapter presents two preliminary parts of the experimental study performed towards the characterization of fracture toughness of pultruded GFRP materials: (i) mechanical property characterization of all materials, including elastic, strength and fibre layup; (ii) development of a sound experimental methodology to determine transverse fracture properties in pultruded GFRP materials.

The characterization of material properties is crucial to the determination of fracture properties, as most experimental methodologies discussed in Chapter 2 require the knowledge of material properties to apply data reduction methods. Section 3.2 presents a summary of the performed tests, as well as the results obtained for each pultruded GFRP material.

Section 3.3 presents the development of an accurate experimental methodology for the determination of fracture toughness in pultruded GFRP materials. This was a complex task to perform, as there is very little information on the fracture properties of pultruded GFRP materials [3.1, 3.2]; they are expected to present different challenges in respect to CFRP materials used in the automotive and aerospace industries, given their differences in mechanical properties, section thicknesses and fibre layups [3.1].

The experimental methodology focused in a first stage on transverse tensile cases, given the wider range of validated test methods [3.3], in comparison to compressive fracture tests. The methodology presented herein (Section 3.3) is applied to a wide variety of materials in Chapter 4, whereas the development of compressive fracture tests is detailed in Chapter 5.

3.2. Overview of mechanical characterization programme

The experimental mechanical characterization campaign was a crucial step to enable (i) the determination of fracture toughness, as data reduction methods rely on material elastic properties; and (ii) to enable the development of FE numerical models. The experimental programme included the following tests:

- Tensile tests [3.4];
- Iosipescu shear tests [3.5];
- Combined load in compression (CLC) tests [3.6];
- Calcination tests [3.7].

In regard to previous research, performed by the author for his MSc dissertation, the main upgrades in material characterization consisted of the (i) Iosipescu [3.5], (ii) CLC [3.6] and (iii) calcination tests [3.7]. The CLC test setup was prepared within the context of this thesis, being of crucial importance to accurately characterize transverse compressive properties for web-crippling studies. Each material was mechanically characterized through a minimum of six specimens, for each mechanical property. The calcination tests were also a relevant upgrade, in regard to earlier studies, as they provide complementary information to the determined mechanical properties.

3.2.1. Materials

A total of five materials were experimentally characterized in the context of this thesis, all obtained from off-the-shelf pultruded GFRP profiles. These materials were sourced from a total of four suppliers, Alto Perfis Pultrudidos, Lda. (Portuguese manufacturer), Creative Pultrusions (US manufacturer), Fiberline Composites (Danish manufacturer) and STEP – Sociedade Técnica de Estruturas Pultrudidas (Portuguese supplier). These companies were labelled as “A”, “C”, “F” and “S”, respectively. All pultruded profiles consist of I-section beams, with exception of one U-section profile. In addition to these materials, mechanical characterization results were provided for a pultruded plate [3.8], also produced by Alto Perfis Pultrudidos, Lda. This plate was included in the fracture toughness characterization process, and thus its mechanical properties are included in the summary provided in section 3.2.6. Table 3.1 presents a summary of these materials, including their dimensions and manufacturer or supplier.

Table 3.1: Geometry and manufacturer information of test materials.

Profile designation	I150-A	I152-C	I200-F	I150-S	U150-S	P300-A
Manufacturer	A	C	F	S	S	A
Height [mm]	150	152	200	150	150	300*
Thickness [mm]	8.1	6.3	9.9	8.1	7.7	5.3

* width of the pultruded plate.

The I150-A profile was submitted to additional tests, as in an earlier stage small defects were found in the initial batch of material, showing signs of insufficient bond between the matrix and fibres. This material was still considered for the studies performed ahead, despite some uncertainties regarding its in-plane transverse properties.

The specimens referred to ahead were named in the following order: (i) test material; (ii) specimen orientation in respect to roving direction, longitudinal (L) and in-plane transverse (T); and (iii) specimen number.

3.2.2. Tensile tests

3.2.2.1. Test setup

The tensile test setup consists of two wedge grips mounted on an Instron universal testing machine. The grips were devised so that, with increasing applied displacements, the gripping pressure increases, preventing slippage of the specimens. Figure 3.1 illustrates the test setup.

Displacements were monitored through a video-extensometry system. In order to have more accurate results, the specimens were painted with white matte paint and targets were marked with a black marker pen (as displayed in Figure 3.1). Specimens were loaded at a 2 mm/min (cross-head) displacement rate and failure was only considered to be valid when damage developed outside the gripped areas of each specimen.

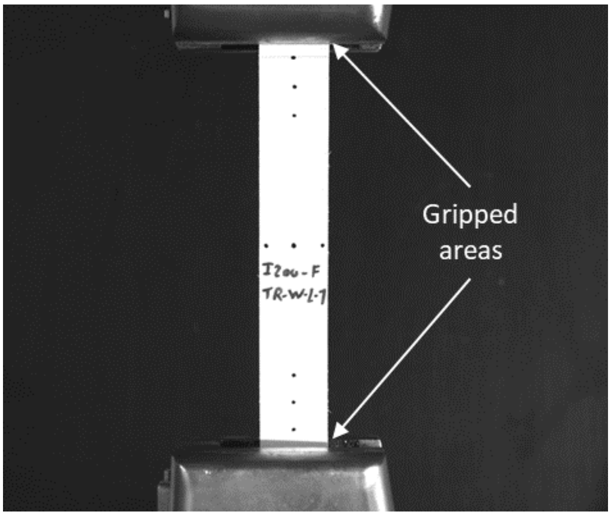

Figure 3.1: Mechanical characterization tensile test of I200-F-L-1 specimen.

3.2.2.2. Specimen geometries

Two different specimen geometries were considered: (i) longitudinal specimens taken from the web areas were prepared in accordance with ISO-527-4 [3.4], presenting a nominal length of 250 mm and a width of 25 mm; and (ii) transverse specimens taken from the web were prepared with lengths of 120 mm, for profiles with a height of 150 mm, and 160 mm for the I200-F profile. The specimens with 250 mm of length were prepared to present gripping lengths of 50 mm on each side, whereas the shorter specimens were prepared to present 30 mm gripping lengths on each side. Figure 3.2 illustrates both specimen geometries.

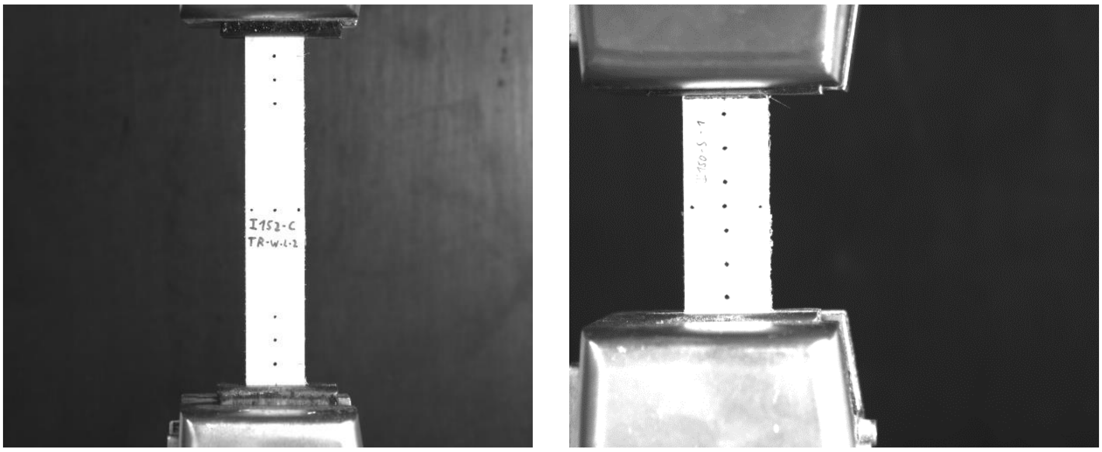

(a) (b)

Figure 3.2: Specimen geometries of tensile tests: (a) longitudinal specimen I152-C-L-2; (b) transverse specimen I150-S-T-1.

3.2.2.3. Experimental results

Aside from the expectable high discrepancies between longitudinal and transverse elastic and strength properties, the failure modes were also different in these tests, in a trend that was reported for all materials: (i) longitudinal specimens presented significant signs of delamination in large areas of the specimens after damage initiation; (ii) transverse specimens presented more localized damaged areas, with lower levels of delamination. These failure modes are displayed in Figure 3.3.

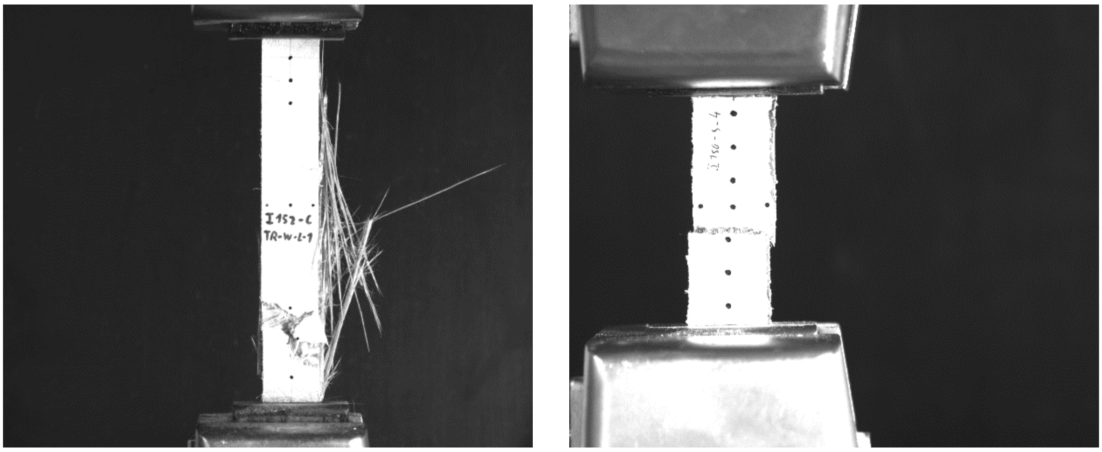

(a) (b)

Figure 3.3: Failure modes of tensile tests: (a) longitudinal specimen I152-C-L-1; (b) transverse specimen I150-S-T-4.

The elastic modulus was determined by processing stress *vs*. strain curves. The strains were determined through the video-extensometry outputs, whereas the stress levels were determined by dividing the applied strength by the average section area of each specimen (three separate measurements of width and thickness were registered per specimen). Figure 3.4 presents representative stress *vs*. strain curves for longitudinal (Figure 3.4 (a)) and transverse (Figure 3.4 (b)) specimens.

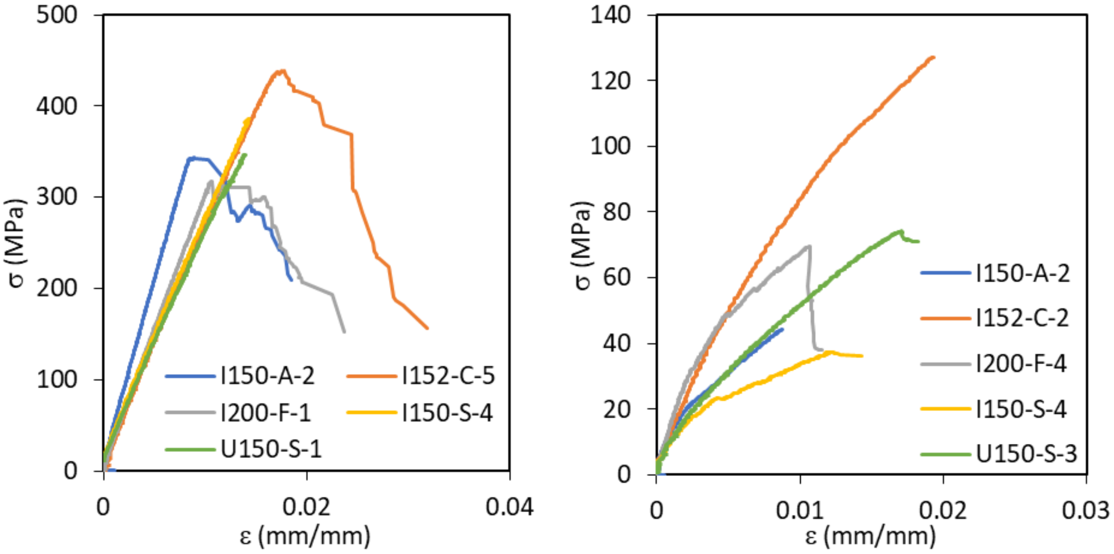

(a) (b)

Figure 3.4: Representative stress *vs*. strain curves of tensile tests: (a) longitudinal specimens; (b) transverse specimens.

Figure 3.4 clearly shows that the longitudinal tensile specimens present significantly lower scatter, for different materials, than their transverse tensile counterparts. The longitudinal tensile ultimate stresses ranged from ≈300 MPa to ≈450 MPa, whereas the transverse tensile ultimate stresses ranged from ≈40 MPa to ≈130 MPa. It is also noticeable that the transverse specimens present a more non-linear behaviour, which can be attributed to a higher contribution of the resin material to the structural behaviour in the transverse direction.

Table 3.2 presents a summary of tensile elastic and strength properties for all six pultruded GFRP materials. A significant variability can be observed in Table 3.2, in particular regarding transverse elastic and strength properties. The I152-C results stand-out as the highest transverse tensile strength, whereas the I150-S presents the overall lowest transverse tensile strength. Table 3.2 also highlights previous conclusions that longitudinal properties present a considerably lower variability, when compared with transverse properties.

The I150-A specimens were found to present small defects, attributed to poor fibre/matrix bonding. These defects were found to have little influence on the longitudinal specimens, which presented the highest elastic modulus of the experimental programme; however, these defects did affect the transverse specimens significantly, as the specimens consistently failed in sections close to these defects. In fact, initial mechanical characterization tests led to average transverse tensile elastic modulus values of 6.6 GPa and ultimate stress values of 26 MPa. These values were subsequently discarded, after additional tests on a more recent batch of profiles (showing reduced signs of these defects), which led to the results presented in Figure 3.4 and Table 3.2. The fracture tests and web-crippling tests detailed in this thesis were performed with profiles taken from this more recent batch of profiles.

Table 3.2: Tensile elastic and strength properties of test materials – average ± standard deviation.

Material	I150-A	I152-C	I200-F	I150-S	U150-S
Longitudinal elastic modulus [GPa]	43.5 ±1.4	28.8 ±2.2	29.6 ±1.6	30.0 ±2.4	26.6 ±1.4
Transverse elastic modulus [GPa]	9.6 ±1.6	10.3 ±0.5	11.9 ±0.9	5.5 ±0.4	5.8 ±0.4
Longitudinal ultimate stress [MPa]	383.7 ±23.5	426.0 ±14.6	322.6 ±10.4	376.5 ±20.0	347.1 ±10.2
Transverse ultimate stress [MPa]	45.0 ±1.7	121.3 ±8.5	70.7 ±1.8	33.8 ±6.1	69.5 ±6.1

3.2.3. Iosipescu shear tests

3.2.3.1. Test setup

The implemented test setup followed the specifications of ASTM D5379 / D5379M - 05 [3.5]. This test methodology has been found to present more accurate results than 10º off-axis tests, which seemed to underestimate the shear strength of materials [3.9]. The setup illustrated in Figure 3.5 is connected to an Instron universal test machine.

Load was applied under displacement control, at a rate of 2mm/min and strain measurements were performed with the aforementioned video-extensometry system. Specimen surfaces were prepared similarly to previously reported tensile tests, in order to provide accurate measurements through the video-extensometry system.

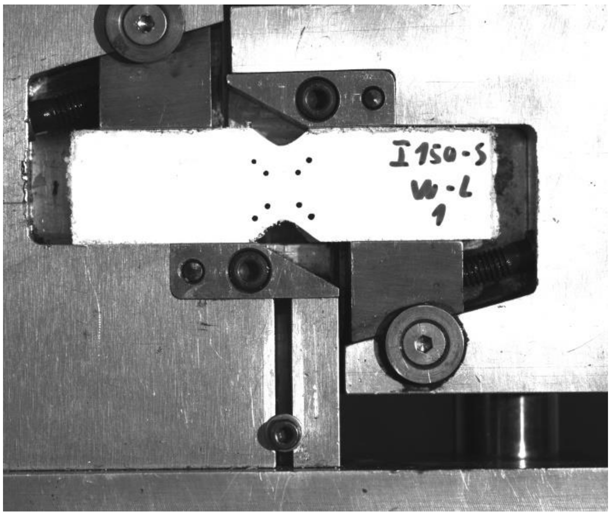

Figure 3.5: Mechanical characterization shear test of I150-S specimen.

3.2.3.2. Specimen geometries

The shear test specimens comprised a rectangular shape, of 76 by 20 mm, with two V-shaped notches inserted in the centre of the specimen, leading to a narrow width of 12 mm. The specimen geometry is illustrated in Figure 3.6.

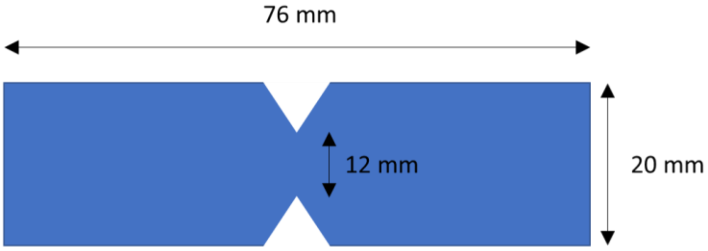

Figure 3.6: Shear test specimen geometry.

The test specimens were taken from the web of each profile, aligned with the longitudinal direction. The V-notches were inserted through abrasive tools, positioning the specimens at a 45° angle, in respect to the abrasive disk.

3.2.3.3. Experimental results

Aside from a few cases with diverging failure modes, namely crushing of the shear specimen arms, most specimens presented a typical shear induced failure, as depicted in Figure 3.7.

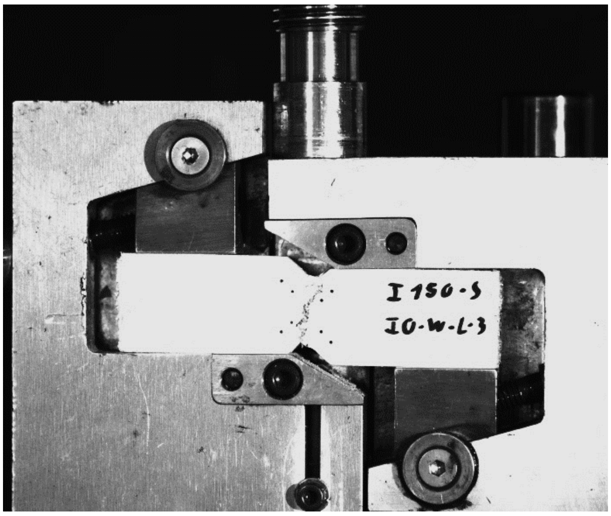

Figure 3.7: Failure mode of I150-S-L-3 specimen.

Figure 3.8 presents shear stress *vs*. strain curves for a representative specimen of each material. The results presented in Figure 3.8 show a relatively low variability, both in terms of shear elastic modulus and ultimate shear strength. The measured shear elastic modulus and strength are reported in Table 3.3, showing relatively narrow ranges for both shear properties: (i) the average shear elastic modulus varies between 2.9 and 4.2 GPa; and (ii) the average shear ultimate stress varies between 48 and 71 MPa.

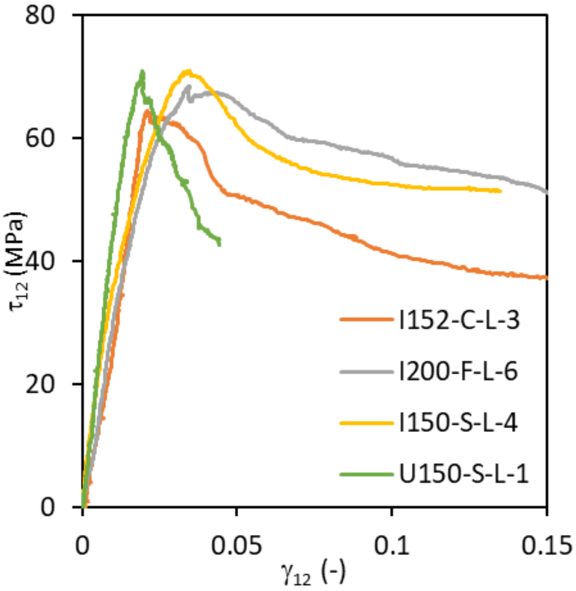

Figure 3.8: Representative shear stress *vs*. strain curves.

Table 3.3: Shear elastic and strength properties of test materials – average ± standard deviation.

Material	I150-A	I152-C	I200-F	I150-S	U150-S
Shear elastic modulus [GPa]	3.1 ±0.5	4.2 ±0.6	2.9 ±0.4	3.2 ±0.4	4.2 ±0.6
Shear ultimate stress [MPa]	47.7 ±4.5	65.3 ±2.1	67.1 ±2.0	69.8 ±4.9	70.8 ±6.2

3.2.4. Compressive tests

3.2.4.1. Test setup

In the course of the author's MSc dissertation [3.10], compressive tests were performed in accordance to the ASTM D 695-02 standard [3.11]; however, experimental results showed that unintended delamination occurred in the tests, as perfect orthogonality was difficult to achieve in the test specimen top and bottom surfaces. In addition, alternative compressive tests were performed, with a similar setup to tensile tests (load applied in opposite direction); however, this methodology proved difficult to implement, as relatively long specimens were required, potentially triggering early onsets of buckling failure. Figure 3.9 illustrates the aforementioned test setups [3.10].

The CLC test configuration, standardized in ASTM D6641/D6641M – 09 [3.6] aims to implement simultaneous loading through compression by contact at the top and bottom faces of the specimen, as well as through shear at its four gripped faces. In addition, the top and bottom faces are easily corrected, so that they do not protrude out of the test fixture. The test fixture used in these tests is illustrated in Figure 3.10. The specimens were loaded at a (cross-head) displacement rate of 1 mm/min.

(a) (b)

Figure 3.9: Previously performed compressive tests [3.10]: (a) specimen in accordance to ASTM D 695-02 [3.11]; (b) tensile test-based specimen.

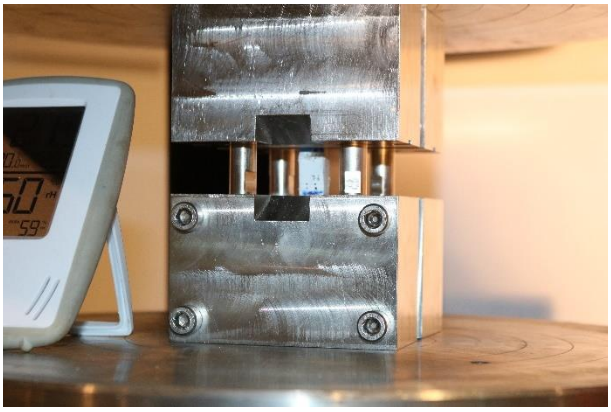

Figure 3.10: Combined load in compression (CLC) test.

3.2.4.2. Specimen geometries

Similarly to previously reported tensile tests, two specimen geometries were considered for the CLC tests: (i) in accordance to the ASTM D6641/D6641M – 09 standard [3.6], longitudinal specimens and transverse specimens of I200-F profile were prepared with 150 mm of length; and (ii) transverse specimens of profiles with heights of 150 mm were prepared with a nominal length of 120 mm. All specimens were prepared with a nominal width of 16 mm. Figure 3.11 depicts standard and shorter CLC specimens.

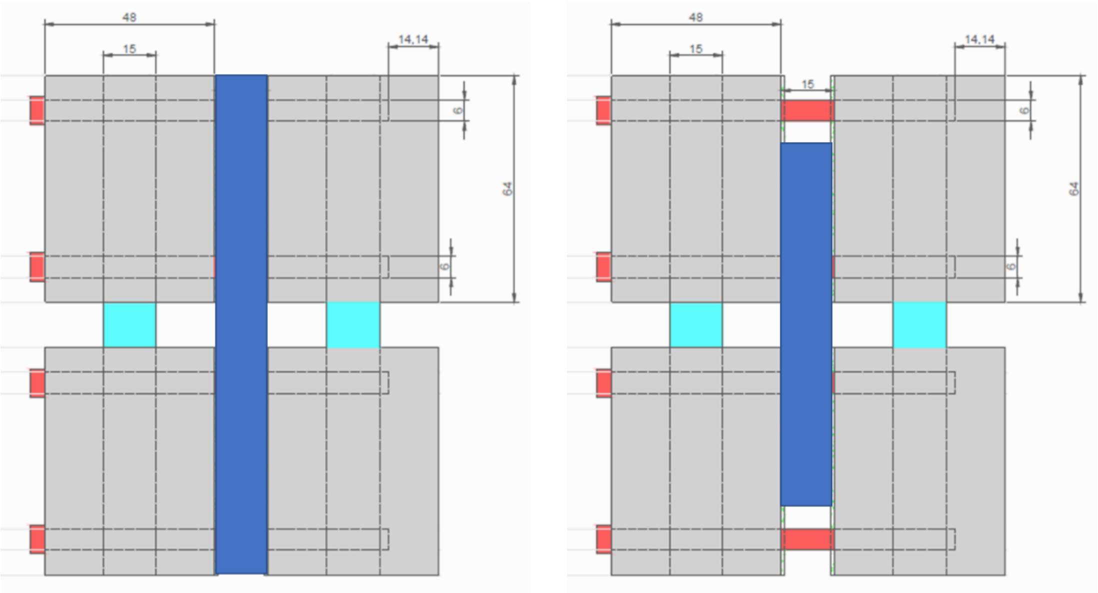

(a) (b)

Figure 3.11: Schematic of CLC specimen geometries (side view of test fixture): (a) longitudinal specimen in accordance to D6641/D6641M – 09 [3.6]; (b) shorter transverse specimen, loaded only through the shear induced by the test rig.

Naturally, the shorter specimens, depicted in Figure 3.11 (b), were only loaded through the shear induced by the pressure on each pair of steel blocks, positioned at their side faces. Despite this limitation, the test results were considered as valid, as their failure modes were in line with the standard guidelines, with damage developing in the free section of each specimen.

3.2.4.3. Experimental results

Figure 3.12 presents failure modes for longitudinal (Figure 3.12 (a)) and transverse (Figure 3.12 (b)) specimens. Longitudinal failure was found to promote significant delamination, noticeable by several fibres protruding from the specimen, similarly to the failure mode reported for longitudinal tensile tests (see Figure 3.3 (a)). In a different trend, transverse CLC specimens presented a more localized damage profile, also in line with transverse tensile tests (see Figure 3.3 (b)).

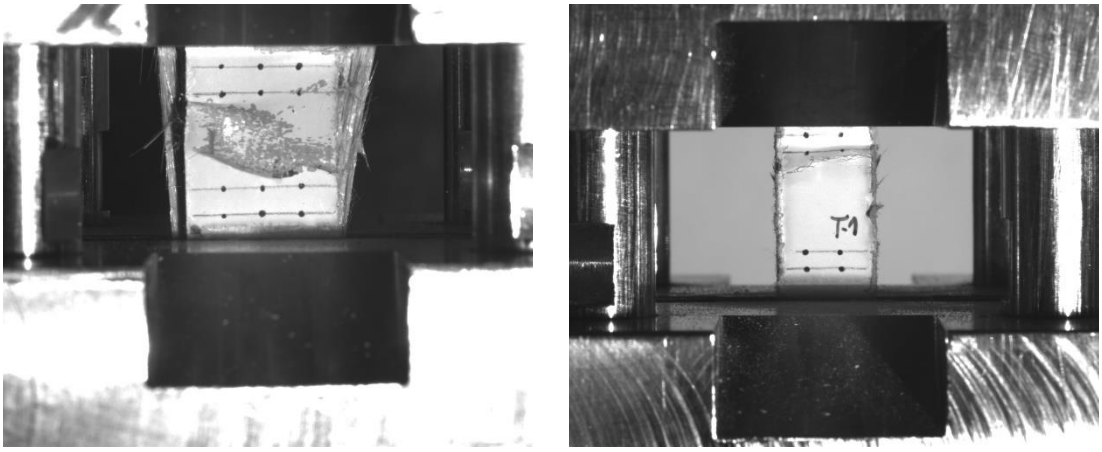

(a) (b)

Figure 3.12: Failure modes of CLC tests: (a) longitudinal specimen I200-F-L-1; (b) transverse specimen I200-F-T-1.

Figure 3.13 presents compressive stress *vs*. strain results for a representative specimen of each material. In a different trend to transverse tensile results discussed in Section 3.2.2.3, the transverse compressive results show lower, albeit significant, levels of variability across different materials.

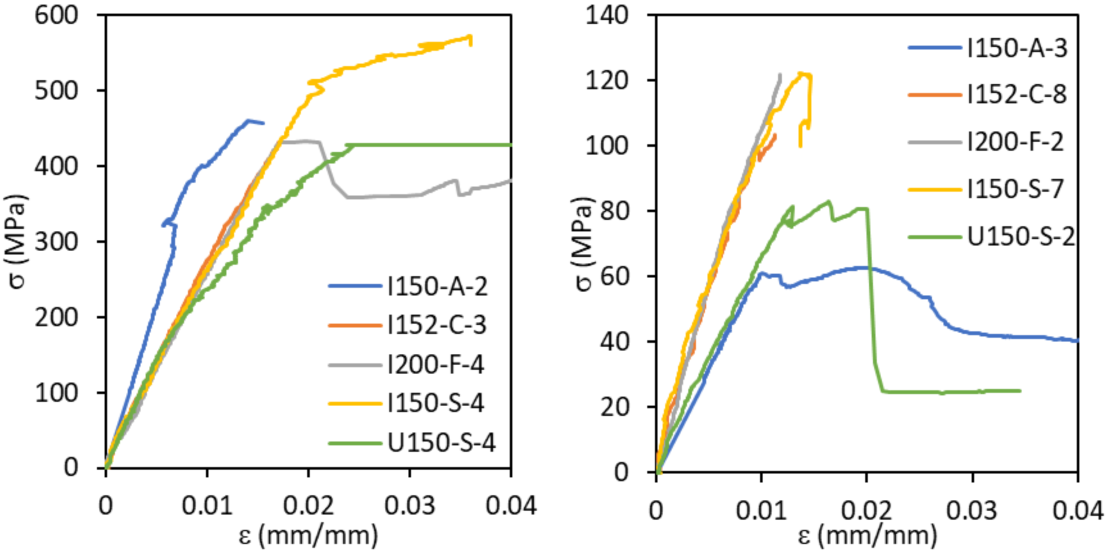

(a) (b)

Figure 3.13: Representative stress *vs*. strain curves of CLC tests: (a) longitudinal specimens; (b) transverse specimens.

The CLC test results are summarized in Table 3.4. A relatively low variability is found in the results. A relevant exception is the I150-A material, which stands out with the highest longitudinal elastic modulus and the lowest transverse compressive strength, indicating that most of the fibre content should be aligned in the longitudinal direction. The aforementioned manufacturing defects found in the I150-A profile did not seem to affect transverse compressive tests as significantly as reported for transverse tensile tests.

Table 3.4: Compressive elastic and strength properties of test materials – average ± standard deviation.

Material	I150-A	I152-C	I200-F	I150-S	U150-S
Longitudinal elastic modulus [GPa]	44.0 ±2.7	24.6 ±0.7	29.9 ±1.9	28.1 ±3.4	25.8 ±2.6
Transverse elastic modulus [GPa]	7.8 ±0.8	10.9 ±1.3	10.8 ±1.8	9.3 ±0.8	6.5 ±0.6
Longitudinal ultimate stress [MPa]	445.6 ±48.7	436.9 ±26.4	441.5 ±28.7	550.5 ±70.4	450.6 ±22.8
Transverse ultimate stress [MPa]	60.1 ±7.0	104.2 ±11.0	121.6 ±16.6	122.9 ±7.5	83.5 ±7.1

The I150-A material was also tested in accordance to the ASTM D 695-02 standard [3.11]. Table 3.5 presents a comparison of results obtained from both test methods, clearly showing that those determined through the ASTM D 695-02 standard [3.11] are significantly lower than those determined through the CLC test configuration, for both elastic (influence of local deformation at end sections contacting loading plates) and strength properties. This significant discrepancy found between test methods had influence in both numerical and analytical studies performed by the author in his MSc dissertation [3.10].

Table 3.5: Elastic and strength compressive properties of I150-A profiles measured through ASTM D 695-02 and ASTM D6641/D6641M – 09.

Material	ASTM D 695-02 [3.11]	ASTM D6641/D6641M – 09 [3.6]
Longitudinal elastic modulus [GPa]	26.4	44.0
Transverse elastic modulus [GPa]	2.7	7.8
Longitudinal ultimate stress [MPa]	374.6	445.6
Transverse ultimate stress [MPa]	42.3	60.1

3.2.5. Calcination tests

3.2.5.1. Test setup

The calcination tests were performed based on the methodology of ISO 1172 [3.7], by heating the specimens to 800 °C, for a period of at least 8 hours. This process burned-off the resin, leaving only the fibre material, enabling an analysis into the fibre content mass percentage and into the fibre layup of each material. A minimum of two specimens were burned-off per material.

3.2.5.2. Specimen geometries

These experiments were performed using square shaped specimens, taken from the web of each profile, with 60x60 mm dimensions. Weight measurements were performed for each individual layer, giving additional information into which layers presented higher fibre content. Figure 3.14 illustrates the specimen shape.

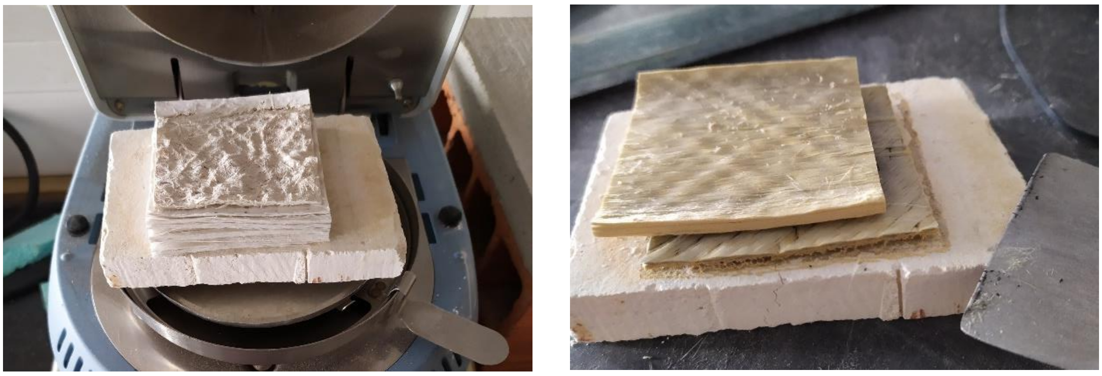

(a) (b)

Figure 3.14: Calcination test specimens: (a) I150-A-1; (b) I152-C-1.

3.2.5.3. Experimental results

Table 3.6 presents a summary of fibre content mass percentages, for all test materials. The layers found in each material were decomposed into the following categories: (i) roving layers (R), consisting of longitudinal fibres, constitute the main fibre reinforcement in pultruded GFRP materials; (ii) continuous filament layers (C), consisting of randomly oriented fibres, provide global albeit weaker reinforcement; (iii) woven layers with 0° and 90° fibres (W), which provide significant reinforcement in the in-plane transverse direction; and (iii) quasi-isotropic layers with ±45° and 90° oriented fibres (Q), providing significant reinforcement for the in-plane transverse direction, as well as significant shear reinforcement. Table 3.6 also includes results for the P300-A material, which was included in this stage of the study.

The weight distribution of these layers was further decomposed in Table 3.6, in respect to the fibre orientations within each layer. To this end, [0/90] layers were considered to present a half of the fibre weight in each direction, whereas for [+45/90/-45] layers, each direction was attributed one third of the layer weight.

Table 3.6: Fibre weight percentage and fibre layup characterization of test materials.

Material	Fibre weight [%]	Layup	Fibre weight per orientation [%]			
			0º	±45º	90º	C
I150-A	76	C/W/R/C/R/W/C	78	0	4	17
P300-A	73	C/R/C/W/C/R/C/W/C/R/C	58	0	12	30
I152-C	68	C/Q/R/Q/C	55	25	12	8
I200-F	64	C/W/R/W/C	73	0	8	19
I150-S	62	C/R/C/R/C/R/C/R/C	71	0	0	29
U150-S	66	C/Q/R/Q/Q/R/Q/C	67	19	7	8

* The fibre weight percentage per orientation was calculated assuming that 0/90 woven layers (W) have an even distribution between both orientations (50% per orientation) and that the -45/90/45 layers (Q) are also evenly distributed (33% per orientation).

Table 3.6 shows similar fibre weight percentage results for all test materials, varying from 64% to 76%. In a different perspective, Table 3.6 clearly illustrates the wide variety of fibre layups across these six test materials. Three major fibre layup groups may be established, as a function of the different transverse reinforcement layers: (i) materials exclusively reinforced in the transverse direction through continuous filament mats (I150-S), in what consists of a mostly unidirectional layup; (ii) materials reinforced with [0/90] woven layers (I150-A, P300-A and I200-F); and (iii) materials reinforced through ±45° and 90° oriented layers (I152-C and U150-S), which could be compared to a quasi-isotropic layup.

Table 3.6 presents results for the I150-A profiles that are in line with previously reported mechanical characterization results, which suggested that most of the fibre content is oriented in the longitudinal direction. To some extent, the higher fibre content weight percentage of this material may have led to the small defects found out and attributed to low fibre/matrix bonding. In a different perspective, the values presented in Table 3.6 may also be implemented to estimate a global in-plane transverse reinforcement percentage, taking into account the fibre weight of 90° oriented layers and 45° oriented layers (multiplied by a factor of $1/\sqrt{2}$ to account for the angle deviation), whereas randomly oriented layers (C) are disregarded. Table 3.7 presents a summary of the transverse reinforcement percentage for all six test materials. In this respect, a significant range can be found in the results of Table 3.7, as the transverse reinforcement percentage varies from ≈0% up to ≈30%.

Table 3.7: Transverse reinforcement percentage of test materials.

Material	I150-A	P300-A	I152-C	I200-F	I150-S	U150-S
Transverse Reinf. [%]	4	12	30	8	0	20

Table 3.7 shows that the I152-C profile presents the highest levels of transverse fibre reinforcement, a result that is in line with previously reported transverse tensile test results, which showed that this material presented the highest transverse tensile ultimate stress.

3.2.6. Overview of results

Table 3.8 presents a summary of fibre layups, elastic and strength properties. The fibre orientations described in the previous subsection agree relatively well with the reported material properties. The mechanical characterization of P300-A materials is also included, having been performed in [3.8].

Table 3.8: Summary of mechanical properties determined for pultruded GFRP test materials.

Material	Layup	Trans. Reinf. %	E_{11}^{+} [GPa]	E_{11}^{-} [GPa]	E_{22}^{+} [GPa]	E_{22}^{-} [GPa]	G_{12} [GPa]	σ_{u11}^{+} [MPa]	σ_{u22}^{+} [MPa]	σ_{u22}^{-} [MPa]	τ_{u12} [MPa]
I150-A	W	4.5	43.5	44.0	9.6	7.8	3.1	384	45	60	48
I152-C	Q	29.7	28.8	24.6	10.3	10.9	4.2	416	121	104	65
I200-F	W	8.3	29.6	29.9	11.9	10.8	2.9	323	71	122	67
I150-S	C	0.0	30.0	28.1	5.5	9.3	3.2	377	34	123	70
U150-S	Q	20.0	26.6	25.8	5.8	6.5	4.2	347	70	84	71
P300-A [3.8]	W	12.3	33.9	33.7	12.2	15.1	5.4	258	71	135	82

It is noteworthy that the I150-S materials, which present very low levels of transverse reinforcement, present the lowest transverse tensile strength; however, this material presents the highest transverse compressive strength. In this respect, the different resins and production processes may also impact the results; however, these parameters could not be taken into account, as they were not released by the manufacturers. It is also noteworthy that the I150-A material, despite presenting [0/90] woven layers, presents low transverse tensile strength, as well as the lowest transverse compressive strength. This was partly attributed to the aforementioned production defects.

The transverse reinforcement percentage appears to present a non-linear influence on the transverse tensile ultimate stress, as the material presenting the highest percentage of transverse reinforcement also presents the highest transverse tensile ultimate stress (I152-C), but several materials with percentages ranging from the 8% to 20% present similar transverse tensile ultimate stresses of ≈70 MPa (P300-A, I200-F, U150-S).

3.3. Preliminary experimental fracture tests

3.3.1. Tensile test configuration summary

As summarized in Chapter 2, there are several experimental and analytical methodologies that may be implemented in the experimental characterization of fracture properties of composite materials. The following test methodologies were considered: (i) CT test configuration; (ii) DCB test configuration; (iii) bending test configurations; and (iv) size effect methodologies.

The CT test configuration has been implemented in a significant number of experimental studies regarding translaminar fracture toughness [3.3], mostly within the context of CFRP materials, including stacked laminates [3.12], woven laminates [3.13] and non-crimp fibre (NCF) laminates [3.14]. Furthermore, several data reduction methods have been implemented with this test configuration, including closed form analytical expressions [3.15], FE-based J-integral [3.12] and compliance calibration methods [3.16, 3.17].

Specimen preparation is a complexity typically attributed to CT tests, as the accuracy of energy release rate estimates, especially in the damage initiation stage, have been shown to significantly depend on the refinement of the initial notch tip [3.18].

The DCB and bending test configurations share a common liability in regard to this study, as both these test configurations have been mainly implemented regarding intralaminar phenomena, which present much lower fracture toughness values than translaminar phenomena [3.12]. Therefore, these configurations were not considered as ideal starting points for this study.

A different methodology would consist of using scaled DEN specimens to determine the R-curve of each material as a function of the size-effect law [3.19]. This methodology has an added benefit, as the test specimens do not require a sharp notch tip, as most other fracture test configurations [3.19]. However, this test configuration would require a considerably larger number of tests per material, several for each specimen scale. Furthermore, the higher levels of variability of pultruded GFRP materials could undermine an accurate measurement of the size-effect law and their higher thickness may also lead to delamination phenomena, which would render the DEN tests useless.

Considering the previously gathered information regarding these various test configurations, the CT test configuration was chosen as a starting point for the experimental study. This decision was based on the more solid field of application of CT tests. In addition to standard CT tests, some variants have also been developed, such as the ECT [3.20], OCT [3.21] and WCT [3.13]. These test configurations, which consist of different modifications of the standard CT test configuration, were considered for a second stage, as a function of the preliminary CT test results.

3.3.2. CT test programme

3.3.2.1. Materials

The preliminary experimental tests were conducted on the I200 pultruded GFRP profile supplied by Fiberline Composites (I200-F). This material presents significant transverse reinforcement provided by woven [0/90] layers. The CT specimens were taken from the web of the profile and the initial notches were cut parallel to the roving direction, so that the transverse direction of the material could be assessed.

3.3.2.2. Specimen geometry

The CT specimen geometry is illustrated in Figure 3.15, consisting of an approximately squared shape with 60 mm of width and 58 mm of height. CT specimens were machined through a 2 mm thick circular saw blade, to create most of the initial notch length, and through a 0.6 mm thick circular saw blade, for additional 5 mm, resulting in a thin square shaped notch tip, illustrated in Figure 3.16.

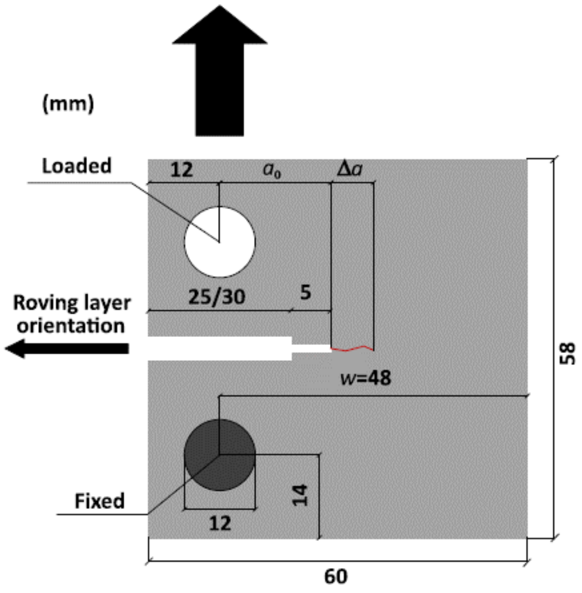

Figure 3.15: CT specimen geometry (thickness of 9.9 mm).

The CT tests comprised two nominal initial notch lengths, of 30 and 35 mm, which result in a distance from the load application axis to the notch tip of a_0=18 mm and a_0=23 mm, respectively (see Figure 3.15). For each initial notch length, three CT specimens were tested. The following nomenclature was used: CT_23_1 is specimen #1 of CT tests with a_0=23 m.

Figure 3.16: Square shaped notch tip of CT specimen.

3.3.2.3. Test setup

Figure 3.17 illustrates the test setup implemented for CT and WCT tests (discussed in Section 3.3.3). The load was applied through steel loading pins, attached to an *Instron* universal testing machine, with capacity of 250 kN and a load cell with precision of ≈0.01 kN. CT tests were conducted through displacement control, at a rate of 0.5 mm/min.

A video-extensometry system was used to monitor the crack mouth opening displacement (CMOD) in CT tests (high-resolution camera from Sony, model XCG 5005E, with Fujinon lens). The targets used for this purpose are illustrated in Figure 3.17 (b), also illustrating targets used to monitor the crack tip opening displacement (CTOD), implemented for WCT tests (see Section 3.3.3). To improve the accuracy in the monitoring of the targets, each specimen was painted with white matte paint and the targets were marked with a black marker pen. In order to assess crack propagation, the posterior face of the specimen was monitored through a microscopic camera (Dino-Lite Edge Digital Usb Microscope, model AM7915MZT), positioned as illustrated in Figure 3.17 (c).

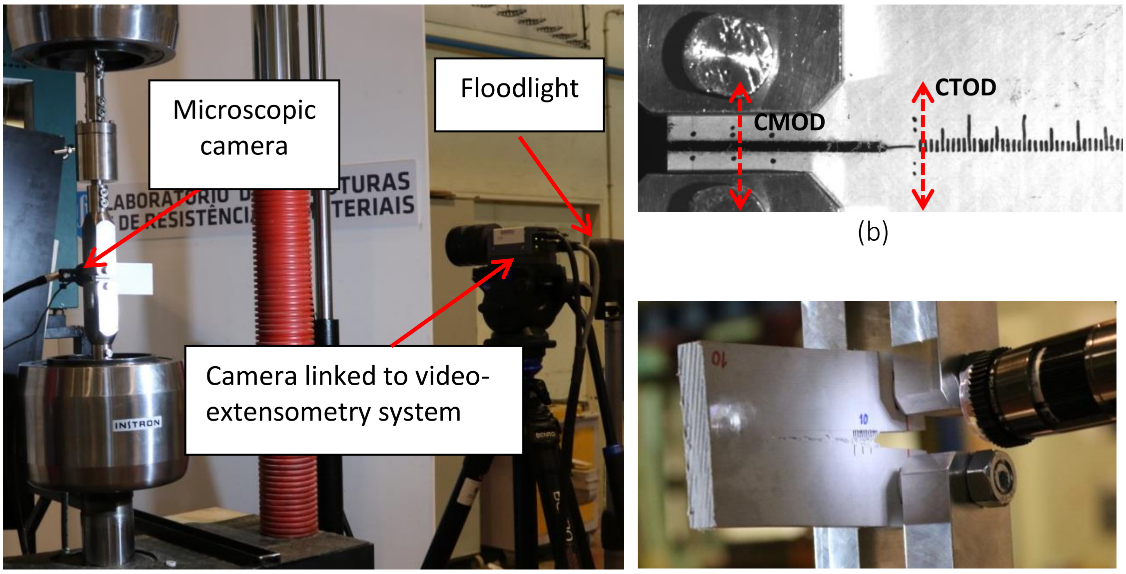

(b)

(a) (c)

Figure 3.17: Experimental test setup implemented for CT and WCT tests: (a) test setup; (b) picture taken from video-extensometry footage; (c) positioning of microscopic camera.

3.3.2.4. Data reduction

The R-curve method was implemented, by measuring the energy release rate throughout crack propagation. To determine the energy release rate, several data reduction methods were applied: (i) ASTM E399 [3.22], a standard developed for metallic materials, which may be adapted to orthotropic materials; (ii) FE based J-integral estimates; (iii) Compliance calibration (CC), based on FE models and visual observation of crack propagation.

The ASTM E399 standard [3.22] was developed specifically for CT specimen geometries. It is the simplest method to extract the energy release rate from fracture tests; however, it has been shown to present a relevant margin of error [3.12, 3.15]. This has been attributed to the isotropic material background of its formulations, initially developed for metallic materials. The energy release rate is estimated through expressions (3.1)-(3.3),

$$G = \frac{K_I^{\,2}}{\sqrt{2E_{11}E_{22}}}\sqrt{\sqrt{\frac{E_{11}}{E_{22}}}+\frac{E_{11}}{2G_{12}}-\upsilon_{12}} \tag{3.1}$$

$$K_I = \frac{F}{t\sqrt{w}}f\left(\frac{a}{w}\right) \tag{3.2}$$

$$f\left(\frac{a}{w}\right) = \frac{2+\frac{a}{w}}{(1-\frac{a}{w})^{1.5}}\left[0.886+4.64\left(\frac{a}{w}\right)-13.32\left(\frac{a}{w}\right)^2+14.72\left(\frac{a}{w}\right)^3-5.6*\left(\frac{a}{w}\right)^4\right] \tag{3.3}$$

where G is the laminate energy release rate, E_{11} is the elastic modulus in the crack direction (longitudinal direction of the profile), E_{22} is the elastic modulus in the load direction (transverse direction), G_{12} is the shear elastic modulus, ν_{12} is the Poisson's ratio; K_I is the mode I stress intensity factor, F denotes the load measured at a given stage of crack propagation, t is the specimen thickness, a represents the length of the crack, measured from the centre of the loading holes, including the initial notch length a_0 and the crack propagation length Δa (as illustrated in Figure 3.15), w denotes the distance between the centre of the loading holes and the opposite face of the specimen.

In a more complex approach, FE models were developed for a range of crack lengths, to determine the J-integral variation as a function of crack length. *Abaqus* commercial software [3.23] was implemented to perform this linear elastic analysis, based on 0.2 mm S4R shell elements. These elements and mesh size were selected after an initial mesh sensitivity analysis. A load of 1 N was applied through coupling restraints, to the upper half of the top loading hole, which was also restrained regarding the horizontal displacements; whereas the lower half of the bottom loading hole was restrained regarding all displacements. Ortega *et al.* [3.24] have shown that these boundary conditions have negligible influence on the results.

Through these models, illustrated in Figure 3.18, the unit J-integral is determined for a range of crack lengths so that the experimental result for a given crack length can be determined by computing the load level at that crack increment. Despite being a more complex method, it is expected to yield more reliable results [3.12] and thus it was applied to both test configurations.

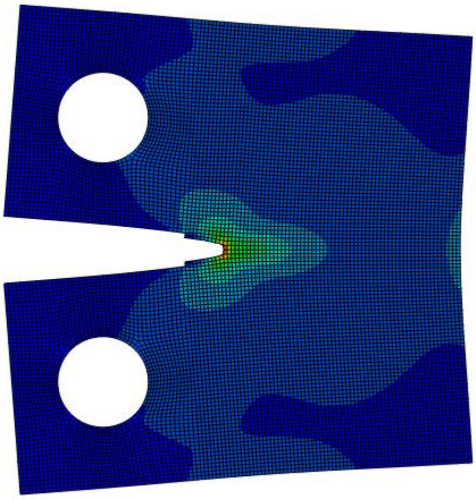

Figure 3.18: FE elastic numerical model, loaded with a unit load (1 N).

The J-integral/crack length ratio was determined by defining the crack tip for each targeted crack growth. To this end, the "Seam" tool was used to propagate the crack further for each increment. As the first J-integral contours are usually inaccurate, the fifth contour was selected for all crack growth stages. The J-integral curve was then fitted by a polynomial function, so it could be extrapolated for any crack length.

In a complementary perspective, CC was implemented in parallel to the FE J-integral method. This method consists of correlating the compliance variation of a specimen to crack growth. In this instance, the previously detailed FE models were used to determine the compliance *vs*. crack length ratio by extracting the vertical displacement produced by 1 N, for a range of crack lengths. This numerical CC curve can be fitted through an analytical expression,

$$C = (\alpha a + \beta)^{\chi} \tag{3.4}$$

where C stands for compliance and α, β, χ are fitting parameters. Expression (3.4) was reported by Laffan *et al.* [3.17] to provide a good fit to CC curves. Finally, these parameters can be used to determine the energy release rate as detailed in (3.5),

$$G = \frac{P}{2t}\alpha\chi C^{\frac{\chi-1}{\chi}} \tag{3.5}$$

Where G is the energy release rate at a given load increment P. Expression (3.5) can be applied to any crack propagation increment, also in accordance to [3.17]. The energy release rate estimates of these three methods, considering a unit load, are illustrated in Figure 3.19.

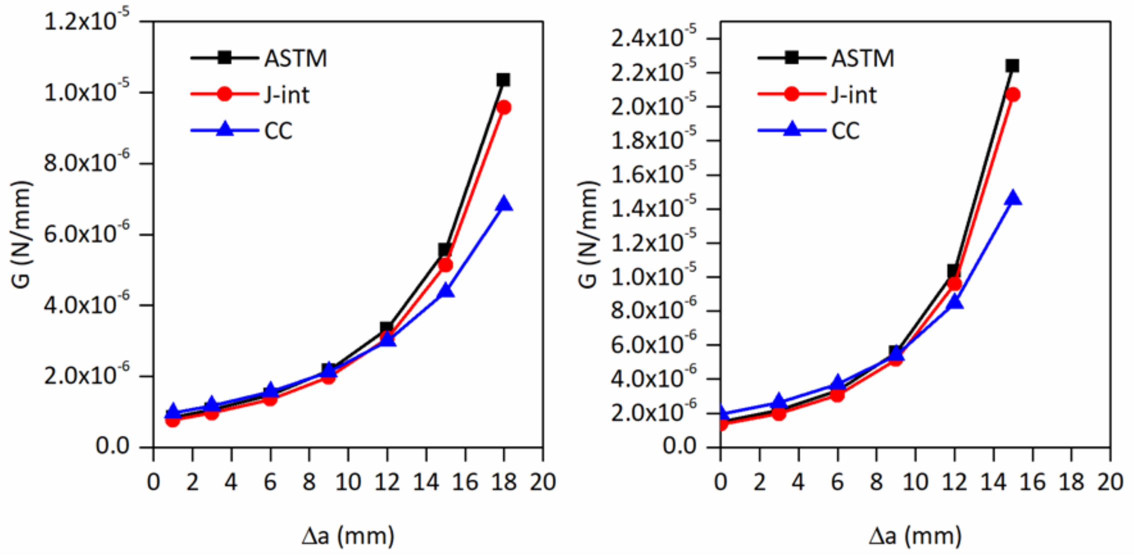

(a) (b)

Figure 3.19: G *vs*. Δa curves, for an applied load of 1 N, including different data reduction methods: (a) CT specimen, a_0=18 mm; (b) CT specimen, a_0=23 mm.

Figure 3.19 shows a good agreement between all three methods for crack propagation lengths up to ≈13 mm, a point from which the compliance calibration results start diverging. This was attributed to the calibration process, which focused on lower crack propagation lengths. It should also be highlighted that once the crack tip reaches an area closer to the posterior face of the specimen, some interaction should be anticipated between the stresses at the crack tip and the compressive stresses at the posterior face, which can potentially influence the energy release rate measurements [3.20].

3.3.2.5. CT test experimental results

3.3.2.5.1. Failure modes

Crack propagation patterns are presented in Figure 3.20, based on footage taken through the microscopic camera. Despite the irregular crack growth pattern observed, all crack measurements were made with respect to the specimen horizontal axis, as the cracks globally progress transversely to the load direction. Figure 3.20 also shows that the cracks initiated close to the corners of the initial notch.

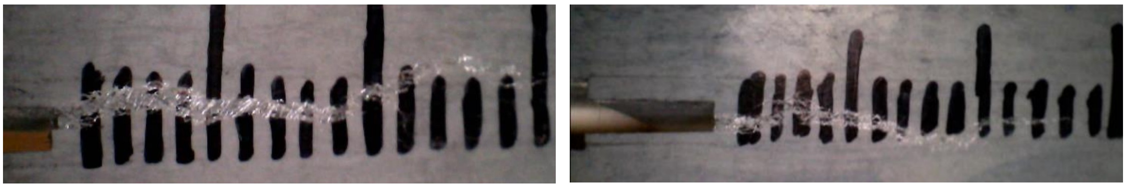
(a) (b)

Figure 3.20: Crack growth of CT specimens: (a) a_0=18_2; (b) a_0=18_3.

3.3.2.5.2. Load vs. displacement curves

The CT load *vs*. displacement curves for each initial notch length are displayed in Figure 3.21. As expected, lower initial notch lengths presented higher stiffness and strength results. A significant scatter can also be found in the results, with relative differences of 15% and 18% of ultimate strength, for a_0=18 mm and a_0=23 mm respectively; possible reasons for such variations are discussed ahead. It is also noteworthy that the softening stages of a_0=18 mm and a_0=23 mm curves converge.

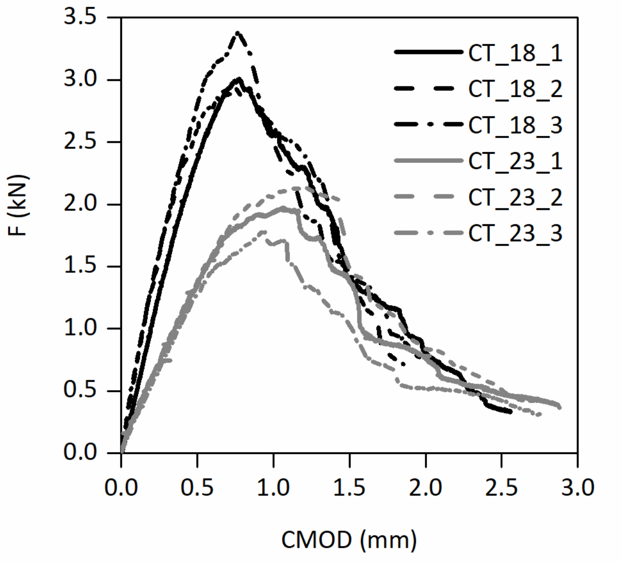

Figure 3.21: Load *vs*. CMOD curves of CT tests for a_0=18 mm and a_0=23 mm.

3.3.2.5.3. Energy release rate results

Crack propagation in CT specimens was only monitored through the microscopic camera and thus it was only measured for a length of 15 mm. This length was selected to ensure that crack propagation was clearly distinguishable. Furthermore, as stated above, when the crack develops towards the posterior face of the specimen, the energy release rate results may be affected by compressive stresses developing in the vicinity of that edge.

Figure 3.22 presents a comparison between G *vs.* Δa curves obtained from ASTM E399, J-integral and CC methods, for specimen CT_18_1 (Figure 3.22 (a)), as well as a comparison between G *vs.* Δa curves for a_0=18 mm and a_0=23 mm, considering only the J-integral results (Figure 3.22 (b)).

Figure 3.22 (a) shows a good agreement between all methods, particularly for the early stages of crack propagation. Whereas Figure 3.22 (b) clearly shows that, despite the high levels of scatter, the specimens presenting lower initial notch lengths (a_0=18 mm) reach higher values of energy release rate. No stable propagation stage is discernible through the results presented in Figure 3.22 (b).

Taking into consideration the J-integral method, the specimens with a_0=18 mm and a_0=23 mm reached average maximum energy release rate values of 28.8 N/mm and 18.6 N/mm, respectively. As the specimens did not reach a stable propagation stage, this difference can be attributed to the short length available for crack propagation, as different initial notch lengths appear to lead to different fracture toughness estimates, prior to ultimate failure, and thus, lead to different stages of crack propagation. This trend indicates significant specimen geometry dependency, which is further discussed in the following section.

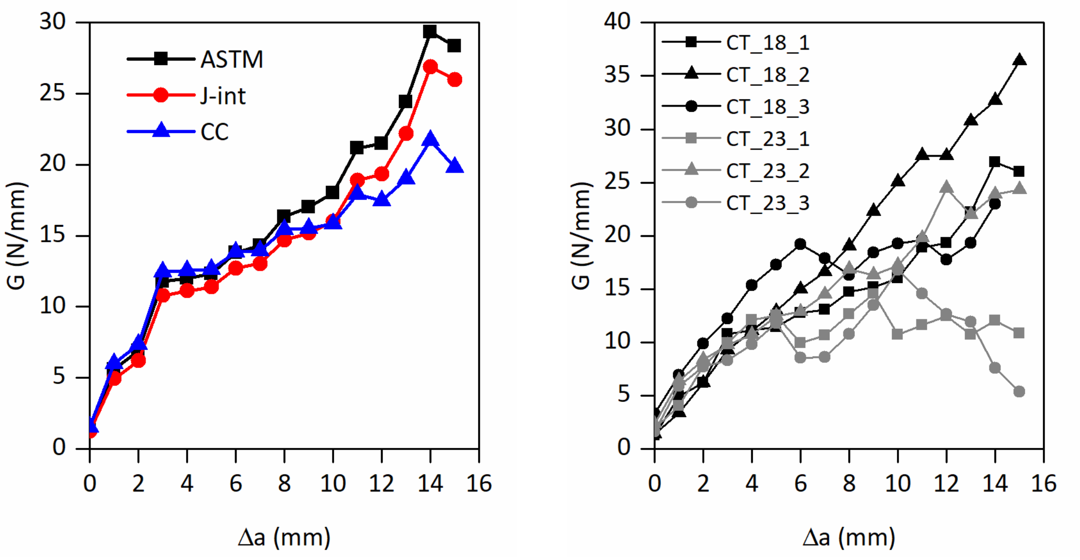

(a) (b)

Figure 3.22: Energy release rate (G) *vs.* Δa curves: (a) overview of data reduction methods for specimen CT_18_ 1; (b) comparison between a_0=18 mm and a_0=23 mm for J-integral results.

3.3.2.6. Preliminary findings

Several issues were found with the CT fracture tests presented above. Firstly, the initial notch tip shape promoted irregular damage initiation, beginning in the corners of the squared notch tip. This should not affect damage propagation significantly [3.18], however it should contribute to higher scatter in the results of early propagation stages.

The most significant issue observed in the CT test results was specimen geometry dependency, as comparing energy release rate estimates for both initial notch lengths led to considerable differences. As was previously mentioned, fracture tests of composite materials may present significant dependency on specimen geometry. Ortega *et al.* [3.25] proposed a characteristic material length (l_M), which could be used as a measure of specimen geometry dependency by comparison with specimen dimensions. This characteristic length is given by,

$$l_M = \frac{G_c E'}{\sigma_u^2} \tag{3.6}$$

where E' is the equivalent plane stress or plane strain elastic modulus, σ_u is the material ultimate stress and G_c is the fracture toughness. The equivalent plane stress elastic modulus can be determined as,

$$E' = \frac{\sqrt{2E_{11}E_{22}}}{\sqrt{\sqrt{\frac{E_{11}}{E_{22}}} + \frac{E_{11}}{2G_{12}} - \upsilon_{12}}} \tag{3.7}$$

Ortega *et al.* [3.25] proposed that fracture specimens that present dimensions similar to l_M may lead to overestimations of energy release rate results. To apply this assessment to CT tests, the authors considered the normalized characteristic length, $\bar{l}_M$, given by,

$$\bar{l}_M = \frac{l_M}{w} \tag{3.8}$$

where w is the aforementioned distance between the centre of the loading holes and the opposite face of the specimen. In particular, Ortega *et al.* [3.25] reported that high normalized characteristic lengths ($\bar{l}_M$) lead to significant overestimations of energy release rate results: they referred that $\bar{l}_M$ ratios of 1 should result in overestimations higher than 20%, whereas $\bar{l}_M$ ratios lower than 0.5 should provide more accurate results.

These formulations were applied to CT and WCT test configurations, as the WCT test configuration is the only CT-based variant to present a higher width/notch ratio. The resulting values of $\bar{l}_M$ for CT and WCT specimen geometries are detailed in Table 3.9. These estimates have been updated with the fracture toughness determined from the J-integral average of WCT test results (20.2 N/mm), as presented in Section 3.3.3.

Table 3.9: Characteristic lengths for CT and WCT specimen configurations.

Configuration	w [mm]	G_c [N/mm]	l_M [mm]	$\bar{l}_M$ [mm]
CT	48	20.2*	42.2	0.88
WCT	108			0.39

* updated with FE-based J-integral estimates of WCT tests.

The CT test $\bar{l}_M$ ratio presented in Table 3.9 highlights the limitations of CT tests for this material. Furthermore, it is also shown that the WCT tests significantly mitigate this limitation, as they present a much lower $\bar{l}_M$ ratio (below 0.5). In face of these results, the WCT test configuration was selected as the subsequent experimental step for assessing fracture properties of pultruded GFRP materials.

Finally, a different issue was found in respect to crack propagation and its irregular crack path. This behaviour suggested that the crack profile through the thickness may be irregular and that superficial monitoring methods may not correctly assess the crack-tip position. Therefore, the WCT tests were developed with an added data reduction method, modified compliance calibration (MCC), which aims to estimate crack length as a function of compliance.

3.3.3. WCT test programme

3.3.3.1. Materials

The WCT tests were performed for the same material, I200-F profile, acquired from Fiberline Composites. In a similar fashion to previously reported CT tests, the WCT specimens were taken from the web of the profile and the initial notches were cut parallel to the roving direction.

3.3.3.2. Specimen geometry

The WCT specimen consists of a CT specimen with doubled width, allowing for higher lengths of crack propagation, as displayed in Figure 3.23. The WCT test has received less attention from the scientific community in recent years, mostly due to its higher propensity for buckling failure when compared to CT specimens [3.13], especially for thin CFRP laminates. This, however, is less likely to be problematic in pultruded GFRP materials, which typically present lower ultimate stresses and higher thicknesses.

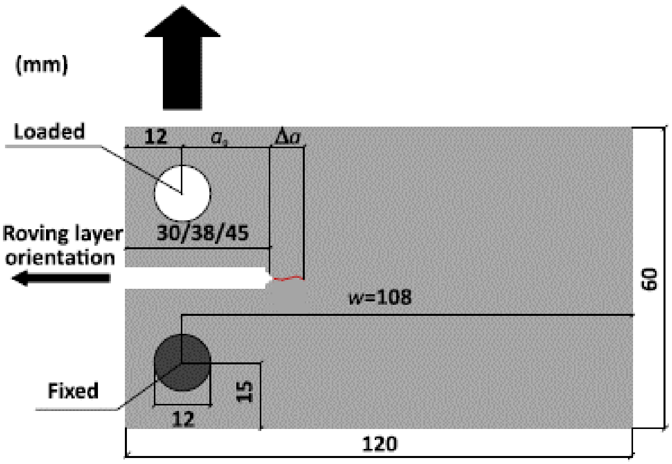

Figure 3.23: WCT specimen geometry (thickness of 9.9 mm).

Another relevant difference between these experimental campaigns pertains to the initial notch tip shape. Experimental footage of CT tests, taken from the microscopic camera, showed that the cracks initiated in the notch tip corners of several specimens (see Figure 3.20). The WCT specimens were thus prepared through a different process, which consisted of sharpening the notch tip through a 0.3 mm thick wire saw, as displayed in Figure 3.24.

Figure 3.24: Round shaped notch tip of WCT specimen.

WCT tests included three initial notch lengths, of 30, 38 and 45 mm, resulting in a_0 lengths of 18, 26 and 33 mm. As the scatter found in CT results was significant, a minimum of six WCT specimens were tested per initial notch length. Additionally, in order to implement MCC, discussed ahead, some WCT tests were subjected to loading/unloading cycles and thus, these tests were also classified as “M” or “C”, regarding monotonic and cyclic loading conditions. The following nomenclature was used: WCT_18_2_C is WCT specimen #2, with a_0=18 mm, submitted to load/unload cycles.

3.3.3.3. Test setup

The test setup of WCT tests is identical to that detailed for CT tests (see Figure 3.17). However, a displacement rate of 1 mm/min was implemented for most WCT tests, in order to have similar test durations, in comparison to previous CT tests. As previously mentioned, the CT specimens were continuously loaded until failure, whereas some WCT specimens were subjected to loading/unloading cycles after the ultimate load had been reached. The video-extensometry methodology was implemented to monitor the crack tip opening displacement (CTOD) in WCT tests, a measure that is intended to determine the cohesive law of the material, by differentiating the energy release rate results in respect to CTOD [3.26]. The video-extensometry system was also implemented to monitor crack growth in WCT tests, by drawing a millimetric scale in front of the crack tip and increasing the contrast of the camera, so that damage may be more clearly perceived and monitored.

3.3.3.4. Data reduction

Aside from the data reduction methods reported for CT tests, MCC was developed similarly to standard CC, taking into consideration the same formulations. The advantage of MCC is that it relies on experimental compliance measurements to determine the effective crack length, circumventing the need to optically measure the crack. Several research works have concluded that the MCC is the most efficient method to determine the energy release rate in fracture tests [3.16, 3.27], as compliance calibration can be performed through FE models and optical measurements of crack propagation are circumvented. A required step to perform MCC was to implement loading/unloading cycles. In this study, the compliance was measured in both loading and unloading stages, which showed an overall good agreement. Figure 3.25 presents energy release rate estimates for a unit load, including all the previous data reduction methods (at this stage, CC and MCC are identical). As would be expected, the ASTM E399 [3.22] results are geometry dependent and cannot be applied to WCT tests. CC results seem to underpredict J-integral results, but only for considerably long crack lengths.

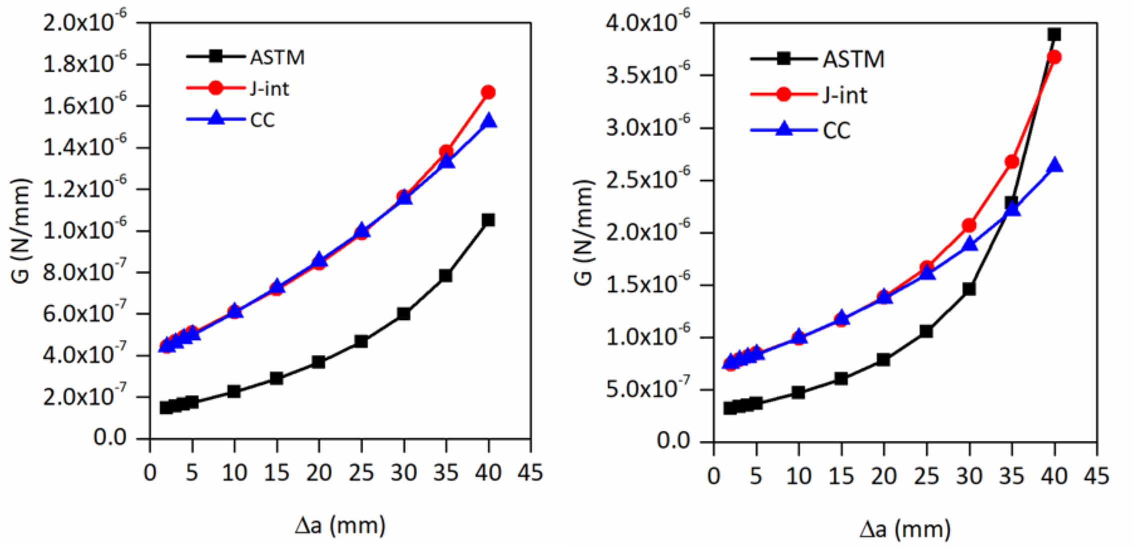

(a) (b)

Figure 3.25: Energy release rate (*G*) *vs*. *Δa* curves, for an applied load of 1 N, including different data reduction methods: (a) WCT specimen, a_0=18 mm; (b) WCT specimen, a_0=33 mm.

3.3.3.5. WCT test experimental results

3.3.3.5.1. Failure modes

Figure 3.26 presents representative crack propagation patterns of WCT specimens, visible through the video-extensometry (figure 3.26 (a)) and microscopic (figure 3.26 (b)) cameras. Note that Figure 3.26 (b) shows crack initiation at the centre of the initial notch, thus validating the notch insertion process used for WCT specimens.

The crack growth patterns displayed in Figure 3.26 are in line with those found in CT specimens, clearly showing an irregular crack path that develops longitudinally across the specimen. As performed for CT tests, all crack measurements were performed in respect to the central horizontal axis of each specimen and did not take into account the vertical projection of irregular crack growth patterns.

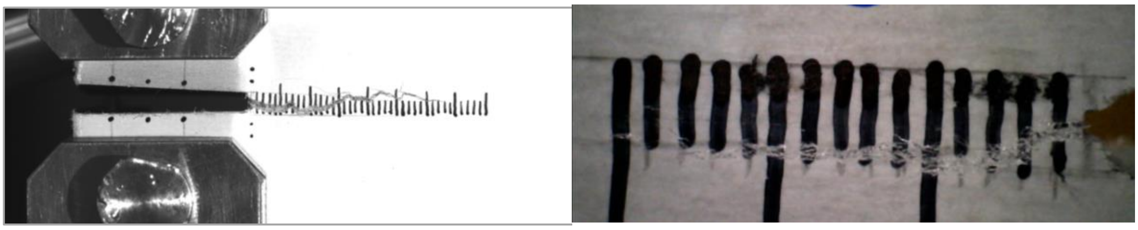

(a) (b)

Figure 3.26: Crack growth patterns of WCT specimens: (a) picture taken from video-extensometry footage (WCT_18_3); (b) picture taken from microscopic camera (WCT_18_5).

3.3.3.5.2. Load vs. displacement curves

The WCT load *vs*. displacement curves are displayed in Figure 3.27, for both monotonic and cyclic loading. Figure 3.27 clearly shows that for all initial notch lengths the load/unload cycles had no significant influence on the softening slope and, thus, should not affect the energy release rate.

Overall, the WCT specimens presented higher ultimate failure loads than their CT counterparts. This result was somehow expected, as the WCT specimens presented a larger area for crack growth. The ultimate failure loads of WCT specimens were less scattered than the CT ones. This may be attributed to the fact that all WCT specimens reached a stable crack propagation stage (as detailed ahead), whereas CT specimens have reached different stages of crack propagation, as a function to the initial notch length; note that the intrinsic material variability, discussed ahead, should affect both types of geometry.

Finally, Figure 3.27 (d) presents a comparison of load *vs*. displacement curves for the specimens under monotonic loading and including all three initial notch lengths. It can be seen that the specimens with lower initial notch lengths presented overall higher strength and stiffness values; this result is logical and in line with CT test results. Figure 3.27 (d) also shows that the softening stages converge across all initial notch lengths, similarly to CT test results.

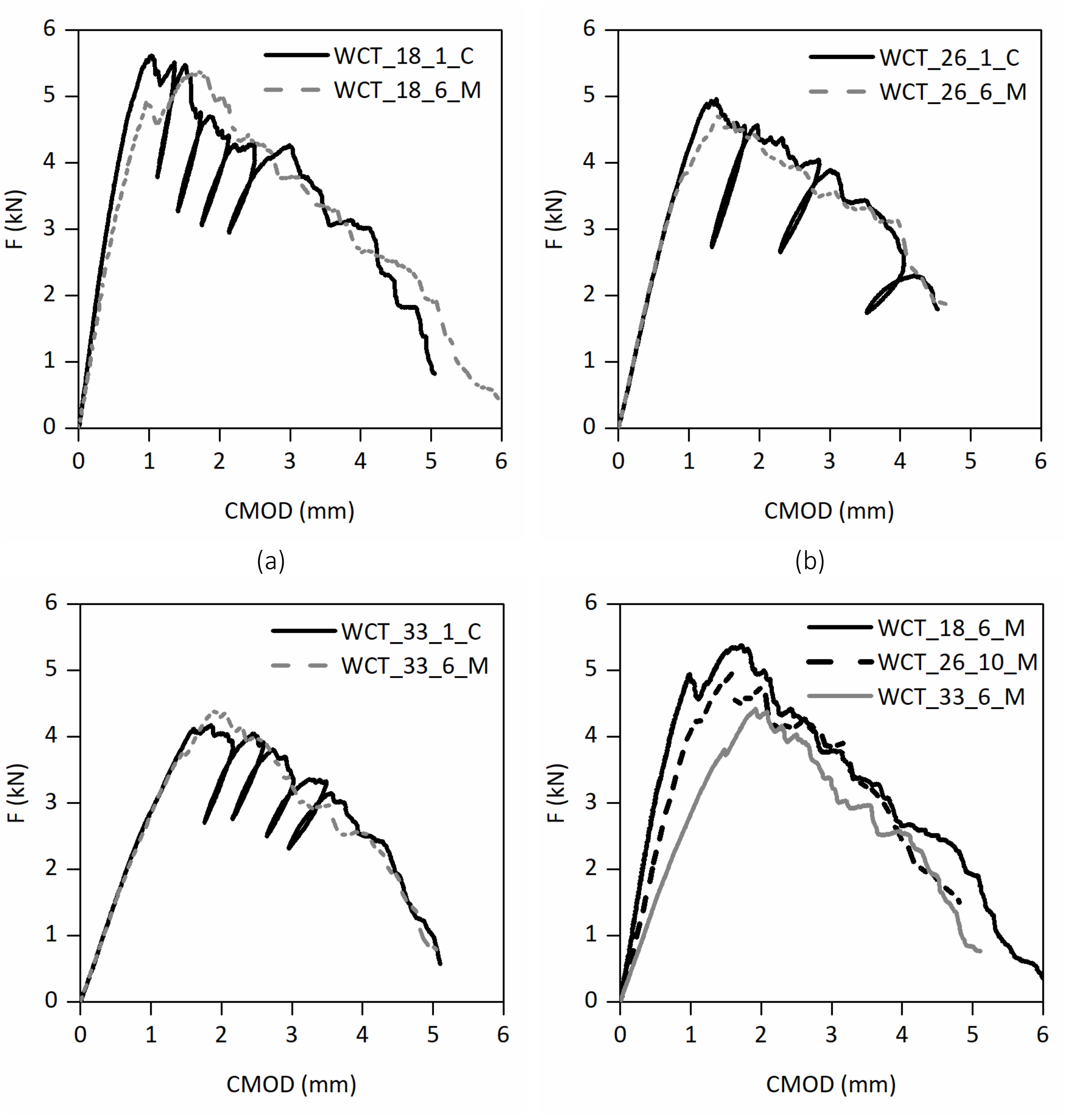

(a) (b)

(c) (d)

Figure 3.27: Load *vs*. CMOD curves of WCT tests:
(a) a_0=18 mm; (b) a_0=26 mm; (c) a_0=33 mm; (d) comparison for monotonic loading.

3.3.3.5.3. Energy release rate results

The WCT test specimens were monitored in respect to crack propagation through both the video-extensometry and microscopic cameras, which enabled a more detailed assessment of damage initiation, through the microscopic camera, complemented by the footage of the video-extensometry system, which captured the whole specimen. Figure 3.28 presents a comparison of measurements between the microscopic camera and video-extensometry for a specimen with a_0=26 mm (WCT_26_2_C), showing a good agreement between crack propagation on both front and posterior faces. The specimens were also monitored in respect to CTOD, by tracking the targets marked on each side of the crack tip. Figure 3.29 presents *G vs*. CTOD curves for the WCT_26_1_C specimen, regarding the aforementioned processing methods (J-integral, CC and MCC).

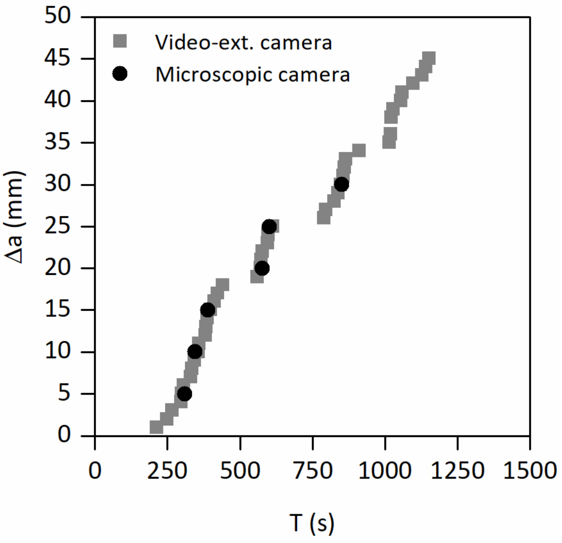

Figure 3.28: Crack propagation (Δa) *vs*. Time (T) curves, based on video-extensometry and microscopic measurements for WCT_26_2_C specimen.

The results summarized in Figure 3.29 clearly show that the WCT specimens reach a stable propagation stage, after a steeply increasing trend at damage initiation. This is a clearly different trend to that reported for previous CT tests. It is also noteworthy that, for a_0=18 mm, the overall J-integral results for WCT (21.9 N/mm) are 30% lower than the CT corresponding results (28.8 N/mm). These results are in accordance with the conclusions presented by Ortega *et al.* [3.25], associating smaller specimen sizes to significant overestimations of the energy release rate (higher than 20%).

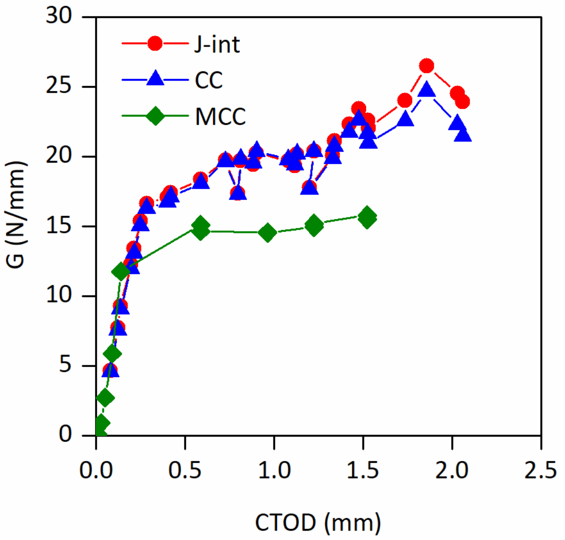

Figure 3.29: Energy release rate (G) *vs*. CTOD curves for different data reduction methods (WCT_26_1_C).

The results presented in Figure 3.29 show a good agreement between J-integral and CC methods. However, the MCC results are significantly lower than the ones obtained with the other two methods at the propagation stage, despite showing a similar slope for lower values of CTOD. This trend is attributed to different potential causes: (i) the crack front may develop differently along the various laminae and thus the crack length measured at the visible surface may be overestimated; (ii) the compliance calibration may not match the actual specimen behaviour; (iii) the elastic properties considered in FE models may not correlate well with the experiments. Finally, as the MCC method was applied to both loading and unloading cycles, showing a good agreement, measurement errors were ruled out. These measurements are schematically illustrated in Figure 3.30.

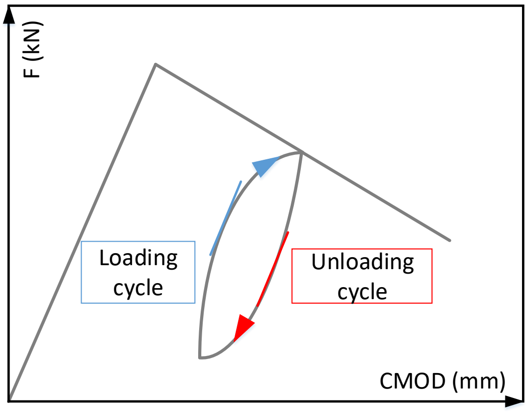

Figure 3.30: Schematic illustration of loading/unloading cycles at post-peak descending path.

At this stage, the first possible cause is considered to be the most significant, as the crack propagation was not monitored along the thickness, within the different laminae. Furthermore, the CC results are in line with J-integral results and thus the second possible cause is less plausible. Finally, the elastic properties were validated by comparing the crack growth rates based on visual measurements (“Visual”) to analytical predictions based on modified compliance calibration (“MCC”). A comparison of crack growth rates is presented in Figure 3.31, comprising results of specimen WCT_26_5_C. Figure 3.31 clearly shows that visual and compliance-based crack growth rates are similar, presenting a constant offset.

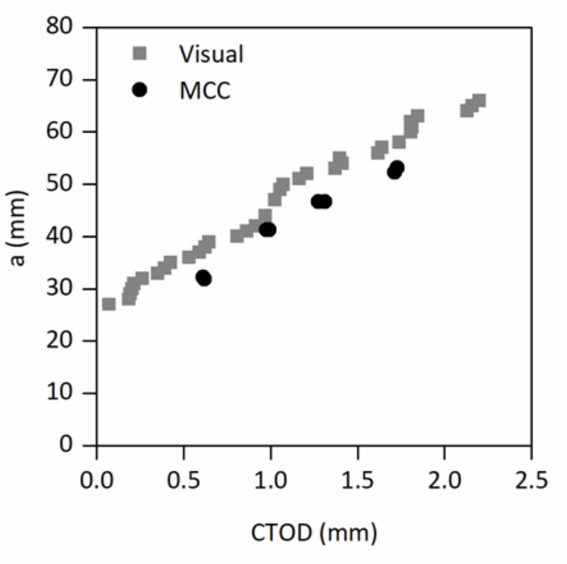

Figure 3.31: Overview of visual observation based and modified compliance calibration based crack propagation of specimen WCT_26_5.

Previous research works have found discrepancies between MCC and other data reduction methods. Laffan *et al.* [3.16] reported different results based on visual observations and MCC; however, the MCC results were higher than standard CC results. These discrepancies were also attributed to differences between visual observations and effective crack lengths. On a different note, Laffan *et al.* [3.16] proposed that pulled-out fibres may affect the compliance measurements in loading/unloading cycles, during the propagation stage. This may be considered as a potential cause for the discrepancy between MCC and remaining results, as discrepancies were only found in the stable propagation stage, where loading/unloading cycles were performed; however, this potential issue should have a significant impact in the comparison of “visual” measurements and MCC based estimates. The results shown in Figure 3.31 do not seem to support this hypothesis.

Bergan *et al.* [3.27] compared MCC results to J-integral calculations based on DIC measurements. In this case, MCC results were reported to be slightly lower than those based on DIC measurements. Abdullah *et al.* [3.28] reported significant differences between MCC and visually based results. In fact, MCC results almost doubled visually based results for low increments of crack growth. To further analyse this discrepancy between MCC and other data reduction methods, other pultruded materials should be tested and a more refined monitoring approach should be considered to assess the crack growth at lamina level. The results can also be further validated by implementing the results in FE models.

Figure 3.32 presents J-integral results plotted as a function of CTOD for all initial notch lengths. These results show a good agreement across the various notch lengths, as most data points are contained within 15 and 25 N/mm. However, these data still present relevant scatter, with an average COV of 10% for each initial notch length. This result is in line with previous research [3.29], where significant scatter has been reported in experimental energy release rate estimates. It should be highlighted that these CTOD measurements pertain only to the initial crack tip and, therefore, once a stable propagation stage is reached (at CTOD≈0.75 mm), the CTOD measurements no longer pertain to the current crack tip.

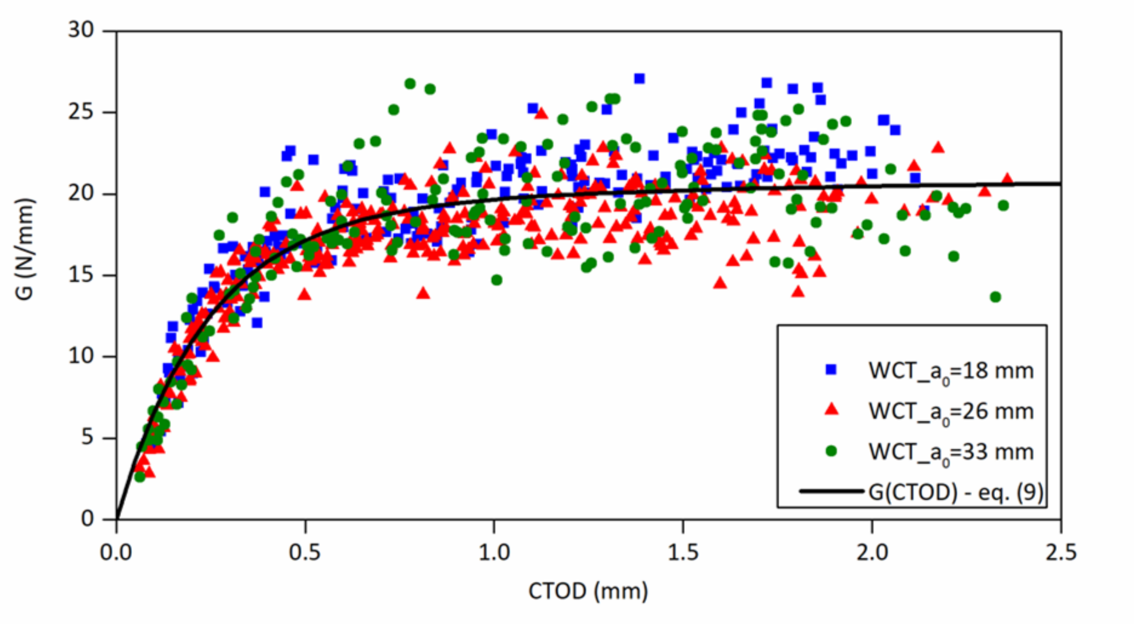

Figure 3.32: Energy release rate (*G*) *vs*. CTOD curves of WCT tests, based on the J-integral method and analytical fitting of results.

The averaged energy release rate results, including the coefficient of variation (*CoV*), are summarized in Table 3.10, for each value of a_0 and data reduction method. To this end, the results were selected for CTOD values equal or higher than 1 mm, where the stable propagation stage initiates.

The results presented in Figure 3.32 and Table 3.10 still show some discrepancies for different initial notch lengths. However, taking into consideration the inherent variability of GFRP materials, these differences are considered natural and typical of pultruded GFRP profiles [3.1]. It is also noteworthy that the energy release rate (overall average of 20.2 N/mm) is significantly higher than those reported in the literature (7.7-8.9 N/mm) [3.1, 3.2]. This fact is attributed to the fibre layup of the I200 profile used in these experiments, which comprises cross-ply laminae, thus increasing the transverse fracture properties when compared to standard continuous filament mats.

Table 3.10: Summary of fracture toughness average results – average ± *CoV*.

a_0 [mm]	J-integral [N/mm]	CC [N/mm]	MCC [N/mm]
18 mm	21.9 ±8.7%	21.2 ±8.2%	17.3 ±13.9%
26 mm	19.1 ±9.9%	19.8 ±12.2%	17.04 ±5.6%
33 mm	20.2 ±14.7%	17.61 ±15.8%	13.9 ±6.2%
Overall results	20.2 ±12.5%	19.6 ±13.8%	16.2 ±13.8%

The results presented in Table 3.10 clearly show that the WCT tests, when applied to this material, show a negligible level of geometry dependency: despite the significant range of initial notch lengths tested, no significant discrepancies were found in the results. The scatter of results was also assessed by determining the normal distributions that would fit the experimental results; this assessment is displayed in Figure 3.33, including peak G values and probability density. These distributions provide the following 90% confidence intervals for different methods: (i) 16.0-24.3 N/mm (J-integral), (ii) 15.6-23.5 N/mm (CC) and (iii) 12.7-19.8 N/mm (MCC). It can thus be concluded that a significant level of scatter is present in these results, regardless of the data reduction method. Figure 3.33 highlights further the discrepancy between MCC and the other data reduction methods (J-integral and CC).

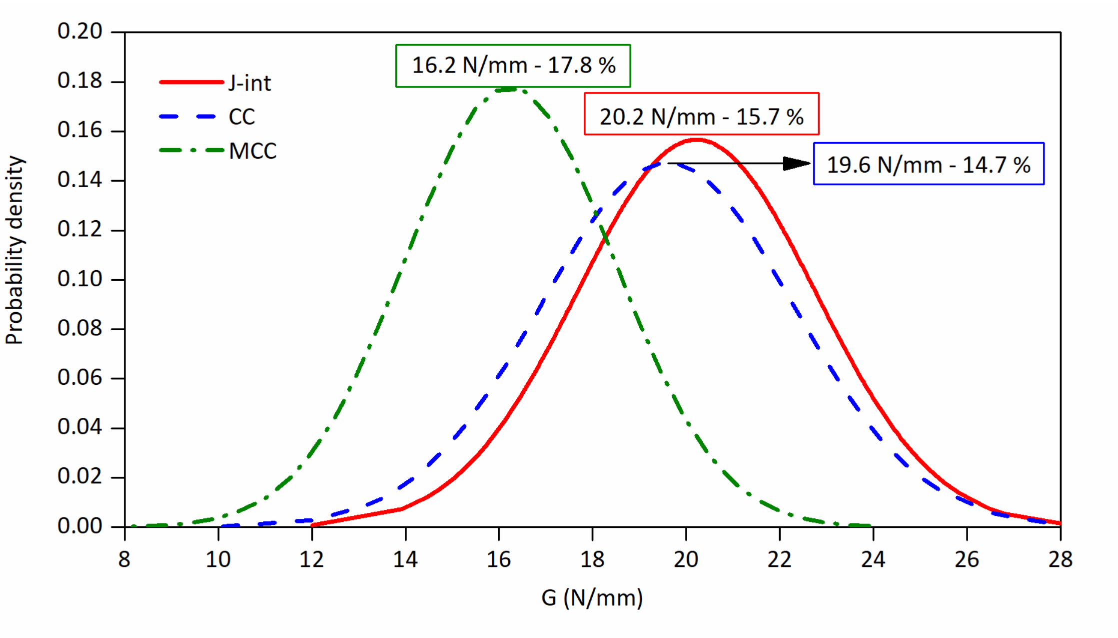

Figure 3.33: Normal distributions of energy release rate results.

3.3.3.5.4. Cohesive laws

As previously mentioned, the cohesive law may be determined by differentiating the *G vs*. CTOD curves with respect to CTOD. To this end, the energy release rate results determined through each data reduction method were fitted through an analytical function. In this regard, several fitting functions may be considered, such as exponential, polynomial or logarithmic expressions. However, it is important to ensure that both the initial slope and the propagation stage are well fitted, which is not trivial to achieve with either standard exponential or logarithmic functions. To improve the approximation of the fitting function, an exponential expression with two separate components was implemented, as proposed by Joki *et al.* [3.30]. This two-exponential formula is given by,

$$G(CTOD) = J_1\left(1 - e^{-CTOD/d_1}\right) + J_2\left(1 - e^{-CTOD/d_2}\right) \tag{3.9}$$

where J_1, d_1, J_2 and d_2 are fitting parameters. An additional parameter may be considered to define the energy release rate at CTOD=0 mm. By differentiating this function with respect to CTOD, the cohesive law formula is obtained and reads,

$$\sigma(CTOD) = \frac{\partial G}{\partial CTOD} = \frac{J_1}{d_1}e^{-CTOD/d_1} + \frac{J_2}{d_2}e^{-CTOD/d_2} \tag{3.10}$$

where σ denotes the cohesive stress. The fitting parameters were determined by using *IBM SPSS statistics 24* [3.31] and conducting a non-linear regression for all energy release rate data points. The fitting parameters, as well as the cohesive stress and fracture toughness are reported in Table 3.11, for each data reduction method. Besides the J-integral energy release rate results, Figure 3.32 also displays the obtained fitting function (equation (3.9)). Figure 3.34 presents the cohesive laws (equation (3.10)) obtained from the experimental results, for the three data reduction methods.

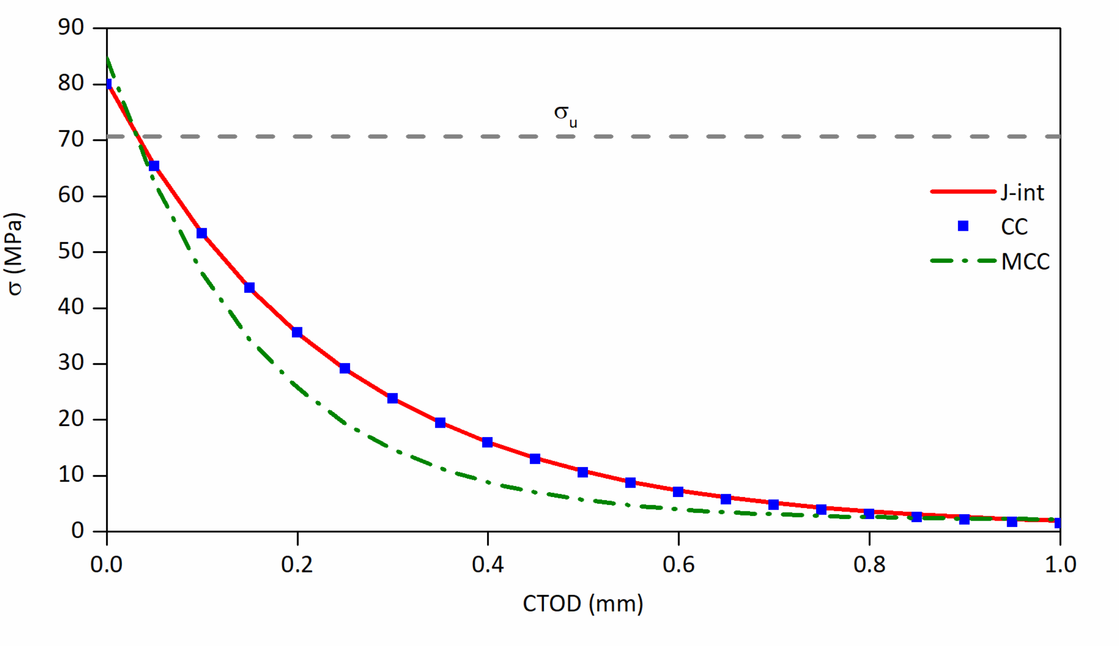

Figure 3.34: Transverse tensile laminate level cohesive laws for I200 profile.

Table 3.11 presents similar results for the maximum cohesive stress (σ_c), across all data reduction methods. This evidence was somehow expected as the cohesive stress is extrapolated from the initial slope of the *G vs*. CTOD curves, which showed a good agreement among the different methods, as illustrated in Figure 3.32. The fracture toughness measured as the area under the cohesive law also show a good agreement to the average values presented in Table 3.10.

Table 3.11: Summary of fitting parameters and cohesive law results.

Method	J_1 [N/mm]	d_1 [mm]	J_2 [N/mm]	d_2 [mm]	σ_c [MPa]	G_c [N/mm]
J-integral	18.87	0.2391	2.130	1.416	80.44	20.34
CC	0.3955	0.2470	19.35	0.2470	79.95	19.77
MCC	8245	4006	13.19	0.1597	84.67	16.39

The lower fracture toughness results for MCC impact the resulting cohesive law, which presents a more conservative slope than those of J-integral and CC cohesive laws. It is also noteworthy that these cohesive stresses are higher than the material transverse tensile ultimate stress (70.7 MPa, average), although presenting a similar order of magnitude. Li *et al.* [3.32] also found discrepancies between cohesive and material ultimate stresses. On a different note, Bergan *et al.* [3.27] reported results which showed that the distance between targets may affect CTOD measurements, artificially increasing the initial slope of *G vs*. CTOD curves, and thus the cohesive stress. This aspect was not taken into account in these calculations and may have contributed to the difference between cohesive and ultimate stresses.

Despite the differences between data reduction methods and the level of scatter reported for energy release rate results, the resulting cohesive laws illustrated in Figure 3.34 show a good overall agreement. The cohesive laws determined from J-integral and CC methods are nearly identical, while the cohesive law obtained from MCC is more conservative, in face of its lower fracture toughness.

3.4. Conclusions

This chapter detailed two preliminary but essential components of the experimental and numerical studies reported in this thesis: (i) the mechanical characterization of the materials; and (ii) the establishment of an accurate experimental method to assess the transverse tensile fracture properties of pultruded GFRP materials.

The first component of this study provided insights into the tensile, compressive and shear mechanical properties of the test materials to be experimentally tested and numerically simulated in this thesis. In addition, the fibre layups of these materials were characterized and the fibre content attributed to each material in-plane direction.

The mechanical characterization showed that the various test materials present comparable longitudinal mechanical properties, but significantly different transverse mechanical properties. Furthermore, significant differences were found in the analysis of the fibre layup of each material. This variability should provide an important basis for the analysis of the influence of fibre layup on transverse fracture properties.

The second component of this chapter comprised two separate experimental campaigns, involving Compact Tension (CT) and Wide Compact Tension (WCT) test specimens. The CT tests presented a higher level of scatter and were unable to reach a stable propagation stage. CT tests also showed significant specimen geometry dependency and overestimated the energy release rate. On the other hand, WCT tests provided energy release rate results with lower levels of scatter, which were implemented to determine the laminate level cohesive laws. Therefore, it was concluded that WCT tests are advantageous in studying fracture of pultruded materials, allowing for higher and more stable crack growths.

Four data reduction methods were considered in this study: ASTM E399, J-integral, standard compliance calibration (CC) and modified compliance calibration (MCC). The ASTM formulations provided results for CT tests with a good level of agreement in comparison to other data reduction methods. However, these formulations were not applicable to WCT tests. The J-integral method provided reliable results for both CT and WCT test configurations. By applying this method to WCT tests, an average fracture toughness of 20.2 N/mm was determined for the pultruded profile tested. The CC method also provided reliable results for both test configurations, showing a higher level of agreement with J-integral results in WCT tests, with an average fracture toughness of 19.6 N/mm. Finally, the MCC method was implemented for WCT tests to circumvent visual measurements of crack propagation. The MCC results were considerably lower than the other visually based methods, with an average fracture toughness of 16.2 N/mm, which corresponds to an average variation of -20% compared to J-integral results. These variations are in line with some previously reported discrepancies; however, in order to better understand this difference between visual observations and MCC, it will be important to validate this result for other pultruded GFRP materials.

Following this preliminary study, two subsequent steps were naturally considered: (i) implementing the methodology with other pultruded materials with different fibre layups and material properties, in order to define fracture property ranges for this type of material and eventually correlate such fracture properties with the fibre layups and material properties; (ii) developing a numerical study based on non-linear FE models with the goal of validating both fracture toughness and the ensuing cohesive laws. These steps were pursued in this thesis and are presented in Chapter 4.

3.5. References

[3.1] El-Hajjar R., Haj-Ali R., Mode-I fracture toughness testing of thick section FRP composites using the ESE(T) specimen, *Engineering Fracture Mechanics*, 72, pp. 631-643, 2005.

[3.2] Liu W., Feng P., Huang J., Bilinear softening model and double K fracture criterion for quasi-brittle fracture of pultruded FRP composites, *Composite Structures*, 160, pp. 1119-1125, 2016.

[3.3] Laffan, M. J., Pinho, S. T., Robinson, P., & Mcmillan, A. J., Translaminar fracture toughness testing of composites: A review. *Polymer Testing*, 31(3), pp. 481-489, 2012.

[3.4] ISO 527:1997, “Plastics – Determination of Tensile Properties”, International Organization for Standardization, Geneva, 1997.

[3.5] ASTM D5379-05, “Standard test method for shear properties of composite materials by the V notched beam method”, ASTM, West Conshohocken, PA: ASTM, 2000.

[3.6] ASTM D6641 / D6641M – 09, “Standard Test Method for Compressive Properties of Polymer Matrix Composite Materials Using a Combined Loading Compression (CLC) Test Fixture”, ASTM International, West Conshohocken, Pennsylvania, 2009.

[3.7] ISO 1172, “Textile-glass-reinforced plastics — Prepregs, moulding compounds and laminates — Determination of the textile-glass and mineral-filler content — Calcination methods”, International Organization for Standardization, Geneva, 1996.

[3.8] Proença, M., Garrido, M., Correia, J.R. , “Mechanical Characterization Tests of the Constituent Materials of Pultruded Composite Sandwich Panels for Application in Building Floors, Report IST-4.1”, Project ADI 2015/03480 “EASYFLOOR – Desenvolvimento de Painéis Sanduíche Compósitos para a Reabilitação de Pisos de Edifícios“, CERIS Report DTC n.º 9/2019, April, 2019.

[9] Hodgkinson J. M., *Mechanical Testing of Advanced Fibre Composites*, CRC Press, Cambridge, England, 2000.

[3.10] Almeida-Fernandes, L., *Structural behaviour of GFRP beams subjected to concentrated loads: experimental tests, numerical modeling and analytical study*, MSc dissertation in Civil Engineering, Instituto Superior Técnico, Lisbon, Portugal, 2014 [In Portuguese].

[3.11] ASTM D 695-02, “Standard Test Method for Compressive Properties of Rigid Plastics”, ASTM, West Conshohocken, Pennsylvania, 2006.

[3.12] Pinho, S.T., Robinson, P., Iannucci, L., Fracture toughness of the tensile and compressive fibre failure modes in laminated composites, *Composites Science and Technology*, 66(13), pp. 2069-2079, 2006.

[3.13] Blanco, N., Trias, D., Pinho, S.T., Robinson, P., Intralaminar fracture toughness characterisation of woven composite laminates. Part I: Design and analysis of a compact tension (CT) specimen, *Engineering Fracture Mechanics*, 131, pp. 349-360, 2014.

[3.14] Gigliotti, L., Pinho, S. T., Translaminar fracture toughness of NCF composites with multiaxial blankets. *Materials & Design*, 94, pp. 410-416, 2015.

[3.15] Jose, S., Kumar, R.K., Jana, M.K., Rao, G.V., Intralaminar fracture toughness of a cross-ply laminate and its constituent sub-laminates, *Composites Science and Technology*, 61(8), pp. 1115-1122, 2001.

[3.16] Laffan, M. J., Pinho, S. T., Robinson, P., Iannucci, L., Measurement of the in-situ ply fracture toughness associated with mode I fibre tensile failure in FRP. Part I: Data reduction, *Composites Science and Technology*, 70(4), pp. 606-613, 2010.

[3.17] Laffan, M.J., Pinho, S.T., Robinson, P., Iannucci, L., Measurement of the in-situ ply fracture toughness associated with mode I fibre tensile failure in FRP. Part II: Size and lay-up effects, *Composites Science and Technology*, 70(4), pp. 614-621, 2010.

[3.18] Laffan, M.J., Pinho, S.T., Robinson, P., Mcmillan, A.J., Translaminar fracture toughness: The critical notch tip radius of 0 ° plies in CFRP, *Composites Science and Technology*, 72(1), pp. 97-102, 2011.

[3.19] Catalanotti, G., Arteiro, A., Hayati, M., Camanho, P. P., Determination of the mode I crack resistance curve of polymer composites using the size-effect law, *Engineering Fracture Mechanics*, 118, pp. 49-65, 2014.

[3.20] Underwood, J.H., Eidinoff, H.L., Kortschot, M.T., Wilson, D.A., Lloyd, W.R., Ashbaugh, N., *Technical Report ARCCB-TR-95013: Methods and results from Interlaboratory tests of carbon / epoxy laminates*, US army armament research, development and engineering center, 1995.

[3.21] Kongshavn, I., Poursartip, A., Experimental investigation of a strain-softening approach to predicting failure in notched fibre-reinforced composite laminates, *Composites Science and Technology*, 59(1), pp. 29-40, 1999.

[3.22] ASTM E399-90, “Standard test method for plane-strain fracture toughness of metallic materials”, ASTM, Annual Book of ASTM Standards, 1993.

[3.23] Simulia, “Abaqus/CAE 2018”, 2018.

[3.24] Ortega, A., Maimí, P., González, E. V., Ripoll, L., Compact tension specimen for orthotropic materials, *Composites Part A: Applied Science and Manufacturing*, 63, pp. 85-93, 2014.

[3.25] Ortega, A., Maimí, P., González, E. V, & Trias, D., Specimen geometry and specimen size dependence of the R -curve and the size effect law from a cohesive model point of view, *International Journal of Fracture*, 205, pp. 239-254, 2017.

[3.26] Sørensen, B.F., Jacobsen, T.K., Determination of cohesive laws by the J integral approach, *Engineering Fracture Mechanics*, 70(14), pp. 1841-1858, 2003.

[3.27] Bergan, A., Dávila, C., Leone, F., Awerbuch, J., Tan, T.M., A mode I cohesive law characterization procedure for through-the-thickness crack propagation in composite laminates, *Composites Part B: Engineering*, 94, pp. 338-349, 2016.

[3.28] Abdullah, S.I.B.S., Iannucci, L., Greenhalgh, E.S., On the translaminar fracture toughness of Vectran/epoxy composite material, *Composite Structures*, 202, pp. 566-577, 2018.

[3.29] Gonzáles, L., Knauss, W.G., Scaling global fracture behavior of structures-sized laminated composites. *International Journal of Fracture*, 118(4), pp. 363-394, 2002.

[3.30] Joki, R.K., Grytten, F., Hayman, B., Sørensen, B.F., Determination of a cohesive law for delamination modelling - accounting for variation in crack opening and stress state across the test specimen width, *Composites Science and Technology*, 128, pp. 49-57, 2016.

[3.31] IBM, “SPSS statistics”, version 24, 2016.

[3.32] Li, S., Thouless, M.D., Waas, A.M., Schroeder, J.A., Zavattieri, P.D., Use of a cohesive-zone model to analyze the fracture of a fiber-reinforced polymer-matrix composite, *Composites Science and Technology*, 65, pp. 537-549, 2005.

Chapter 4. Effect of fibre layup in transverse tensile fracture

4.1. Introduction

The numerical simulation of damage in composite materials is still a challenging issue [4.1, 4.2]. This is particularly the case of pultruded glass fibre reinforced polymer (GFRP) materials used in the construction industry. These materials present higher levels of variability [4.3], lower fibre layup refinement and, furthermore, they have received less attention from the scientific community when compared to composites for automotive and aerospace applications [4.4].

Many previous studies have highlighted the significant variability of the elastic and strength properties of commercial pultruded profiles [4.3] and this naturally needs to be duly taken into account in their design; however, such an assessment has not yet been performed regarding the fracture properties of pultruded profiles. This is a significant gap in research, since these properties are needed for the advanced numerical simulation of a wide range of problems involving pultruded GFRP structures [4.1, 4.2, 4.5]. Failure modes, such as web-crippling of beams under localized loads/reactions [4.6, 4.7] or shear-out of bolted connections [4.8], have been poorly simulated through continuum mechanics and stress-based criteria due to the absence of a reliable database on GFRP fracture properties.

In face of this limitation, fracture properties have been implemented as damage control parameters [4.1, 4.2, 4.5, 4.9-4.11]. Because the experimental research on these properties is still scarce, some numerical investigations simply assume fracture parameters given within the current and very limited state of the art [4.2, 4.9, 4.10], while others have calibrated these fracture parameters through trial-and-error comparison between full-scale numerical and experimental results [4.1, 4.5, 4.11]. In this calibration procedure, fracture properties are input data and failure loads of structural models are output data that must agree with the experimental results of structural tests. It should be noted that, given the non-linear nature of these analyses, only a cumbersome trial-and-error procedure can provide estimated values of fracture properties. The present study aims at filling this gap, by experimentally determining the laminate fracture properties of several pultruded GFRP materials, shedding light into the variability of these properties and thus enabling the advanced numerical simulation of pultruded GFRP structures.

To the author’s best knowledge, only a few experimental studies have focused on the assessment of the fracture toughness (G_c) of pultruded GFRP materials [4.12, 4.13]. El-Hajjar and Haj-Ali [4.12] determined the stress intensity factor (which can be converted to energy release rate (G) as a function of elastic properties) for the longitudinal and transverse directions of a pultruded GFRP material. Whereas Liu *et al.* [4.13] studied the transverse energy release rate and cohesive law shape of a pultruded GFRP material, through notched three-point bending tests. These investigations addressed materials with only two types of layers: (i) roving layers, the main reinforcement, oriented in the longitudinal direction, and (ii) continuous filament mats (CFM), composed of randomly oriented fibres, comprising the transverse reinforcement. Table 4.1 presents a summary of values for the transverse tensile G_c (represented by G_2^+ for numerical purposes) reported in the literature, obtained from either experimental or numerical studies and those readily assumed (*i.e.*, with no direct experimental or numerical basis). All these studies focused on pultruded GFRP materials.

Table 4.1: Summary of results available in the literature for the transverse tensile G_c [N/mm] of pultruded GFRP materials.

Research work	Resin material	Experimental	Numerical	Assumed
El-Hajjar and Haj-Ali [4.12]	Polyester	8.9*	-	-
Liu *et al.* [4.13]	Not referred	7.8	-	-
Barbero *et al.* [4.1]	Epoxy	-	11.5	-
Li *et al.* [4.11]	Polyester	-	11.5	-
Lapczyk *et al.* [4.9]	Epoxy	-	-	1.0
Girão *et al.* [4.2]	Not referred	-	-	1.2

* Estimated as a function of the reported stress intensity factor.

Table 4.1 shows that the values of G_c present considerable scatter; moreover, in some numerical investigations [4.2, 4.9], relatively low values were considered, similar to those attributed to purely intralaminar phenomena. Table 4.1 also shows that numerical calibration through trial-and-error procedures may be a reasonable predictor of transverse tensile G_c values, despite the differences between results reported in [4.1, 4.11] and those experimentally determined in [4.12, 4.13]. Additionally, it is worth referring that some manufacturers are progressively replacing CFM layers by woven and oriented transverse reinforcements. This higher ratio of transverse reinforcement should result in a significant increase of transverse elastic and strength properties [4.14], and of fracture properties.

Considering the limited experimental data currently available, the methodology detailed in [4.15] was implemented for a total of five additional pultruded GFRP materials (see Chapter 3). This methodology consisted of implementing compact tension (CT) and wide compact tension (WCT) test configurations, to determine the transverse tensile G_c and cohesive law shape of the laminate. In addition to the experimental characterization of fracture properties, this chapter includes a numerical study, which consisted of implementing the experimentally based fracture properties of each material into non-linear damage models, within the framework of *Abaqus* [4.16].

The main objective of the numerical study is to validate experimentally based fracture properties. Validation was performed by comparing load *vs*. displacement curves from numerical models and experimental fracture tests. The numerical models developed in this study are based on a continuum damage formulation that implements the Hashin criterion [4.17] to determine damage initiation and on two alternative cohesive laws for damage evolution: (i) a linear cohesive law, using built-in tools available in *Abaqus* [4.16]; and (ii) an exponential cohesive law, implemented with user-defined material subroutines (UMAT), also in *Abaqus* [4.16].

This chapter is organized as follows: (i) the materials tested in the experimental investigation, the specimen geometries, test setups and data reduction methods are presented (Section 4.2); (ii) the experimental results are detailed regarding the various test configurations (Section 4.3) [4.18]; (iii) the numerical models are detailed (Section 4.4); (iv) experimental and numerical results are compared (Section 4.5) [4.19]; and (v) the main conclusions of this study are drawn (Section 4.6).

4.2. Experimental study

4.2.1. Materials

Table 4.2 summarizes the web thickness (t_w) (of the web for I and U shapes) and the following material properties of the different GFRP materials: (i) tensile modulus in longitudinal (E_{11}^+) and transverse (E_{22}^+) directions; (ii) in-plane shear modulus (G_{12}); (iii) tensile strength in longitudinal (σ_{u11}^+) and transverse (σ_{u22}^+) directions; and (iv) in-plane shear strength (τ_{u12}). The tensile properties were determined according to ISO527-4 [4.20], while the shear properties were determined as per ASTM D 5379M - 05 [4.21], as detailed in Chapter 3.

Table 4.2: Main geometric and average mechanical properties of the various pultruded GFRP materials used in the experiments.

Material	t_w [mm]	E_{11}^+ [GPa]	E_{22}^+ [GPa]	G_{12} [GPa]	σ_{u11}^+ [MPa]	σ_{u22}^+ [MPa]	τ_{u12} [MPa]	Fibre weight [%]	Transv. Reinf.	Fibre weight per orientation [%]*			
										0º	45º	90º	C
I150-A	8.1	43.5	9.6	3.1	384	45	48	76	W	78	0	4	17
P300-A	5.3	33.9	12.2	5.4	258	71	82	73	W	58	0	12	30
I152-C	6.3	28.8	10.3	4.2	416	121	65	68	Q	55	25	12	8
I150-S	8.1	30.1	5.5	3.2	377	34	70	62	C	71	0	0	29
U150-S	7.7	26.6	5.8	4.2	347	70	71	66	Q	67	19	7	8
I200-F	9.9	29.6	11.9	2.9	323	71	67	64	W	73	0	8	19

* The fibre weight percentage per orientation was calculated assuming that 0/90 woven layers (W) have an even distribution between both orientations (50% per orientation) and that the -45/90/45 layers (Q) are also evenly distributed (33% per orientation).

Table 4.2 also presents a summary of the fibre weight percentages, layups and fibre orientation weight distributions. To assess the fibre layup, coupons taken from each material were calcinated up to 800 °C, thus causing the thermal decomposition of the polymeric resin. CFM, roving, 0/90 woven and -45/90/45 quasi-isotropic layers are labelled as “C”, “R”, “W” and “Q”, respectively.

The experimental programme included five different pultruded GFRP materials obtained from three suppliers: one 150 mm high I-section profile (I150) and a 300 mm wide plate (P300), produced by *Alto Perfis Pultrudidos*, Portugal (A); one 152 mm high I-section profile (I152), manufactured by *Creative Pultrusions*, USA (C); and two profiles, I150 and U150 (150 mm high channel section), provided by *STEP*, Portugal (S). Each material is identified by their shape, height and supplier. Table 4.2 also includes the material used for preliminary fracture tests (detailed in Chapter 3), labelled I200-F, which was acquired from Fiberline Composites, from Denmark. This material was only considered in the present chapter regarding the comparison of different layups and the numerical study.

Table 4.2 shows that the GFRP materials used in the experimental investigation present significant differences in terms of geometries (thicknesses ranging from 5.3 mm to 9.9 mm) and cover a wide range of mechanical properties (e.g., σ_{u22}^{+} varies from 34 to 121 MPa). There is also a wide variety of fibre layups, from nearly unidirectional layups (I150-S) to quasi-isotropic layups (I152-C). This wide sample of materials was considered in order to provide insight into the variability of fracture properties across structural grade off-the-shelf pultruded GFRP profiles, designed for civil engineering applications.

The differences in the fibre layups also seem to be reflected in the transverse tensile elastic modulus and strength of the various GFRP materials. In this respect, the relatively low mechanical properties in the transverse direction of I150-S specimens are attributed to their transverse reinforcement being solely composed of CFM layers, which are expected to provide a weaker level of transverse reinforcement.

It is worth noting that I150-A specimens presented significantly low transverse tensile properties, although their fibre layup is comparable to that of the P300-A and I200-F specimens; aside from differences inherent to the fibre content of each material, this worse performance of the I150-A profile was also attributed to a lower fibre-matrix bond (before testing, some specimens presented through-thickness cracks). This issue led to additional mechanical characterization tests on a different batch of profiles, showing significantly lower signs of defects. This second stage of mechanical characterization tests led to the properties conveyed in Table 4.2. In an initial stage a σ_{u22}^{+} value of 26 MPa and a E_{22}^{+} value of 6.6 GPa were determined for this material.

These defects should naturally also affect the data reduction methods, as the characterization tests in the I150-A specimens may not be fully representative of the actual material elastic and strength properties (*cf.* Section 4.3). These doubts, in regard to the transverse tensile behaviour of the I150-A profile, ultimately led to the exclusion of compliance calibration data reduction methods for this material, as well as the exclusion of this material from the numerical study performed in this chapter.

4.2.2. Specimen geometry

Three specimen geometries were considered - CT, scaled-up CT and WCT - illustrated in Figure 4.1. The WCT geometry has twice the width of a CT specimen, thus enabling higher lengths of crack propagation. Scaled-up CT specimens were solely used for I152-C specimens, as WCT tests of this material proved unsuccessful in achieving significant crack propagation lengths, due to premature failure at the load bearing holes. These scaled-up CT specimens (Figure 4.1 (b)) are proportional to those presented in Figure 4.1 (a), scaling up the specimen width from 60 mm to widths of 80 mm and 100 mm.

For each profile, two specimens with height of ≈60 mm were taken from the web, which presented nominal height of 120 mm. Therefore, the crack growth regions are positioned at ≈30 mm from the mid-height of the web and ≈30 mm from the web-flange round fillet. Scaled-up CT specimens present even higher distances to the web-flange round fillet.

CT specimens were machined using a 0.6 mm thick circular saw blade, resulting in a thin square shaped notch tip. Because the microscopic camera footage used in the instrumentation (*cf.* Chapter 3) showed that the cracks often initiate in the sharp corners, both WCT and scaled-up CT specimens were sharpened with a 0.3 mm wire saw. Both notch tip shapes are displayed and discussed in Chapter 3.

Finally, it should be noted that baseline CT tests included two nominal initial notch lengths of 30 mm and 35 mm, resulting in distances from the axis of load application to the notch tip (a_0) of 18 mm and 23 mm (see Figure 4.1), whereas scaled-up CT tests presented a range of a_0 lengths spanning from 20 mm to 32 mm. Finally, WCT tests were prepared with initial notch lengths of 30 mm and 40 mm, resulting in a_0 lengths of 18 mm and 28 mm. The total distance of the crack tip to the load application axis is referred to in the following sections as "a" ($a = a_0+\Delta a$).

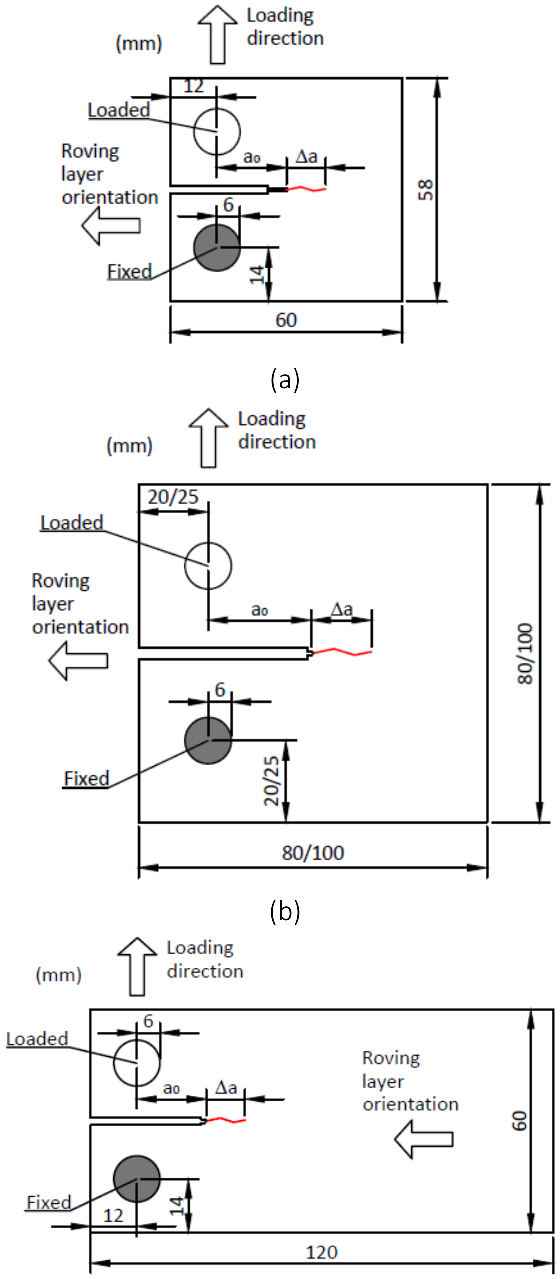

(a)

(b)

(c)

Figure 4.1: Specimen geometry: (a) CT test; (b) scaled-up CT test; (c) WCT test.

The CT tests were performed in an initial stage, as detailed in Chapter 3, providing preliminary but useful information for scaled-up CT and WCT tests, conducted in a second stage. Despite the previously discussed issues regarding CT tests in Chapter 3, CT test results were also included in the present chapter for two main reasons: (i) to allow assessing the specimen geometry dependency of different materials; and (ii) to provide a wider validation basis for numerical models.

The following specimen nomenclature is used herein: (i) CT specimens are labelled as "I150-S-CT-18-#", where "I150-S" identifies the material, "CT" defines the test configuration, "18" corresponds to the a_0 length and "#" is the specimen number; (ii) scaled-up CT specimens are referred to as "I152-C-CT(80)-28.5", where "80" indicates the specimen width of 80 mm and "28.5" indicates the a_0 length (no specimen number was considered here, as there were no repetitions of a_0 lengths); (iii) WCT specimens are identified as "I150-A-WCT-28-#", using the same labelling adopted for CT specimens.

Table 4.3 summarizes the experimental programme, with a total of 84 tests, distributed as follows: (i) 24 CT tests, (ii) 13 scaled-up CT tests and (iii) 47 WCT tests. Most materials were tested by means of six CT and ten WCT specimens, whereas the I150-A material was only tested through WCT tests. For the I152-C material, fewer WCT tests were performed as initial tests displayed secondary failure modes and scaled-up CT tests were performed in order to increase the crack propagation length.

Table 4.3: Overview of experimental programme, as a function of nominal a_0 lengths [mm].

Material	CT tests		Scaled-up CT tests	WCT tests	
	a_0=18	a_0=23	20<a_0<32	a_0=18	a_0=28
I150-A	-	-	-	4	5
P300-A	2	4	-	5	5
I152-C	3	3	13	1	4
I150-S	3	3	-	5	6
U150-S	3	3	-	6	6

4.2.3. Test setup

Load was applied through steel loading pins, attached to an Instron universal testing machine with a load bearing capacity of 250 kN and a load cell accuracy of ≈0.01 kN. All tests were conducted under displacement control at rates of 0.5 mm/min (CT) and 1.0 mm/min (WCT). A video-extensometry equipment (high resolution camera from Sony, model XCG 5005E with Fujinon lens) with a resolution of 5 MP, a data acquisition rate of 10 Hz and an image acquisition of 1 FPS was used to monitor the crack mouth opening displacement (CMOD) in both test configurations. This methodology was also implemented to monitor the crack tip opening displacement (CTOD) in WCT tests. The targets used for this purpose are illustrated in Figure 4.2. To improve the monitoring of the targets, each specimen was painted with white matte paint and the targets were added with a black marker pen.

In order to further assess the crack propagation, the back face of the specimen was monitored, in a length of 15 mm, through a microscopic camera (Dino-Lite Edge Digital USB Microscope, model AM7915MZT) with a resolution of 5 MP and a maximum frame rate of 30 FPS. The crack growth of WCT specimens was also monitored through the video-extensometry footage, which enabled the measurement of crack growth in longer lengths. Figure 4.3 illustrates the footage taken from the microscopic camera.

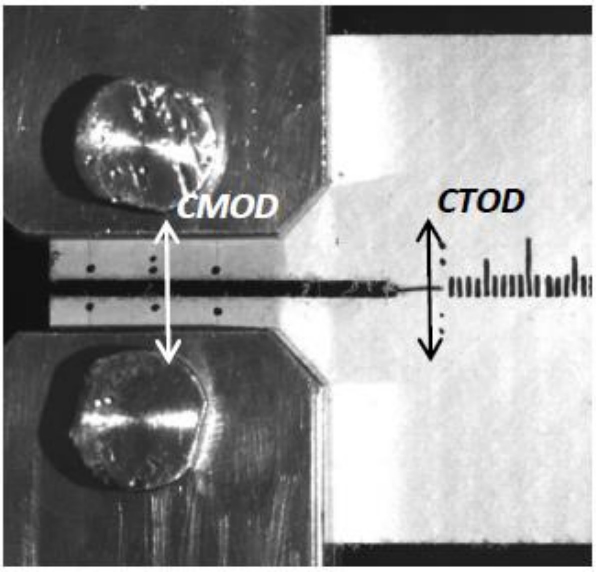

Figure 4.2: Target location for the video-extensometry camera.

As several data reduction methods are based on visual measurements of crack growth, these were validated by comparing footage taken from the microscopic camera and the video-extensometry camera (only in WCT tests). In CT tests, specimens were loaded at a constant rate up to failure, whereas most WCT specimens were subjected to loading/unloading cycles after reaching the ultimate load. The loading/unloading protocol was based on displacement intervals as a function of the displacement applied by the test machine when the ultimate load was reached (d_u): the loading/unloading cycles were performed in regular intervals of 0.2xd_u. The unloading was performed as a 30% load decrease, with respect to the load applied at the beginning of each unloading cycle. These cycles were implemented to measure the compliance variation at different stages of crack growth.

Figure 4.3: Picture taken from microscopic camera footage.

4.2.4. Data reduction methods

Several data reduction methods can be implemented to determine the variation of energy release rate with the crack growth or CTOD. In this study, the following four methods were implemented (further details are given in Chapter 3):

- ASTM E399-90 [4.22], a standard developed for isotropic metallic materials, which has also been applied to composite materials in some investigations [4.23, 4.24, 4.25]. Pinho *et al.* [4.24] have shown that this standard provides results with significant margins of error, as orthotropy was not considered in its formulation. It is thus a simplified approach to determine G variation throughout a CT test; since it is geometry dependent, it was not applied to WCT tests.
- J-integral method, based on finite element (FE) models [4.24, 4.25]. A more accurate approach that consists of developing FE models with a large range of crack growth increments, in order to assess G variation as a function of crack length. This is a cumbersome approach, as it must be developed separately for each material. In the present study, *Abaqus* [4.16] commercial software was used to develop these FE models. S4R shell elements were implemented, with an average size of 0.2 mm. The J-integral was calculated by establishing the crack tip position in each model and applying a unit load (1 N). The crack was extended through the "Seam" tool, enabling a more straightforward process to generate the various models.
- Compliance calibration method (CC) [4.25, 4.26], also based on FE models. This methodology consists of correlating the specimen compliance and the crack length measured from visual observation, so that G can be determined as a function of compliance variation. To this end, the aforementioned FE models were used to determine the compliance/crack length variation, which was then fitted through an analytical function.
- Modified compliance calibration (MCC), which differs from the previous methods, as crack growth is determined as a function of compliance instead of visual observations [4.14, 4.25, 4.27]. MCC was applied only to WCT tests, which were subjected to loading/unloading cycles, to determine the compliance in various crack propagation stages.

4.3. Experimental results

This section reports the results obtained for the three different test configurations: (i) baseline CT tests; (ii) scaled-up CT tests (performed only on I152-C materials); and (iii) WCT tests. In the following sub-sections, three types of results are presented and discussed for each configuration: the load *vs.* displacement curves, the failure modes, and energy release rate results.

4.3.1. Baseline CT test results

Figure 4.4 presents load (F) *vs*. displacement (CMOD) curves of representative specimens taken from each pultruded material with a_0 lengths of 18 mm (Figure 4.4 (a)) and 23 mm (Figure 4.4 (b)). The different materials present a qualitatively similar response, with an initial linear branch, followed by progressive stiffness reduction until the ultimate load is reached and ending in a progressive softening trend. However, the various materials present different ultimate loads and softening slopes.

The results depicted in Figure 4.4 correlate well with the aforementioned σ_{u22}^{+} values, with I152-C specimens presenting (by far) the highest ultimate loads (despite presenting lower thickness than most of the other materials) and I150-S specimens presenting the lowest ultimate loads.

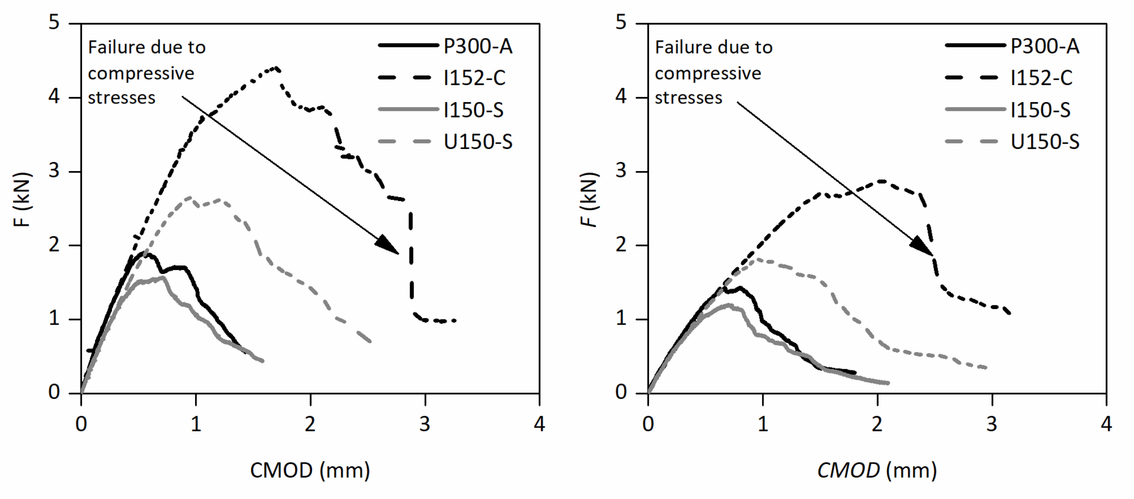

(a) (b)

Figure 4.4: Representative load *vs*. CMOD curves for CT specimens: (a) a_0 length of 18 mm; (b) a_0 length of 23 mm.

Figure 4.5 displays examples of crack propagation footage taken from the microscopic camera for P300-A-CT-23-3 (Figure 4.5 (a)) and I150-S-CT-18-3 (Figure 4.5 (b)). As illustrated in Figure 4.5, a significant number of specimens exhibited irregular crack patterns. Despite this intrinsic irregularity, for the sake of consistency all crack measurements were made with respect to the specimen central horizontal axis (*i.e.*, the horizontal projection of crack).

(a) (b)

Figure 4.5: Crack growth patterns in CT test specimens (scale marker used to validate measurements from microscopic camera): (a) P300-A-CT-23-3; (b) I150-S-CT-18-3.

Figure 4.6 (a) illustrates the typical failure mode, which involved the propagation of a crack (in the horizontal direction, transverse to the load) due to tensile stresses. The only exceptions were the I152-C specimens, which, after the same type of crack propagation, finally failed due to compressive stresses at the face opposite to the initial notch, as depicted in Figure 4.6 (b). These compressive stresses caused delamination, which enabled post-local buckling of these delaminated plies and thus, the failure of the specimen. The considerably higher σ_{u22}^{+} exhibited by this material (121 MPa) contributed to a significantly higher ultimate load, which may have triggered this compressive failure mode.

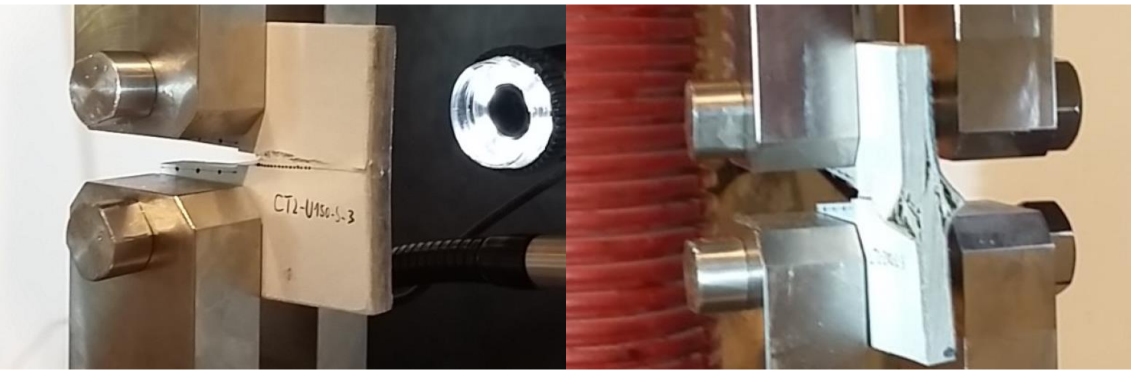

(a) (b)

Figure 4.6: Failure modes in CT tests: (a) crack growth due to tensile stresses; (b) delamination and post-local buckling of delaminated plies in the face opposite to the initial notch.

In the CT tests the CTOD was not monitored and thus *G* results are plotted as a function of crack growth (*Δa*, *cf*. Figure 4.1). In order to assess data reduction variability, Figure 4.7 presents representative examples of *G* variation for two different materials (P300-A-CT-18-1 and I150-S-CT-18-1) as a function of *Δa*, including three distinct data reduction methods (ASTM, J-integral and CC). It can be seen that all three data reduction methods provide similar *G* results until crack propagation reached ≈10 - 12 mm. As crack propagation increases further, the scatter between data reduction methods increases and CC results deviate significantly, presenting lower values than the other methods. These discrepancies should be attributed to the compliance fitting functions (such discrepancies between CC and other data reduction methods have also been reported in previous research, e.g. [4.25]. The simplified boundary conditions may also contribute to this difference, namely for higher crack lengths, as the compliance increases at a higher rate.

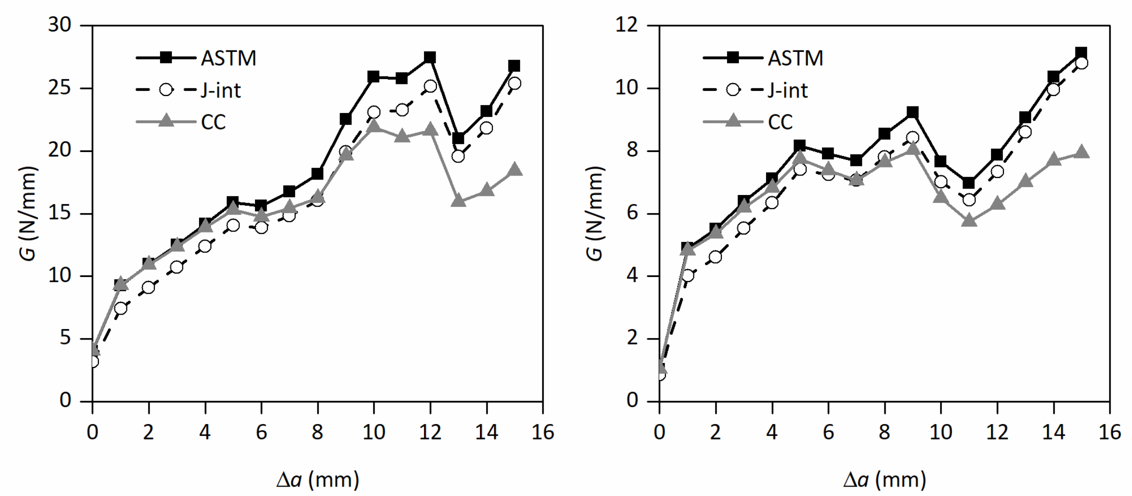

(a) (b)

Figure 4.7: Energy release rate (*G*) *vs*. crack growth (*Δa*), for different data reduction methods: (a) specimen P300-A-CT-18-1; (b) specimen I150-S-CT-18-1.

Stable crack growth rates were observed for all specimens, with exception of I152-C specimens, which presented stable crack growth rate up to a propagation length of 10-12 mm, after which unstable collapse occurred due to the aforementioned compressive failure at the posterior face. Figure 4.8 presents, as an example, the crack growth rates for a CT-I150-S specimen.

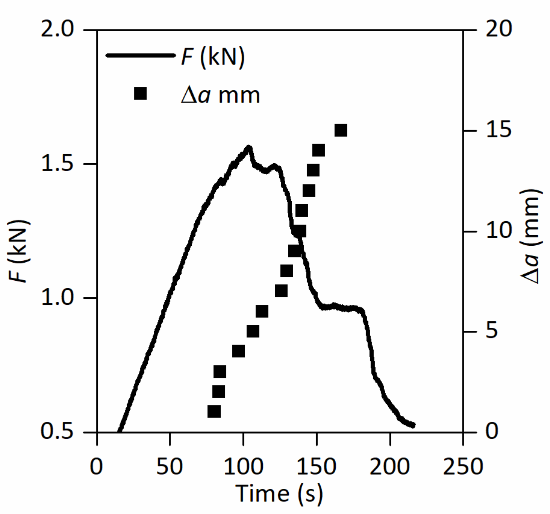

Figure 4.8: Crack growth rate (Δa) and load (F) *vs*. time curves of CT-I150-S specimen with a_0=18 mm.

Figure 4.9 presents the variation of J-integral based G as a function of crack growth (Δa) for the different materials and a_0 lengths. The results presented in Figure 4.9 have in common an overall growing trend, as G increases with Δa. However, P300-A and U150-S (Figures 4.9 (a) and (d)) present a more non-linear trend, as G stabilizes or even decreases for Δa longer than 10 mm. On the other hand, I152-C and I150-S specimens present a more significant increasing trend, particularly noticeable for I152-C results, which show an almost linearly increasing trend, with G reaching values higher than 100 N/mm.

For all materials, despite the significant levels of scatter, the average results determined for lengths a_0 = 23 mm were significantly lower than those for a_0 = 18 mm. This was attributed to the specimen geometry, which enabled only short crack propagation lengths before ultimate failure took place. It is worth mentioning that one U150-S-CT specimen had a significant energy release rate drop near the stable propagation stage (see Figure 4.9 (d)). This was attributed to a significantly steeper softening slope, when compared to other specimens of the same material.

Table 4.4 presents the average of maximum values of G obtained from CT tests, using the different data reduction methods. In line with the load *vs.* displacement curves, the I152-C and I150-S materials present the overall highest and lowest results, respectively. These range from 8 to 118 N/mm, highlighting the variability of transverse tensile fracture properties of pultruded GFRP materials. Table 4.4 presents maximum values for G, which should be considered as a lower bound of the actual CT test results of G_c, as the G *vs*. Δa curves did not reach a stable plateau.

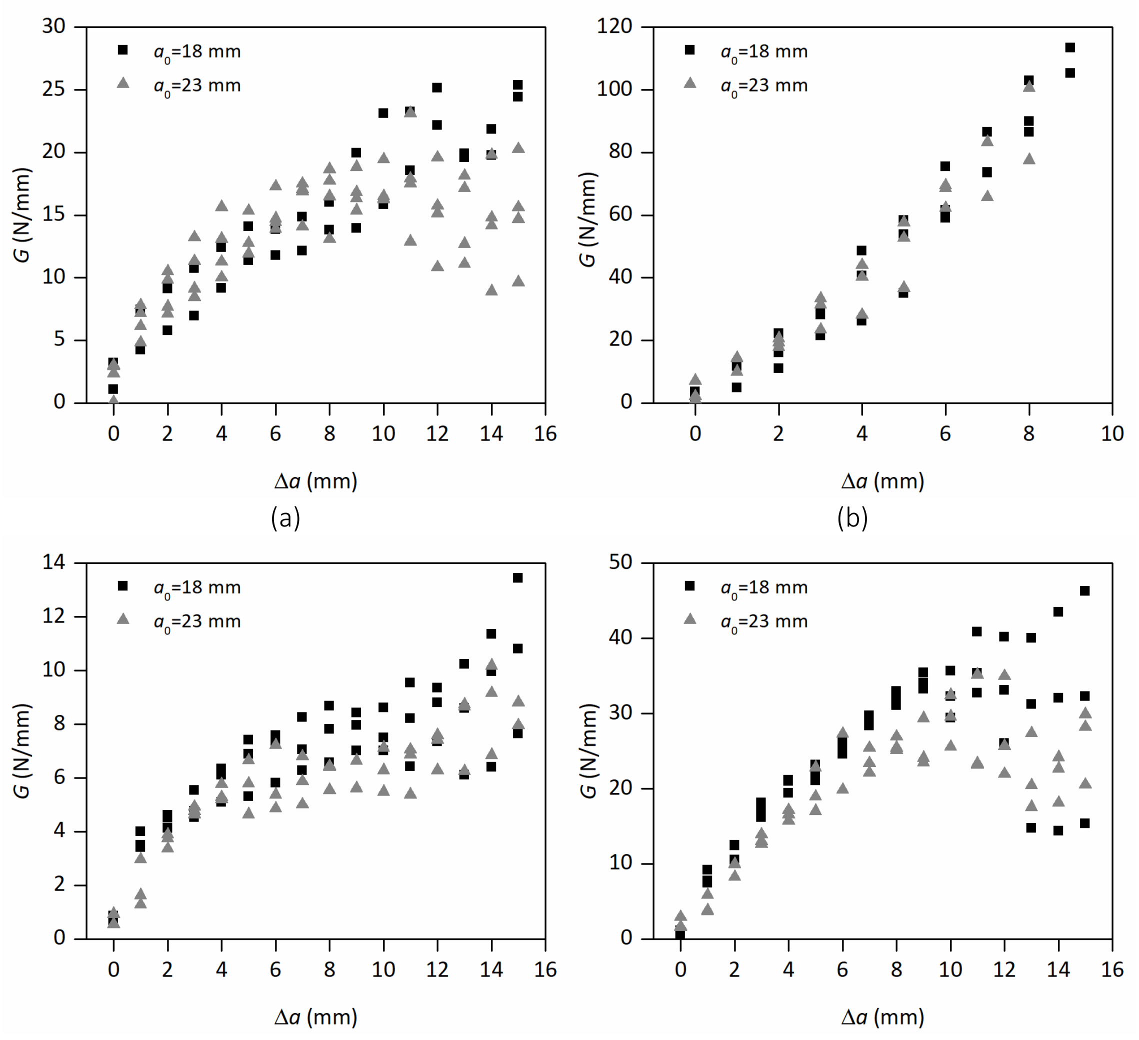

(a)

(b)

(c)

(d)

Figure 4.9: J-integral based energy release rate (*G*) *vs*. crack growth (*Δa*), from CT tests for different a_0 lengths: (a) P300-A; (b) I152-C; (c) I150-S; (d) U150-S.

Table 4.4: Maximum energy release rate values (average ± CoV) obtained from CT tests for different values of a_0 [mm], using different data reduction methods.

Material	ASTM E399 [N/mm]		J-integral [N/mm]		CC [N/mm]	
	a_0 = 18	a_0 = 23	a_0 = 18	a_0 = 23	a_0 = 18	a_0 = 23
P300-A	27.4 -*	23.6 ±17%	24.9 -*	23.2 ±15%	20.5 -*	23.1 ±17%
I152-C	117.5 ±5%	87.2 ±17%	107.1 ±5%	82.5 ±20%	102.7 ±4%	71.2 ±17%
I150-S	11.4 ±19%	9.0 ±15%	11.0 ±21%	9.1 ±12%	8.5 ±15%	7.7 ±6%
U150-S	43.5 ±13%	34.1 ±15%	38.6 ±17%	31.1 ±16%	31.3 ±12%	30.7 ±9%

*Only two specimens were tested.

4.3.2. Scaled-up CT test results

Figure 4.10 shows load (*F*) *vs*. displacement (CMOD) curves of representative scaled-up I152-C specimens with widths of 80 mm (Figure 4.10(a)) and 100 mm (Figure 4.10(b)), for different a_0 lengths (illustrated in Figure 4.1). The results displayed in Figure 4.10 show a similar trend to those of CT tests. As expected, the increase of specimen width leads to a significant increase of stiffness and ultimate load. Figure 4.10 also illustrates the significant impact of the initial notch length in CT tests for both specimen widths, regarding both stiffness and ultimate failure load.

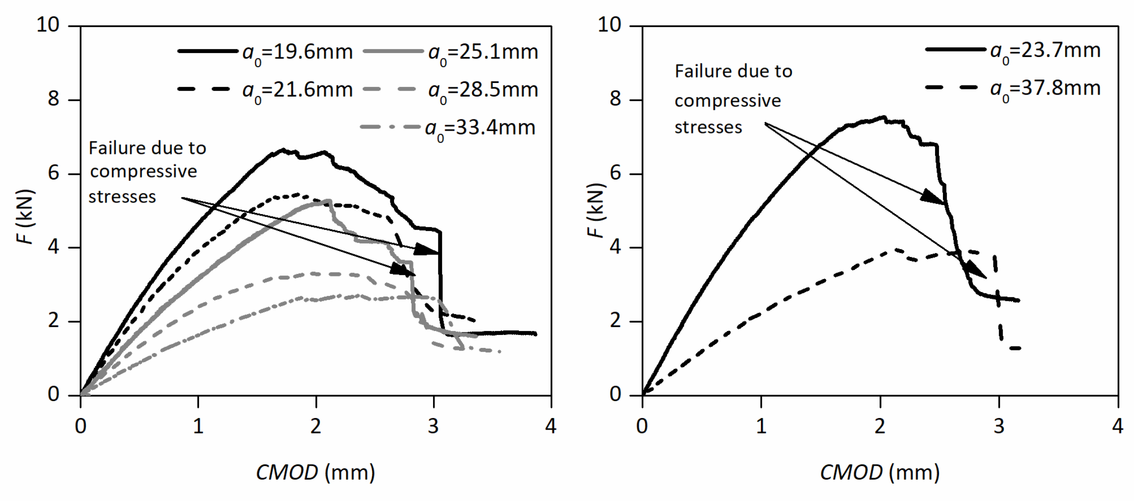

(a) (b)

Figure 4.10: Load (F) *vs*. CMOD curves of I152-C specimens obtained from scaled-up CT tests, for different a_0 lengths: (a) width of 80 mm; (b) width of 100 mm.

The failure mode of scaled-up CT specimens was identical to that shown for I152-C-CT specimens. After an initial stage of stable crack propagation, the specimens failed due to compressive stresses at the posterior face, which promoted delamination and post-local buckling of the delaminated and compressed plies, as depicted in Figure 4.11. The occurrence of this failure mode also affected the load *vs*. CMOD curves (*cf.* Figure 4.10), which present a sudden and nearly vertical softening slope at failure. Stable crack growth rates were observed for all specimens, until unstable collapse occurred due to the aforementioned compressive failure at the face opposite to the initial notch.

Figure 4.12 presents the variation of J-integral based results for scaled up I152-C specimens as a function of crack growth (Δa, see Figure 4.1), for widths of 80 mm and 100 mm (CT(80) and CT(100), respectively). Figure 4.12 also includes the J-integral based results obtained from the standard CT specimens of the same I152-C material (CT-60), previously reported in Section 4.3.1.

Figure 4.12 presents a similar linear growing trend of *G* with Δa for all specimen geometries. In line with the higher ultimate loads illustrated in Figure 4.10, the maximum *G* results of scaled-up CT tests are also considerably higher than those of baseline CT tests. This is attributed to the higher crack propagation lengths reached by the scaled-up specimens, as all specimen geometries presented similar results for lower crack propagation lengths (< 9 mm). These higher propagation lengths were reached as the scaled-up CT specimens were less prone to compressive failure at the face opposite to the initial notch. The linear increasing trend noticeable across all specimen widths indicates that in spite of the increased specimen width the stable propagation stage was not reached. In other words, the values obtained are a lower bound of the actual material fracture toughness. The higher *G* results of scaled-up specimens may be attributed to the longer crack propagation lengths that are developed before local buckling failure is triggered. However, results obtained for 100 mm wide specimens are not significantly higher (or even too different) than their 80 mm counterparts.

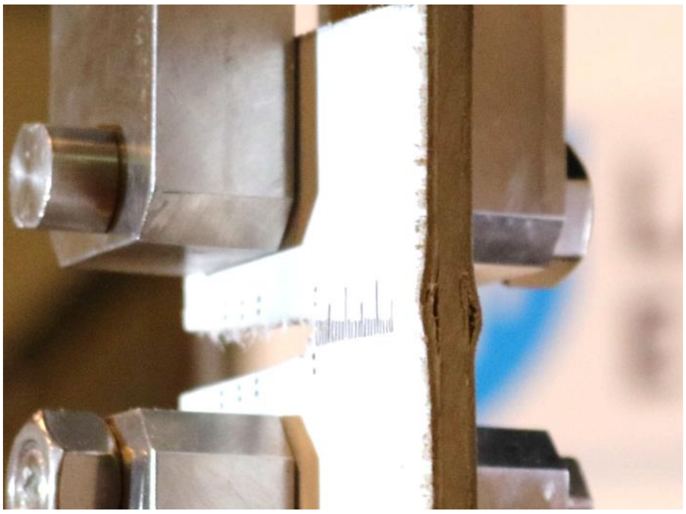

Figure 4.11: Delamination at the face opposite to the initial notch of a scaled-up CT specimen.

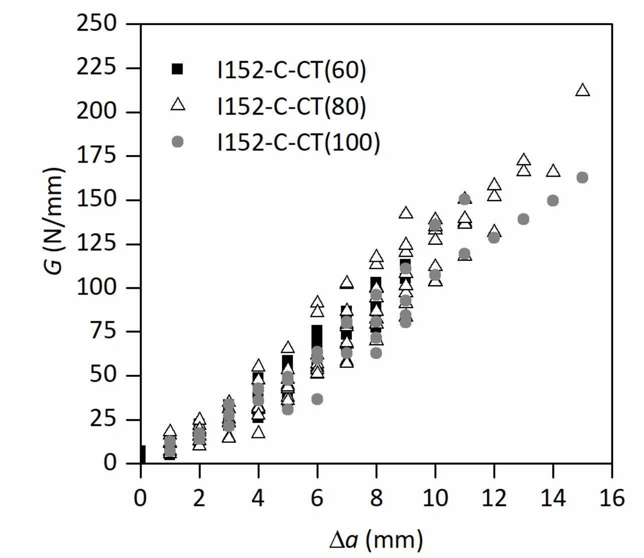

Figure 4.12: J-integral based energy release rate (*G*) *vs*. crack growth (Δa) of I152-C-CT specimens, for specimen widths of 60 mm (CT-60), 80 mm (CT-80) and 100 mm (CT-100).

In spite of not leading to the full cohesive law of this material, these results were differentiated in respect to CTOD, to determine an estimate for the maximum cohesive stress presented by this material, of 184 MPa.

4.3.3. WCT test results

Figure 4.13 presents a summary of load (*F*) *vs*. displacement (CMOD) curves for WCT specimens of all five GFRP materials, including both initial notch lengths. These curves also illustrate the various loading/unloading cycles performed per test. In Chapter 3, it has been shown that such cycles have no influence in the softening slope.

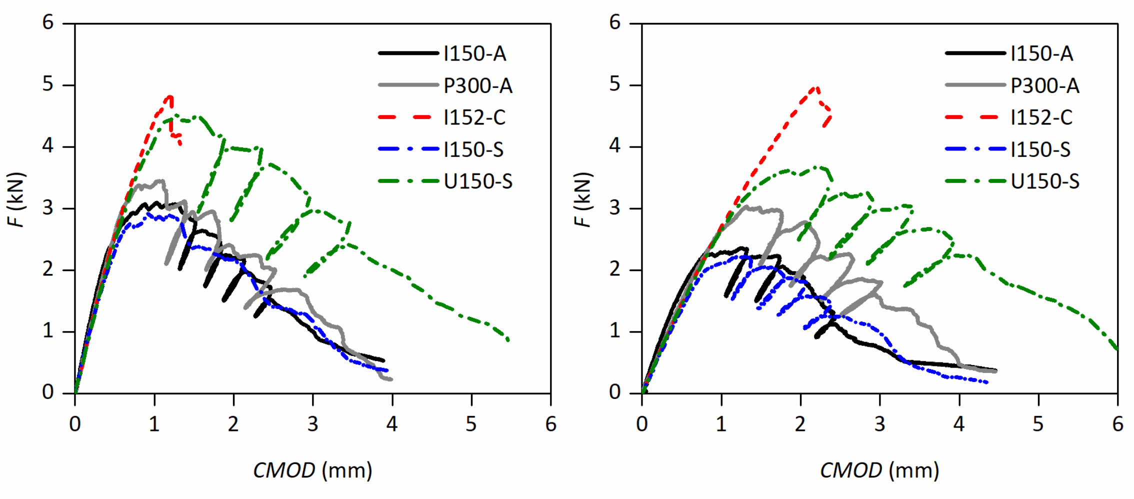

(a) (b)

Figure 4.13: Load *vs*. CMOD curves for different pultruded GFRP materials obtained from WCT tests: (a) a_0 = 18 mm; (b) a_0 = 28 mm.

The results depicted in Figure 4.13 clearly indicate different behaviours among the various materials (and fibre layups) tested. The two materials with quasi-isotropic layups (I152-C and U150-S) clearly stand-out with the highest ultimate loads, whereas the remainder of the materials (I150-A, I150-S and P300-A) present similar load *vs*. displacement curves, despite their differences in thickness and material properties. This will be further assessed by developing FE models, calibrated with the previous elastic and strength properties (aside from the fracture properties presented ahead), and by comparing numerical and experimental load/displacement curves for these materials.

The failure modes observed in the WCT tests are displayed in Figure 4.14. With some exceptions (described ahead), the standard failure mode consisted of crack propagation due to tensile stresses, similarly to the previous test configurations. In some cases, ultimate failure occurred due to compressive stresses at the posterior face. However, compressive based damage only became noticeable after significant crack propagation had taken place and, therefore, the tests were considered valid. Stable crack growth rates were observed across all specimens. In some specimens, unstable crack growth rates occurred due to compressive stresses at the posterior end, similarly to the previously reported I152-C CT and scaled-up CT specimens. However, unstable crack growth rates were only observed after significant crack growth lengths had been reached.

The following specimens presented different failure modes: (i) some I150-A specimens and I152-C specimens with a_0 = 18 mm collapsed due to failure at the load application holes, while (ii) I152-C specimens with a_0 = 28 mm presented global buckling coupled with bearing hole failure. Due to these failure modes, the WCT tests for the I152-C specimens (failure at the bearing hole for applied loads of nearly 5 kN) were considered unsuccessful; consequently, the aforementioned scaled-up CT tests were developed to enable the propagation of cracks with larger lengths.

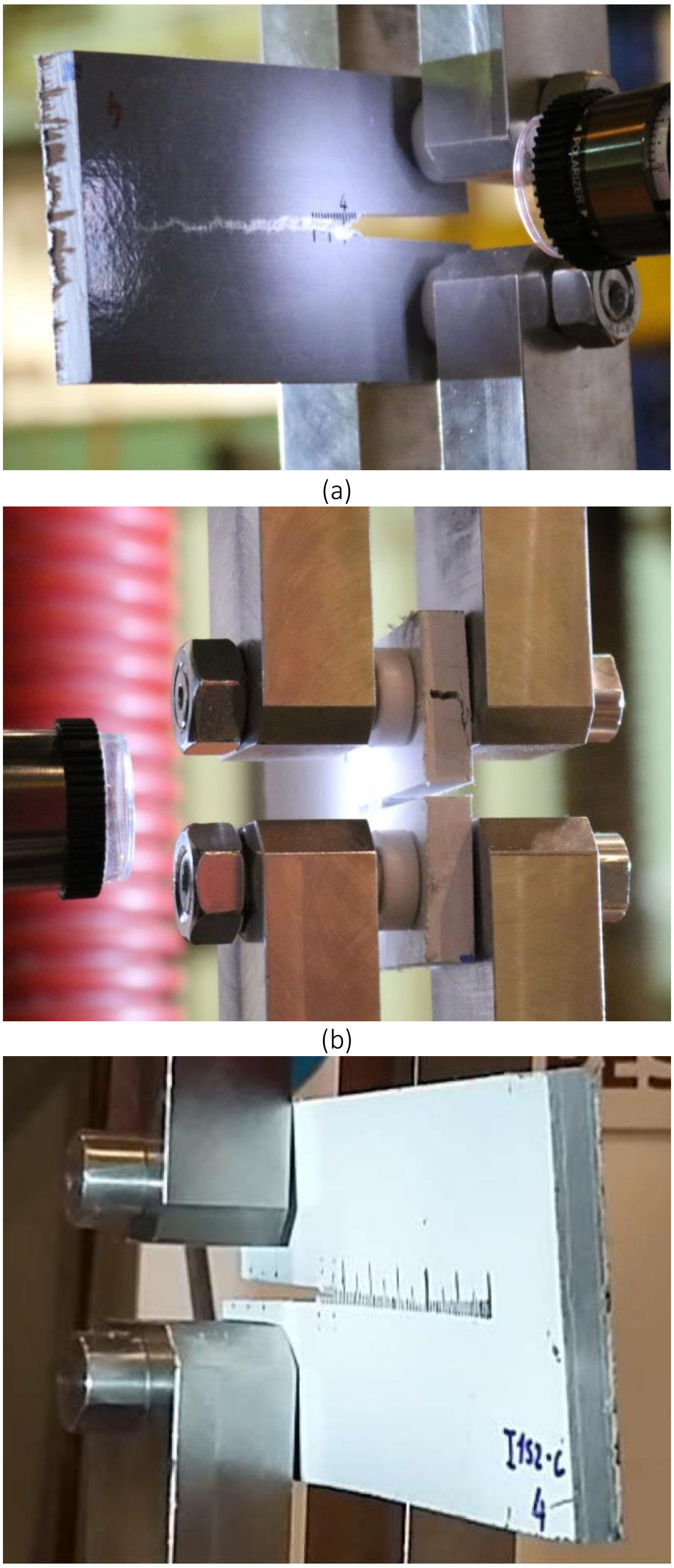

(a)

(b)

(c)

Figure 4.14: Failure modes for WCT tests: (a) crack propagation (standard failure mode); (b) failure at the load application holes; (c) global buckling.

Figure 4.15 illustrates the variation of *G* obtained from three data reduction methods (J-integral, CC and MCC) as a function of CTOD for two representative specimens (I150-S-WCT-28-5 and P300-A-WCT-18-4). Similarly to the results presented in Chapter 3, the MCC data reduction method yields considerably lower results than those determined through visual measurements of crack growth. Figure 4.15 shows that the magnitude of such differences varied among the materials tested: (i) for I150-S (Figure 4.15 (a)) differences between MCC and other methods are relatively low, whereas (ii) for P300-A (Figure 4.15 (b)) such relative differences are about 30%.

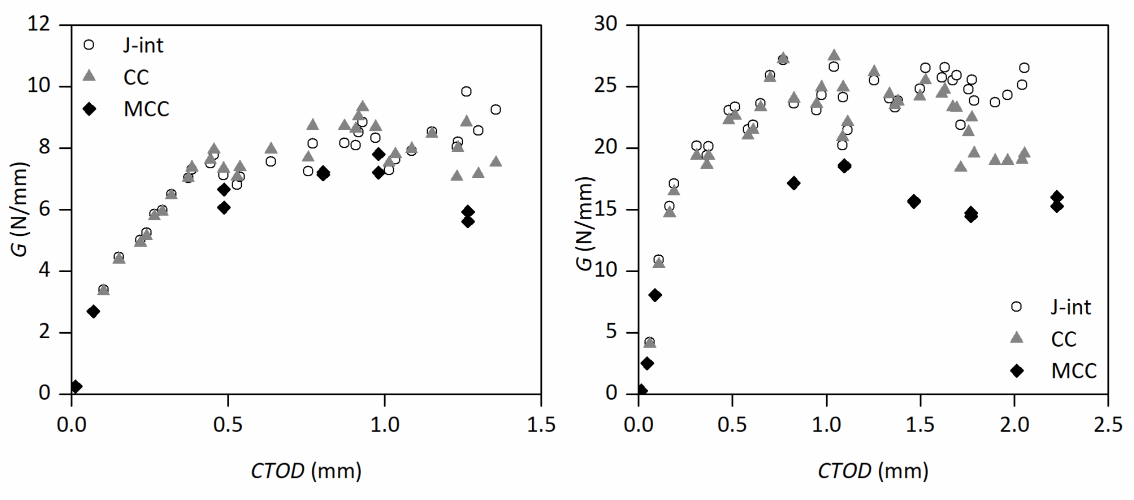

(a) (b)

Figure 4.15: Energy release rate (*G*) *vs*. CTOD, for different data reduction methods: (a) I150-S-WCT-28-5; (b) P300-A-WCT-18-4.

As the visually based CC results match considerably well the results based on J-integral, the above-mentioned difference between MCC and visually based methods was mainly attributed to the possible heterogeneous through-the-thickness crack growth within each material. This discrepancy can also be attributed to the loading/unloading cycles. Laffan *et al.* [4.25] reported that fibre pull-out may render these cycles inaccurate in estimating the compliance variation. The results displayed in Figure 4.15 are consistent with this explanation, as most deviations in MCC results occur during the stable propagation stage (where the loading/unloading cycles were performed), whereas in the initial increasing slope the results are similar to those determined through visual observation-based methods. This analysis is furthered in Section 4.5, by establishing which data reduction method leads to a better fit between numerical and experimental results.

The I150-A CC and MCC results were disregarded, as previously mentioned (see Section 4.2.1), due to discrepancies found in its transverse tensile mechanical properties. The FE-based J-integral approach should also be affected by these uncertainties, however, the magnitude of their influence should be lower.

Figure 4.16 presents a comparison of J-integral based *G vs*. CTOD results for different a_0 lengths, including all materials tested. In order to enable a comparison between CT and WCT based results, Figure 4.16 also includes the averaged maximum *G* values, determined through CT tests for a_0 lengths of 18 mm. Figure 4.16 shows a significant variation of *G* across different materials. It should be mentioned that the WCT energy release rate results are lower than those determined through CT specimens with a_0 = 18 mm, which is particularly noticeable for U150-S specimens (Figure 4.16 (d)). This specimen geometry dependency is in accordance with the results reported by Ortega *et al.* [4.28], who reported that smaller specimens are expected to yield overestimations of fracture properties. The results presented in Chapter 3 also displayed this trend, showing that CT specimens are more sensitive and dependent on specimen geometry.

It is also noteworthy that, in the WCT tests, the estimates of *G* reach a stable propagation stage (a plateau in *G vs*. CTOD curves), in contrast with the increasing trend found in CT tests. Some I150-A specimens seemed to reach this stage at the last crack growth increments (Figure 4.16 (a)).

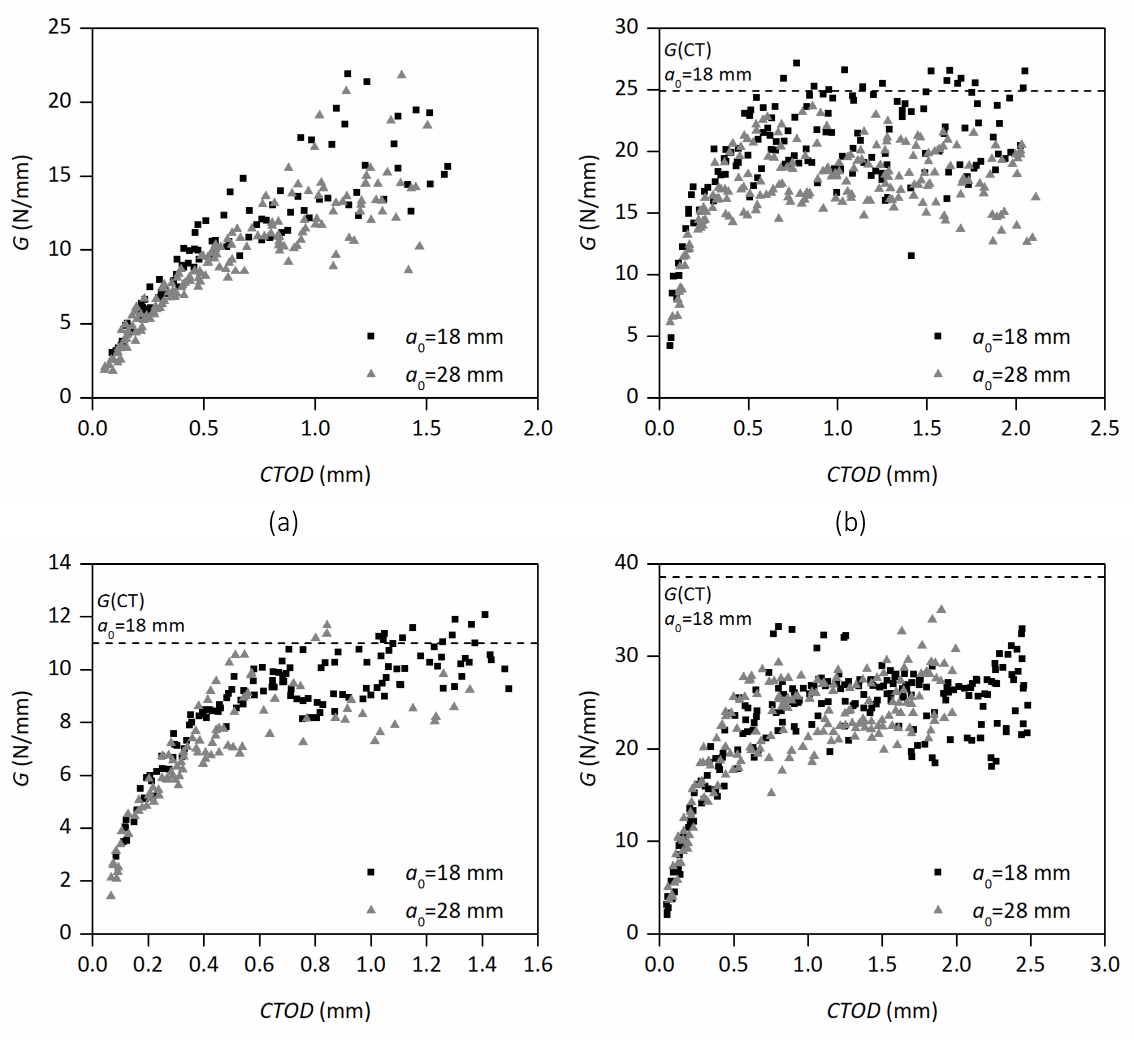

(a) (b)

(c) (d)

Figure 4.16: J-integral based energy release rate (*G*) *vs*. CTOD from WCT tests for different a_0 lengths: (a) I150-A; (b) P300-A; (c) I150-S; (d) U150-S (averaged maximum *G* values from CT tests for a_0 = 18 mm are plotted as dashed lines).

Figure 4.16 also shows that most materials present slightly higher G_c values for 30 mm notched specimens (a_0 = 18 mm) when compared to 40 mm notched specimens (a_0 = 28 mm). However, this variation is lower than that reported for CT tests. The energy release rate results were also plotted against the crack propagation lengths, as illustrated in Figure 4.17. The results shown in Figure 4.17 highlight the crack propagation lengths required to reach a stable propagation stage, which varied from ≈15 mm (P300-A and U150-S) to ≈30 mm (less clear trend for I150-A specimens).

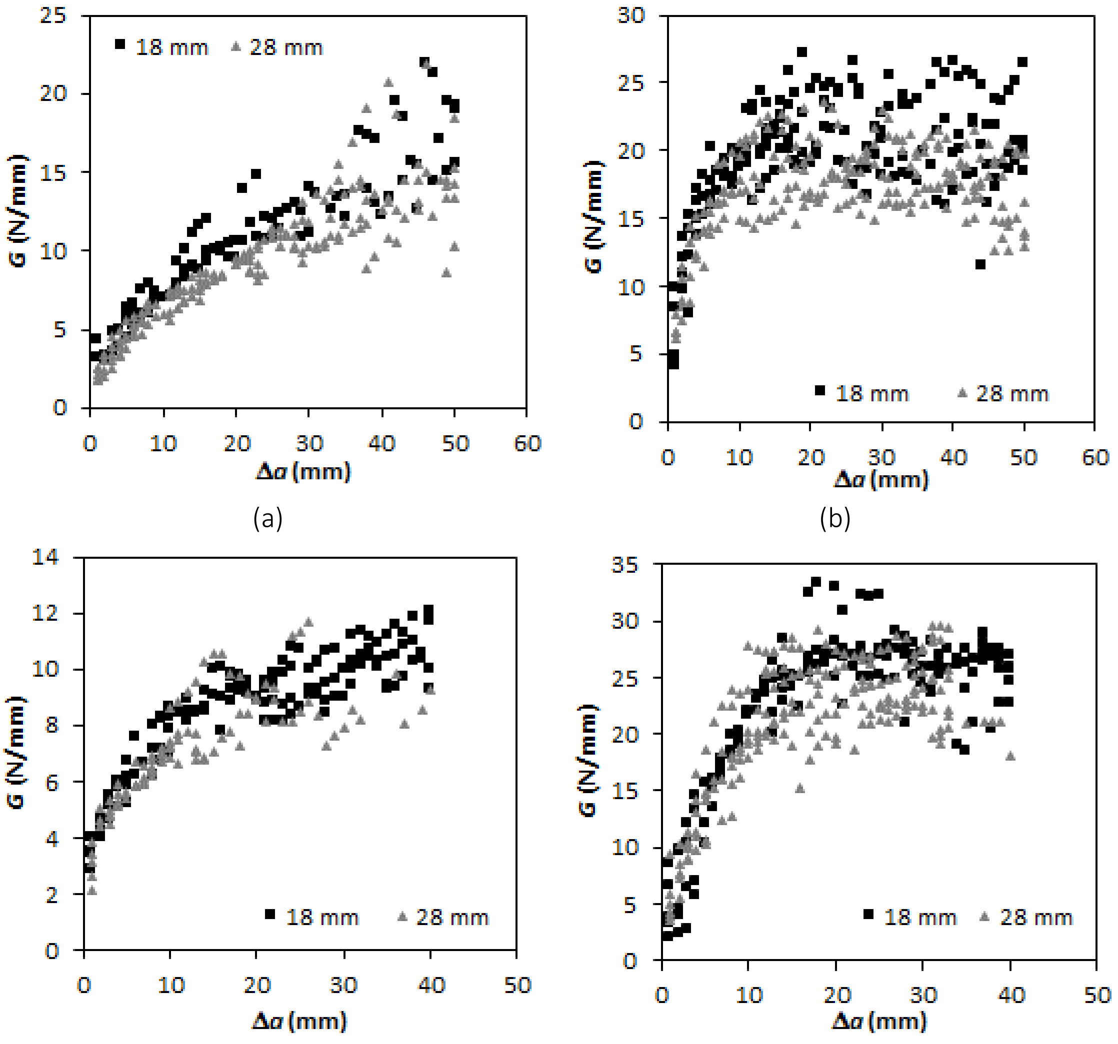

(a) (b)

(c) (d)

Figure 4.17: J-integral based energy release rate (G) *vs.* Δa from WCT tests for different a_0 lengths: (a) I150-A; (b) P300-A; (c) I150-S; (d) U150-S.

For all materials, the results obtained present significant scatter, particularly noticeable for higher values of CTOD. This evidence is in accordance with previous studies, where significant variability was also found in G_c results [4.25, 4.29]. Table 4.5 presents a summary of G_c values obtained from WCT tests for all materials, using the different data reduction methods and a_0 lengths.

The sample of materials presented in Table 4.5 resulted in a range of G_c results between 7 and 27 N/mm, which clearly exceeds the values previously reported in the literature (*cf.* Table 4.1). This range encompasses materials with σ_{u22}^{+} that range from 25 to 70 MPa. The results in Table 4.5 do not show a clear trend between the J-integral and CC results, besides the fact that they are quite similar. It would not be expected that the relative differences between data reduction methods should be constant across all materials, as they present significant differences in elastic and strength properties, besides different levels of orthotropy, which may affect the data reduction methods differently.

The I150-A specimens showed the highest levels of scatter, whereas the U150-S specimens showed lower levels of variability and a higher consistency amongst different initial notch lengths and data reduction methods. To some extent, these different levels of variability should be associated to differences in quality control, possibly lower in I150-A material. As a final note, the I150-A results presented in Table 4.5 were determined by considering the updated E_{22}^{+} of 9.6 GPa. Previous estimates, based on an elastic modulus of 6.6 GPa led to 16.2 and 13.3 N/mm, for a_0 lengths of 18 and 28 mm, respectively [4.18].

Table 4.5: Fracture toughness (G_c) from WCT tests for different a_0 lengths [mm] – average ± coefficient of variation.

Material	J-integral [N/mm]		CC [N/mm]		MCC [N/mm]	
	a_0 = 18	a_0 = 28	a_0 = 18	a_0 = 28	a_0 = 18	a_0 = 28
I150-A	13.6 ±16%	11.1 ±20%	-	-	-	-
P300-A	21.3 ±14%	18.1 ±13%	20.7 ±16%	18.8 ±13%	14.5 ±15%	14.4 ±20%
I150-S	9.9 ±9%	8.8 ±14%	10.7 ±8%	8.9 ±16%	7.7 ±2%	6.6 ±12%
U150-S	25.8 ±12%	24.9 ±13%	27.0 ±13%	27.4 ±12%	19.6 ±7%	19.3 ±6%

4.3.4. Cohesive law assessment

In order to determine the cohesive law of each material (at the laminate level), the *G vs*. CTOD curves were fitted through an exponential expression. The exponential expression with four fitting parameters proposed by Joki *et al*. [4.30] was considered, as detailed in Chapter 3. By using expression (3.9) and differentiating *G* with respect to CTOD, expression (3.10) is obtained, providing an estimate of the cohesive law of the material. The fitting parameters in (3.9) were determined using *IBM SPSS statistics 24* [4.31] commercial software. To that end, for each data reduction method and initial notch length, a non-linear regression was performed. As an illustrative example, Figure 4.18 depicts the results and fitting functions for I150-S and U150-S materials, which represent the materials with highest and lowest differences of G_c across different a_0 lengths. These materials present different levels of geometry dependency, as the I150-S fitting curves for 18 and 28 mm a_0 lengths present a significant deviation, whereas for U150-S the curves for both a_0 lengths are nearly identical.

Figure 4.19 presents a summary of the cohesive laws obtained for all materials, including different data reduction methods and a_0 = 18 mm. Table 4.6 presents a summary of the corresponding cohesive stresses (σ_c) and also the ultimate (σ_{u22}^{+}) stresses of the different materials, as a reference. As previously mentioned, I150-A results do not include compliance calibration methods (*cf.* Section 4.3.3). This material was also an exception, as the maximum stress estimated by differentiating the *G vs*. CTOD curve (32 MPa) is lower than the ultimate stress determined through mechanical characterization tests (45 MPa), whereas all other materials presented higher maximum cohesive stresses than their transverse tensile strength.

The laminate level cohesive laws illustrated in Figure 4.19 show a good agreement between J-integral and CC results, whereas the MCC cohesive laws are more conservative, in line with their corresponding lower G_c results. The shapes of these cohesive laws differ considerably from the standard linear cohesive law implemented in *Abaqus* [4.16] commercial software.

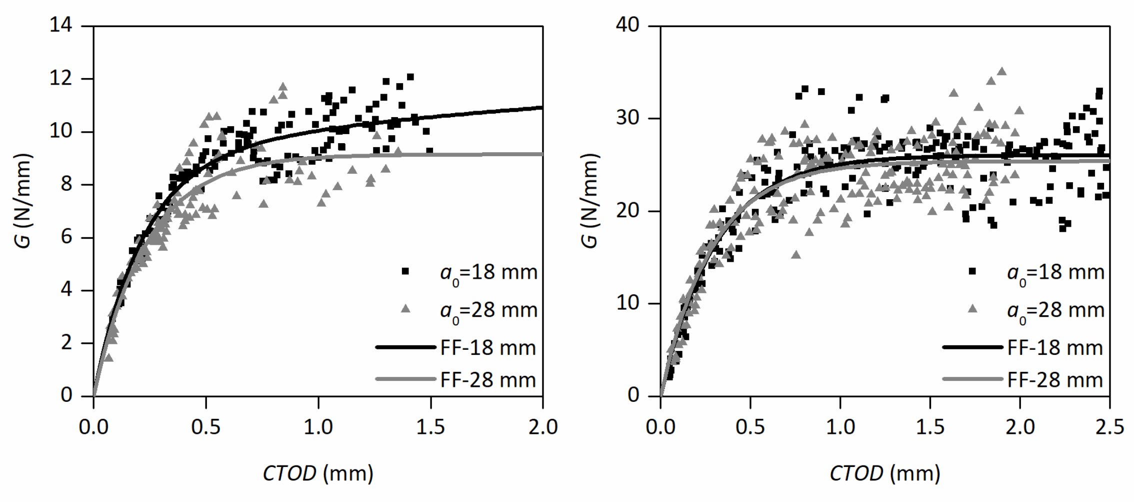

(a) (b)

Figure 4.18: Exponential fitting functions (FF) of energy release rate (*G*) results: (a) J-integral based I150-S-WCT results; (b) J-integral based U150-S-WCT results.

Table 4.6 shows that for most materials (exception being the I150-A profile), the maximum cohesive stresses determined through *G vs*. CTOD results are higher than their σ_{u22}^{+} values. This can be partly attributed to the distance between the targets used to measure CTOD (4 mm), which has been reported by Bergan *et al*. [4.27] to result in overestimations of the initial slope of *G vs.* CTOD curves. This may also be attributed to size effects, as the cohesive stresses are determined from a small area near the crack tip. The P300-A results present the highest variations between cohesive and tensile strengths, with relative differences of 98%. It should also be highlighted that the failure modes of tensile mechanical characterization and fracture tests are considerably different, as the first typically present a more brittle failure with signs of delamination and the latter present more stable damage propagation with significant signs of fibre bridging and reduced indications of delamination. These differences may also contribute to differences found between maximum cohesive and ultimate stresses. The I150-A maximum cohesive stresses are lower than those initially estimated by considering a lower transverse tensile elastic modulus (6.6 GPa), which were determined to be 37.3 and 36.2 MPa, for initial notch lengths of 30 and 40 mm, respectively [4.18].

The implementation of these cohesive laws in FE models took into account the determined cohesive stresses, as well as the material transverse tensile strengths. This step was considered important to further validate this methodology, aside from establishing the reliability of visual observation and compliance-based methods.

4.3.5. Discussion of experimental results

This section presents a summary and discussion of WCT test results, based on the results presented in the previous sections, which are analysed together with those presented in Chapter 3 concerning a pultruded GFRP I-section profile produced by *Fiberline Composites* (I200-F). In this section, the results are analysed as a function of fibre layup, comprising the following three main categories: (i) CFM transverse reinforcement (I150-S); (ii) woven cross-ply [0/90] oriented layers (I150-A, P300-A and I200-F); and (iii) [45/90/45] oriented layers (I152-C and U150-S).

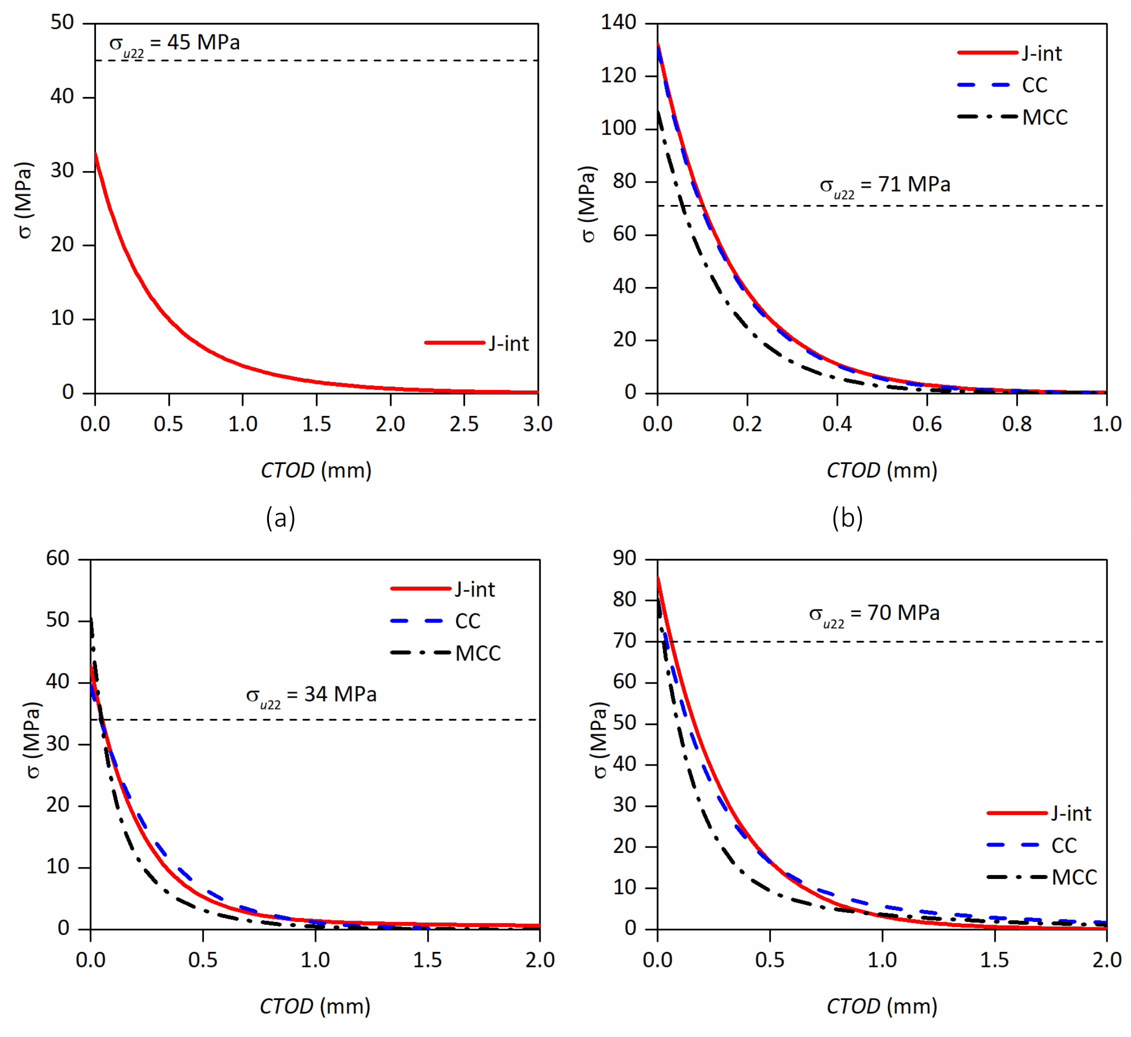

(a) (b)

(c) (d)

Figure 4.19: Laminate level cohesive laws: (a) I150-A-WCT-18; (b) P300-A-WCT-18; (c) I150-S-WCT-18; (d) U150-S-WCT-18 (average transverse tensile strengths, σ_{u22}^{+}, marked as dashed lines).

Table 4.6: Summary of cohesive (σ_c) and ultimate transverse tensile stresses (σ_{u22}^{+}), for different a_0 lengths [mm].

Material	σ_c [MPa]						σ_{u22}^{+} [MPa]
	J-integral		CC		MCC		
	$a_0 = 18$	$a_0 = 28$	$a_0 = 18$	$a_0 = 28$	$a_0 = 18$	$a_0 = 28$	
I150-A	32.4	33.9	-	-	-	-	45.0
P300-A	132.3	123.9	130.9	140.9	106.5	112.1	71.1
I150-S	42.8	39.1	39.6	38.8	50.4	45.2	33.8
U150-S	85.5	89.0	80.3	73.9	80.4	71.7	69.9

In order to further investigate the intrinsic variability of each material, as well as to compare the fracture properties of the different materials, the energy release rate data in the propagation stage were fitted with normal distributions. This procedure is illustrated in Figure 4.20 for U150-S material and J-integral results. In this case, lengths a_0 = 18 mm and a_0 = 28 mm produced similar average G_c values of 25.8 and 24.9 N/mm, respectively.

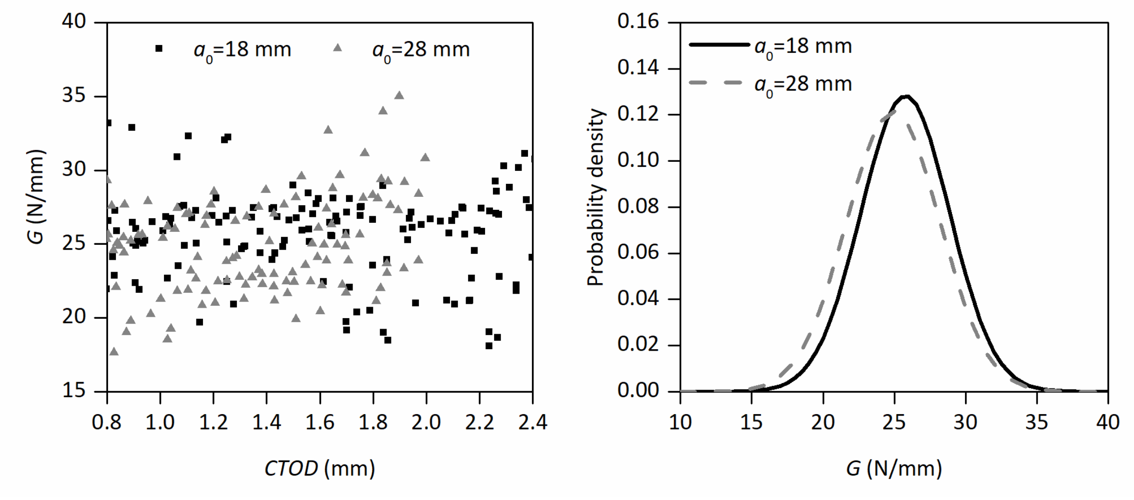

(a) (b)

Figure 4.20: Statistical study of J-integral based fracture toughness (G_c) results for U150-S profile, for different a_0 lengths: (a) stable propagation stage results; (b) normal distributions.

Figure 4.21 presents an overview of normal distributions for G_c, including J-integral and MCC results. This figure highlights the influence of fibre layup on fracture toughness, with (i) the three materials reinforced with woven cross-ply layers presenting average results of G_c between 14 and 21 N/mm; (ii) the material with CFM reinforcement (I150-S) presenting the lowest performance (and also the lowest scatter), and (iii) angled ply material (U150-S) exhibiting the highest performance (note that I152-C results are not plotted as a stable propagation plateau was not attained).

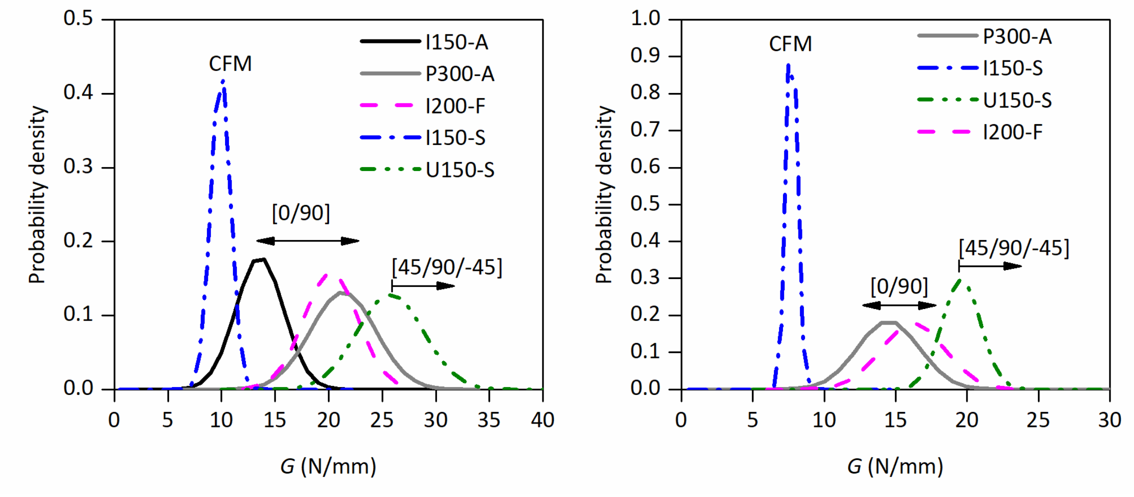

(a) (b)

Figure 4.21: Statistical normal distributions of G_c results for different materials and for a_0 = 18 mm, obtained from different methods: (a) J-integral; (b) MCC.

Figure 4.22 illustrates G_c *vs*. transverse reinforcement percentage, which takes only into account the layers oriented at 90º and ±45º (according to their angle). In order to consider the different fibre orientations, the 45º angled fibres were multiplied by a factor of √2/2 (sin(45º)), and then added to the 90º angled fibres. This figure shows (i) a moderate increase up to 20% of transverse reinforcement (G_c from 10 N/mm to 26 N/mm), followed by (ii) a very significant growth, from 20% to 30% (G_c conservative value of 160 N/mm). This trend, illustrated by an exponential fitting function, must be further validated by testing other pultruded materials.

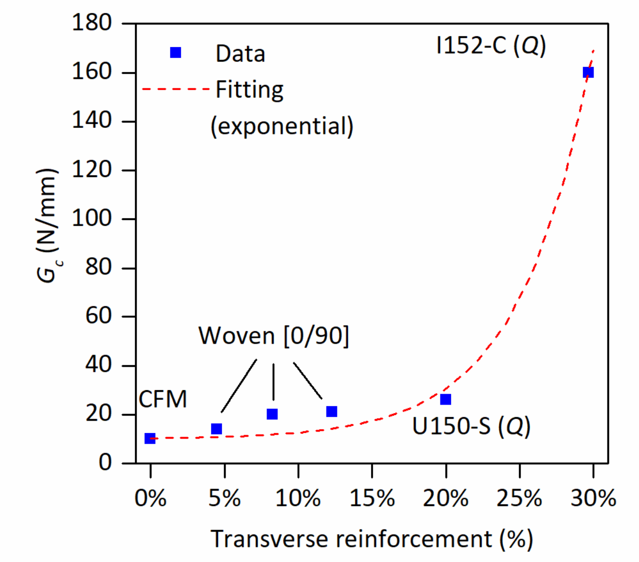

Figure 4.22: G_c *vs*. transverse reinforcement percentage, considering ±45º and 90º oriented layers.

Figure 4.23 presents an overview of laminate level cohesive laws for all tested materials, in terms of absolute (Figure 4.23 (a)) and normalized values with respect to the cohesive stresses σ_c (Figure 4.23 (b)). These results show once again the significant variability across different materials regarding the cohesive laws. The P300-A and I200-F materials have almost identical average G_c results (21.3 and 20.2 N/mm respectively), however, their cohesive law shapes differ considerably, in particularly regarding σ_c. This shape should be particularly relevant in improving the applicability of the reported G_c results to other loading cases [4.32]. This topic is further assessed in the numerical study presented in Section 4.4.

Regarding the cohesive stress, all methods yield similar results. However, in what concerns G_c, two methods present similar results (J-integral and CC), which are based on visual measurements of crack growth. In a different approach, MCC is based on measurements of compliance to determine the actual crack front position. All three methods present similar results before the stable propagation plateau, a point from which the MCC yields lower energy release rate results. In fact, Table 4.5 shows a significant difference between the MCC method and the remainder, with differences of G_c ranging from 20% to 30%, when compared to J-integral results. This is, at this time, believed to be related to the loading/unloading cycles performed to measure the specimen compliance, which were necessary to perform MCC, but may be affected by pulled-out fibres. The experimental results seem to support this conclusion, as the material with lower fracture toughness and therefore with lower levels of fibre bridging (I150-S), presents a lower difference between optically based methods and MCC, when compared to materials that presented higher levels of fracture toughness and fibre bridging (as illustrated in Figure 4.15).

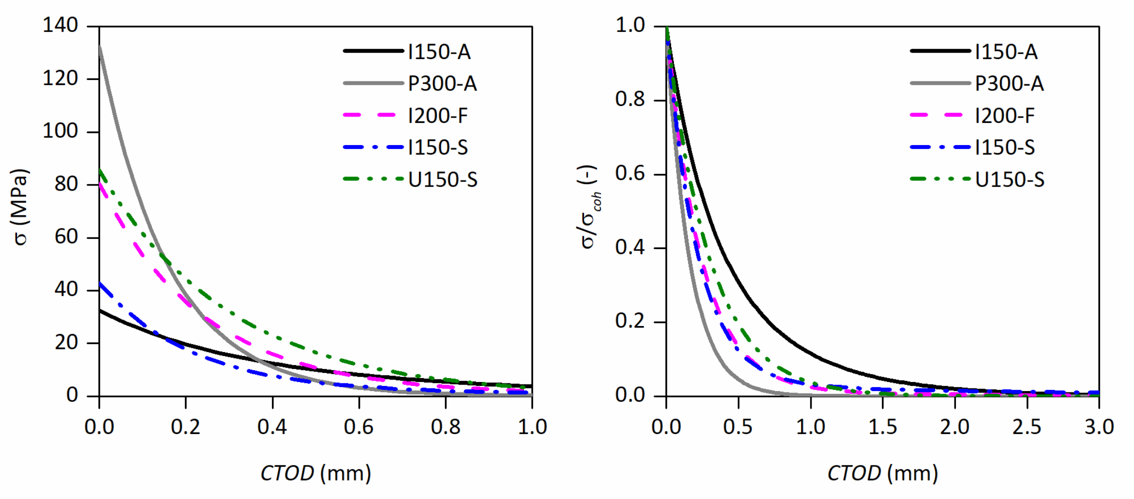

(a) (b)

Figure 4.23: Laminate level cohesive laws, for an a_0 length of 18 mm: (a) J-integral based cohesive laws; (b) J-integral dimensionless laminate level cohesive laws.

Finally, the scaled-up CT tests yielded a cohesive stress of 184 MPa. It is noteworthy that the thinnest materials (P300-A and I152-C) present the highest differences between transverse tensile ultimate stresses and cohesive stresses, ranging from 50% to 86%, whereas in the other materials such differences range from 13% to 26% (considering the J-integral method). This difference between cohesive stress and material strength was attributed to the failure modes of each test: (i) the coupons tested to evaluate the material strength present a pure brittle failure (sudden collapse), associated with matrix cracking and delamination, while (ii) the specimens tested to evaluate the cohesive stress present a more progressive failure, governed by fibre bridging.

4.4. Numerical study

4.4.1. Overview

The numerical study detailed ahead was performed in three main stages: (i) a preliminary study, which aimed at validating the geometry of the models, the data reduction methods and the damage parameters to be used as input; (ii) a comprehensive study performed for all materials and test configurations, focusing on the comparison of experimental and numerical load *vs.* CMOD curves; and (iii) a more detailed study on damage propagation and numerical stress states, which focused on a lower number of test series. The numerical results section (Section 4.5) is thus divided into these three stages: (i) Preliminary study; (ii) load *vs*. CMOD curves; and (iii) damage propagation.

The models presented ahead are based on two different damage evolution models: (i) *Abaqus* Standard built-in tools [4.16], which include a linear damage progression law; and (ii) a UMAT model, in which an exponential cohesive law was implemented. Another parameter that was considered in the analysis was the numerical transverse tensile strength (σ_{22}^{+}). Two different values were considered per material: (i) the material strength measured through mechanical characterization tests (σ_{u22}^{+}); and (ii) the cohesive stress measured through the initial slope of G *vs.* CTOD experimental results. These two sets of properties promote two different numerical analyses, (i) the effect that the shape of the cohesive law can have on the results, for the same ultimate stress level and G_c; and (ii) the effect of considering different ultimate stresses, for the same cohesive law and G_c.

Given these various damage parameters, the following nomenclature was used: (i) linear cohesive law, denoted by “L”; (ii) exponential cohesive law, denoted by “E”; (iii) models based on the material strength, labelled by “σ_u”; and (iv) models based on the cohesive stress, labelled by “σ_c”. Therefore, each numerical model is identified first by the cohesive law and then by the ultimate stress, resulting in a total of four possible combinations (L-σ_u, L-σ_c, E-σ_u and E-σ_c). As an example, WCT-I200-F-E-σ_c denotes a WCT test of I200-F material, simulated with a UMAT-based numerical model calibrated with an exponential cohesive law (E) and considering the cohesive stress (σ_c). Additionally, the initial notch length (a_0) may be added to these references in brackets, when relevant.

4.4.2. Geometry

The geometry considered for each model followed that of specimens used in the experiments, as illustrated in Figure 4.1. In order to ascertain that the differences found between experimental and numerical results could be attributed to the material input parameters and not to geometry discrepancies, the experimental average initial notch lengths were considered for each experimental series, instead of using the same nominal length for all test series. The notch tip shape was modelled to present a round shape, after the mesh sensitivity tests performed in the parametric study, as detailed ahead.

4.4.3. Material properties

The material properties considered in the FE models were those obtained from the mechanical characterization tests, given in Table 4.2. Being the focus of this study, the transverse tensile fracture toughness (G_2^+) was based on the experimental results presented in Tables 4.5 and 4.6. The transverse compressive fracture toughness G_2^- was assumed equal to G_2^+, with exception of the I152-C model; here, this parameter was expected to be relevant, as the experimental tests showed a higher propensity for compressive failure, after significant crack growth lengths. Therefore, the G_2^- value was calibrated as a function of the fitting of numerical and experimental load *vs.* CMOD curves. The longitudinal fracture properties G_1^+ and G_1^- were assumed equal to 100 N/mm (typical value found in the literature [4.2]), as they are expected to have a low impact on the results.

As reported in the experimental study (see Section 4.3.3), the I150-A material was not considered for this numerical study, due to significant discrepancies found in mechanical characterization tests, regarding the transverse tensile strength and elastic modulus. These discrepancies were attributed to small defects found in the web of the profiles and attributed to imperfect bonding between the resin and fibre materials.

4.4.4. Finite element mesh

As a result of the parametric study detailed ahead, the models with built-in tools of CT tests were designed with a 0.5 mm FE size, whereas the remaining models were prepared with an average FE size of 1 mm, in order to reduce computational time. Finally, the models developed for damage evolution assessment also featured a 0.5 mm FE size, in order to improve the accuracy of damage growth tracking. All models were developed with CPS4 plane stress and full integration elements, as the geometry and loading are included in a bi-dimensional plane.

4.4.5. Boundary conditions

All boundary conditions were imposed at the loading holes through the “Coupling” tool. The centre of each loading hole was rigidly connected to the relevant semi-circle of its perimeter, in order to mimic the hard contact that occurred in experimental tests. One loading hole was horizontally and vertically restrained, whereas the other was horizontally restrained but vertically moved by an imposed displacement. This methodology was validated by comparing load *vs.* CMOD curves obtained from simulations and tests, as displayed ahead in the numerical results section (Section 4.5). Figure 4.24 illustrates the assessment of boundary conditions, through the comparison between CMOD *vs.* CTOD curves obtained from numerical analyses and experimental tests.

Figure 4.24 shows a nearly identical behaviour between the numerical curve and the corresponding experimental curves, with a non-linear trend that corresponds to damage evolution, followed by a more linear slope, corresponding to a stage where the crack tip area is fully damaged. These results validate the geometry of the model, the boundary conditions and the material properties used as input.

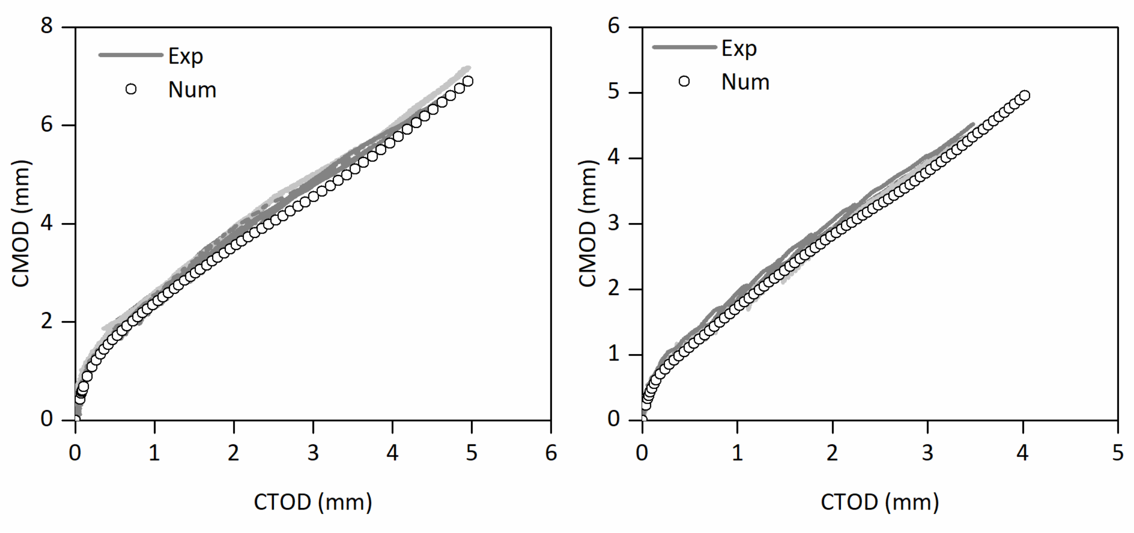

(a) (b)

Figure 4.24: CMOD *vs.* CTOD experimental (Exp) and numerical (Num) results: (a) WCT-P300-A-E-σ_c (a_0=18 mm); (b) WCT-U150-S-E-σ_c (a_0=28 mm).

4.4.6. Damage initiation and evolution

4.4.6.1. Failure criteria

The Hashin criterion [4.17] was employed to determine damage initiation. This criterion, readily available in commercial software, has been widely adopted in previous studies. The Hashin criterion includes four different damage components: (i) fibre tension, d_f^t; (ii) fibre compression, d_f^c; (iii) matrix tension, d_m^t; and (iv) matrix compression, d_m^c. The failure initiation criterion (*F*) for each damage component is detailed below,

$$F_f^t = \frac{\hat{\sigma}_1^2}{X_t^2} + \alpha \frac{\hat{\tau}_{12}^2}{S_L^2} < 1.0 \quad if \quad \hat{\sigma}_1 \geq 0 \tag{4.1}$$

$$F_f^c = \frac{\hat{\sigma}_1^2}{X_c^2} < 1.0 \quad if \quad \hat{\sigma}_1 < 0 \tag{4.2}$$

$$F_m^t = \frac{\hat{\sigma}_2^2}{Y_t^2} + \frac{\hat{\tau}_{12}^2}{S_L^2} < 1.0 \quad if \quad \hat{\sigma}_2 \geq 0 \tag{4.3}$$

$$F_m^c = \frac{\hat{\sigma}_2^2}{4S_T^2} + \left(\frac{S_{c,2}^2}{4S_T^2} - 1\right)\frac{\hat{\sigma}_2}{Y_c} + \frac{\hat{\tau}_{12}^2}{S_L^2} < 1.0 \quad if \quad \hat{\sigma}_2 < 0 \tag{4.4}$$

where X_t and Y_t are the tensile ultimate stresses of the fibre and matrix, respectively; X_c and Y_c are the compressive ultimate stresses of the fibre and matrix, respectively; S_L corresponds to the longitudinal shear ultimate stress; S_T is the transverse shear ultimate stress; finally, α determines the influence of shear stresses in fibre tensile failure. In this study, this interaction is not relevant as longitudinal stresses have no influence in the experimental failure modes, and thus α was set to zero.

The effective stress $\hat{\sigma}$ is computed using the linear transformation presented in equation (4.5),

$$\begin{Bmatrix} \hat{\sigma}_1 \\ \hat{\sigma}_2 \\ \hat{\tau}_{12} \end{Bmatrix} = \begin{bmatrix} \frac{1}{1-d_f} & 0 & 0 \\ 0 & \frac{1}{1-d_m} & 0 \\ 0 & 0 & \frac{1}{1-d_s} \end{bmatrix} \begin{Bmatrix} \sigma_1 \\ \sigma_2 \\ \tau_{12} \end{Bmatrix} \tag{4.5}$$

where d_f, d_m and d_s are damage variables, as described in the following section.

4.4.6.2. Damage evolution

The damage variables corresponding to the fibre (d_f), matrix (d_m) and shear (d_s) failure are defined in equations (4.6)-(4.8). The shear damage variable is indirectly determined as a function of the remaining damage variables.

$$d_f = \begin{cases} d_f^t & if \quad \hat{\sigma}_1 \geq 0 \\ d_f^c & if \quad \hat{\sigma}_1 < 0 \end{cases} \tag{4.6}$$

$$d_m = \begin{cases} d_m^t & if \quad \hat{\sigma}_2 \geq 0 \\ d_m^c & if \quad \hat{\sigma}_2 < 0 \end{cases} \tag{4.7}$$

$$d_s = 1 - \left(1 - d_f^t\right)\left(1 - d_f^c\right)\left(1 - d_m^t\right)\left(1 - d_m^c\right) \tag{4.8}$$

After damage initiation, the elastic constitutive relation is rewritten as follows:

$$\begin{Bmatrix} \sigma_{11} \\ \sigma_{22} \\ \tau_{12} \end{Bmatrix} = \frac{1}{D} \begin{bmatrix} (1-d_f)E_{11} & \left(1-d_f\right)(1-d_m)\nu_{21}E_{22} & 0 \\ (1-d_f)(1-d_m)\nu_{12}E_{11} & (1-d_m)E_{22} & 0 \\ 0 & 0 & (1-d_s)G_{12}D \end{bmatrix} \begin{Bmatrix} \varepsilon_{11} \\ \varepsilon_{22} \\ \varepsilon_{12} \end{Bmatrix} \tag{4.9}$$

$$D = 1 - \left(1 - d_f\right)(1 - d_m)\nu_{12}\nu_{21} \tag{4.10}$$

where σ and τ represent the stresses, ε represents the strains, *E* is the elastic modulus in either the longitudinal ($_1$) or transverse ($_2$) directions. Finally, G_{12} and ν_{12}, ν_{21} correspond respectively to shear modulus and Poisson ratios. Viscous regularization was implemented to facilitate convergence in both conventional and UMAT *Abaqus* models. A value of 1E-4, validated in previous studies [4.33, 4.34], was found to produce adequate results.

4.4.6.3. Cohesive laws

As mentioned, cohesive laws with two different shapes were considered: (i) linear; and (ii) exponential. The difference between these two formulations is qualitatively illustrated in Figure 4.25 and is further detailed ahead in equations (4.11) and (4.12).

4.4.6.3.1. Linear Softening

The most straightforward damage evolution law is a linear cohesive law. A typical formulation for such a cohesive law is given below,

$$d_i = \frac{\delta_{eq}^{u}(\delta_{eq}-\delta_{eq}^{0})}{\delta_{eq}(\delta_{eq}^{u}-\delta_{eq}^{0})} \quad \text{if} \quad \delta_{eq}^{0} \leq \delta_{eq} \leq \delta_{eq}^{u} \tag{4.11}$$

where d_i is a given damage variable, δ_{eq} is the equivalent displacement, δ_{eq}^{0} is the equivalent displacement at damage initiation and δ_{eq}^{u} is the equivalent displacement at $d_i = 1$.

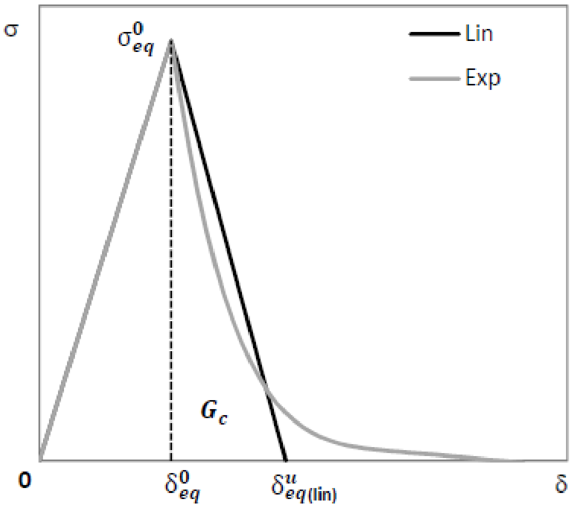

Figure 4.25: Qualitative comparison between linear (Lin) and exponential (Exp) cohesive laws, considering an identical fracture toughness.

4.4.6.3.2. Exponential Softening

As presented in previous sections, an exponential cohesive law should be more representative of the actual damage propagation in composite materials [4.30]. As this option is not currently available for orthotropic materials in *Abaqus* built-in tools, this law was taken into account in the user-defined material (UMAT) subroutines by implementing the following equation,

$$d_i = 1 - \frac{\delta_{eq}^{0}}{\delta_{eq}} e^{\left[-\frac{\sigma_{eq}^{0}}{G_c}(\delta_{eq}-\delta_{eq}^{0})\right]} \quad \text{if} \quad \delta_{eq}^{0} \leq \delta_{eq} \tag{4.12}$$

where G_c is the fracture toughness, and σ_{eq}^{0} is the stress level at damage initiation.

4.5. Numerical results

4.5.1. Preliminary study

4.5.1.1. Parametric study

A preliminary parametric study was performed for one of the materials (I200-F) and one of the test configurations (baseline CT), with the goal of validating the element mesh size and notch tip shape. The mesh size was evaluated by developing L-σ_u models (linear cohesive law with material strength) with FE sizes varying from 0.25 to 1.00 mm. The notch tip was modelled with two different shapes: (i) a square shaped notch, similar to the CT test specimens, and (ii) a semi-circular shape, similar to the WCT test specimens. Figure 4.26 presents the FE meshes that were considered, as well as the different notch shapes.

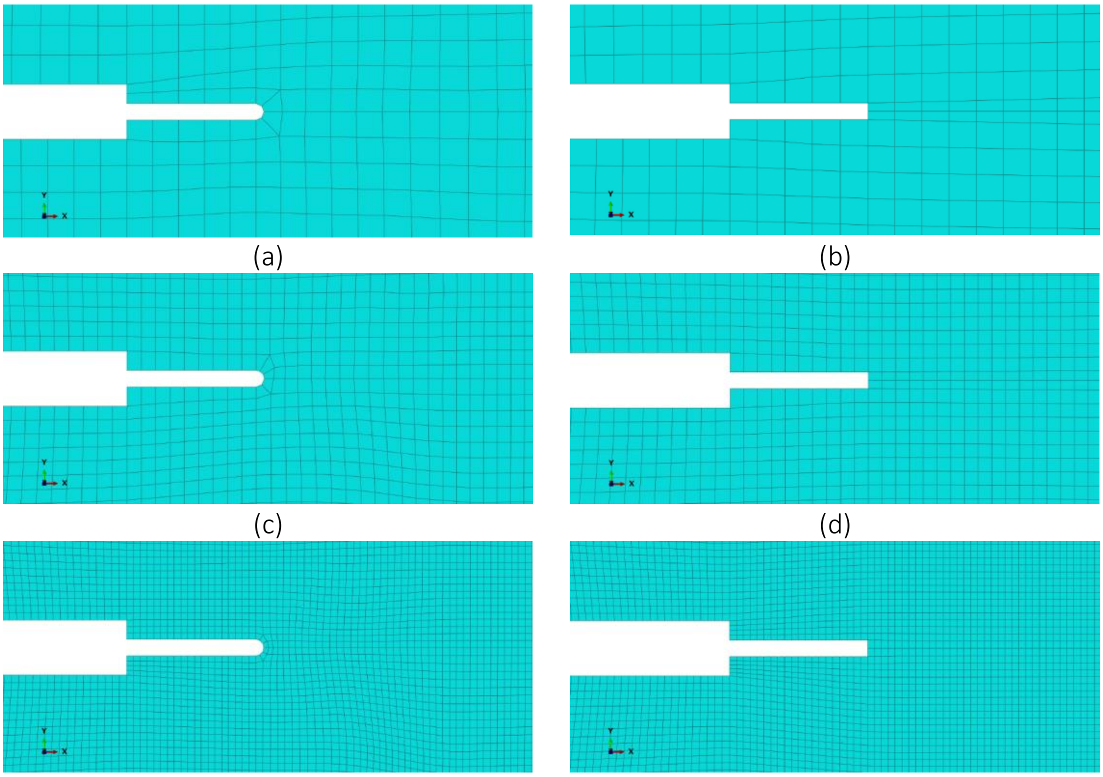

(a) (b)

(c) (d)

(e) (f)

Figure 4.26: FE meshes implemented in the parametric study of CT-I200-F (a_0=18 mm):
(a) round shape with 1.00 mm elements; (b) square shape with 1.00 mm elements;
(c) round shape with 0.50 mm elements; (d) square shape with 0.50 mm elements;
(e) round shape with 0.25 mm elements; (f) square shape with 0.25 mm elements.

Figure 4.27 presents the load *vs.* CMOD curves based on the meshes and notch tip shapes presented in Figure 4.26. The models with square shaped notch (Figure 4.27 (a)) were found to have significantly higher mesh sensitivity when compared to those presenting a round notch shape (Figure 4.27 (b)). This sensitivity is visible not only in the difference between post-peak descending branches but also in the maximum load. Based on these results, the numerical models/results presented ahead are all based on round shaped notch tips. A more detailed study on mesh sensitivity of damage models for composite materials can be found in [4.34].

Figure 4.28 illustrates the load *vs*. CMOD curves for different cohesive laws and ultimate transverse tensile stresses for the WCT-I150-S-a_0=28 mm (Figure 4.28 (a)) and WCT-P300-A-a_0=28 mm (Figure 4.28 (b)) models. It is shown that changing the cohesive law (L *vs*. E) affects the load *vs.* CMOD curves at damage initiation and up to the softening branch. It can also be seen that changing the value of the numerical transverse tensile strength (σ_c *vs*. σ_u) affects a larger area of the load *vs.* CMOD curve, as damage initiation is also affected by this parameter. In Figure 4.28 (a), the influence of changing between material strength (σ_u=34 MPa) and cohesive stress (σ_c=41 MPa) leads to a slightly lower increase of ultimate load than that caused by changing from exponential (E) to linear (L) cohesive laws. On the contrary, Figure 4.28 (b) shows a case where considering the cohesive stress (σ_c=132 MPa) instead of the material strength (σ_u=71 MPa) has a more significant effect, with the E-σ_c model providing higher loads than the L-σ_u model.

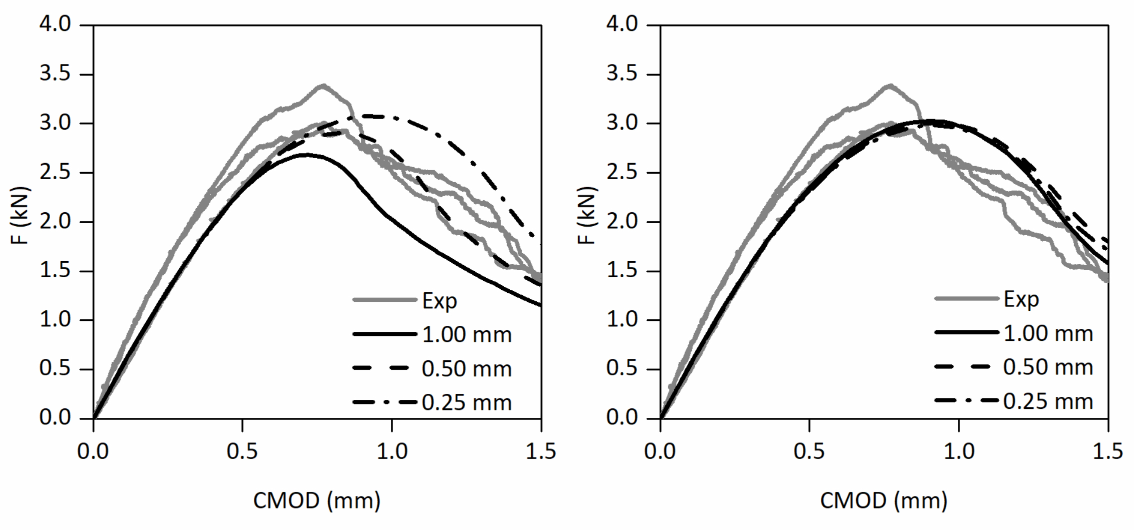

(a) (b)

Figure 4.27: Mesh sensitivity study for CT-I200-F-L-σ_u (a_0=18 mm) models: (a) rectangular shaped notch tip; (b) round shaped notch tip.

Figure 4.28 clearly shows that both damage parameters can have a significant impact in the numerical load *vs.* CMOD curves. It is also noteworthy that the influence of these parameters is different across different materials: (i) changing from linear (L) and exponential (E) cohesive laws has a similar effect in different materials; (ii) changing between the material strength (σ_u) and cohesive stress (σ_c) can have significantly different effects, as a function of the σ_c/σ_u ratio (which varies among the materials tested).

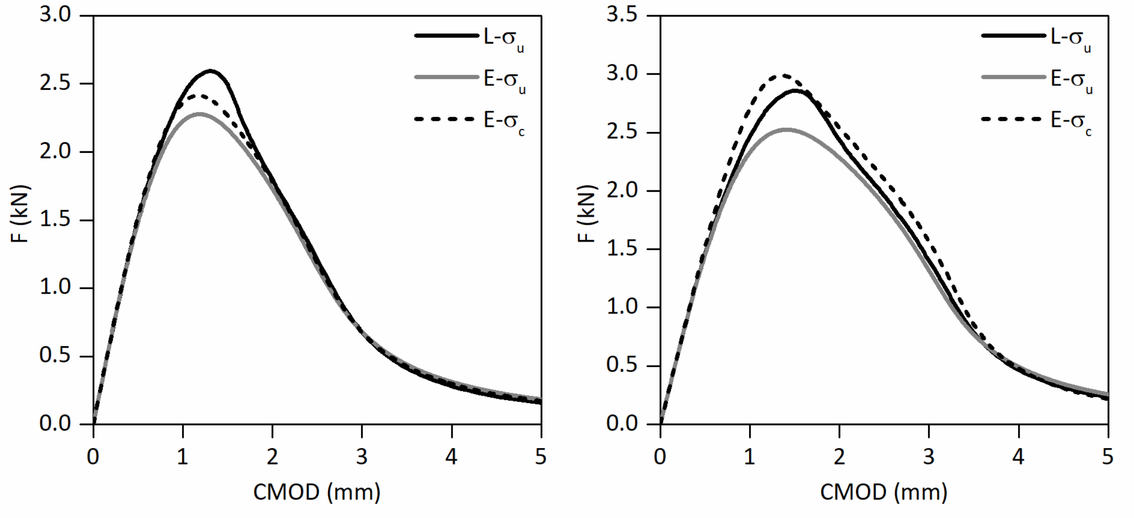

(a) (b)

Figure 4.28: WCT numerical load *vs.* CMOD curves: (a) I150-S (a_0=28 mm); (b) P300-A (a_0=28 mm).

4.5.1.2. Data reduction methods

Before developing the models for all the materials and test configurations, a preliminary assessment was performed to select the most suited data reduction method. In this regard, as J-integral and CC results are quite similar, a comparison was only performed for J-integral and MCC results. The results shown in this section were obtained using *Abaqus* built-in tools and the

L-σ_u model. Figure 4.29 presents a comparison between experimental and numerical load *vs.* CMOD curves, for four different materials.

In general, it is clear that the load *vs.* CMOD curves obtained from numerical analyses agree quite well with those obtained experimentally. Figure 4.29 also shows that considering the MCC-based fracture toughness leads to underestimations of the ultimate load, which is particularly noticeable for P300-A and I150-S materials (Figures 4.29 (b) and (c)). Therefore, the numerical results presented next are based on the FE based J-integral data reduction method. At this time, both the J-integral and CC methods are considered to be the most reliable among those tested in, whereas the MCC method has been confirmed to be incompatible with loading/unloading cycles [4.25].

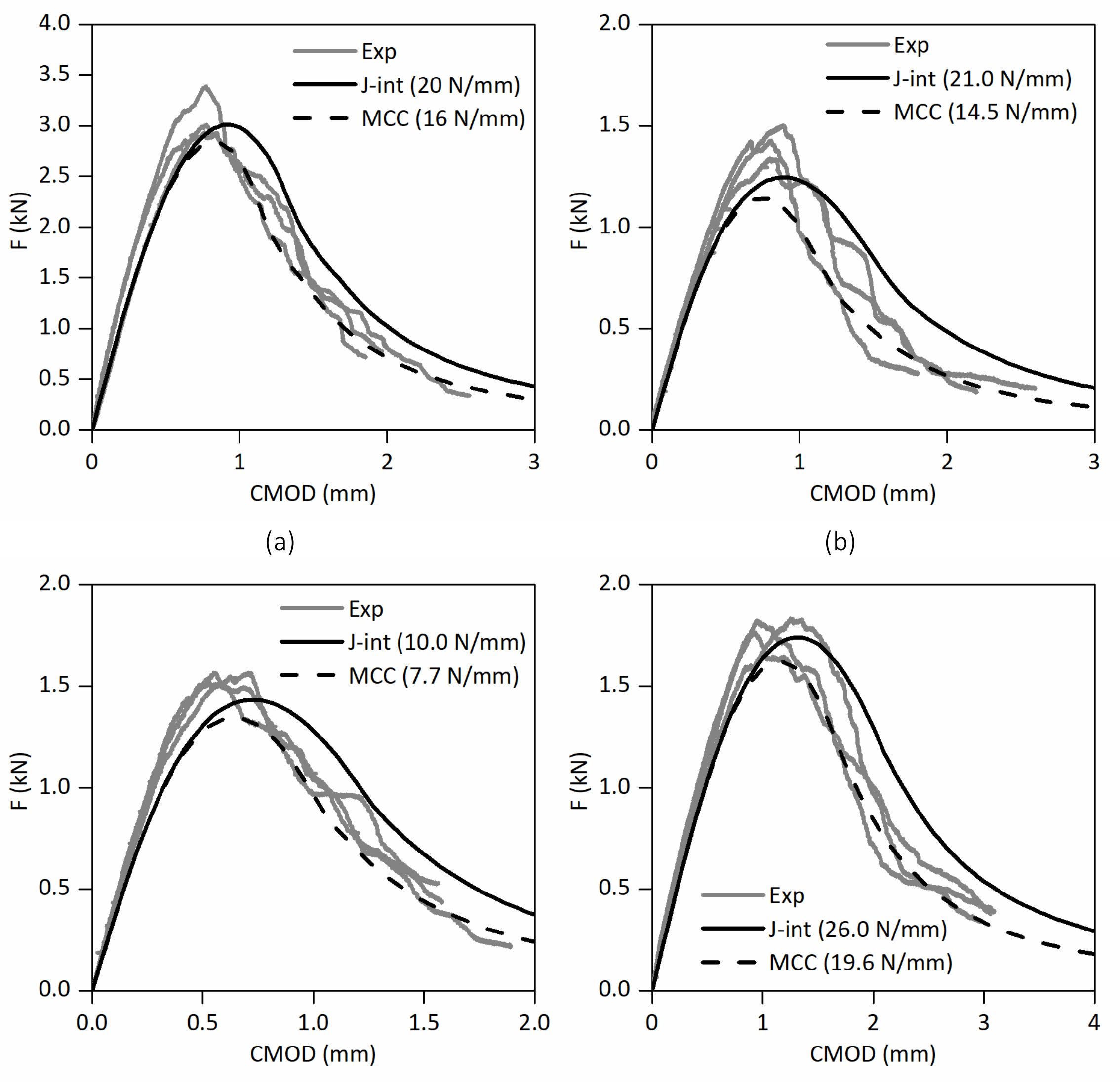

(a) (b)

(c) (d)

Figure 4.29: Experimental (Exp) and numerical (L-σ_u) CT load *vs.* CMOD curves (based on J-integral and MCC): (a) I200-F (a_0=18 mm); (b) P300-A (a_0=23 mm); (c) I150-S (a_0=18 mm); (d) U150-S (a_0=23 mm).

4.5.1.3. Ultimate loads

In order to select the damage parameters that produce a better fit between numerical and experimental results, a preliminary study was performed, consisting of running a model for each combination of cohesive law shapes (L and E) and ultimate stresses (σ_u and σ_c). These numerical results were then compared to experimental results, in terms of ultimate loads. Table 4.7 presents a summary of ratios between numerical and average experimental ultimate loads, for both CT and WCT tests.

Table 4.7: Averaged ratios between numerical results and mean experimental ultimate loads for both CT and WCT tests.

Material	L-σ_u	L-σ_c	E-σ_u	E-σ_c
I200-F	0.999	1.041	0.890	0.927
P300-A	0.947	1.170	0.842	1.058
I150-S	1.016	1.093	0.893	0.964
U150-S	0.998	1.076	0.879	0.954
Overall	0.990	1.095	0.876	0.976

The results detailed in Table 4.7 clearly show that two numerical models stand out in terms of accuracy: (i) the linear cohesive law calibrated with the material strength (L-σ_u model), and (ii) the exponential cohesive law calibrated with the cohesive stress (E-σ_c model). The other two combinations consistently either overestimated (L-σ_c model) or underestimated (E-σ_u model) the experimental results. Given these results, the sections ahead only include numerical results obtained from the two most accurate models, L-σ_u and E-σ_c.

4.5.2. Load *vs*. displacement curves

4.5.2.1. WCT tests

The WCT tests are presented firstly as they were used to determine both the fracture toughness and the cohesive parameters taken as input in the various models. It was thus expected that the numerical models would simulate accurately the experimental WCT tests. Figure 4.30 presents a summary of numerical and experimental load *vs.* CMOD curves for WCT tests of four materials.

Figure 4.30 shows an overall good agreement for both L-σ_u and E-σ_c models; however, for the I200-F and U150-S materials, the models underestimate the softening slope (Figures 4.30 (a) and (d)). It is also noteworthy that the E-σ_c model presents a higher ultimate load than the L-σ_u model only in the simulation of the P300-A profile. This is due to the aforementioned higher discrepancy between the values of σ_c and σ_u for this specific GFRP material (132 *vs.* 71 MPa).

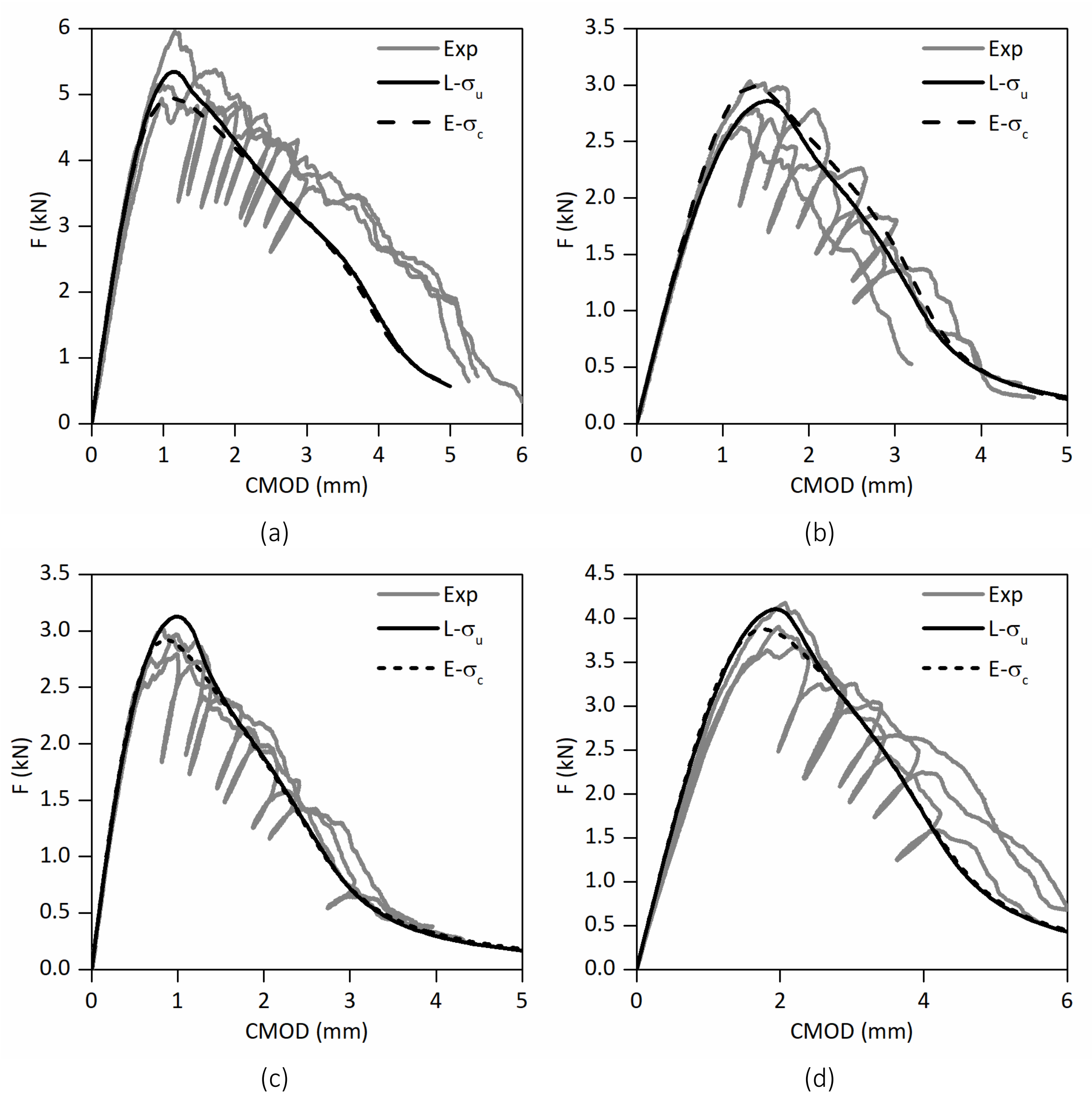

Figure 4.30: Experimental (Exp) and numerical (L-σ_u and E-σ_c) WCT load *vs.* CMOD curves: (a) I200-F (a_0=18 mm); (b) P300-A (a_0=28 mm); (c) I150-S (a_0=18 mm); (d) U150-S (a_0=28 mm).

4.5.2.2. Baseline CT tests

The baseline CT tests pose a more relevant challenge to these numerical models, due to their significantly lower width (compared to WCT tests) and subsequent potential influence of size effects [4.28]. This issue was previously addressed experimentally, by comparing baseline CT and WCT predictions of G_c. The experimental results reported, both in Section 4.3.3 and Chapter 3, showed that the G_c results obtained from CT tests were considerably higher than those derived from WCT tests, and thus CT tests were considered inaccurate. Figure 4.31 presents the numerical and experimental load *vs.* CMOD curves for baseline CT tests on four different profiles.

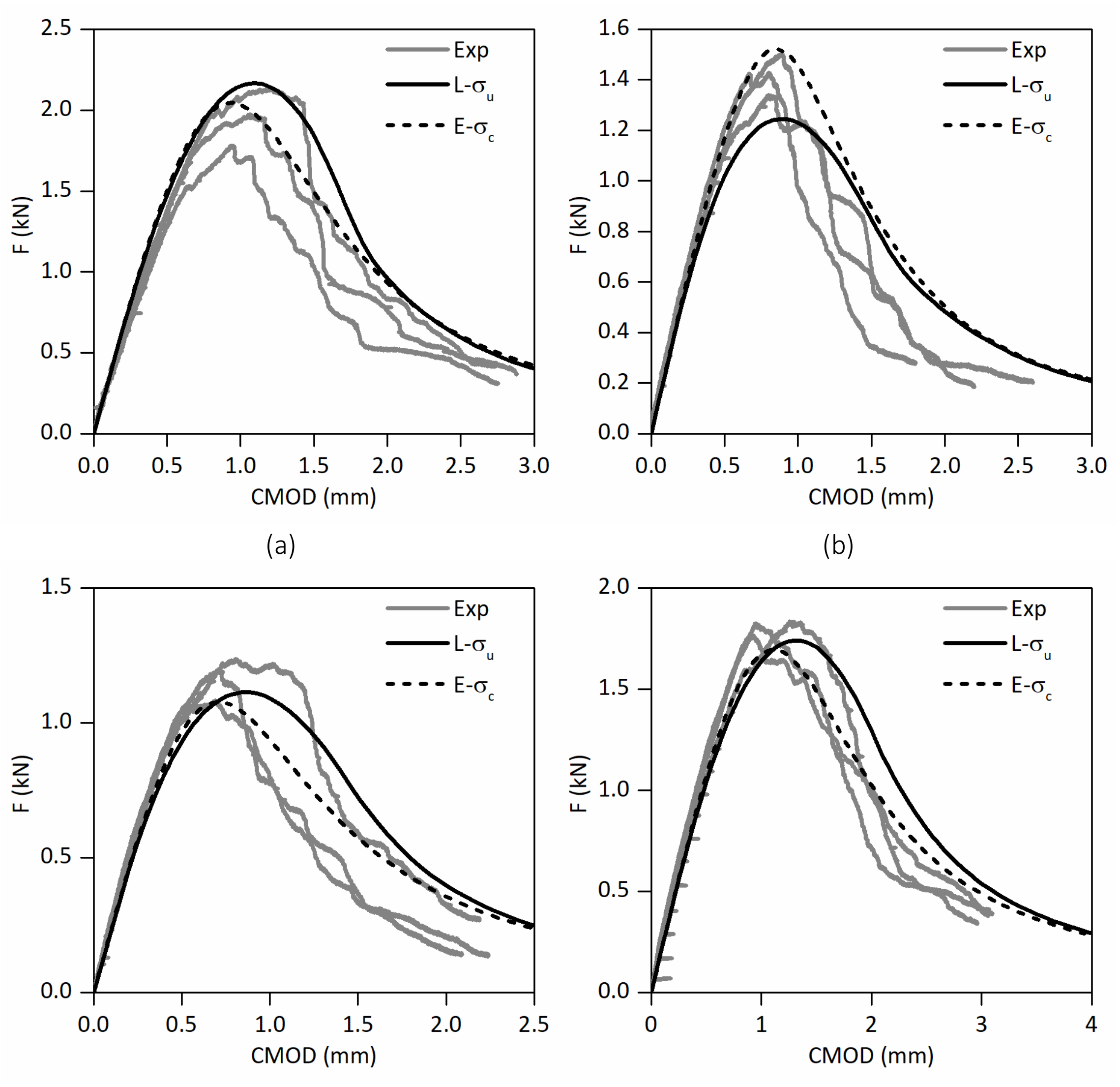

(a) (b)

(c) (d)

Figure 4.31: Experimental (Exp) and numerical (L-σ_u and E-σ_c) baseline CT load *vs.* CMOD curves: (a) I200-F (a_0=23 mm); (b) P300-A (a_0=23 mm); (c) I150-S (a_0=23 mm); (d) U150-S (a_0=23 mm).

Figure 4.31 shows a good agreement between numerical and experimental results, especially regarding the ultimate loads. It is noteworthy that, unlike the previously shown WCT results, for some materials the numerical models seem to overestimate the softening slope. This discrepancy between WCT and CT numerical results may indicate some level of geometry dependency of the measured fracture properties.

4.5.2.3. Scaled-up CT tests

Figure 4.32 presents experimental and numerical load *vs.* CMOD curves of scaled-up CT tests. As mentioned, this test configuration was only implemented for the I152-C profile and a conservative G_2^+ value of 160 N/mm was assumed because several test specimens reached this threshold. As the specimens presented a compressive dominated failure, G_2^- was calibrated to provide the best fit to experimental results, resulting in a value of 35 N/mm.

The load *vs.* CMOD results presented in Figure 4.32 seem to indicate that the value considered for G_2^+ (160 N/mm) may be lower than the actual G_c value, as the numerical ultimate loads are significantly lower than the experimental ones. This is in line with the experimental results reported in Section 4.3.2, which suggest that the G_c value of this material may reach up to 200 N/mm.

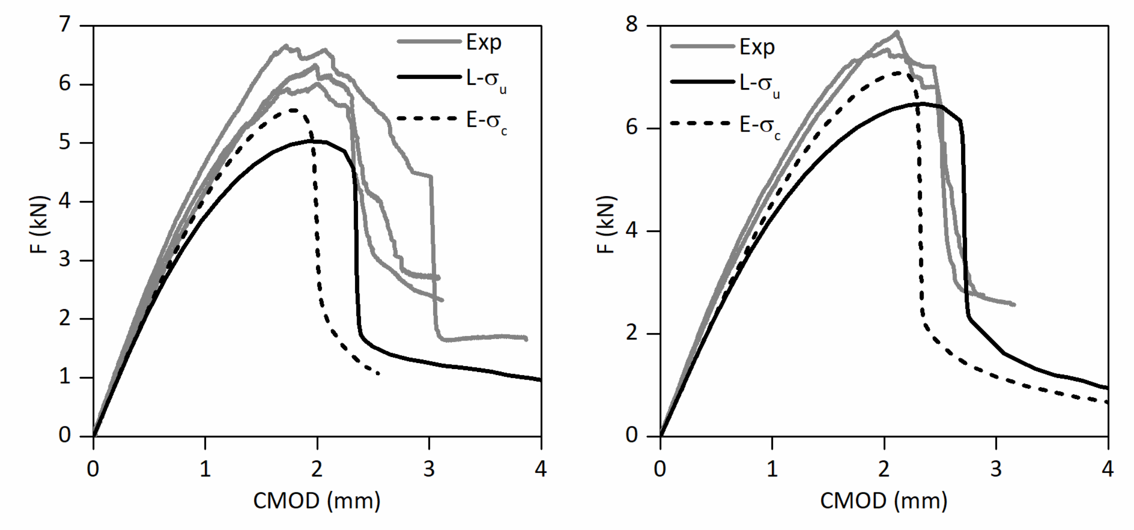

(a) (b)

Figure 4.32: Experimental (Exp) and numerical (L-σ_u and E-σ_c) scaled-up CT-I152-C load *vs.* CMOD curves: (a) 80 mm specimens with a_0=20.0 mm; (b) 100 mm specimens with a_0=24.5 mm.

4.5.3. Damage propagation

4.5.3.1. Damage evolution vs. crack growth

In this section, a brief study on damage evolution is presented and validated by comparing numerical simulations with experimental crack growth measurements. Figure 4.33 presents a comparison between damage propagation obtained from simulations and crack growth measured from experimental tests, for different damage thresholds: (i) d_m^t>0, which means that a crack will open at the onset of damage initiation; (ii) d_m^t=1, which corresponds to assuming that a crack will only be visible after the material is fully damaged; and (iii) d_m^t≥0.5, which is an intermediate scenario. As the crack growth (*Δa*) experimental measurements began when the crack reached 1 mm of length, these thresholds were also considered for a damage propagation length of 1 mm in the numerical results.

Regarding the WCT-U150-S (a_0=28 mm) series, Figure 4.33 (a) shows crack growth *vs.* CMOD curves obtained from simulations and tests and Figure 4.33 (b) shows damage initiation results plotted over the load *vs.* CMOD curves, also obtained from numerical analyses and experimental tests (representative specimen).

The results presented in Figure 4.33 indicate that the intermediate damage threshold (d_m^t≥0.5) provides a better fit in terms of crack initiation compared with the other two thresholds (d_m^t>0 and d_m^t=1). However, Figure 4.33 (a) shows that there is a slight discrepancy between the experimental crack growth rate and the numerical damage evolution slope. This discrepancy is within an acceptable margin of error, as the models are homogenized through the thickness and thus do not take into account the heterogeneous layup of the material.

After this initial assessment, a damage threshold of 0.5 was considered in subsequent studies. Figure 4.34 present a comparison between *Δa vs.* CMOD curves for four different profiles obtained from baseline CT and WCT tests and the corresponding numerical simulations, considering L-σ_u and E-σ_c models.

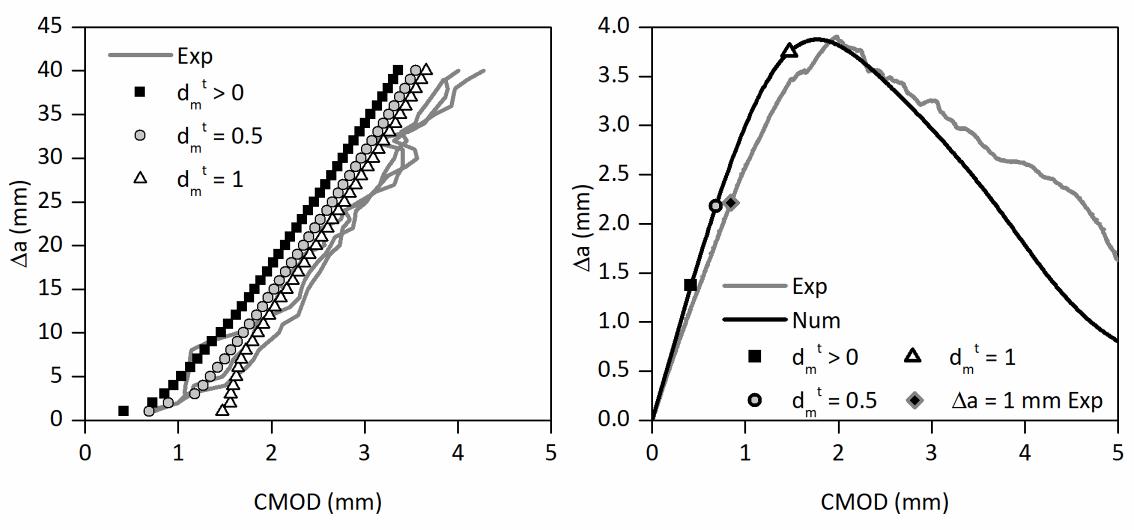

(a) (b)

Figure 4.33: Experimental (Exp) *vs.* numerical (Num, E-σ_c) damage initiation and propagation of WCT-U150-S (a_0=28 mm) series: (a) Δa *vs.* CMOD curves; (b) numerical damage initiation thresholds in load *vs.* CMOD curves and experimental crack growth initiation (Δa = 1 mm).

Figure 4.34 illustrates a similar qualitative trend (identical Δa *vs.* CMOD slopes) but visible quantitative differences (up to ≈5 mm) between numerical damage evolution and experimental crack growth rates. In all materials, for both types of models considered (L-σ_u and E-σ_c) the numerical simulations slightly overestimate the experimentally determined crack lengths. However, given the simplifications assumed in these numerical models, the differences found can still be considered quite acceptable. Figure 4.34 also shows a reduced difference between the L-σ_u and E-σ_c models, in respect to damage evolution. However, a general trend can be identified, with E-σ_c models presenting a lower damage evolution rate and thus a better fit to experimental crack growth rates.

4.5.3.2. Damage and stress evolution ahead of the crack tip

This section presents an assessment of the damage evolution and stress states throughout the crack growth path. This study was performed for a length of 40 mm ahead of the crack tip, as this was the monitored length in fracture tests. Results obtained for the series WCT-P300-A-a_0=18 mm are presented next, as an example.

Figure 4.35 presents the damage evolution (parameter d_m^t) throughout the length defined above, for different levels of CMOD. Figure 4.35 illustrates the difference between considering a linear and an exponential cohesive law (L-σ_u *vs.* E-σ_u), as well as the difference between considering the material strength and the cohesive stress (E-σ_u *vs.* E-σ_c).

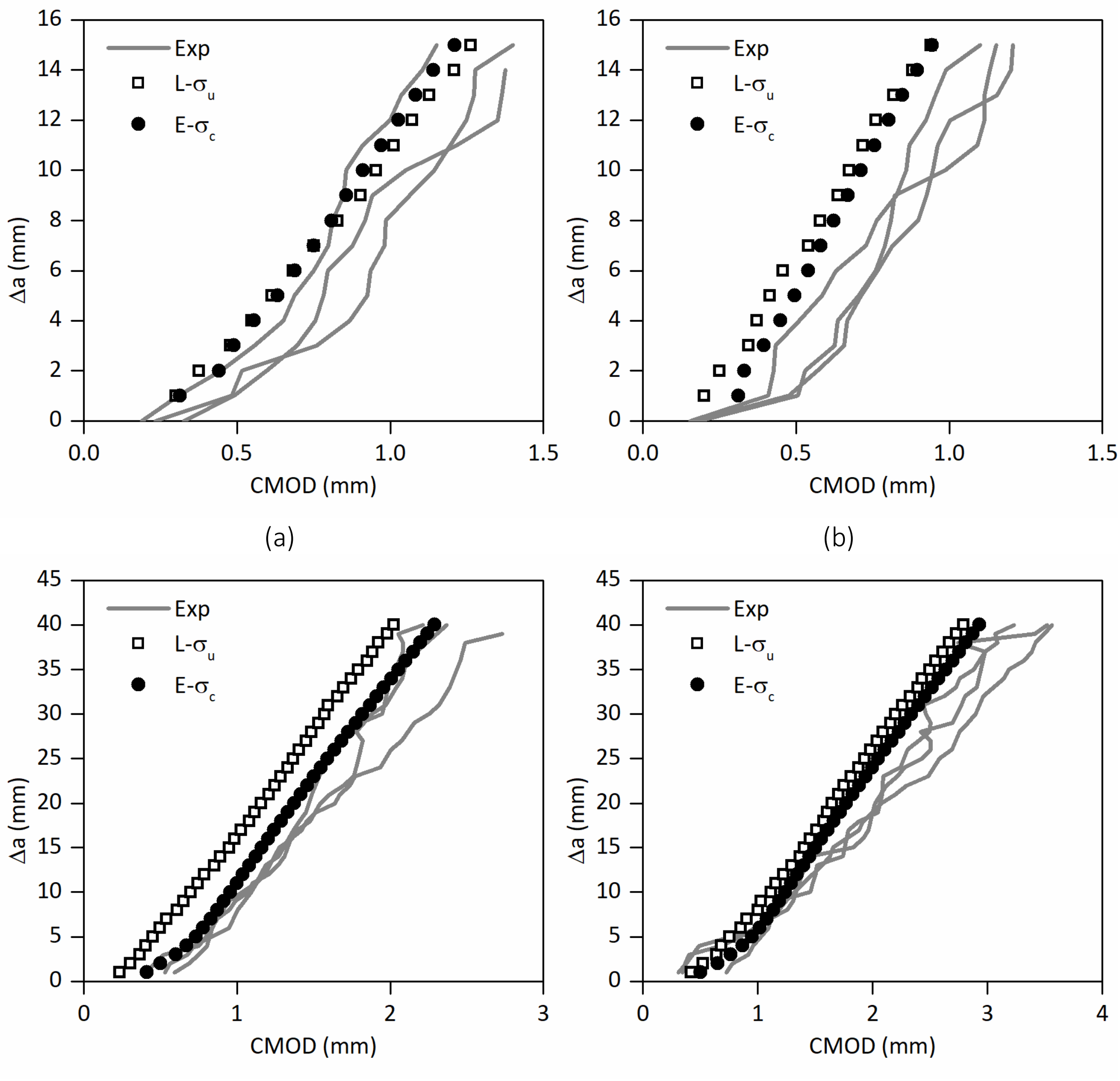

(a) (b)

(c) (d)

Figure 4.34: Experimental (Exp) and numerical (L-σ_u and E-σ_c) crack growth rates (Δa) *vs.* CMOD: (a) CT-I200-F (a_0=18 mm); (b) CT-I150-S (a_0=18 mm); (c) WCT-P300-A (a_0=18 mm); (d) WCT-U150-S (a_0=18 mm).

In this specific material, the aforementioned significant difference between material strength and cohesive stress leads to a higher damage evolution rate for the L-σ_u model, when compared to the E-σ_c model. This result is in line with Figure 4.34 (c), where the E-σ_c model presents a lower damage evolution rate. It is noteworthy that the different models provide relatively similar load *vs.* CMOD curves (Figure 4.35 (b)), despite the different damage evolution trends (Figure 4.35 (a)). Figure 4.35 also shows that the E-σ_u model presents the highest damage evolution rate, which is in line with its worse fit to experimental results, as summarized in Table 4.7.

Figure 4.36 illustrates the evolution of transverse stress (σ_{22}) with Δa, for the same CMOD levels presented in Figure 4.35 and obtained from the same models. As expected, the maximum transverse stresses shown in Figure 4.36 (a) closely follow the damage propagation shown in Figure 4.35 (a), in respect to Δa, as the transverse stress is progressively reduced behind the crack tip (damaged area). Figure 4.36 also shows that despite the similar load *vs.* displacement curves of L-σ_u and E-σ_c models, there can be significant differences in the stress states obtained from numerical analyses, as the E-σ$_c$ results present a significantly higher peak stress, which also leads to a slower progression of damage.

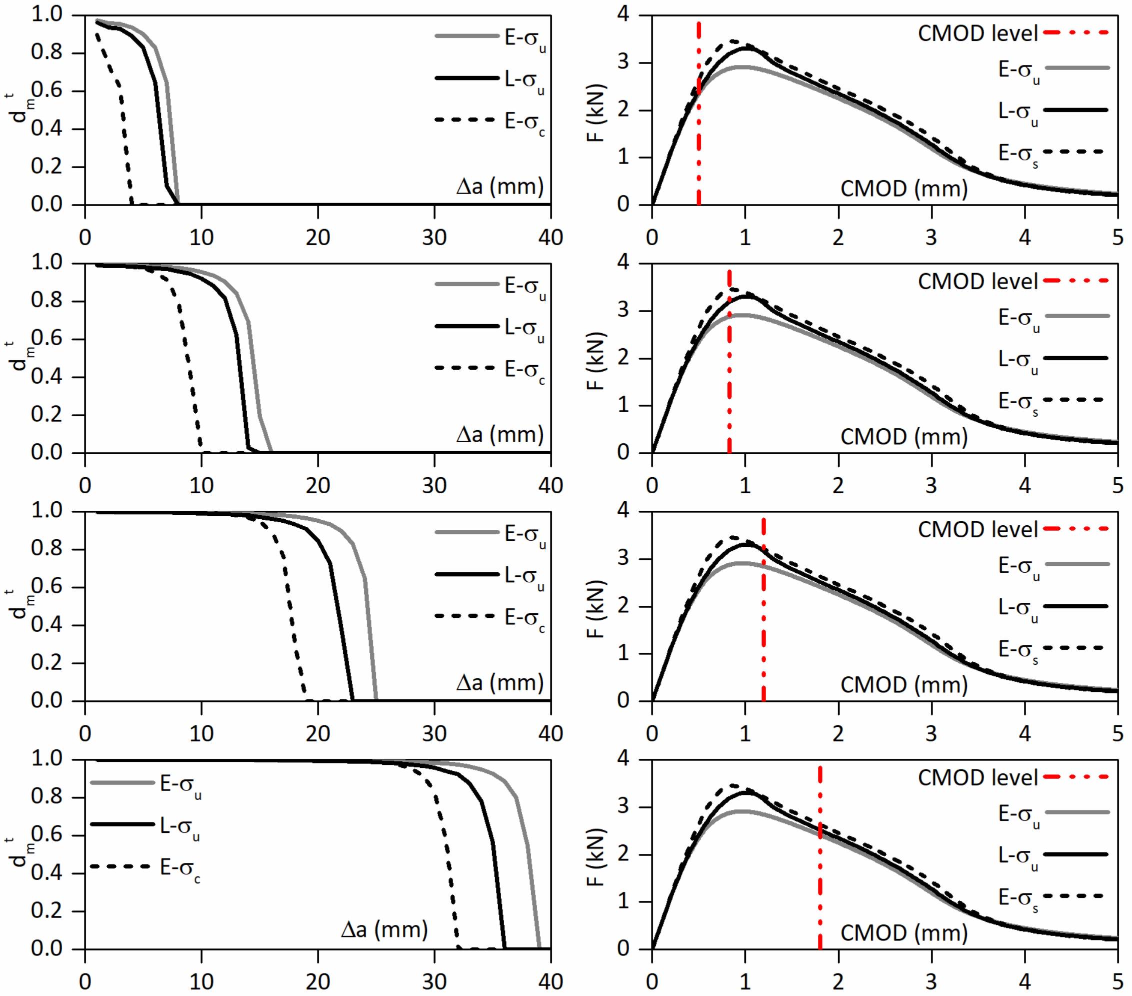

(a) (b)

Figure 4.35: Transverse tensile damage (d_m^t) propagation ahead of crack tip for different points of the load *vs.* CMOD curves, in different models of WCT-P300-A (a_0=18 mm) series: (a) damage envelops; (b) load *vs.* CMOD evaluation points (vertical red dashed lines).

Figure 4.37 presents, for both L-σ$_u$ and E-σ$_c$ models, the longitudinal (σ_{11}) and transverse (σ_{22}) stress contours near the crack tip area, for CMOD=1.8 mm (i.e., the last CMOD level presented in Figures 4.35 and 4.36). The different transverse peak stresses at the crack tip are easily noticeable. Furthermore, the E-σ$_c$ model (Figure 4.37 (d)) seems to present a higher concentration of transverse stresses in a narrower area around the crack tip, when compared to the L-σ$_u$ model (Figure 4.37 (c)). This difference is in line with the different ultimate stresses considered for each model. Both models were calibrated with the same G_2^+ value (21 N/mm), but the E-σ$_c$ model adopted the highest ultimate stress (132 > 71 MPa). This is why the E-σ$_c$ model exhibits a more brittle response and thus a narrower distribution of stresses around the crack tip. This result is also in line with the stress profiles depicted in Figure 4.36.

Among the pultruded GFRP materials tested, the material from the P300-A profile presents the lowest longitudinal strength (σ_{u11}^+=258 MPa) and is the only material where numerical longitudinal stresses have reached the material strength, with model E-σ$_c$ (Figure 4.37 (b)). However, no relevant numerical damage evolution was recorded on the longitudinal direction for this material. Therefore, the longitudinal fracture parameters (G_1^+ and G_1^-) were found to have no impact in these simulations. Furthermore, for all other materials, the longitudinal stresses were found to be considerably lower than the longitudinal material strength.

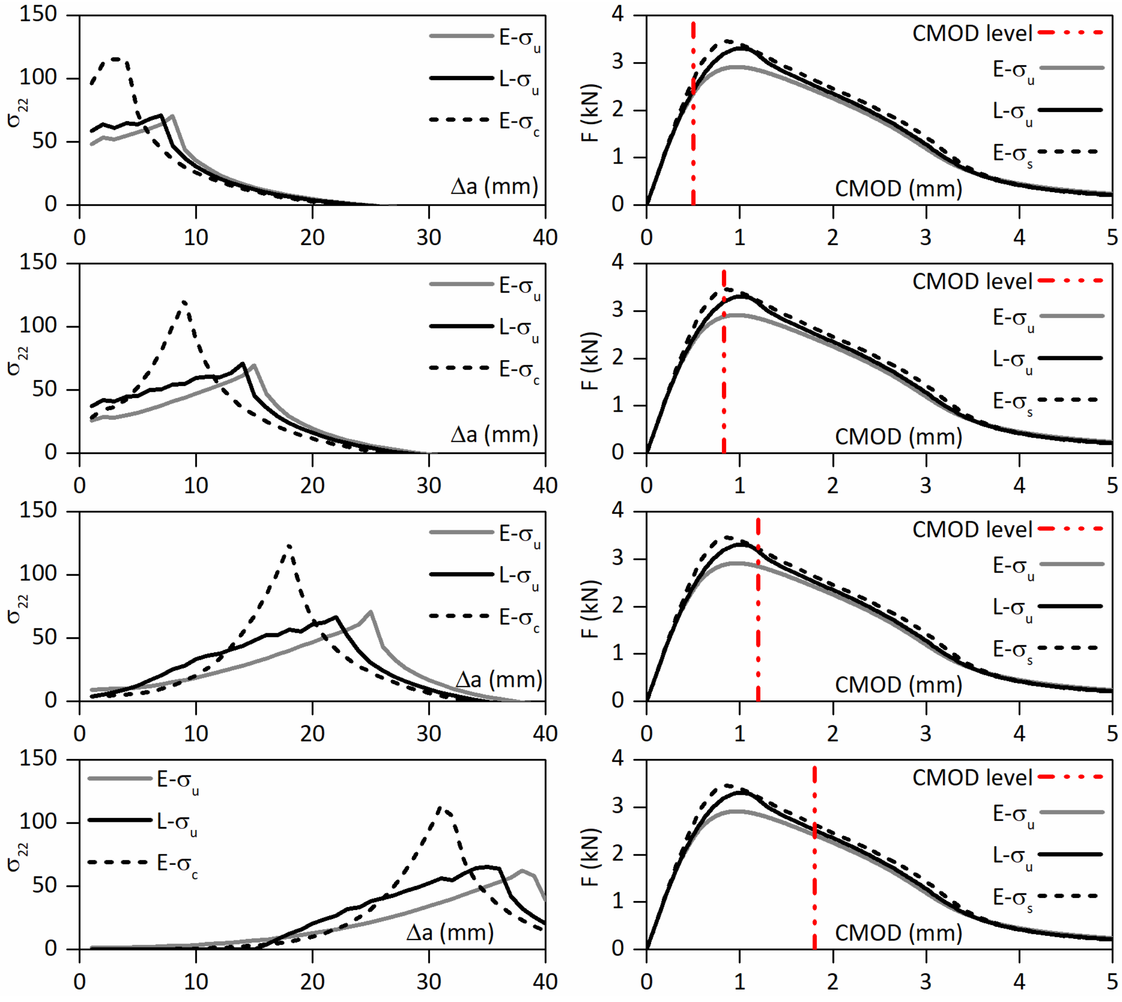

(a) (b)

Figure 4.36: Transverse stress profiles ahead of crack tip for different points of the load *vs.* CMOD curves, in different models of WCT-P300-A-a_0=18mm series: (a) transverse stress envelops; (b) load *vs.* CMOD evaluation points (vertical red dashed lines).

4.5.4. Discussion of numerical results

The models presented above, calibrated with experimentally based fracture toughness parameters, provided numerical results that showed a good agreement with test results. It should be highlighted that these materials present a wide range of elastic and strength properties, and that no calibration was performed in these numerical simulations other than testing different cohesive laws and alternating between the material strength and the cohesive stress, for the numerical transverse tensile strength (σ_{22}^{+}).

Despite this wide variety of materials, the simplified numerical methodology yielded ultimate loads with relative differences to test data that varied between -10% and +11% for L-σ_u models and between -12% and +15% for E-σ_c models. These results are within typical coefficients of variation exhibited by pultruded GFRP materials in material characterization tests [4.3]. It is also noteworthy that, despite leading to similar load *vs.* displacement curves, for some materials the L-σ_u and E-σ_c model results presented relevant differences in terms of transverse stress states (σ_{22}). These discrepancies may be used for further validation, by monitoring the strain fields in experimental tests (possibly through digital image correlation measurements) and comparing these data to numerical results.

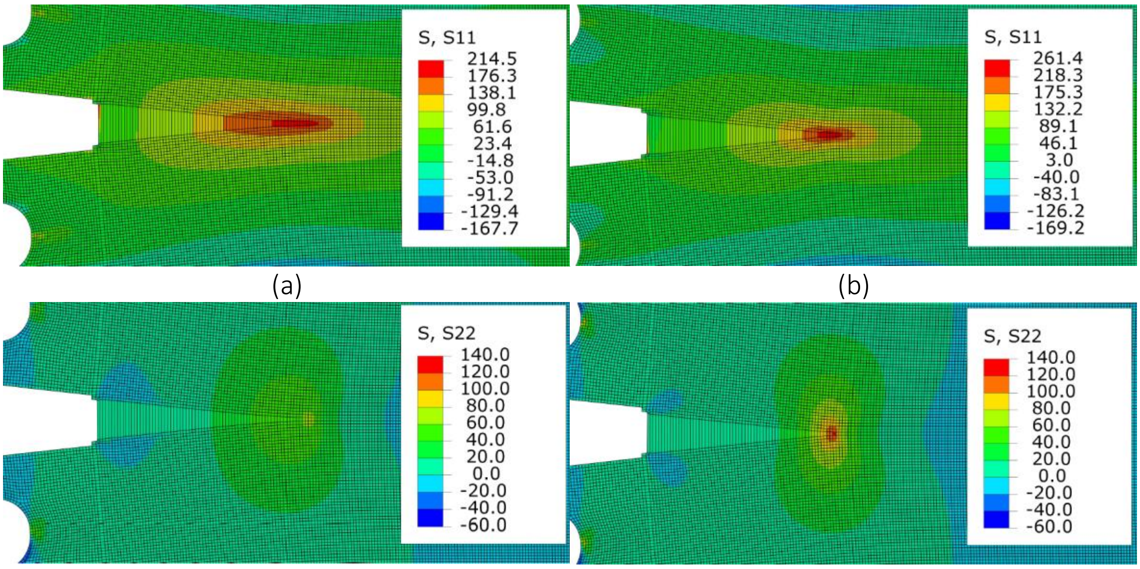

(a) (b)

(c) (d)

Figure 4.37: Stress contours (values in MPa, according to colour scale) of WCT-P300-A (a_0=18 mm) models for CMOD = 1.8 mm: (a) L-σ_u model, longitudinal stresses; (b) E-σ_c model, longitudinal stresses; (c) L-σ_u model, transverse stresses; (d) E-σ_c model, transverse stresses.

There are also some less clear trends in the results. Firstly, there is a low impact in changing from a simplified model, calibrated with a linear cohesive law and material strength, to a more complex model with an exponential cohesive law and cohesive stress. The major differences between these models were only visible in terms of damage propagation and stress profiles ahead of the crack tip. Regarding damage propagation, the E-σ_c models showed a better fit to experimental results; however, the difference between L-σ_u and E-σ_c model results was low for the several studied materials.

As previously noted, the exponential cohesive law provided the best fit to experimental load *vs*. displacement curves, when calibrated with the cohesive stress measured through experimental fracture tests. This cohesive stress may fit well with the damage propagation patterns of fracture tests, however, it is less clear that it will correctly simulate cases where damage is more brittle, such as mechanical characterization tests, in which damage develops uniformly in a localized section of the specimen. In that instance, considering the cohesive stress should lead to numerical overestimations of the experimental ultimate load. Therefore, it is still unclear which is the better solution between L-σ_u and E-σ_c models for a generalised case. This discussion leads to the need of a more complex damage initiation and evolution analysis, which accounts for different types of damage, such as matrix cracking or fibre bridging, in respect to different ultimate stresses. This will be an important step towards a robust numerical methodology valid for more complex cases.

Another point of interest in the results pertains to the possible geometry dependency of the experimentally determined fracture properties. Despite the good agreement between numerical and experimental ultimate loads, across different test configurations, a diverging trend can be seen in the results: some models overestimated the softening slope of baseline CT tests and underestimated the softening slopes of WCT tests, for the same material. This issue, which would have been expected to be mitigated by including an exponential cohesive law, should be further investigated by testing specimens with a wider range of geometries.

4.6. Conclusions

The study presented in this chapter addressed the experimental characterization of the transverse tensile fracture properties of different pultruded GFRP materials and their implementation in finite element numerical models.

WCT tests were successfully implemented to determine the fracture toughness, whereas CT tests were proven to be inadequate within the context of R-curve methods. Furthermore, WCT tests showed low levels of specimen geometry dependency, providing similar energy release rate results (variations ranged from 3% and 24%) for significantly different initial notch lengths (variation of 33%). Among the four data reduction methods that were implemented, the modified compliance calibration presented significantly lower estimates of G_c compared to the remainder methods. This fact was attributed to the influence of fibre pull-out in loading/unloading cycles, as it was established that visually based fracture toughness estimates provided a better fit between numerical and experimental load *vs*. displacement curves.

Given the sample of materials, with a range of transverse tensile strengths between 25 and 70 MPa and a range of transverse reinforcement percentages between 0% and 20%, the G_c results varied between 9 N/mm, for weakly reinforced materials, to 27 N/mm, for materials with more complex transverse reinforcements. Outside this range, for the I152-C material, which presented a higher tensile strength of 121 MPa and a higher transverse reinforcement percentage of 30%, G results ranged between 100 and 200 N/mm, one order of magnitude higher than the remainder. The use of exponential fitting laws enabled a successful prediction of laminate level cohesive laws, showing a reduced level of variability for each material, considering different data reduction methods and initial notch lengths.

The numerical models included two cohesive law shapes, linear and exponential, besides two different values for the transverse ultimate tensile stress per material: (i) the material strength, determined through mechanical characterization tests; and (ii) the cohesive stress, measured from the initial slopes of G *vs*. CTOD curves of WCT tests. These evolution parameters led to a total of four different damage evolution sets of properties, of which two models were found to yield numerical ultimate loads with higher accuracy: (i) a model calibrated through a linear cohesive law and the material strength (L-σ_u); and (ii) a model calibrated through an exponential cohesive law and the cohesive stress measured through WCT fracture tests (E-σ_c). The L-σ_u models, in spite of being a more simplified methodology, yielded the overall best fit between numerical and experimental average ultimate loads; whereas the E-σ_c models yielded the best fit between numerical damage evolution and experimental crack growth, when a numerical damage threshold of $d_m^t \geq 0.5$ was considered.

Despite the reported promising results, there were also some relevant questions raised that require further research: (i) the numerical results show a different fit to the softening stage of baseline CT and WCT load *vs.* displacement curves, which may indicate some level of geometry dependency of the experimentally determined fracture toughness; (ii) the applicability of the E-σ_c models to other experimental tests, namely mechanical characterization tests, should yield overestimations of the failure loads, as the cohesive stress was found to be significantly higher than the material strength in some materials.

In order to simulate more generalized and complex cases, these two topics should be addressed in the future, (i) analytically, through a more complex damage formulation, in particular regarding different failure modes connected to transverse tension, such as matrix cracking, delamination or fibre bridging; and (ii) experimentally, by applying this methodology to a wider experimental program in terms of test configurations and geometry ranges.

4.7. References

[4.1] Barbero, E. J., Cosso, F. A., Roman, R., & Weadon, T. L., Determination of material parameters for Abaqus progressive damage analysis of E-glass epoxy laminates. *Composites Part B: Engineering*, 46, pp. 211-220, 2013.

[4.2] Girão Coelho, A. M., Toby Mottram, J., & Harries, K. A., Finite element guidelines for simulation of fibre-tension dominated failures in composite materials validated by case studies. *Composite Structures*, 126, pp. 299-313, 2015.

[4.3] Correia, J. R., Branco, F. A., Silva, N. M. F., Camotim, D., & Silvestre, N., First-order, buckling and post-buckling behaviour of GFRP pultruded beams. Part 1: Experimental study, *Computers and Structures*, 89, pp. 2052-2064, 2011.

[4.4] Laffan, M. J., Pinho, S. T., Robinson, P., & Mcmillan, A. J., Translaminar fracture toughness testing of composites: A review. *Polymer Testing*, 31(3), pp. 481-489, 2012.

[4.5] Nunes F., Silvestre N., & Correia J. R. Progressive damage analysis of web crippling of GFRP pultruded I-sections, *Journal of Composites for Construction*, 21(3), pp. 1-13, 2016.

[4.6] Almeida-Fernandes, L., Gonilha, J.A., Correia, J.R., Silvestre, N., Nunes, F., Web-crippling of GFRP pultruded profiles. Part 1: Experimental study, *Composite Structures*, 120, pp. 565-577, 2015.

[4.7] Almeida-Fernandes, L., Nunes, F., Silvestre, N., Correia, J.R., Gonilha, J.A., Web-crippling of GFRP pultruded profiles. Part 2: Numerical analysis and design, *Composite Structures*, 120, pp. 578-590, 2015.

[4.8] Martins, D., Proença, M., Correia, J.R., Gonilha, J., Arruda, M., Silvestre, N., Development of a novel beam-to-column connection system for pultruded GFRP tubular profiles, *Composite Structures*, 171, pp. 263-276, 2017.

[4.9] Lapczyk, I., & Hurtado, J. A., Progressive damage modeling in fiber-reinforced materials. *Composites Part A: Applied Science and Manufacturing*, 38(11), pp. 2333-2341, 2007.

[4.10] Xin, H., Mosallam, A., Liu, Y., Xiao, Y., He, J., Wang, C., Jiang, Z., Experimental and numerical investigation on in-plane compression and shear performance of a pultruded GFRP composite bridge deck, *Composite Structures*, 180, pp. 914-932, 2017.

[4.11] Li Z., Khennane A., Hazell P.J., Brown A.D., Impact behaviour of pultruded GFRP composites under low-velocity impact loading, *Composite Structures*, 168, pp. 360-371, 2017.

[4.12] El-Hajjar R., Haj-Ali R., Mode-I fracture toughness testing of thick section FRP composites using the ESE(T) specimen, *Engineering Fracture Mechanics*, 72, pp. 631-643, 2005.

[4.13] Liu W., Feng P., Huang J., “Bilinear softening model and double K fracture criterion for quasi-brittle fracture of pultruded FRP composites”, *Composite Structures*, 160, pp. 1119-1125, 2016.

[4.14] Laffan, M.J., Pinho, S.T., Robinson, P., Iannucci, L., Measurement of the in-situ ply fracture toughness associated with mode I fibre tensile failure in FRP. Part II: Size and lay-up effects, *Composites Science and Technology*, 70(4), pp. 614-621, 2010.

[4.15] Almeida-Fernandes, L., Silvestre, N., Correia, J. R., Characterization of transverse fracture properties of pultruded GFRP material in tension, *Composites Part B: Engineering*, 175, 107095, 2019.

[4.16] Simulia, “Abaqus/CAE 2018”, 2018.

[4.17] Hashin, Z., Rotem, A., A fatigue criterion for fiber-reinforced materials, *Journal of Composite Materials*, 7, pp. 448-464, 1973.

[4.18] Almeida-Fernandes, L., Correia, J. R., Silvestre, N., Transverse fracture behaviour of pultruded GFRP materials in tension: Effect of fibre layup, *Journal of Composites for Construction*, 24(4), 04020019, 2020.

[4.19] Almeida-Fernandes, L., Silvestre, N., Correia, J. R., Arruda, M. R. T., Fracture toughness-based models for damage simulation of pultruded GFRP materials, *Composites Part B: Engineering*, 186, 107818, 2020.

[4.20] ISO 527:1997, "Plastics – Determination of Tensile Properties", International Organization for Standardization (ISO), Geneva, 1997.

[4.21] ASTM D5379-05, "Standard test method for shear properties of composite materials by the V-notched beam method", West Conshohocken, Pennsylvania, ASTM, 2000.

[4.22] ASTM E399-90, "Standard test method for plane-strain fracture toughness of metallic materials", ASTM, Annual Book of ASTM Standards, 1993.

[4.23] Jose, S., Ramesh Kumar, R., Jana, M. K., Venkateswara Rao, G., Intralaminar fracture toughness of a cross-ply laminate and its constituent sub-laminates, *Composites Science and Technology*, 61(8), pp. 1115-1122, 2001.

[4.24] Pinho, S. T., Robinson, P., & Iannucci, L., Fracture toughness of the tensile and compressive fibre failure modes in laminated composites, *Composites Science and Technology*, 66(13), pp. 2069-2079, 2006.

[4.25] Laffan, M. J., Pinho, S. T., Robinson, P., Iannucci, L., Measurement of the in-situ ply fracture toughness associated with mode I fibre tensile failure in FRP. Part I: Data reduction, *Composites Science and Technology*, 70(4), pp. 606-613, 2010.

[4.26] Pappas, G., Botsis, J., Intralaminar fracture of unidirectional carbon/epoxy composite: experimental results and numerical analysis. *International Journal of Solids and Structures*, 85-86, pp. 114-124, 2016.

[4.27] Bergan, A., Dávila, C., Leone, F., Awerbuch, J., Tan, T.M., A mode I cohesive law characterization procedure for through-the-thickness crack propagation in composite laminates, *Composites Part B: Engineering*, 94, pp. 338-349, 2016.

[4.28] Ortega, A., Maimí, P., González, E. V, Trias, D., Specimen geometry and specimen size dependence of the R -curve and the size effect law from a cohesive model point of view, *International Journal of Fracture*, 205, pp. 239-254, 2017.

[4.29] Gonzáles, L., Knauss, W.G., Scaling global fracture behavior of structures-sized laminated composites. *International Journal of Fracture*, 118(4), pp. 363-394, 2002.

[4.30] Joki, R.K., Grytten, F., Hayman, B., Sørensen, B.F., Determination of a cohesive law for delamination modelling - accounting for variation in crack opening and stress state across the test specimen width, *Composites Science and Technology*, 128, pp. 49-57, 2016.

[4.31] IBM, "SPSS statistics", version 24, 2016.

[4.32] Li, S., Thouless, M.D., Waas, A.M., Schroeder, J.A., Zavattieri, P.D., Use of a cohesive-zone model to analyze the fracture of a fiber-reinforced polymer-matrix composite, *Composites Science and Technology*, 65, pp. 537-549, 2005.

[4.33] Duarte, A.P.C., Díaz Sáez, A., Silvestre, N., Comparative study between XFEM and Hashin damage criterion applied to failure of composites, *Thin Walled Structures*, 115, pp. 277-288, 2017.

[4.34] Lopes, B., Arruda, M.R.T., Almeida-Fernandes, L., Castro, L., Correia, J.R., *Assessment of Mesh Dependency in the Numerical Simulation of Compact Tension Tests*, CERIS Report, November, 33, 2019.

Chapter 5. Transverse compressive fracture behaviour of pultruded GFRP materials

5.1. Introduction

After successfully characterizing transverse tensile fracture phenomena in pultruded glass fibre reinforced polymer (GFRP) materials, as reported in Chapters 3 and 4, the present chapter addresses the characterization of their transverse compressive fracture behaviour [5.1]. This was a required step to enable the FE numerical simulation of structural cases with transverse compressive loads, as performed in Chapter 7 for web-crippling.

The compressive fracture properties of pultruded GFRP profiles are still very poorly characterized [5.2-5.6]. This fact stems from the complex damage propagation mechanisms that develop under compressive loads, encompassing fibre kinking, delamination, post-failure contact and their interaction. Research efforts have been put forth on studying these various failure modes and their relevance on compressive properties of GFRP materials [5.5, 5.6]. However, there is still very limited information on their compressive fracture properties. This absence constitutes a severe limitation to the reliable use of advanced computational simulations in assessing the strength of GFRP structures or components, thus hindering their widespread use in engineering design practice. For instance, the failure of beam-to-column connections [5.7] and web-crippling of beams [5.8-5.10] cannot be correctly predicted through currently available stress-based criteria. Often, the validation of these computational models requires a trial-and-error adoption of GFRP fracture properties to match the experimental ultimate strength of a given structure or component, which is a cumbersome approach.

The transverse tensile fracture properties of composites have been extensively characterized, mostly for carbon FRP (CFRP) laminates [5.4, 5.6, 5.11, 5.12] and, to some extent, pultruded GFRP materials [5.13-5.16]. Currently, a consistent basis for the assessment of fracture properties exists for tensile loading, but not for compressive loading. This discrepancy may be explained by two factors: (i) as mentioned, the compressive failure mode is more complex than the tensile one, comprising different damage mechanisms [5.4, 5.5]; and (ii) the inadequacy of tensile fracture toughness procedures and techniques when applied to compression [5.3, 5.4]. This inadequacy results from the fact that tensile damage involves crack opening and separation of damaged fronts, while compressive damage involves crushing and continued contribution of the damaged fronts in contact, which lead to residual strength [5.3-5.5] and to an overestimation of fracture properties.

This chapter presents a study on the transverse compressive fracture toughness (G_2^-) and transverse compressive residual strength (σ_r) of pultruded GFRP materials. An experimental study was conducted, based on Compact Compression Tests (CCT)[2], which were coupled with data reduction methods to determine the experimental estimates of energy release rate throughout each test. As fracture tests were expected to overestimate the transverse compressive fracture toughness directly (through data reduction methods, due to contact stresses behind the notch tip), the load *vs*. displacement results were used in an inverse methodology to calibrate the relevant damage parameters and thus establish an estimate of the

---

[2] This nomenclature was used to avoid the overlap between the typical abbreviations of compliance calibration and compact compression tests.

fracture properties [5.17, 5.18]. Therefore, the experimental load *vs*. displacement curves were fitted with numerical results, in order to determine numerical estimates of G_2^-. The aforementioned contact stresses were also taken into account in the calibration of the numerical models, by considering a residual stress for transverse compression. A bilinear cohesive law [5.19] with an initial softening stage (beyond the maximum load) was adopted, followed by a constant σ_r plateau. Therefore, two main parameters were considered in the numerical calibration procedure: (i) G_2^- and (ii) σ_r. These parameters were calibrated for six different pultruded GFRP materials in order to obtain the best fit between experimental and numerical load *vs*. displacement curves and to investigate the influence of varying the fibre reinforcement in those parameters. To this end a user defined material (UMAT) subroutine was developed within the framework of *Abaqus* software [5.20].

5.2. Experimental study

5.2.1. Materials

The present study addressed a total of six polyester based pultruded GFRP materials that have been previously studied in regard to their transverse tensile fracture toughness, as detailed in [5.15, 5.16] (see Chapters 3 and 4). The pultruded GFRP materials were taken from: I-sections of Fiberline Composites (F), Creative Pultrusions (C), Alto Perfis Pultrudidos (A) and STEP (S), a plate from Alto and a U-section from STEP. The material was labelled as follows: (i) section geometry, "I"-section, "U"-section or pultruded plate (P); (ii) profile height or plate width; and (iii) supplier initials. In the experimental programme presented ahead, each material was tested through a minimum of four specimens. The material mechanical properties are summarized in Table 5.1, including longitudinal (1) and transverse (2) properties, for tensile (+) and compressive (-) loading.

The I150-A material was considered in this study, as mechanical characterization tests showed less scatter for compressive properties than tensile properties. This profile had been previously disregarded, in the numerical study of Chapter 4, due to concerns about the potential influence of production defects (low fibre-matrix bond) found in a previous batch, as discussed in Chapter 3.

Table 5.1: Average geometric and mechanical properties of the various pultruded GFRP materials.

Material	Wall thick., t [mm]	Layup	Trans. Reinf. %*	E_{11}^- [GPa]	E_{22}^+ [GPa]	E_{22}^- [GPa]	G_{12} [GPa]	σ_{u11}^+ [MPa]	σ_{u22}^+ [MPa]	σ_{u22}^- [MPa]	τ_{u12} [MPa]
I150-A	8.1	W	4.5	44.0	9.6	7.8	3.1	384	45	60	48
P300-A	5.3	W	12.3	33.7	12.2	15.1	5.4	258	71	135	82
I152-C	6.3	Q	29.7	24.6	10.3	10.9	4.0	416	121	104	65
I200-F	9.9	W	8.3	29.9	11.9	10.8	2.9	323	71	122	67
I150-S	8.1	CFM	0.0	28.1	5.5	9.3	3.2	377	34	123	70
U150-S	7.7	Q	20.0	25.8	5.8	6.5	4.2	347	70	84	71

* considering 90° and 45° (multiplied by $\sqrt{2}/2$) oriented layers; CFM layers were disregarded.

As detailed in Chapter 3, these GFRP materials can be divided in respect to their transverse reinforcements into three main fibre layup categories: (i) unidirectional layups where the transverse reinforcements are made of continuous filament mats (CFM), with randomly oriented fibres, which provide a low reinforcing effect in all directions; (ii) cross-ply materials, transversely reinforced through woven layers with fibres oriented at 0° and 90° in respect to the roving direction (W[0/90]); and (iii) quasi-isotropic layups, reinforced through ±45° and 90° oriented layers (Q). These layups are also identified in Table 5.1, leading to different percentages of transverse reinforcement. These percentages were based on calcination tests (procedure detailed in Chapter 3), considering only 90° and 45° (multiplied by $\sqrt{2}/2$) oriented layers.

The compressive mechanical properties reported for these materials were based on compressive coupon tests. These tests were conducted using a combined load in compression (CLC) test setup, following the specifications of the ASTM D6641M – 09 standard [5.21]. Further details are provided in Chapter 3.

5.2.2. Specimen geometries

After preliminary tests conducted on both (i) CCT specimens with 60 mm of width and (ii) Wide Compact Compression tests (WCCT) with 120 mm of width, several unintended failure modes were detected and thus a scaled-up CCT specimen geometry was implemented with a nominal width of 120 mm. This geometry, detailed in Figure 5.1, contributed to reduce the shear-out failure at the loading holes and enabled the development of significant damage propagation lengths. Given these results, this scaled-up CCT geometry was adopted for all materials. In general, a total of six specimens were tested for each material.

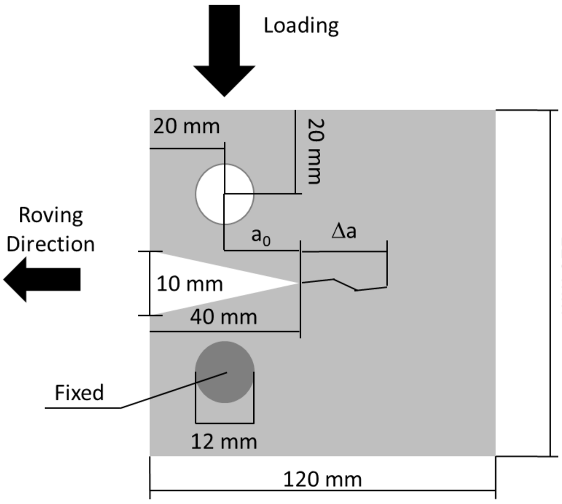

Figure 5.1: Scaled-up CCT specimen geometry.

5.2.3. Test setup

Similarly to experimental tests detailed in Chapters 3 and 4, the specimens were painted with white matte paint and targets were inserted for photogrammetry, using a black marker pen. A video-extensometry equipment (Sony camera, model XCG 5005E with Fujinon lens) with a resolution of 5 MP, a data acquisition rate of 10 Hz and an image acquisition of 1 FPS was used to monitor these targets. This methodology was implemented to monitor the crack mouth closing displacement (CMCD), the crack tip closing displacement (CTCD) and damage propagation (Δa). This last parameter was also monitored through a digital microscope, (Dino-Lite Edge Digital USB Microscope, model AM7915MZT) with a resolution of 5 MP and a maximum frame rate of 30 FPS, facing the posterior face of the specimen. The experimental tests were conducted at a displacement rate of 1.0 mm/min and the measurements are schematically illustrated in Figure 5.2.

5.2.4. Data reduction

A similar approach was considered in regard to previous studies conducted on tensile fracture tests [5.15, 5.16, 5.22, 5.23] (see Chapters 3 and 4), the finite element-based J-integral method was implemented. This method consists of developing a series of numerical models with increasing pre-defined (imposed) damage lengths and having a unit load (1 N) applied. The energy release rate measured in these models is then computed as a function of damage propagation length and experimental applied load [5.4, 5.11, 5.15]. These numerical models are similar to those reported in Chapters 3 and 4, having S4R shell elements and an average mesh size of 0.5 mm. The boundary conditions were applied to the loading holes through a "Coupling" constraint. The J-integral estimates for each damage propagation increment were determined through the "Crack" tool, propagated to each new length by using the "Seam" tool. This methodology has been widely validated for tensile fracture tests [5.4, 5.11], but has been deemed unsuitable for compressive fracture tests [5.3, 5.4] as it neglects the aforementioned contact stresses behind the notch tip that lead to overestimations of G_2^-. Therefore, the experimentally determined energy release rate results presented in the following section should be taken as overestimations of G_2^-. This trend will be further established by comparing such J-integral based predictions of G_2^- to the numerically calibrated results presented in Section 5.4.

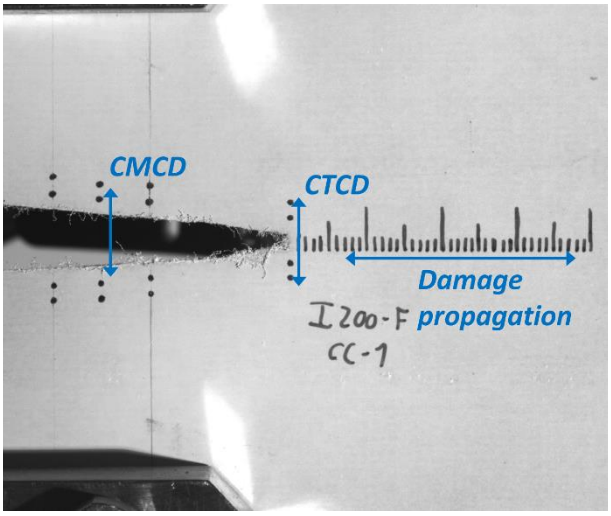

Figure 5.2: CCT video-extensometry measurements.

It should be highlighted that these models are perfectly elastic and they do not aim to simulate the fracture tests, but only the variation of the J-integral estimates for different pre-defined (imposed) damage propagation lengths. In order to simulate the fracture tests, a non-linear damage formulation is required, as detailed in Section 5.3.

5.2.5. Experimental results

5.2.5.1. Failure modes

Due to compressive stresses, all specimens showed initial damage at the notch tip, which propagated in the shape of a kink band associated with interlaminar delamination. After some damage propagation that varied quantitatively across different materials, two main failure modes were reported: (i) buckling failure during the softening stage, which occurred at a stable rate; and (ii) failure due to transverse tensile stresses at the posterior face of the specimen, which was brittle. Figure 5.3 presents an example of compressive damage growth (kink band), buckling failure and tensile failure. The specimens P300-A, I152-C and U150-S presented predominantly buckling failure, while specimens I200-F, I150-A and I150-S exhibited clear signs of tensile failure. Regarding the data reduction process, all measurements were stopped as soon as one of these failure modes was noticeable. Note that tensile failure occurred in those specimens with lowest ultimate transverse tensile stresses (I150-A and I150-S) and highest thickness (I200-F). The other specimens showed evidence of out-of-plane bending during the softening stage, after significant damage propagation had developed.

5.2.5.2. Load vs. CMCD curves

Figure 5.4 presents a summary of load *vs*. CMCD curves, including experimental observations of tensile damage initiation. A similar trend can be found across all materials (except one): initial linear path to the peak (ultimate) load, followed by a nonlinear descending branch and a final softening stage. The exception was I200-F, which showed a slight load drop after the linear path and then recovered in a non-linear trend up to the peak load. This behavioural aspect was attributed to delamination, a phenomenon that is more relevant in thicker materials, such as I200-F (9.9 mm).

Figure 5.4 also highlights a significant variability across different materials, which is in line with the geometry and material properties reported in Table 5.1. This variability is highlighted in the average ultimate load results, which vary from 7.5 kN (P300-A) to 13.0 kN (I200-F), as well as in the softening stages of different materials. It is noticeable that there is a high consistency in stiffness and ultimate load for each material, the exception being I150-S (in this case, two specimens presented larger initial notch lengths and thus presented lower stiffness and ultimate load). The softening slopes ahead of the ultimate load also seem to be consistent across most specimens of a given material, which is a relevant remark regarding the potential calibration of numerical models. In this regard, the I150-A and I150-S specimens were discarded because tensile failure occurred too early and prevented the development of relevant compressive damage lengths. This trend can be observed in Figures 5.4 (b) and (e), where tensile damage initiation occurs in the beginning of the softening stage. Furthermore, Figure 5.4 (e) presents sudden load drops caused by tensile damage in I150-S load *vs*. CMCD curves. Some load drops led to odd readings of data (illustrated in Figure 5.4 (e)), due to the brittle nature of failure and possibly due to the relatively low data acquisition rate (10 Hz).

5.2.5.3. Fracture toughness results

Figure 5.5 presents energy release rate (G) *vs*. CTCD curves for each material. It is noticeable that all materials presented a significant scatter among the various specimens. This scatter was attributed to the complexity of the damage propagation process and to the delamination near the notch tip (kink band), which hindered an accurate and objective measurement of damage propagation. The high scatter, aside from the issue of contact between notch faces, invalidated potential measurements of an initial cohesive stress that could be compared to the material strength, similarly to what was performed in regard to tensile fracture tests (see Chapter 3).

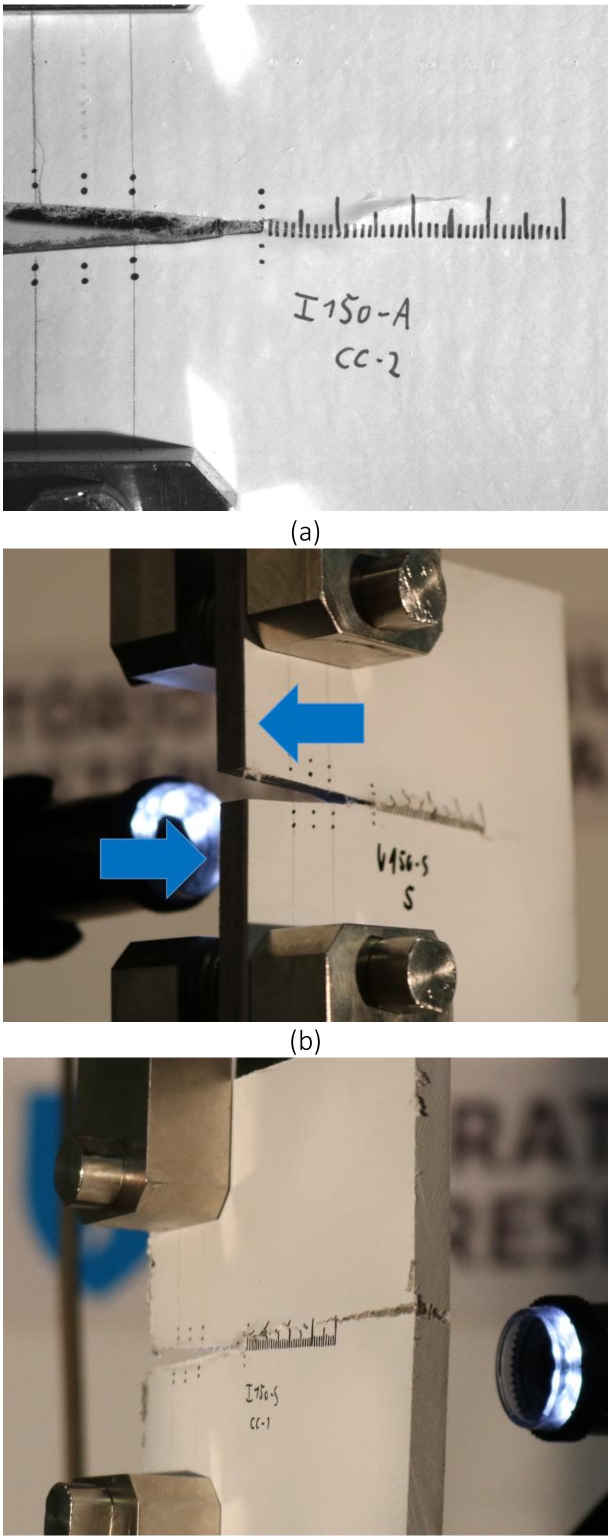

(a)

(b)

(c)

Figure 5.3: CCT failure modes: (a) compressive damage propagation; (b) buckling failure; (c) tensile failure.

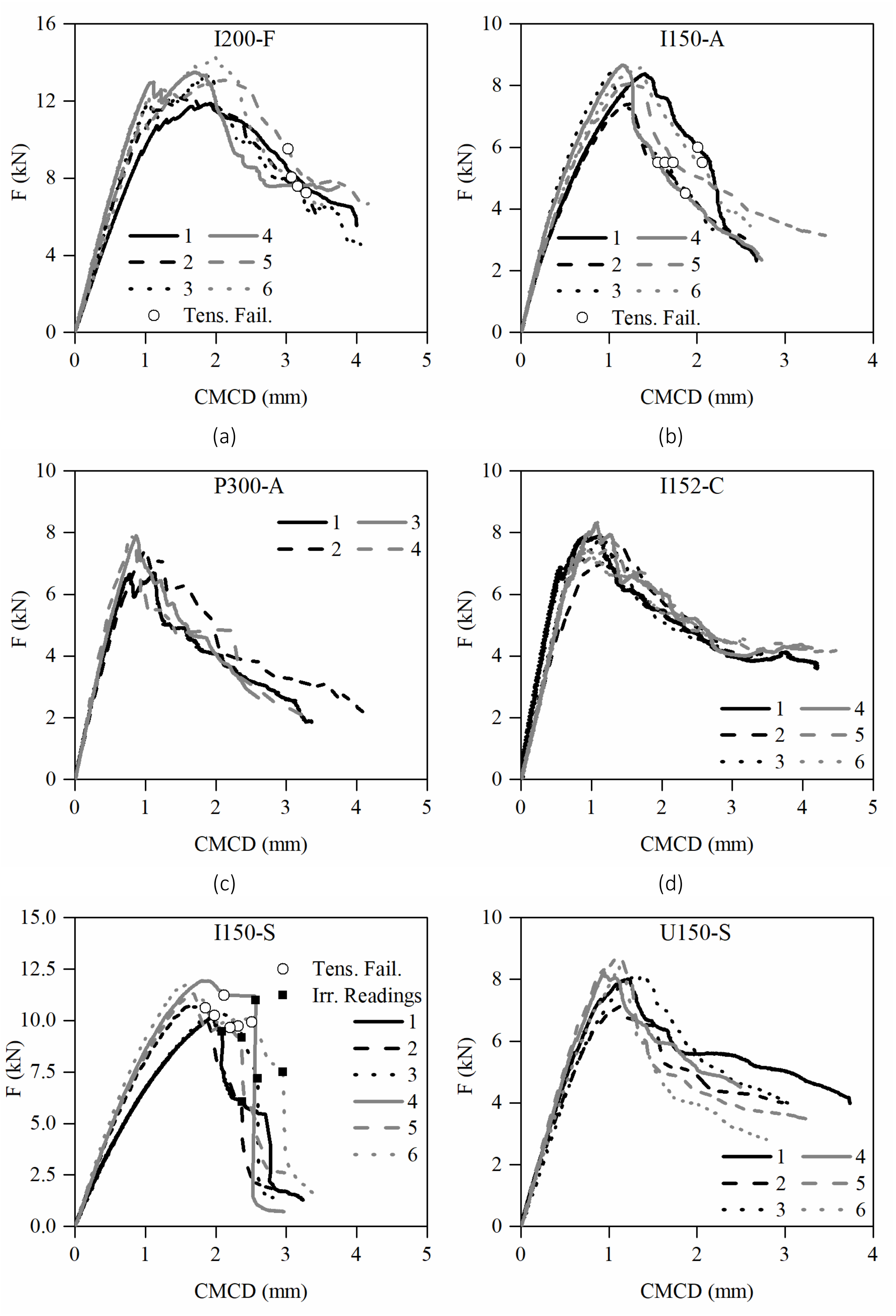

(a) (b)

(c) (d)

(e) (f)

Figure 5.4: Experimental CCT load *vs*. CMCD curves (tensile failure is circled and irregular readings are displayed with square symbols): (a) I200-F; (b) I150-A; (c) P300-A; (d) I152-C; (e) I150-S; (f) U150-S.

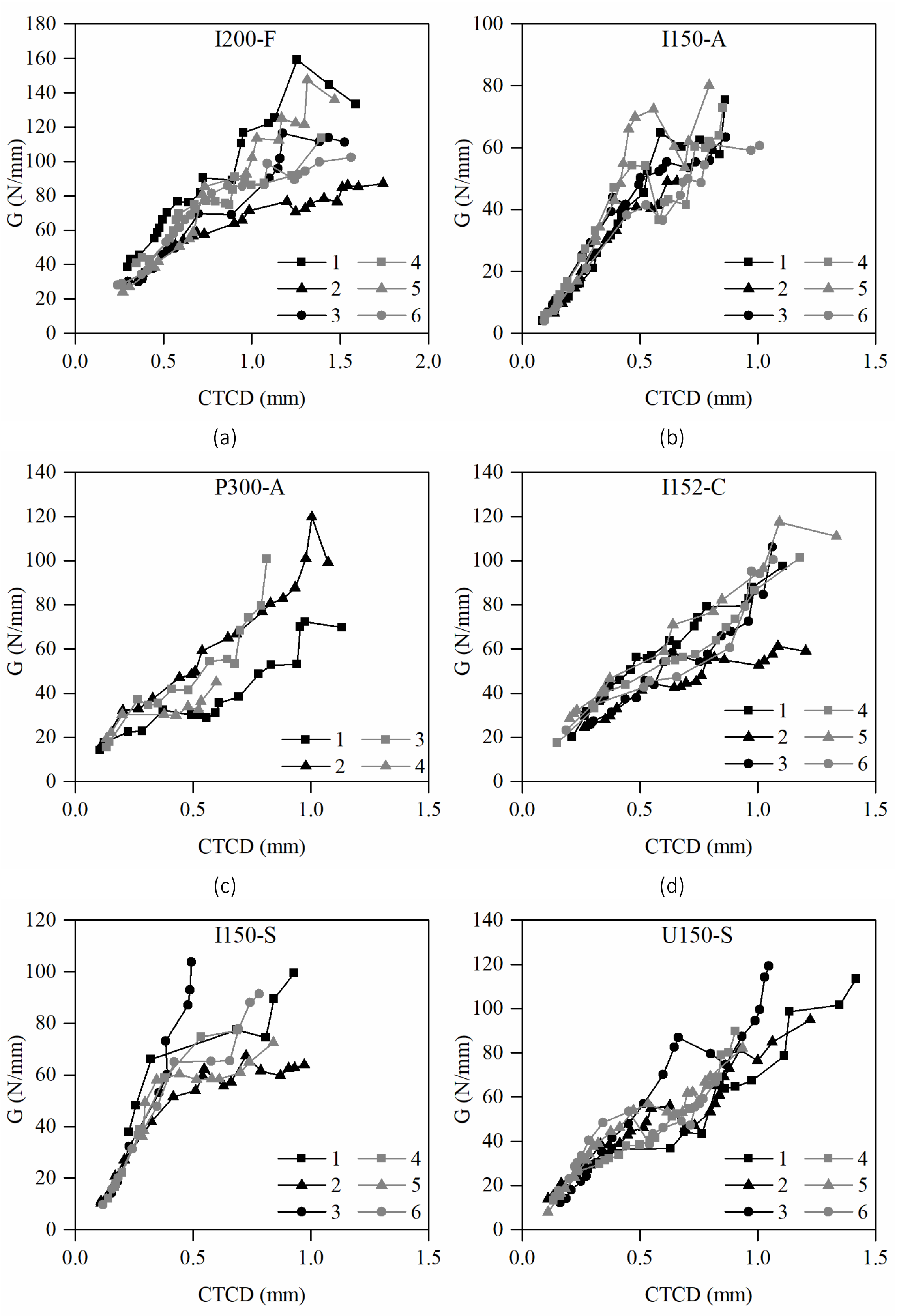

(a) (b)

(c) (d)

(e) (f)

Figure 5.5: FE J-integral based G_2^- *vs*. CTCD curves: (a) I200-F; (b) I150-A; (c) P300-A; (d) I152-C; (e) I150-S; (f) U150-S.

5.3. Numerical study

5.3.1. Geometry and boundary conditions

The geometry adopted for the modelled specimens is that displayed in Figure 5.1. The initial notch length (a_0) matched the average value measured for each material, instead of the nominal value of 40 mm. Initially, the semi-circular notch tip with a radius of 2 mm was inserted, like that of test specimens (Figures 5.6 (a)-(b)). However, preliminary simulations showed that the severe distortion caused to the element mesh surrounding the notch tip led to earlier onsets of damage propagation and, therefore, to lower ultimate loads. Alternatively, a triangular notch tip was implemented, as illustrated in Figure 5.6 (c), which led to a more uniform element mesh and thus to higher ultimate loads.

The boundary conditions were applied at the loading holes (see Figure 5.1). The centre of each loading hole was connected to the relevant half-circumference through the "Coupling" tool, in order to mimic the experimental test. One loading hole was restrained in terms of horizontal and vertical displacements, whereas the other was restrained horizontally and had an imposed vertical displacement. The imposed displacements followed the CMCD monitored for each experimental series. Because the out-of-plane buckling is an inherent phenomenon of the test and does not play a role at the material characterization level, it was not simulated.

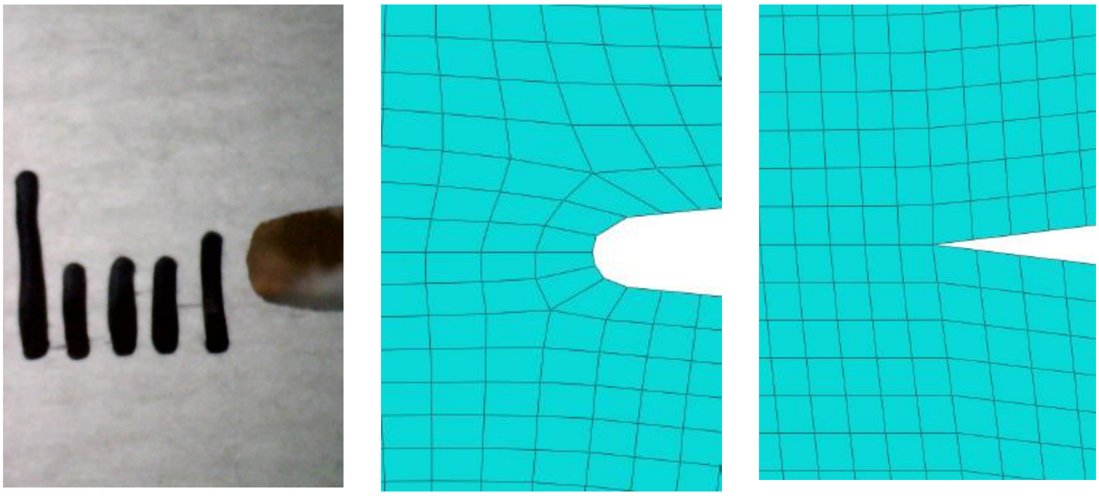
(a) (b) (c)

Figure 5.6: Initial notch tip shapes: (a) I200-F-1 specimen; (b) numerical model with round notch; (c) numerical model with triangular notch.

5.3.2. Material properties and damage

The material properties implemented in the numerical models are those reported in Table 5.1, considering the compressive elastic modulus for the transverse direction (E_{22}^-). Regarding fracture properties, the longitudinal fracture toughness parameters (G_1^+ and G_1^-) were set to 100 N/mm [5.24] and should have no influence on the results (no test showed signs of damage propagation in the longitudinal direction). The transverse tensile fracture toughness (G_2^+) was defined in accordance to the results detailed in Chapters 3 and 4 of this thesis (Table 5.2). These values are particularly relevant in case of tensile failure modes (I200-F, I150-A and I150-S). The cohesive stresses (σ_c) for transverse tensile loading, determined by assessing the G_2^+ *vs*. crack tip opening displacement (CTOD) initial slopes, are also displayed in Table 5.2. It is noteworthy that I150-A is the only material to present $\sigma_c < \sigma_{u22}^+$.

The transverse compressive fracture toughness (labelled as G_2^-) was calibrated as a function of the experimental ultimate loads, considering a range from 0 to 70 N/mm. Finally, the residual stress that results from the contact between notch faces was calibrated for the fitted G_2^- results, as a function of the experimental softening slopes.

Table 5.2: Experimental transverse tensile fracture toughness and cohesive stress results.

Material	I200-F	I150-A	P300-A	I152-C	I150-S	U150-S
G_2^+ [N/mm]	20.2 ± 2.5	13.6 ± 2.2	21.3 ± 3.0	160.0*	9.9 ± 0.9	25.8 ± 3.1
σ_c [MPa]	80	32	132	184	41	86

* as a stable propagation stage was not reached, this value was considered as a conservative estimate.

Damage initiation was determined through the Hashin criterion [5.25]. Damage evolution was implemented through a UMAT subroutine, so that the typical linear law implemented in *Abaqus* [5.20] could be modified. A bilinear cohesive law based on previous studies [5.18, 5.19] was implemented, as illustrated in Figure 5.7. The following customized cohesive law (Figure 5.7) was defined:

- Descending path:

$$\sigma_r = x\sigma_{eq}^0; \quad 0 \le x \le 1; \quad k_r = (1-d_r)k_{eq} \quad k_{eq} = \frac{\sigma_{eq}^0}{\delta_{eq}^0} \tag{5.1}$$

- Point A:

$$\begin{cases} \sigma_r = (1-d_A)k_{eq}\delta_{eq}^A = (1-d_A)\dfrac{\delta_{eq}^A}{\delta_{eq}^0}\sigma_{eq}^0 = x\sigma_{eq}^0 \\ (1-d_A) = \dfrac{\delta_{eq}^0\left(\delta_{eq}^u - \delta_{eq}^A\right)}{\delta_{eq}^A\left(\delta_{eq}^u - \delta_{eq}^0\right)} \end{cases} \Rightarrow \delta_{eq}^A = \delta_{eq}^u - x\left(\delta_{eq}^u - \delta_{eq}^0\right) \tag{5.2}$$

- Residual stress plateau:

$$\begin{aligned} &\sigma_{eq} = (1-d_r)k_{eq}\delta_{eq} = \sigma_r = x\sigma_{eq}^0 \\ &\Leftrightarrow (1-d_r)\frac{\sigma_{eq}^0}{\delta_{eq}^0}\delta_{eq} = x\sigma_{eq}^0 \\ &\Leftrightarrow d_r = 1 - x\frac{\delta_{eq}^0}{\delta_{eq}} \end{aligned} \tag{5.3}$$

where σ_r is the implemented residual stress, σ_{eq}^0 is the material ultimate stress, *x* is the ratio of σ_r/σ_{eq}^0, k_r is the stiffness at the residual stress plateau, d_r denotes the damage variable for the residual stress plateau, k_{eq} is the undamaged stiffness, δ_{eq}^0 is the displacement for the ultimate or cohesive stress, δ_{eq}^u is the displacement for zero stresses, if no residual stress was considered. Other than the customized cohesive law, the damage initiation and evolution expressions are similar to those implemented in *Abaqus* [5.20], as detailed in [5.22].

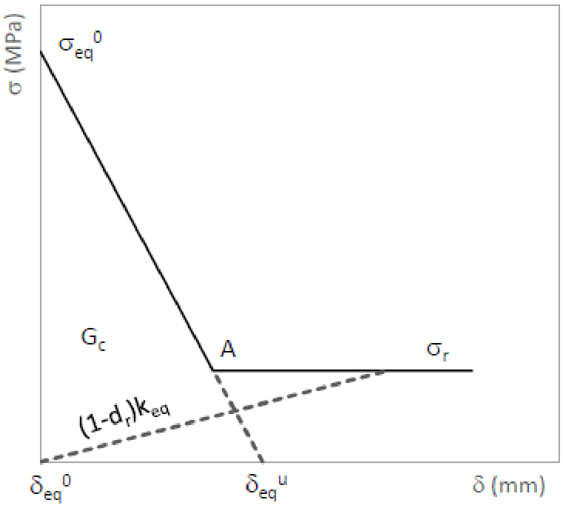

Figure 5.7: Bilinear cohesive law, with residual stress (σ_r).

5.3.3. Finite element mesh

CPS4 finite elements were used because both specimen geometry and loading are in-plane. CPS4 are bi-linear plane stress four node quadrilateral elements, with full integration (four gauss points) and three degrees-of-freedom per node. A parametric study was performed to establish the sensitivity of the results to the mesh average size. Models having meshes with 0.25, 0.5, 1.0 and 2.0 mm finite element sizes were considered for the I152-C material. In this instance, G_2^- was considered as 40 N/mm, corresponding to 25% of G_2^+ (160 N/mm). The residual stress was set to 20% (20.8 MPa) of the transverse compressive strength (σ_{u22}^-). Figure 5.8 presents load *vs*. CMCD curves for the I152-C material obtained from the numerical models with different meshes.

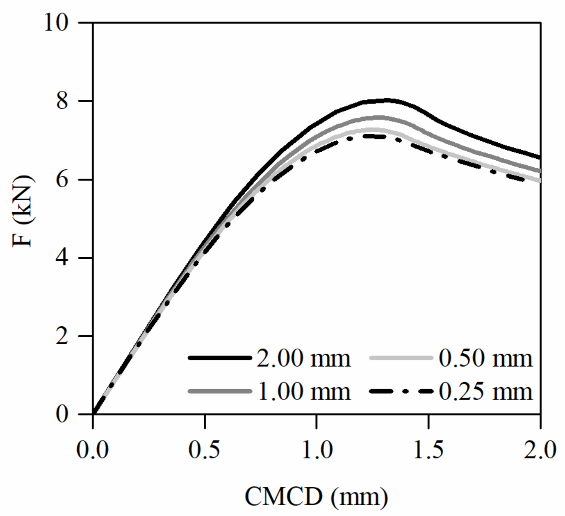

Figure 5.8: Numerical load *vs*. CMCD curves of I152-C material.

Figure 5.8 shows that there is a low sensitivity to the mesh size, as the ultimate loads appear to stabilize for 0.25 and 0.5 mm mesh sizes. These models led to significant differences regarding the number of elements for each element size, as summarized in Table 5.3. The number of elements for meshes with 0.5 mm, 1.0 mm and 2.0 mm sizes was respectively 25%, 6.3% and 1.6% of the mesh with 0.25 mm size.

Table 5.3: Characterization of I152-C FE mesh for different average FE sizes.

Finite element average size	Number of elements	Degrees of Freedom	Total CPU time (s)*	Ultimate load
2 mm	3362	7038	232	8.03
1 mm	13527	27672	3171	7.58
0.5 mm	54240	109718	18564	7.27
0.25 mm	215325	433124	123060	7.12

* Models ran in 3 parallel processors in an Intel(R) Core(TM) i7-6700K CPU @ 4.00 GHz, with 64 GB of RAM.

The 2.0 mm mesh produced an ultimate load with a relative difference of 10.5% to the 0.5 mm mesh, whereas the 1 mm mesh provided an ultimate load with a relative difference of 4.2% in comparison to the 0.5 mm mesh. As computational time is also a relevant issue, the 1.0 mm mesh was selected to run the significant number of models detailed in the following sections, as it presents a reduced relative difference to more refined models, in terms of ultimate load (≈4%), and also a moderate computational time. More details on mesh refinement of finite element models for damage of composite materials can be found in [5.22, 5.23].

5.4. Calibration of damage evolution parameters

The calibration of damage evolution parameters was conducted through a three-step procedure: (i) first, a preliminary calibration of G_2^- was made, as a function of the experimental ultimate loads F_u (Section 5.4.1); (ii) next, the G_2^- results were recalibrated as a function of experimental load *vs*. CMCD curves, and the transverse tensile ultimate stress (σ_{u22}^+) was also assessed, by considering either the material strength (Table 5.1) or the cohesive stress (σ_c, Table 5.2), being validated as a function of experimental observations of tensile damage at the posterior face of the specimen (Section 5.4.2); and, (iii) finally, the residual stresses (σ_r) were calibrated based on the softening slopes of those curves obtained from tests (Section 5.4.3). These analysis steps are illustrated in Figure 5.9. Additionally, for one profile (I150-S), the potential effect of the relative difference between the transverse compressive and tensile elastic moduli (9.3 vs. 5.5 GPa) on numerical predictions of tensile failure was assessed. This analysis was included in step (ii).

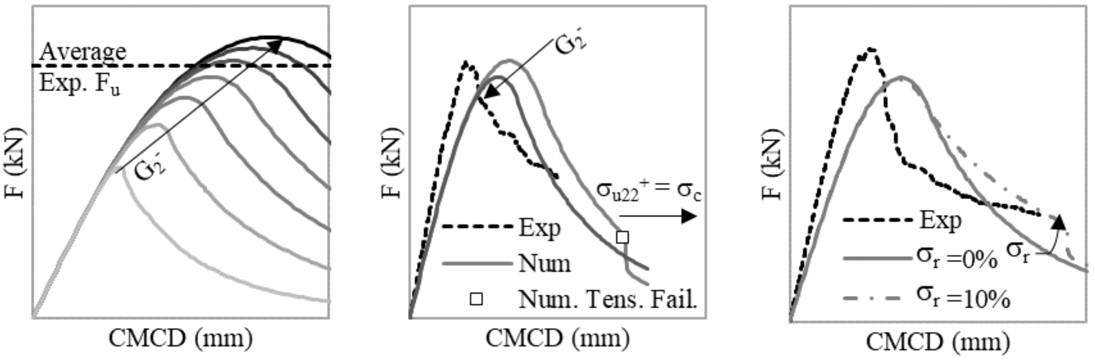

(a) (b) (c)

Figure 5.9: Numerical analysis steps: (a) calibration of G_2^- with average experimental ultimate loads; (b) calibration of G_2^- and assessment of σ_{u22}^+ based on experimental load *vs*. CMCD curves and failure modes; (c) calibration of σ_r with experimental softening slopes.

5.4.1. Ultimate loads

In the preliminary calibration of G_2^- a range between 10 and 70 N/mm was defined and, in this first stage, no residual stress was considered (σ_r=0). Figure 5.10 shows load *vs*. CMCD curves for I152-C and U150-S materials, enabling a comparison between the numerical curves with different G_2^- values and the experimental ones.

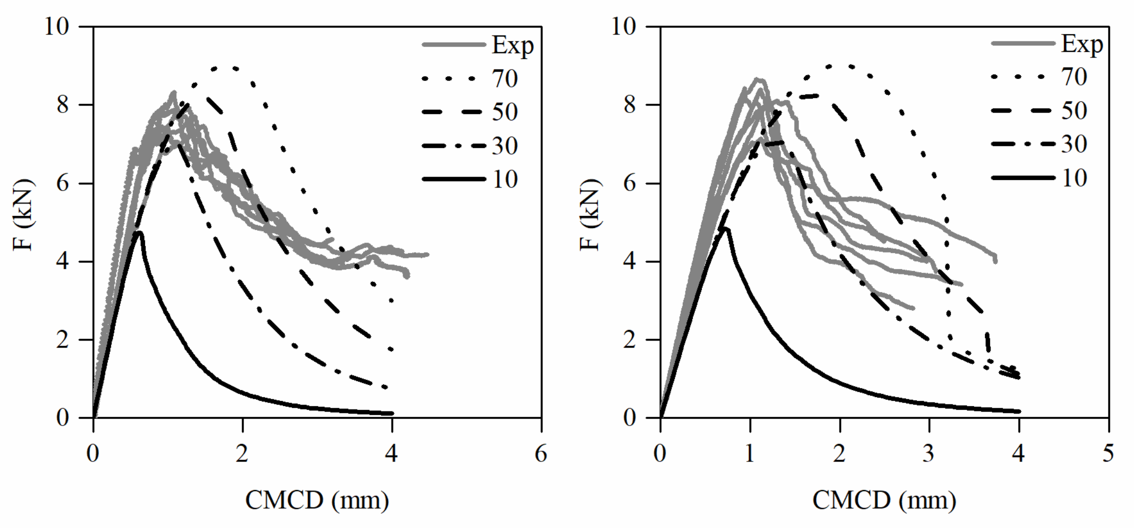

(a) (b)

Figure 5.10: Numerical and experimental load *vs*. CMCD curves, considering input values of G_2^- (N/mm): (a) I152-C; (b) U150-S.

Figure 5.10 illustrates two different scenarios: (i) the curve peak and its initial softening path for the I152-C model with G_2^- = 40 N/mm agrees fairly well with the experimental counterparts (Figure 5.10 (a)); (ii) the U150-S models seem to be unable to reproduce correctly the experimental counterparts (Figure 5.10 (b)). This is particularly noticeable for the numerical curve with G_2^- = 50 N/mm (Figure 5.10 (b)), which reaches an ultimate load similar to that of the experimental tests, but presents a significantly smoother softening path. Figure 5.11 presents the variation, with G_2^-, of the percentage relative difference between the numerical ($F_{u,num}$) and experimental ($F_{u,exp}$) ultimate loads for all materials.

Figure 5.11 illustrates two distinct trends: (i) the models I200-F, P300-A, I152-C and U150-S show the best fit to experimental results when calibrated with G_2^- values between 35 and 50 N/mm; (ii) the models I150-A and I150-S seem to tend asymptotically to the experimental results – note that increasing G_2^- progressively leads to lower increments of ultimate load. This last trend is related to the tensile failure in the models, which develops similarly to experimental tests, in the posterior face of the specimen (see Figure 5.3). This interaction was expected for these materials as they presented tensile failure modes and the lowest ultimate transverse tensile stresses (see Table 5.1). Therefore, an additional analysis was conducted for I150-A and I150-S with increased tensile properties (σ_{u22}^+=200 MPa and G_2^+=100 N/mm), in order to better establish the influence of tensile failure on the results previously presented in Figure 5.11. These new results are presented in Figure 5.12, where models with no tensile failure are labelled "NT".

Figure 5.12 shows a significant difference in the results for I150-S by disregarding the effect of tensile failure, while the results for I150-A are less affected. Through this methodology, updated values for G_2^- were determined for I150-A and I150-S materials. Estimates of G_2^- that minimize the difference between numerical and experimental ultimate loads are summarized in Table 5.4.

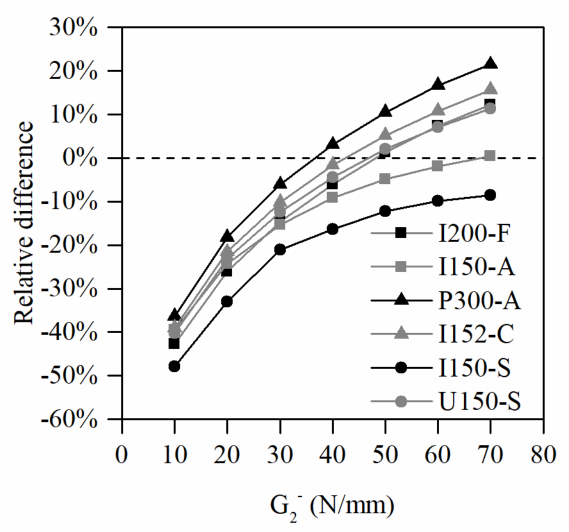

Figure 5.11: Variation, with G_2^-, of the percentage relative difference between the numerical ($F_{u,num}$) and experimental ($F_{u,exp}$) ultimate loads for all materials.

As expected, and due to the aforementioned reasons, the results summarized in Table 5.4 are significantly lower than the experimental ones presented in Figure 5.5 (experimental $G_2^- > 100$ N/mm for most materials). A fracture toughness range between ≈35 N/mm and ≈70 N/mm was determined for the pultruded GFRP materials tested under compression. These values are significantly higher than the typical values of G_2^+ (*cf.* Table 5.2), except for I152-C.

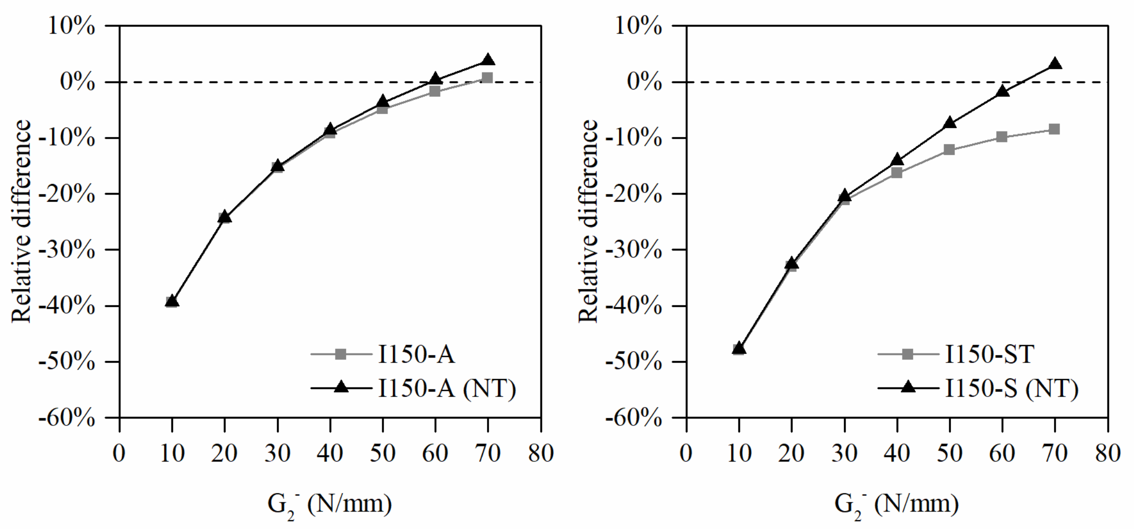

(a) (b)

Figure 5.12: Variation, with G_2^-, of the percentage relative difference between the numerical ($F_{u,num}$)and experimental ($F_{u,exp}$) ultimate loads, disregarding tensile failure: (a) I150-A; (b) I150-S.

Table 5.4: G_2^- values calibrated based on experimental average ultimate loads [N/mm].

Material	I200-F	I150-A	P300-A	I152-C	I150-S	U150-S
G_2^-	48	59	36	42	67	47

5.4.2. Load *vs*. CMCD curves

5.4.2.1. Preliminary results

In this second stage, the previously determined G_2^- values and null residual stress (σ_r) were implemented in the numerical models. Figure 5.13 presents the load *vs*. CMCD curves for all tested materials, obtained from numerical analyses (with and without consideration of tensile failure, respectively "Num" and "Num NT") and from experimental tests ("Exp"). The experimental observations of tensile damage initiation were cross marked in the experimental load *vs*. CMCD curves of Figures 5.13 (a), (b) and (e) ("ETF"). Finally, the numerical tensile failure ("NTF") was also included for the numerical results.

The preliminary results reported in Figure 5.13 show some different trends. Firstly, most numerical results agree well with experimental ones in terms of stiffness – the exceptions are the I150-A and U150-S models, which presented slightly lower stiffness compared to tests. Secondly, experimental and numerical results of both P300-A and I152-C match reasonably well (Figures 5.13 (c) and (d)), moreover as the fitting between numerical and experimental softening slopes is expected to improve by considering $\sigma_r > 0$. Thirdly, the numerical models correctly predict tensile failure for I200-F, I150-A and I150-S, however providing excessively conservative estimates of CMCD for the tensile failure of I200-F and I150-S (Figures 5.13 (a) and (e)). Additionally, the models conservatively predict the occurrence of tensile failure for P300-A (Figure 5.13 (c)), at a CMCD level where experimental tests showed no evidence of tensile failure. Finally, it should be noted that both I150-A and U150-S tests were poorly simulated by the numerical models, as the numerical load *vs*. CMCD curves present a significantly smoother softening trend in the post-peak zone, when compared to experimental curves.

5.4.2.2. Calibration

Considering the results illustrated in Figure 5.13, where some materials presented excessively conservative predictions of tensile failure (Figures 5.13 (a), (c) and (e)), the cohesive stress (see Table 5.2) was thus considered instead of the transverse tensile material strength. This increase of material transverse tensile strength should contribute to a better fit between numerical and experimental predictions of ultimate failure for the I200-F, P300-A and I150-S series. In a different trend, the lower cohesive stress of the I150-A material leads to numerical tensile failure at lower CMCD levels; however, numerical results are in good agreement with documented experimental tensile damage initiation (*cf*. Figure 5.15 (b)).

For I150-A and U150-S materials (Figures 5.13 (b) and (f)), the significantly smoother numerical softening stage seems to indicate that the G_2^- may have been overestimated. This overestimation may indicate that the σ_{u22}^- properties considered for these materials may have been experimentally underestimated. Therefore, for both these cases, the G_2^- parameter was reduced to 40 N/mm to promote a better fit between numerical and experimental load *vs*. CMCD curves; this change had the downside of introducing a higher relative difference in ultimate loads of -10% and -4%, for I150-A and U150-S, respectively (which were still deemed as acceptable).

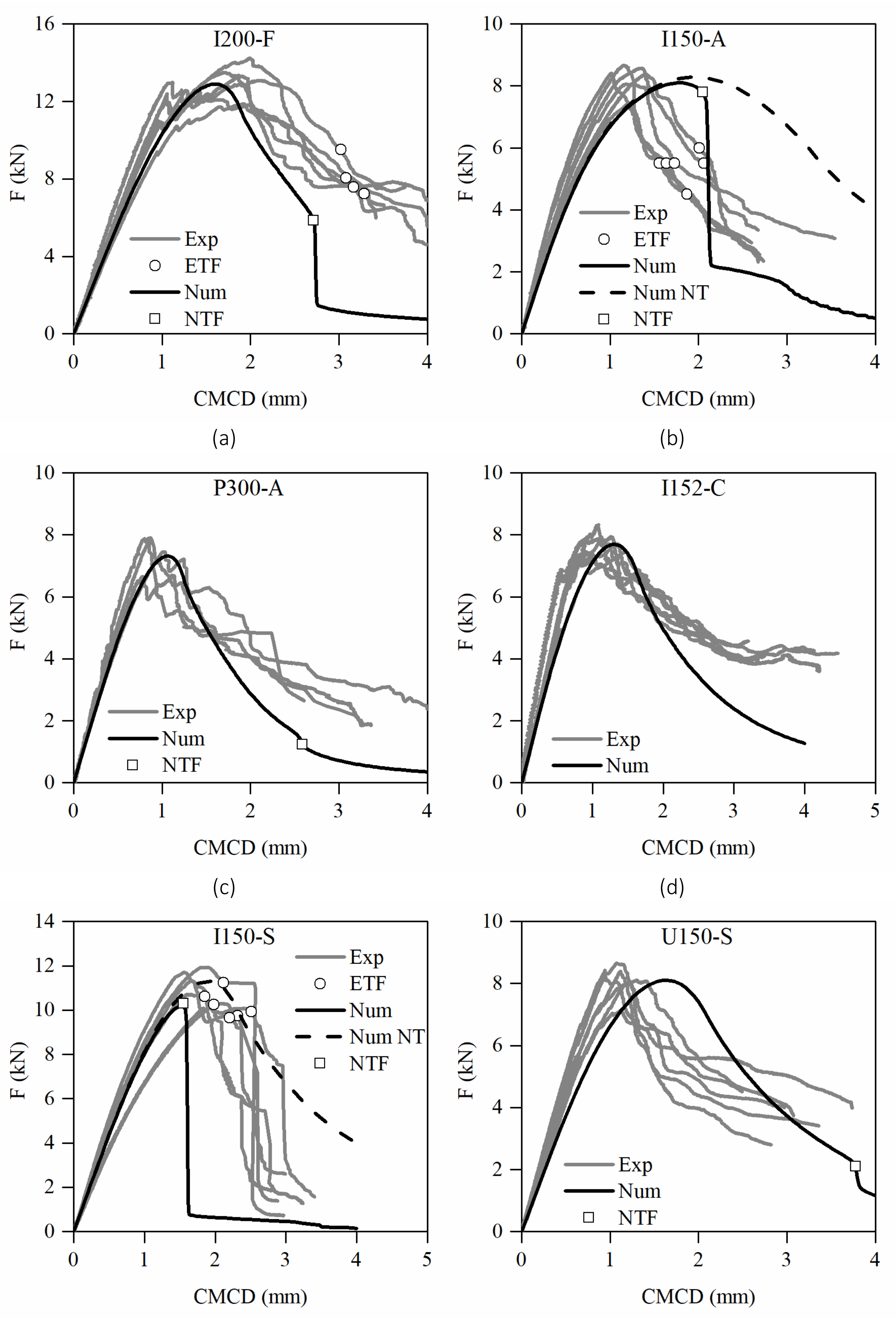

(a) (b)

(c) (d)

(e) (f)

Figure 5.13: Experimental and numerical load *vs*. CMCD curves, including experimental (“ETF”) and numerical (“NTF”) tensile damage: (a) I200-F; (b) I150-A; (c) P300-A; (d) I152-C; (e) I150-S; (f) U150-S.

Figure 5.13 (e) illustrates the impact of considering numerical tensile failure on I150-S results. The discrepancy between tensile failure predictions in numerical and experimental results was addressed by considering the tensile cohesive stress (41 MPa) instead of the material strength (34 MPa) and by analysing the difference between the transverse tensile (E_{22}^{+} = 5.5 GPa) and compressive (E_{22}^{-} = 9.3 GPa) elastic moduli. As the numerical models were developed considering the compressive elastic modulus, this may lead to a fictitious increase of tensile stresses in the posterior face of the specimens. This numerical issue was addressed through three different methods: (i) a model was developed with different and varying elastic moduli (tensile or compressive), as a function of the stress level in each element (positive or negative); (ii) in a more simplified approach, another model was sectioned to present different elastic moduli defined *a priori* in specific regions prone to compressive/tensile stresses; and (iii) finally, another model was developed with artificially increased transverse tensile strength, as a function of the elastic moduli ratio (E_{22}^{-}/E_{22}^{+}) and increased G_2^{+}, as a function of the squared elastic moduli ratio ($(E_{22}^{-}/E_{22}^{+})^2$). The first solution was achieved by adding a condition (if $\sigma_{22}>0$, then $E_{22}=E_{22}^{+}$) to the UMAT subroutine, whereas the second and third solutions were implemented through *Abaqus* built-in tools. These various solutions, which take into consideration the tensile cohesive stress and consider no residual stress, are illustrated in Figure 5.14 and compared to the initial numerical results ("Prelim.") presented in Figure 5.13 (e).

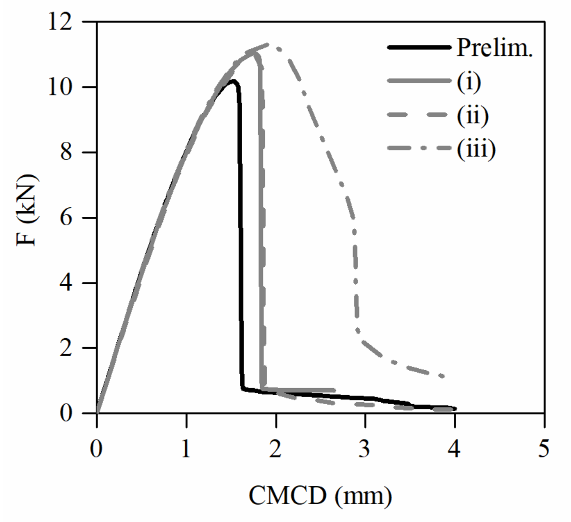

Figure 5.14: Numerical load *vs*. CMCD preliminary ("Prelim.") and calibrated curves for I150-S: (i) different and varying E_{22} as a function of σ_{22}; (ii) model sectioned to present compressive and tensile E_{22} in different regions defined *a priori*; (iii) model with increased σ_{22}^{+} and G_2^{+} properties as a function of the E_{22}^{-}/E_{22}^{+} ratio.

Figure 5.14 clearly shows that the first two solutions, which account for different elastic moduli in tension and compression, led to similar results; whereas increasing the tensile strength and fracture toughness led to an excessive increase of CMCD at brittle failure. In line with these results, the first solution, implemented in the UMAT, was considered to obtain the results described in the following sections.

5.4.2.3. Results from calibrated models

Figure 5.15 presents a summary of numerical and experimental load *vs*. CMCD curves, including the preliminary numerical results ("Prelim."), as well as the calibrated numerical results ("Calibrated"), as a function of the calibrations detailed in the previous section.

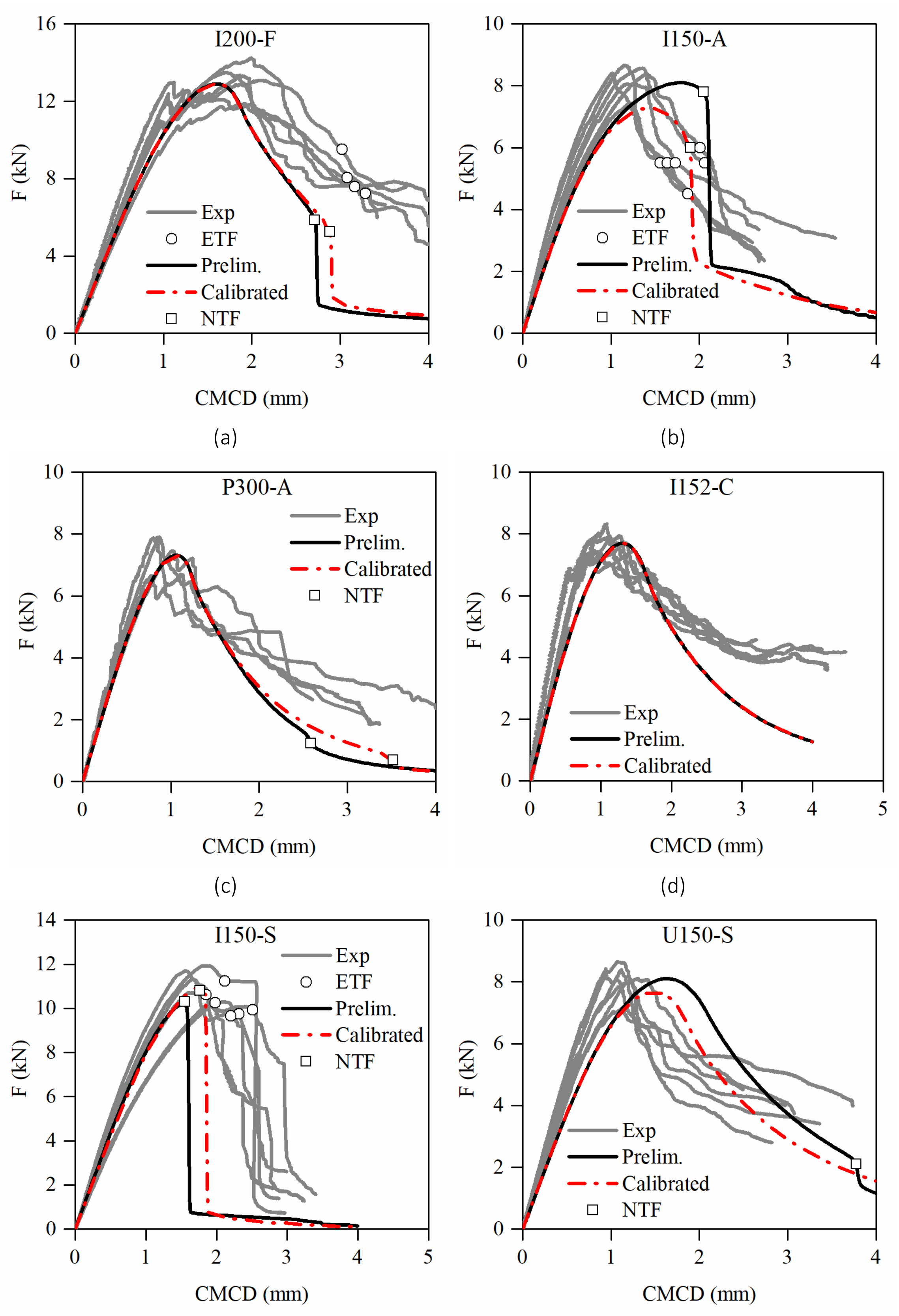

(a) (b)

(c) (d)

(e) (f)

Figure 5.15: Load *vs*. CMCD curves of experimental tests, preliminary models (“Prelim.”) and calibrated (“Calibrated”) models, including experimental (“ETF”) and numerical (“NTF”) tensile damage: (a) I200-F; (b) I150-A; (c) P300-A; (d) I152-C; (e) I150-S; (f) U150-S.

The results displayed in Figure 5.15 present a good fit between numerical and experimental load *vs*. CMCD curves, in terms of both peak loads and failure modes. As a general trend, most numerical results showed a better fit to experimental results when calibrated with the cohesive stress (*vs*. the transverse tensile strength), including I150-A results, despite being the only material where $\sigma_c<\sigma_{u22}^+$.

The experimental and numerical failure modes are compared in Figure 5.16, which illustrates specimens after failure and numerical plots of damage evolution for two distinct cases: (i) I152-C, where damage developed exclusively due to compressive stresses; and (ii) I150-S, where most specimens showed very little compressive damage propagation (≈10 to 15 mm), before tensile damage led to failure. The numerical results are presented with respect to the shear damage parameter "DAMAGESHR" in *Abaqus* built-in tools and output variable "SDV14" in the user subroutine, which is an envelope for other damage parameters [5.20, 5.25]. This variable was chosen to highlight simultaneously tensile and compressive damage.

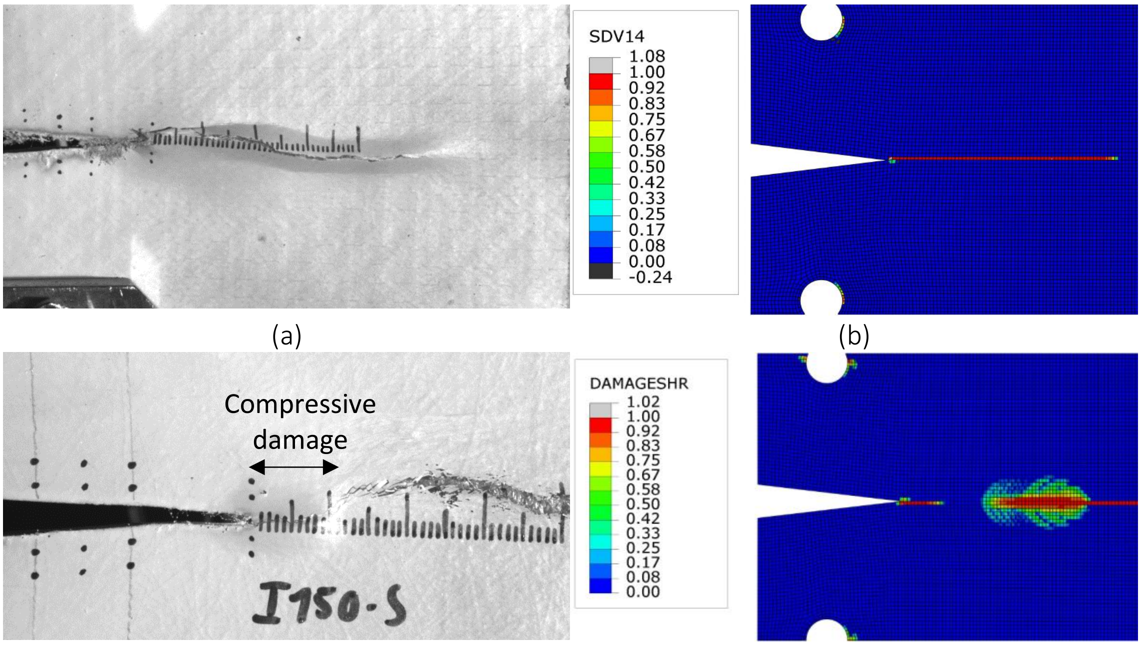

(a) (b)

(c) (d)

Figure 5.16: Experimental failure modes and numerical damage plots (shear damage parameter): (a) I152-C-1; (b) I152-C-Num (UMAT); (c) I150-S-4; (d) I150-S-Num (built-in tools).

5.4.3. Residual stress input calibration

Taking into account the models presented in the previous section, σ_r was finally calibrated to promote the best fit between numerical and experimental softening stages. Two materials were excluded from this analysis, I150-A and I150-S, as tensile failure affected the results early on, thus compromising the validity of the softening stage.

The residual stress analysis focused on the softening slope of these curves. To make this analysis more objective, the experimental curves were used to define an average softening curve. *IBM SPSS* [5.26] software was used to determine an exponential fitting law that produced the best fit to experimental curves. A three-parameter function was used for these calibrations, as follows,

$$F = a.e^{-b.CMCD} + c \tag{5.4}$$

where *a*, *b* and *c* are fitting parameters.

Figure 5.17 presents numerical and averaged experimental load *vs*. CMCD softening curves, considering different values of σ_r, defined as a fraction of σ_{u22}^-. To this end, the experimental load *vs*. CMCD curves were processed to produce an averaged softening curve, thus enabling a comparison between numerical and experimental results. Furthermore, peak load discrepancies were discarded (which are mainly affected by G_2^-, but not by σ_r) as well as stages where tensile damage had initiated. To that end, the load *vs*. CMCD curves presented in Figure 5.17 correspond to the variation of CMCD after the peak load is attained, for a load/ultimate load ratio lower than ≈95%. Therefore, with this procedure, all discrepancies between experimental and numerical results should be solely attributed to the softening slopes.

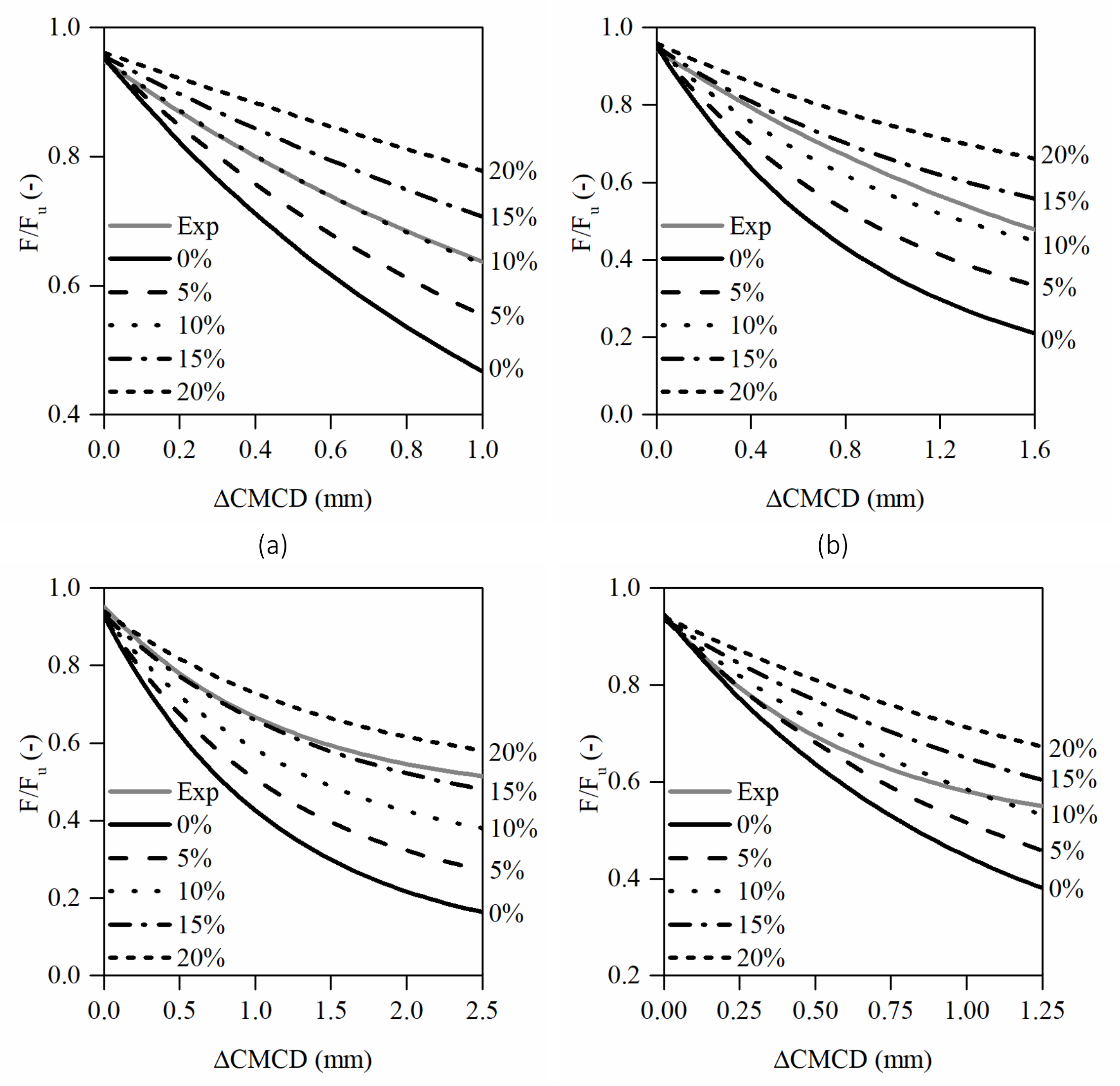

(a) (b)

(c) (d)

Figure 5.17: Experimental and numerical load *vs*. CMCD softening stages, for different σ_r/σ_{u22}^- ratios (%): (a) I200-F; (b) P300-A; (c) I152-C; (d) U150-S.

The results shown in Figure 5.17 illustrate the significant impact of σ_r on the softening stage, as expected. It is noteworthy that adequate results were obtained for all materials for a range of σ_r between 5% and 20% of σ_{u22}^-. It is also noticeable that the models for U150-S were unable to fully capture the experimental softening trend, unlike the models for the remaining GFRP materials. At this time, this is attributed to a potential overestimation of G_2^-, which led to similar ultimate load results, but also to a significantly smoother numerical softening slope near the peak load.

In order to have an objective measure of the fitting of numerical and experimental curves, the numerical softening curves were also fitted with exponential functions as described in expression (5.4). Then, the absolute difference between numerical and experimental curves could be determined. This process led to the results summarized in Figure 5.18.

Figure 5.18 highlights a narrow range between 9% and 16% for the optimal ratios between σ_r and σ_{u22}^- of the four materials analysed, which corresponds to an absolute range between 7.6 MPa (U150-S) to 16.9 MPa (P300-A). From these results, it may be concluded that material properties and fibre layups have low influence on the transverse compressive residual stress; it is possible that such parameter depends mainly on the polymeric matrix. In a different trend, the thinnest materials are those that present higher σ_r values (12.5% and 16%, for P300-A and I152-C, respectively). These results may be related to the fact that thinner materials are typically more resistant to delamination phenomena, which occurred in parallel with compressive damage propagation. Future developments should further assess these trends, so that the residual stress of a given GFRP material can be further established and linked to its geometry, material properties, fibre layup and type of polymer matrix.

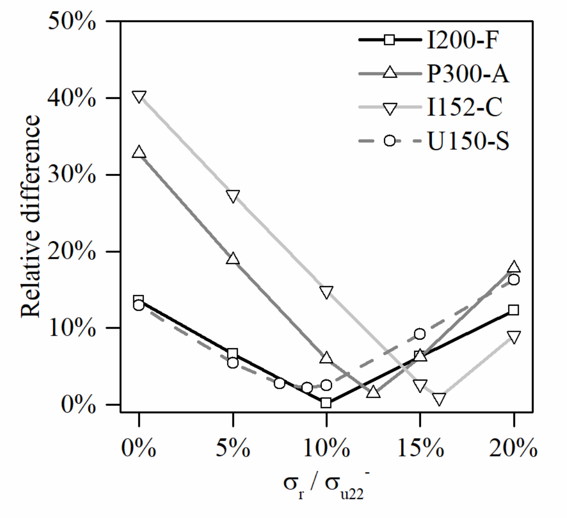

Figure 5.18: Averaged relative difference between numerical and experimental softening curves.

5.5. Comparison between G_2^- and G_2^+

This section presents a brief discussion about the ratio between compressive and tensile fracture properties, also taking into account the transverse reinforcement percentages of each material. Figure 5.19 illustrates the evolution of compressive and tensile (see Chapters 3 and 4) values of fracture toughness with the transverse reinforcement percentage, including fitting functions of these results (FF). It should be taken into consideration that the different resins used for the various materials should influence the compressive results more significantly than the tensile results, which depend foremost of the fibre structure. Despite using only polyester based materials, the exact resin compositions are unknown, and thus the analysis has been kept to the transverse reinforcement percentages and fibre layups, as presented in Table 5.1 and further detailed in Chapter 3.

Figure 5.19 (a) shows different trends between compressive and tensile fracture properties. Unlike G_2^+, which has an increasing trend with the transverse reinforcement, G_2^- presents the highest value for a material with very low transverse reinforcement, solely provided by CFM layers. The other materials present results in a narrow range (36 to 48 N/mm), with an average of 41 N/mm. Aside from one case (I152-C), all materials presented significantly higher transverse compressive fracture toughness, when compared to the transverse tensile fracture toughness.

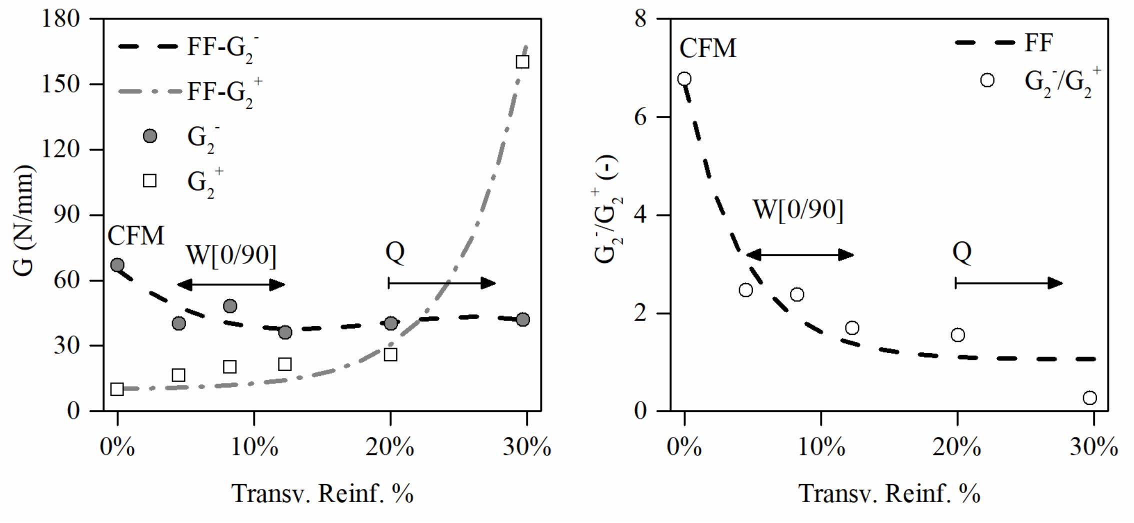

(a) (b)

Figure 5.19: Evolution of fracture toughness results for tension and compression as a function of transverse reinforcement percentages, complemented with fitting functions (FF): (a) absolute values; (b) G_2^-/G_2^+ ratio.

The ratio between transverse compressive fracture toughness and tensile fracture toughness, illustrated in Figure 5.19 (b), presents a clear decreasing trend as a function of the transverse reinforcement percentage. These results must be further validated, namely with other FRP materials with similar fibre layups, in order to assess the validity of this trend. It will also be important to compare similar layups with different polymeric resins, in order to better understand the contribution of the resin to the transverse compressive fracture behaviour of FRP materials.

5.6. Conclusions

This chapter presented a study about the transverse fracture behaviour of pultruded glass fibre reinforced polymer (GFRP) in compression, with focus on the assessment of transverse compressive fracture toughness (G_2^-) and transverse compressive residual strength (σ_r). These properties were assessed through experimental Compact Compression tests. In face of experimental overestimations of fracture toughness, obtained through standard data reduction schemes, a numerical study was conducted to determine these properties by fitting numerical and experimental load *vs.* CMCD curves. The calibration process considered two main parameters, G_2^- and σ_r, which represents the crushing of the material in the damaged area. The G_2^- values varied between 36 and 67 N/mm and the optimal σ_r values ranged from 9% to 16% of the transverse compressive strength (absolute values ranged from 7.6 to 16.9 MPa).

The numerical results showed that thinner materials have slightly higher σ_r/σ_{u22}^- ratios (12.5% and 16%, for P300-A and I152-C, respectively), when compared to thicker materials (10% and

9%, for I200-F and U150-S, respectively), which may be due to the higher proneness to delamination of the latter.

The numerical models were also validated by comparing numerical and experimental failure modes. This procedure involved additional calibration of tensile properties because several specimens presented a failure mode triggered by tensile damage at their posterior face, after compressive damage had initiated. It is noteworthy that most numerical models presented a better agreement to experimental tests when the cohesive stress, previously measured through tensile fracture tests, was considered instead of the mechanically characterized transverse tensile strength. The results also showed a significantly different variation of G_2^- with the transverse reinforcement percentage (45° and 90° oriented layers), when compared to previous results for G_2^+. The G_2^-/G_2^+ ratio was found to drop significantly with the transverse reinforcement percentage, highlighting the possible influence of the polymeric resins used in each material.

The assessment of the fracture behaviour of GFRP materials produced with similar fibre layups but different polymeric resins should be considered as a relevant future development. Finally, as this experimental campaign focused on a single test configuration, it will also be important to confirm the presented compressive fracture properties for a wider range of geometries and test configurations.

5.7. References

[5.1] Almeida-Fernandes, L., Silvestre, N., Correia, J. R., Arruda, M. R. T., Compressive transverse fracture behaviour of pultruded GFRP materials: experimental study and numerical calibration, *Composite Structures*, 247, 112453, 2020.

[5.2] Maimí, P., Camanho, P. P., Mayugo, J. A., & Dávila, C. G., A continuum damage model for composite laminates: Part II - Computational implementation and validation. *Mechanics of Materials*, 39(10), pp. 909-919, 2007.

[5.3] Ratcliffe, J., Jackson, W., & Schaff, J., Predicting the compression strength of impact-damaged sandwich panels. *American Helicopter Society 60th Annual Forum*, Baltimore, 2004.

[5.4] Pinho, S. T., Robinson, P., & Iannucci, L., Fracture toughness of the tensile and compressive fibre failure modes in laminated composites. *Composites Science and Technology*, 66(13), pp. 2069-2079, 2006.

[5.5] Pinho, S. T., Gutkin, R., Pimenta, S., De Carvalho, N. V., & Robinson, P., On longitudinal compressive failure of carbon-fibre-reinforced polymer: from unidirectional to woven, and from virgin to recycled. *Philosophical Transactions of the Royal Society A, Physical and Engineering Sciences*, 370, pp. 1871-1895, 2012.

[5.6] Laffan, M. J., Pinho, S. T., Robinson, P., & Mcmillan, A. J., Translaminar fracture toughness testing of composites: A review. *Polymer Testing*, 31(3), pp. 481-489, 2012.

[5.7] Martins, D., Proença, M., Correia, J. R., Gonilha, J., Arruda, M., & Silvestre, N., Development of a novel beam-to-column connection system for pultruded GFRP tubular profiles. *Composite Structures*, 171, pp. 263-276, 2017.

[5.8] Almeida-Fernandes, L., Gonilha, J., Correia, J. R., Silvestre, N., & Nunes, F., Web-crippling of GFRP pultruded profiles. Part 1: Experimental study. *Composite Structures*, 120, pp. 565-577, 2015.

[5.9] Almeida-Fernandes, L., Nunes, F., Silvestre, N., Correia, J. R., & Gonilha, J., Web-crippling of GFRP pultruded profiles. Part 2: Numerical analysis and design. *Composite Structures*, 120, pp. 578-590, 2015.

[5.10] Nunes F., Silvestre N., Correia J. R. "Progressive damage analysis of web crippling of GFRP pultruded I-sections", *Journal of Composites for Construction*, 21(3), pp. 1-13, 2016.

[5.11] Laffan, M. J., Pinho, S. T., Robinson, P., & Iannucci, L., Measurement of the in situ ply fracture toughness associated with mode I fibre tensile failure in FRP. Part I: Data reduction. *Composites Science and Technology*, 70(4), pp. 606-613, 2010.

[5.12] Laffan, M. J., Pinho, S. T., Robinson, P., & Iannucci, L., Measurement of the in situ ply fracture toughness associated with mode I fibre tensile failure in FRP. Part II: Size and lay-up effects. *Composites Science and Technology*, 70(4), pp. 614-621, 2010.

[5.13] El-Hajjar, R., & Haj-Ali, R., Mode-I fracture toughness testing of thick section FRP composites using the ESE(T) specimen. *Engineering Fracture Mechanics*, 72(4), pp. 631-643, 2005.

[5.14] Liu, W., Feng, P., & Huang, J., Bilinear softening model and double K fracture criterion for quasi-brittle fracture of pultruded FRP composites. *Composite Structures*, 160, pp. 1119-1125, 2016.

[5.15] Almeida-Fernandes, L., Silvestre, N., Correia, J. R., Characterization of transverse fracture properties of pultruded GFRP material in tension, *Composites Part B: Engineering*, 175, 107095, 2019.

[5.16] Almeida-Fernandes, L., Correia, J. R., Silvestre, N., Transverse fracture behaviour of pultruded GFRP materials in tension: Effect of fibre layup, *Journal of Composites for Construction*, in press.

[5.17] Ortega, A., Maimí, P., González, E. V., & Trias, D., Characterization of the translaminar fracture Cohesive Law. *Composites Part A: Applied Science and Manufacturing*, 91, pp. 501-509, 2016.

[5.18] Ortega, A., Maimí, P., Gonzales, E.V, Sainz de Aja, J. R., de la Escalera, F. M., & Cruz, P., Translaminar fracture toughness of interply hybrid laminates under tensile and compressive loads. *Composites Science and Technology*, 143, pp. 1-12, 2017.

[5.19] Zobeiry, N., Vaziri, R., & Poursartip, A., Characterization of strain-softening behavior and failure mechanisms of composites under tension and compression. *Composites Part A: Applied Science and Manufacturing*, 68, pp. 29-41, 2015.

[5.20] Simulia, "Abaqus/CAE 2018", 2018.

[5.21] ASTM D6641 / D6641M – 09, "Standard Test Method for Compressive Properties of Polymer Matrix Composite Materials Using a Combined Loading Compression (CLC) Test Fixture", ASTM International, West Conshohocken, Pennsylvania, 2009.

[5.22] Almeida-Fernandes, L., Silvestre, N., Correia, J. R., Arruda, M. R. T., Fracture toughness-based models for damage simulation of pultruded GFRP materials. *Composites Part B: Engineering*, 186, 107818, 2020.

[5.23] Lopes, B., Arruda, M.R.T., Almeida-Fernandes, L., Castro, L., Correia, J.R., *Mesh Dependency Tests for Orthotropic Continuum Damage Model*, CERIS Report, November, 33, 2019.

[5.24] Girão Coelho, A. M., Toby Mottram, J., & Harries, K. A., Finite element guidelines for simulation of fibre-tension dominated failures in composite materials validated by case studies. *Composite Structures*, 126, pp. 299-313, 2015.

[5.25] Hashin, Z., and Rotem, A., A fatigue criterion for fiber-reinforced materials, *Journal of Composite Materials*, 7, pp. 448-464, 1973.

[5.26] IBM, "SPSS statistics", 2016, version 24.

Part III

Web-crippling of pultruded GFRP profiles

Preamble

Web-crippling is a failure phenomenon caused by the application of concentrated transverse loads in the plane of the web. This is a severe structural case for pultruded GFRP profiles, as their weakest in-plane direction is parallel to the load application direction. Despite its importance, web-crippling still presents significant research needs in regard to composite materials, as very few profile sections and test configurations have been experimentally assessed to date.

Part III presents an experimental, numerical and analytical study with the goal of providing a better understanding of the web-crippling phenomenon. To this end, the data generated by a comprehensive experimental programme of web-crippling tests were used to validate finite element numerical models, providing a steppingstone for the development of novel design guidelines.

Chapter 6. Web-crippling experimental characterization

6.1. Introduction

The web-crippling failure of pultruded glass fibre reinforced polymer (GFRP) beams remains a challenging issue for structural design [6.1, 6.2]. Despite previous research efforts on this topic [6.1-6.7], available design guidelines still provide limited guidance to verify this failure mode (e.g. [6.8-6.10]). This can be attributed to (i) the inherent complexity of the web-crippling failure phenomenon, which may involve either web-crushing or web-buckling (or a combination thereof), (ii) the diversity of test configurations (i.e. load and support conditions) that may be considered and (iii) the significant influence of the bearing length (lb) on the web-crippling response of pultruded profiles [6.1, 6.6].

Web-crippling has been typically assessed through four test configurations: (i) end-one-flange (EOF), which consists of a short three-point bending test, with narrow supports at both beam extremities; (ii) end-two-flange (ETF), consisting of loading both flanges simultaneously in an end section; (iii) interior-one-flange (IOF), which is similar to EOF, but where loading is applied with a narrower bearing plate in the mid-span section; and (iv) interior-two-flange (ITF), which is similar to ETF, but where loading is applied in an interior section. In addition, some authors have considered different configurations for ground supported elements: (i) end bearing with solid ground (EG), where one flange is loaded with a narrow bearing plate in an extremity, whereas the other flange is continuously supported; and (ii) interior bearing with solid ground (IG), which is similar to EG, but where loading is applied in an interior section. These test configurations are illustrated in Figure 6.1.

Borowicz and Bank [6.1] performed experimental tests on I-section profiles and wide flange profiles, through an IOF based test configuration. The authors concluded that the implementation of bearing plates could promote a significant increase of bearing capacity. Following this study, Borowicz and Bank [6.3] investigated the use of different strengthening methods, for pultruded profiles under transverse concentrated loads, with I-section and wide flange sections. The authors concluded that strengthening systems that reinforced the web-flange junction area led to higher increases of bearing capacity, when compared to strengthening systems that reinforced only the web of the profile.

Wu and Bai [6.2] performed EG, IG, ETF and ITF tests on pultruded GFRP profiles with squared hollow sections. The authors considered the same bearing length for all tests, and a consistent failure mode was reported for all tests, consisting of web-crushing near the web-flange junction area. In a following study, Wu *et al.* [6.4] studied strengthening solutions for pultruded profiles with squared hollow sections. Web-crushing failure near the web-flange junction area was also reported for all tests and the strengthening systems were reported to provide significant increases of bearing capacity, in particular when steel channel reinforcements were implemented [6.4]. In a more recent study, Wu *et al.* [6.5] studied the behaviour of pultruded GFRP profiles, with channel sections, in ETF and ITF test configurations. Four profiles were tested, with a fixed bearing length and varied specimen lengths. The failure modes were reported to vary between web-crushing near the web-flange junction and web-buckling at the centre of the web. The authors associated a more brittle failure to specimens with a lower length and web-buckling failure to specimens with slender webs [6.5].

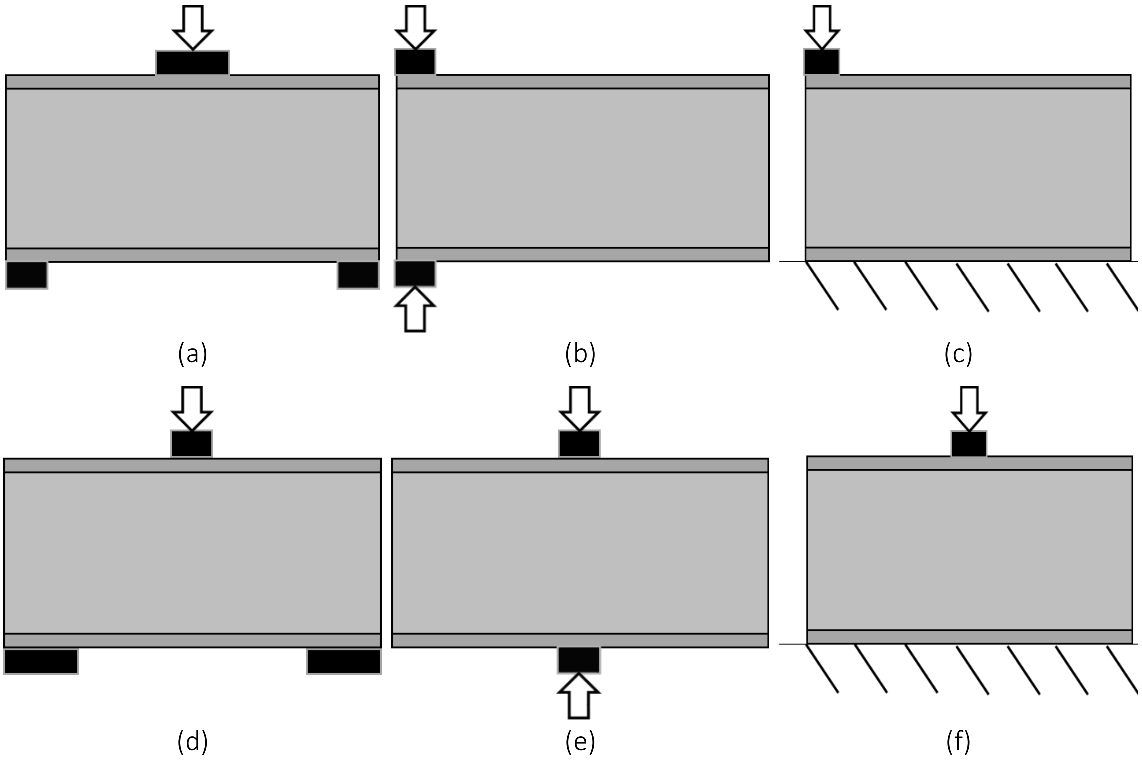

Figure 6.1: Web-crippling test configurations: (a) EOF; (b) ETF; (c) EG; (d) IOF; (e) ITF; (f) IG.

Previous research was also performed by the author of this thesis [6.6, 6.7], consisting of experimental ETF and ITF tests on I-section profiles, with varying bearing lengths [6.6], simulated through numerical models in [6.7]. The experimental tests showed that the bearing length had a significant impact on the stiffness and ultimate load results. The experimental studies detailed above [6.1-6.7] have focused on different aspects of web-crippling test configurations and strengthening methods; however, despite its potential relevance, none of the previous studies has analysed the influence of the fibre layup of the FRP cross-section walls (namely of the transverse reinforcement of the webs) on the resistance to web-crippling.

Several formulae have been proposed in previous studies to predict the failure loads of GFRP profiles under different web-crippling test configurations [6.1, 6.2, 6.7]; however, the expressions derived in those studies are typically applicable to a narrow range of test configurations, geometries, and material properties. This highlights the need for additional experimental results, enabling the development of general design formulae, valid for a wider variety of test configurations, geometries and materials, including profiles with different fibre layups.

Considering these challenges, the experimental study presented in this chapter aimed at addressing the following three complementary objectives: (i) to better characterize and understand the web-crippling phenomenon in pultruded GFRP profiles, with respect to their failure modes, stiffness and ultimate load results; (ii) to provide comprehensive experimental data that can validate non-linear finite element (FE) models accounting for the damage progression in the GFRP material, as developed in [6.11] (see Chapter 7); and (iii) to provide additional experimental results to currently available web-crippling test data, thus enabling the development of design formulae for GFRP profiles, as performed in [6.12] (see Chapter 8).

The present study focused on two web-crippling test configurations, ETF and ITF, in line with previous research conducted by the authors [6.6, 6.7]. The experimental programme presented in [6.6] comprised a wide geometry range for the height (h) of the profiles, between 100 and 400 mm. On the other hand, the study presented in this chapter focused on profiles with similar heights (150 to 200 mm) but presenting significantly different fibre layups. Furthermore, the present experimental study also aimed at obtaining comprehensive local strain measurements (namely the shear and transverse compressive strains on the profiles webs), in order to further validate the numerical models presented in Chapter 7, calibrated with previously determined fracture toughness properties. These strain measurements were also envisioned to provide further insights about the failure mode of each specimen and to enable the determination of effective bearing lengths in the webs of each profile.

6.2. Experimental programme

6.2.1. Materials

The experimental programme included a total of five profiles, as detailed in Table 6.1. Four profiles present an I-section geometry and one profile presents a U-section geometry. These materials were obtained from four different suppliers: (i) Alto Perfis Pultrudidos (A); (ii) Creative Pultrusions (C); (iii) Fiberline Composites (F); and (iv) STEP, Sociedade Técnica de Estruturas Pultrudidas (S). These materials were subjected to mechanical characterization tests, to assess their elastic and strength properties and burn-off tests, to assess the fibre layup, as well as the weight percentage of transverse fibre reinforcement (45° and 90° oriented fibres), this experimental programme is detailed in [6.13, 6.14]. Among the various test materials, three fibre layup categories were established, in respect to transverse reinforcement (see Chapter 3): (i) materials reinforced only with continuous filament mats (C); (ii) materials reinforced with woven [0/90] layers (W); and (iii) materials reinforced with quasi-isotropic [+45/90/-45] layers (Q).

Table 6.1 includes the geometry, layup and mechanical properties determined for each profile, including elastic moduli (E, G) and strength (σ, τ) in the longitudinal (1) and transverse (2) directions. Additionally, the transverse fibre reinforcement percentage was included in Table 6.1, consisting of the sum of 90° oriented fibres and 45° oriented fibres (multiplied by $\sqrt{2}/2$ to account for their angle), whereas continuous filament mat layers were disregarded.

Table 6.1: Average geometric and mechanical properties of each pultruded GFRP profile.

Material	Height x Width [mm]	Wall thick., [mm]	Layup	Tr. Reinf. %	E_{11}^{-} [GPa]	E_{22}^{-} [GPa]	G_{12} [GPa]	σ_{u11}^{+} [MPa]	σ_{u22}^{-} [MPa]	τ_{u12} [MPa]
I150-A	150x 75	8.1	W	4.5	44.0	7.8	3.1	384	60	48
I152-C	152x 76	6.3	Q	29.7	24.6	10.9	4.2	416	104	65
I200-F	200x 100	9.9	W	8.3	29.9	10.8	2.9	323	122	67
I150-S	150x 75	8.1	C	0.0	28.1	9.3	3.2	377	123	70
U150-S	150x 45	7.7	Q	20.0	25.8	6.5	4.2	347	84	71

The I150-A material presents the lowest transverse compressive strength, despite sharing a similar fibre layup with materials that present much higher transverse compressive properties.

These lower transverse elastic and strength properties were attributed to minor defects caused by insufficient levels of fibre/matrix bonding, as reported in Chapter 3. These defects are expected to be more relevant at the coupon level, where a weaker section can lead to specimen failure, than at the structural level.

6.2.2. Specimen geometries

As mentioned, the experimental programme included ETF and ITF tests. The length of the specimens was defined based on a parametric study, in order to assess the influence of specimen length on stiffness and ultimate loads. This study focused on the I150-A profile and encompassed ITF specimen lengths of 1.5h, 2h and 4h (h being the profile height), showing that even lengths of 1.5h led to similar results to lengths of 4h (see section 2.5). Given these results, a specimen length of 2h was defined for the experimental programme.

6.2.3. Test setup

The test setup, illustrated in Figure 6.2, included an Instron universal test machine, used to load the specimens under displacement control, at a rate of 0.01 mm/s. Three different bearing lengths (l_b) of 15, 50 and 100 mm were considered in order to assess the influence of this parameter on stiffness and ultimate loads.

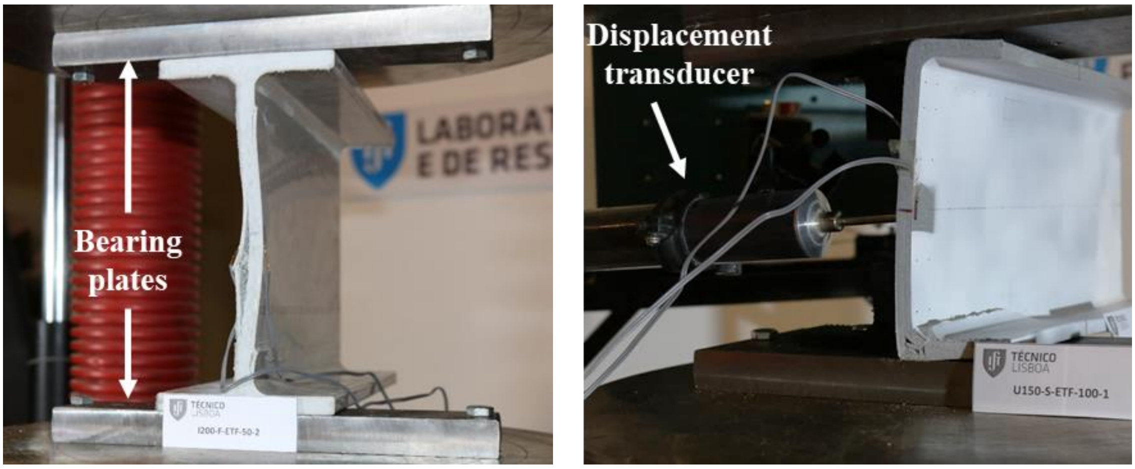

(a) (b)

Figure 6.2: Setup for web-crippling tests: (a) side view of I-section ETF test; (b) U-section ETF test with strain gauges and displacement transducer installed perpendicularly to the web.

Each specimen was painted on one side of the web with white matte paint and dotted with a black marker in order to use a video-extensometry system to monitor the in-plane displacements of the web at different positions. The video-extensometry targets are illustrated in Figure 6.3, including a general set of targets, used to measure the vertical displacement in the web (A), and specific targets used to monitor the shear strains near the edges of the bearing plates (B).

To enable the detection of web-buckling initiation, some specimens were monitored with two strain gauges, bonded vertically to both sides of the web at its mid-depth, in the loaded section. Buckling failure initiation was linked to the beginning of a diverging trend between both strain gauges, which was visually confirmed through a camera positioned to record the side view of the specimen (as illustrated in Figure 6.2 (a)). In some U150-S specimens, because they were expected to buckle and show significant out-of-plane displacements, a displacement transducer was positioned against the back face of their web (see Figure 6.2 (b)), so that the out-of-plane displacements could be measured and later compared to numerical simulations.

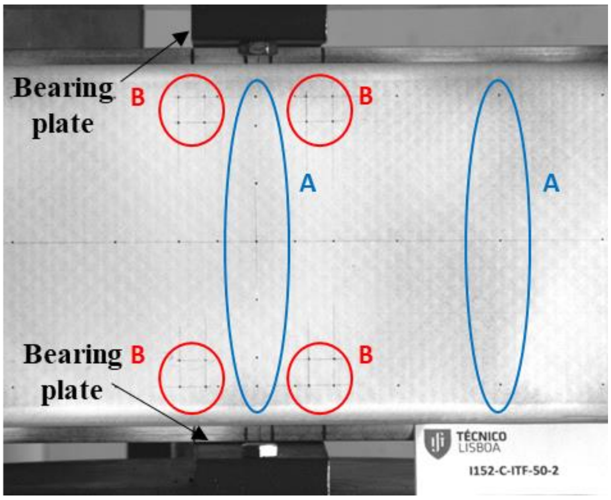

Figure 6.3: Picture taken from video-extensometry system footage, showing targets used to monitor vertical displacements (A) and localized shear strains (B).

6.2.4. Test series

The experimental programme is summarized in Table 6.2, which details the number of tests performed for each material, test configuration and bearing length. The nomenclature used to designate each test series follows the same order, as exemplified for an I150-S specimen, tested in the ETF configuration, with a 50 mm bearing length: I150-S-ETF-50. When relevant, the specimen number was added to this nomenclature. A total of 87 web-crippling tests were conducted.

Table 6.2: Experimental web-crippling programme summary, number of tested specimens.

Profile	ETF			ITF		
	15 mm	50 mm	100 mm	15 mm	50 mm	100 mm
I150-A	3	3	3	3	3	9*
I152-C	3	3	3	4	3	2
I200-F	3	3	2	3	3	3
I150-S	3	3	-	3	3	3
U150-S	-	-	3	3	4	3

* The I150-A-ITF-100 test series included a higher number of specimens in order to test different specimen lengths, of 1.5h, 2h and 4h.

6.2.5. Parametric study

Figure 6.4 presents load *vs*. displacement curves of representative I150-A-ITF-100 specimens with different specimen lengths. The results shown in Figure 6.4 indicate that a length of 1.5h should be considered acceptable, as there are no significant differences in the results obtained for longer lengths. Specimens with lengths of 1.5h and 4h presented average ultimate loads of respectively 70.6±2.4 kN and 71.4±4.5 kN; specimens with length of 2h presented the highest average ultimate load, of 76.2±5.5 kN, which should be attributed to the scatter in test results. Given these results, a length of 2h was considered for all materials and both test configurations.

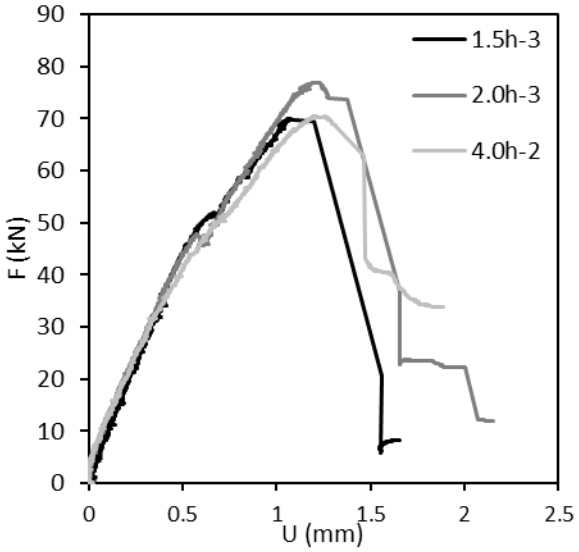

Figure 6.4: Representative load *vs*. displacement curves of I150-A-ITF-100 tests with different specimen lengths.

6.3. Experimental results

The experimental results were assessed in terms of five main parameters: (i) failure modes; (ii) specimen stiffness; (iii) ultimate load; (iv) shear strains at the edges of the bearing plates; and (v) transverse compressive strains along the length of the specimen. These results are presented in the following sub-sections, being discussed and compared for different materials in Section 4. In addition, the out-of-plane displacement of some U-section specimens was also measured, being presented in Section 3.5.

6.3.1. Failure modes

Two main failure modes were found in the experimental tests, which are in line with results of previous research [6.6, 6.7]: (i) web-crushing; and (ii) web-buckling. Web-crushing, consisting of concentrated damage near the web-flange junctions, was observed in most I-section ITF tests, the exception being I152-C-ITF-100, and in all I-section ETF-15 tests. Figure 6.5 presents examples of web-crushing failure.

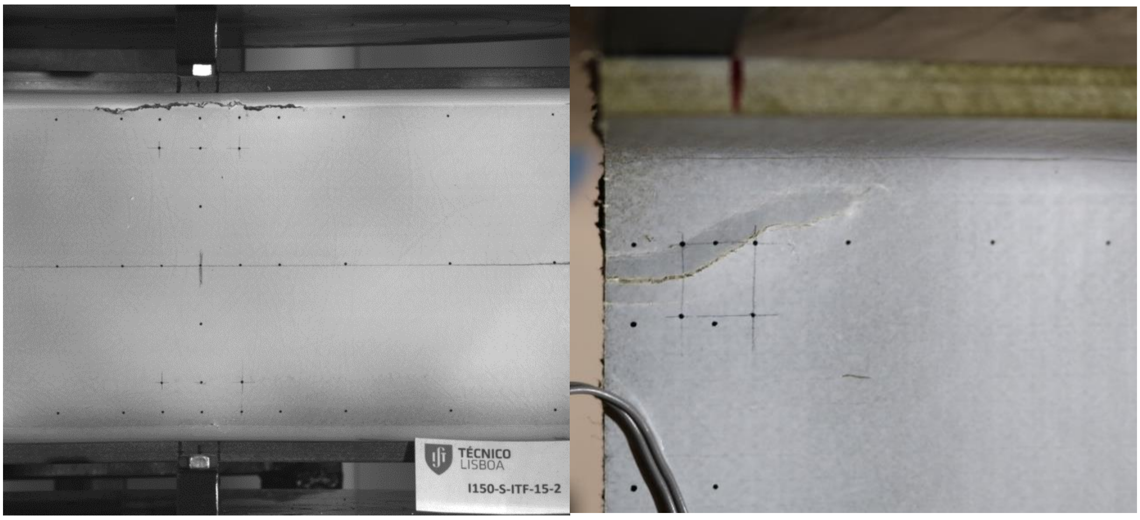

(a) (b)

Figure 6.5: Web-crushing failure modes: (a) I150-S-ITF-15-2; (b) I152-C-ETF-15-1.

One GFRP material, profile I150-A, showed a different pattern of web-crushing failure, as several longitudinal cracks were observed throughout the web depth. This failure mode, depicted in Figure 6.6, was attributed to the aforementioned defects detected in this material.

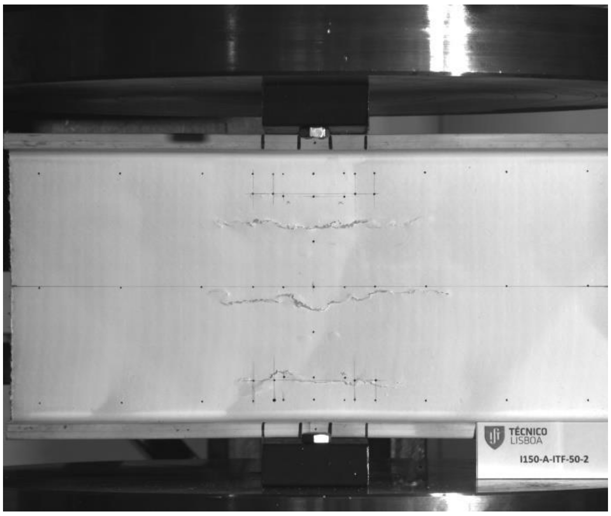

Figure 6.6: Web-crushing failure mode of I150-A-ITF-50-2 specimen.

Web-buckling, involving the relatively sudden out-of-plane bending of the web, was reported for I152-C-ETF-50 and 100 tests. This failure mode is depicted in Figure 6.7. The remaining ETF-50 and 100 test series of I-section profiles, as well as I152-C-ITF-100 tests, presented a mixed failure mode, where damage initiation near the web-flange junction led to posterior web-buckling failure. In these instances, the strain gauge data was used to establish the first failure mode to occur in each test. Figure 6.8 presents the sequence of damage development in the I200-F-ETF-50-2 test: Figure 6.8 (a) shows damage initiation, which occurred close to the web-flange junction, and Figure 6.8 (b) shows the buckling failure mode that occurred subsequently at the centre of the web. Finally, Figure 6.9 presents load *vs*. strain curves for the I200-F-ETF-50-2 specimen (Figure 6.9 (a)) and of a specimen with clear web-buckling failure, I152-C-ETF-50-1 (Figure 6.9 (b)).

Figure 6.7: Web-buckling failure mode of I152-C-ETF-50-1 specimen.

(a) (b)

Figure 6.8: Failure mode of I200-F-ETF-50-2 specimen: (a) damage initiation near the bottom web-flange junction; followed by (b) brittle failure due to web-buckling.

Figure 6.9 clearly shows two different trends, as in Figure 6.9 (a) there is some discrepancy in the strain gauge data, but both strain gauges present a stable slope almost up to failure, whereas in Figure 6.9 (b) the strain gauge curves present different trends, with clearly different slopes developing after a strain of ≈0.005 and a load of ≈22 kN are reached, indicating the onset of web-buckling. Considering similar data to that presented in Figures 6.8 and 6.9 (a), all I-section ETF-50 and 100 specimens were considered to have failed due to web-crushing, with the exception of I152-C-ETF-50 and 100 tests.

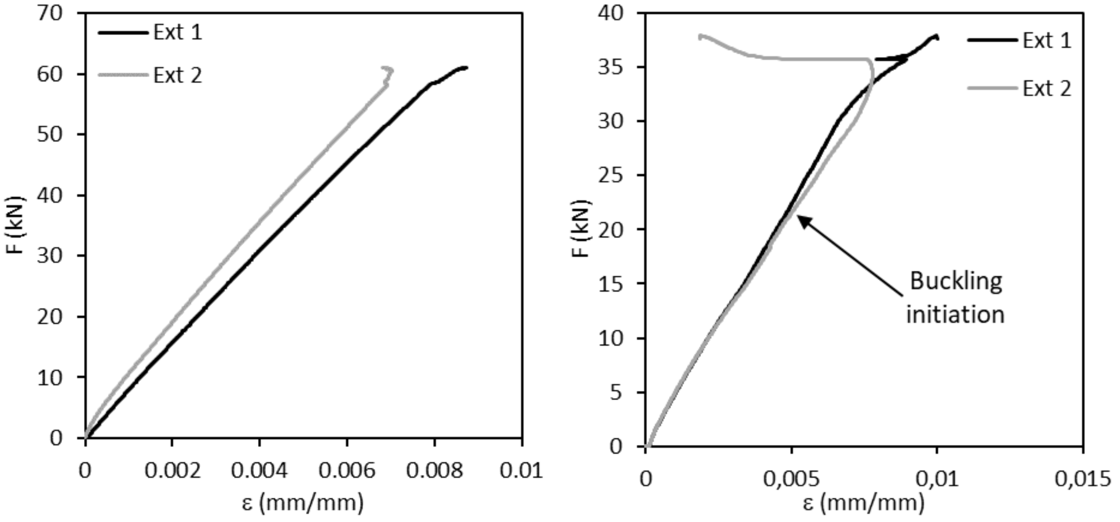

(a) (b)

Figure 6.9: Load *vs*. strain (measured through strain gauges) curves:
(a) I200-F-ETF-50-2 specimen; (b) I152-C-ETF-50-1 specimen.

All U150-S specimens showed a mixed failure mode, with significant out-of-plane displacements developing simultaneously with crushing near the web-flange junctions, as illustrated in Figure 6.10. This failure mode differs from the mixed failure mode found in some I-section tests, as failure developed in a relatively steady rate, with significant out-of-plane displacements at the centre of the web. These out-of-plane displacements naturally affected the video-extensometry measurements and thus, shear and compressive strain measurements were disregarded for U150-S specimens.

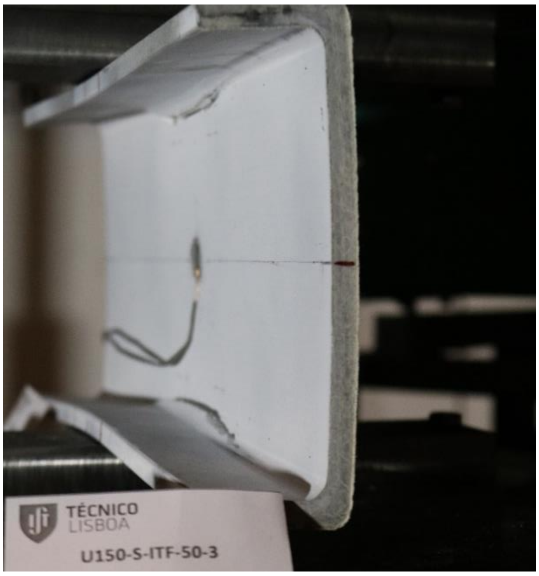

Figure 6.10: Combined web-crushing and web-buckling
failure mode of U150-S-ITF-50-3 specimen.

6.3.2. Load *vs.* displacement curves

Figure 6.11 presents representative load *vs*. displacement curves of ETF tests in I-section profiles, including all three bearing lengths. The displacements presented in Figure 6.11 (and throughout this chapter) were measured through the video-extensometry system, as the crosshead displacement of the test machine involves additional sources of flexibility, including the settlement/deformation of components of the test setup and local effects in load introduction. These displacement measurements were based on targets positioned on the web of each specimen, near each flange (see Figure 6.3, targets A).

Figure 6.11 clearly shows a significant influence of bearing length on the load *vs*. displacement curves, with increasing bearing lengths leading to significant increases of stiffness and ultimate load. Figure 6.12 shows the ITF load *vs*. displacement curves for I-section profiles, also including all three bearing lengths. As expected, the ultimate loads in ITF test series were higher than in the corresponding ETF series, as the former configuration is more stable; consequently, the former led to clear web-crushing failure modes for almost all test series (an exception being the mixed failure mode of I152-C-ITF-100 specimens).

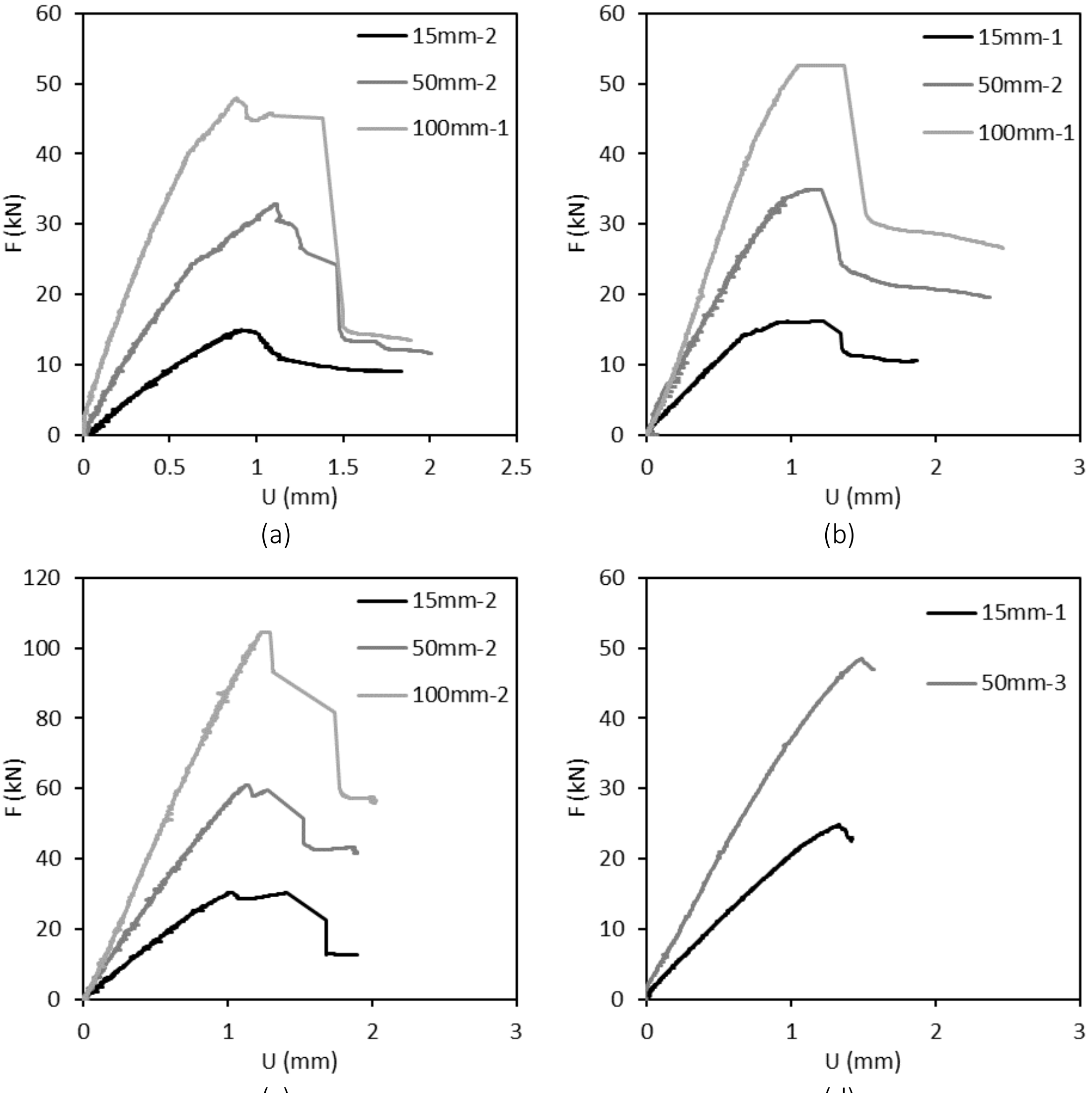

(a) (b) (c) (d)

Figure 6.11: Representative load *vs*. displacement curves of I-section profile ETF tests (one specimen per bearing length): (a) I150-A; (b) I152-C; (c) I200-F; (d) I150-S.

In agreement with the ETF results shown in Figure 6.11, the ITF test results presented in Figure 6.12 highlight the impact of increasing the bearing length on the load *vs*. displacement curves, namely in providing higher ultimate loads. The load *vs*. displacement curves in Figures 6.11 (d) and 6.12 (d) do not present the post peak stage, as the brittle failure led to erroneous readings of the video-extensometry setup (in some cases, the track of the targets was lost).

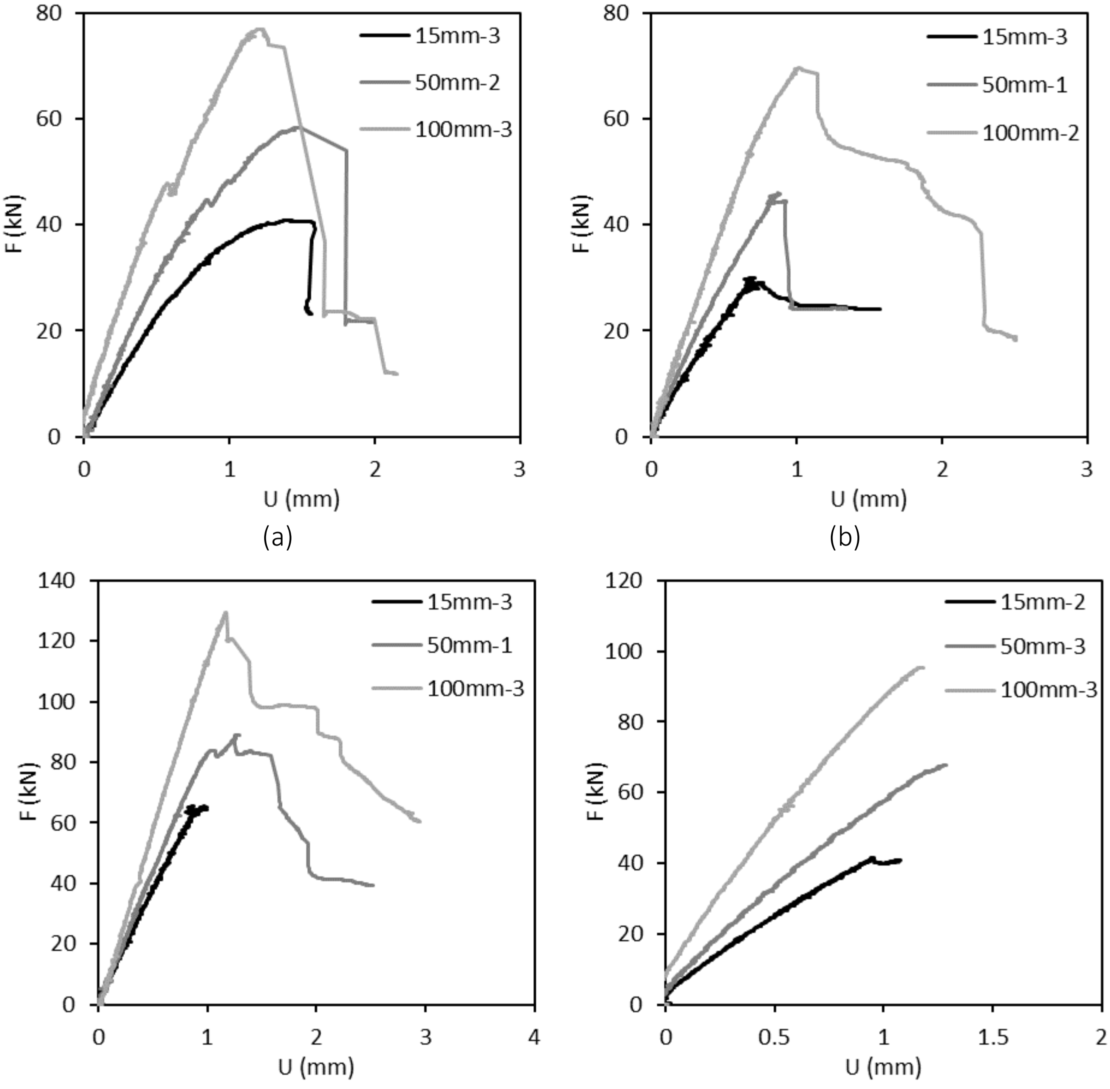

(a) (b)

(c) (d)

Figure 6.12: Representative load *vs*. displacement curves of I-section profile ITF tests (one specimen per bearing length): (a) I150-A; (b) I152-C; (c) I200-F; (d) I150-S.

Finally, Figure 6.13 presents representative load *vs*. displacement curves for the U150-S series, for both ETF and ITF test configurations. In this case, the crosshead displacement of the test machine is presented, as the video-extensometry measurements were affected by the out-of-plane displacements that developed nearly from the beginning of these tests.

It is noteworthy that the load *vs*. displacement curves shown in Figure 6.13 are considerably different from the previous ones, obtained for the I-section profiles (*cf*. Figures 6.11 and 6.12). As mentioned, the U150-S specimens showed a combined and progressive web-crushing and web-buckling failure mechanism, which resulted in a load plateau with significant in-plane displacements after an initial peak load was attained: for the ETF test series, this load plateau was lower than the peak load; on the other hand, for the more stable ITF test series, the load plateau was similar to the peak load (for a bearing length of 15 mm, the load even increased after the initial peak load). Wu *et. al.* [6.5] found a similar trend in U-section profiles tested in both ETF and ITF configurations, with a constant plateau developing after an initial peak load. However, this trend occurred only for one of the series tested by the authors [6.5].

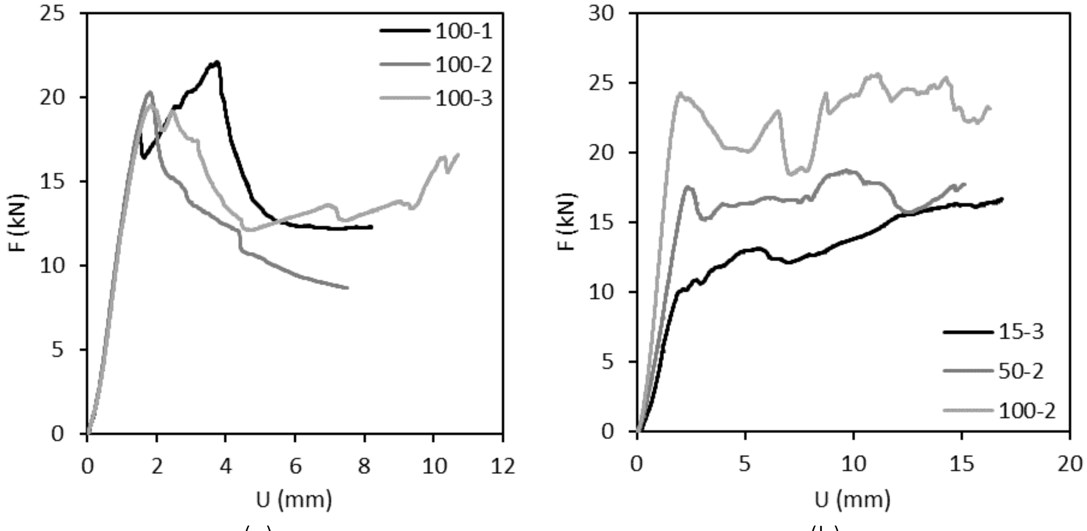

(a) (b)

Figure 6.13: Representative load *vs*. displacement curves of U-section profile tests: (a) ETF-100; (b) ITF (one specimen per bearing length).

6.3.3. Local shear strains

As mentioned, local shear strains (γ_{12}) were measured with two purposes: (i) to provide relevant data allowing to validate the FE numerical models, presented in Chapter 8, also (ii) to contribute to a better understanding of the role of shear stresses in web-crushing failure.

Figure 6.14 presents load *vs*. shear strain curves of representative ETF specimens of each I-section profile, including results for each bearing length. As shown in Figure 6.3 (targets B), video-extensometry targets were marked near the top and bottom bearing plates, which are both included in Figure 6.14. It should be noted that these results should underestimate the maximum shear strains at the web-flange junction, since the targets were positioned a few millimetres below the web-flange junction radius, so that they could be positioned in a plane surface.

The results shown in Figure 6.14 include significant noise, which stems from (i) the fact that the camera had to be positioned at a significant distance from the specimen (in order to capture the entire web height), and (ii) the small size of the squared target area (10 mm between targets). The noise level in the results presented in Figure 6.14 was reduced by using a moving average for 10 consecutive measurements. Despite such noise, these measurements provided results that show a general linear behaviour with progressive stiffness reduction prior to failure, establishing a clear order of magnitude for the maximum shear strains attained in the different test series, which ranged from 0.004 to 0.008.

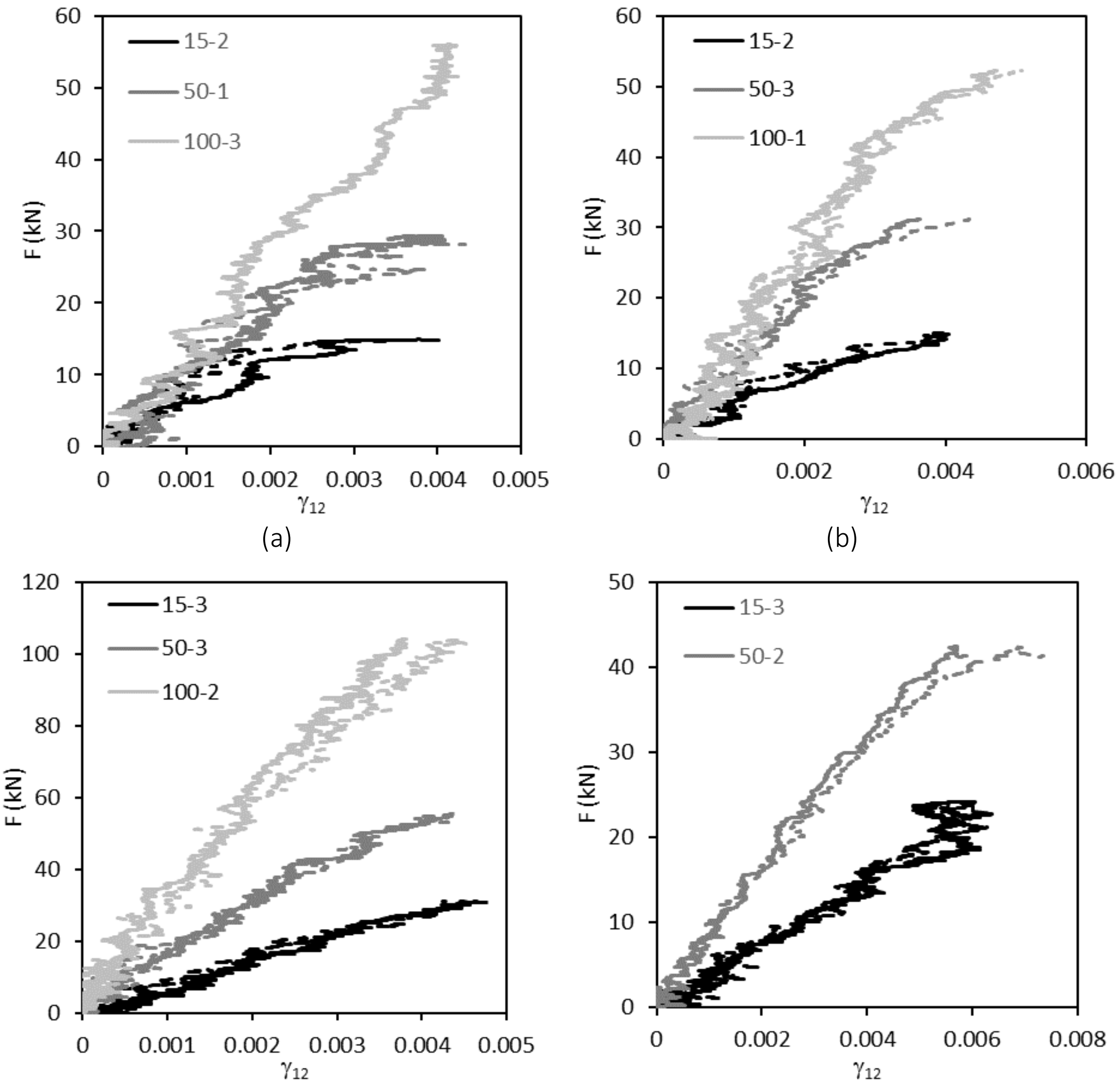

(a) (b)

(c) (d)

Figure 6.14: ETF load *vs*. shear strain curves measured through video-extensometry: (a) I150-A; (b) I152-C; (c) I200-F; (d) I150-S.

Figure 6.15 presents load *vs*. shear strain curves for all ITF I-section profiles; in this case, a total of four groups of targets were considered for each representative specimen. The I150-A-ITF-100 test series were performed in an initial stage and the shear strains near the bearing plates were not monitored. It should also be noted that all ITF-15 test series were monitored with targets positioned in a rectangular shape, which presented diagonal angles of ≈36°/54° instead of 45°. This discrepancy was corrected by determining the shear strain as a function of the strains at 0°, 90° and 36°, similarly to the procedure typically applied to a strain gauge rosette [6.15]. In line with the ETF series, and due to the same reasons, results obtained for the ITF tests present significant noise. Also compared to ETF tests, the ITF results present similar ranges for ultimate shear strains, spanning from 0.004 to 0.010, with the curves presenting a similar overall development. The higher shear strain levels in ITF tests are logical, considering the overall higher ultimate loads attained in these series. These results are further analysed in Section 4.

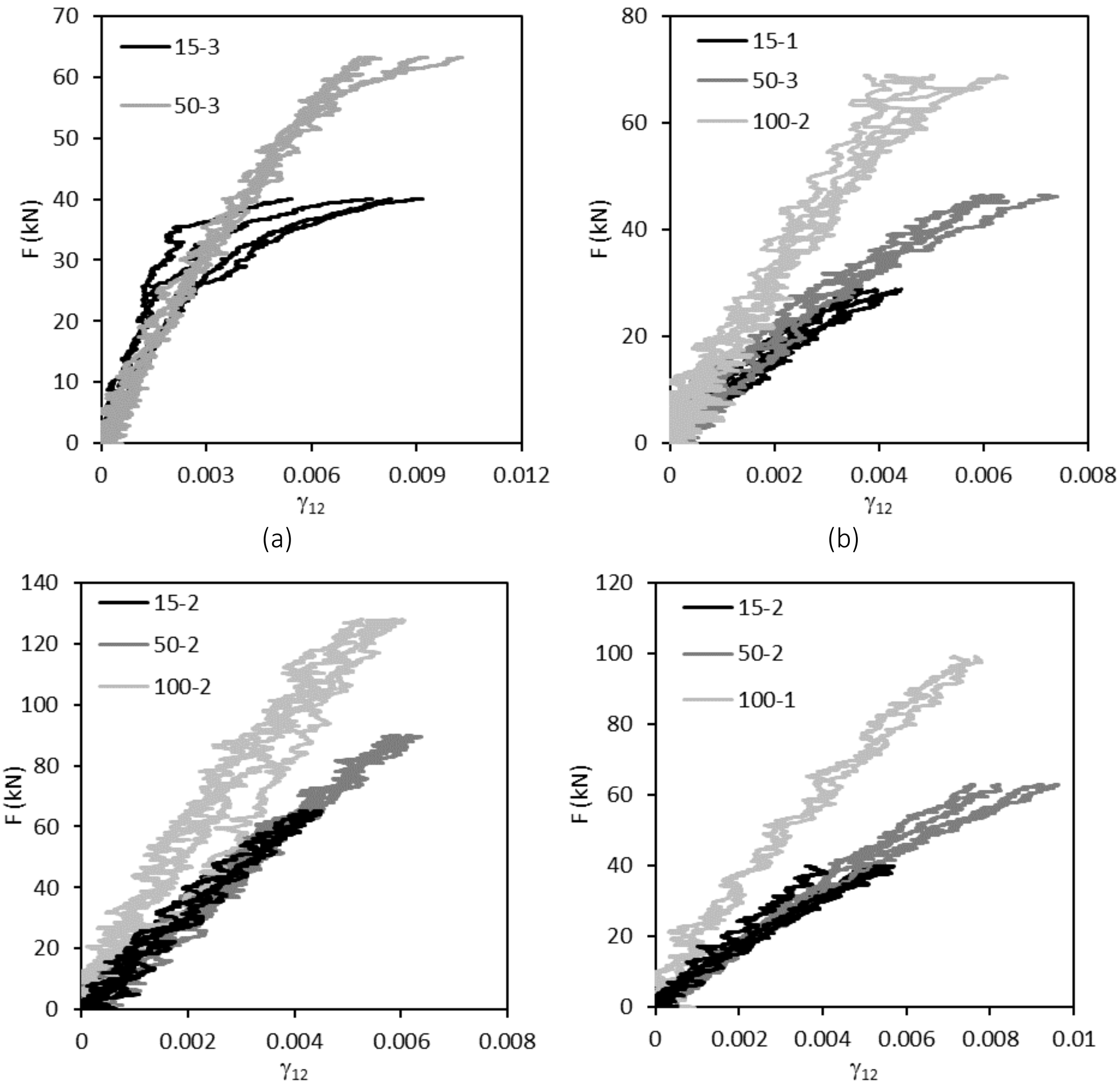

(a) (b)

(c) (d)

Figure 6.15: ITF load *vs*. shear strain curves measured through video-extensometry: (a) I150-A; (b) I152-C; (c) I200-F; (d) I150-S.

6.3.4. Transverse compressive strain profiles

The compressive behaviour of each specimen was monitored through video-extensometry targets near each web-flange junction (targets A in Figure 6.3), which enabled the assessment of transverse strain profiles (ε_{22}) for each specimen, along its length. The nominal gauge lengths between video-extensometry targets were 115 and 150 mm, for specimens with section heights of 150 and 200 mm, respectively.

This analysis was performed for the ultimate load stage, before significant damage propagation occurred, on test series that showed consistent signs of web-crushing failure, including all ITF series (with exception of I152-C-ITF-100) and all ETF-15 series. Figure 6.16 presents the transverse compressive strain distributions measured for ETF-15 test series. As expected, significant transverse compressive strains were measured only in a relatively narrow length of the specimen, between 100 and 120 mm.

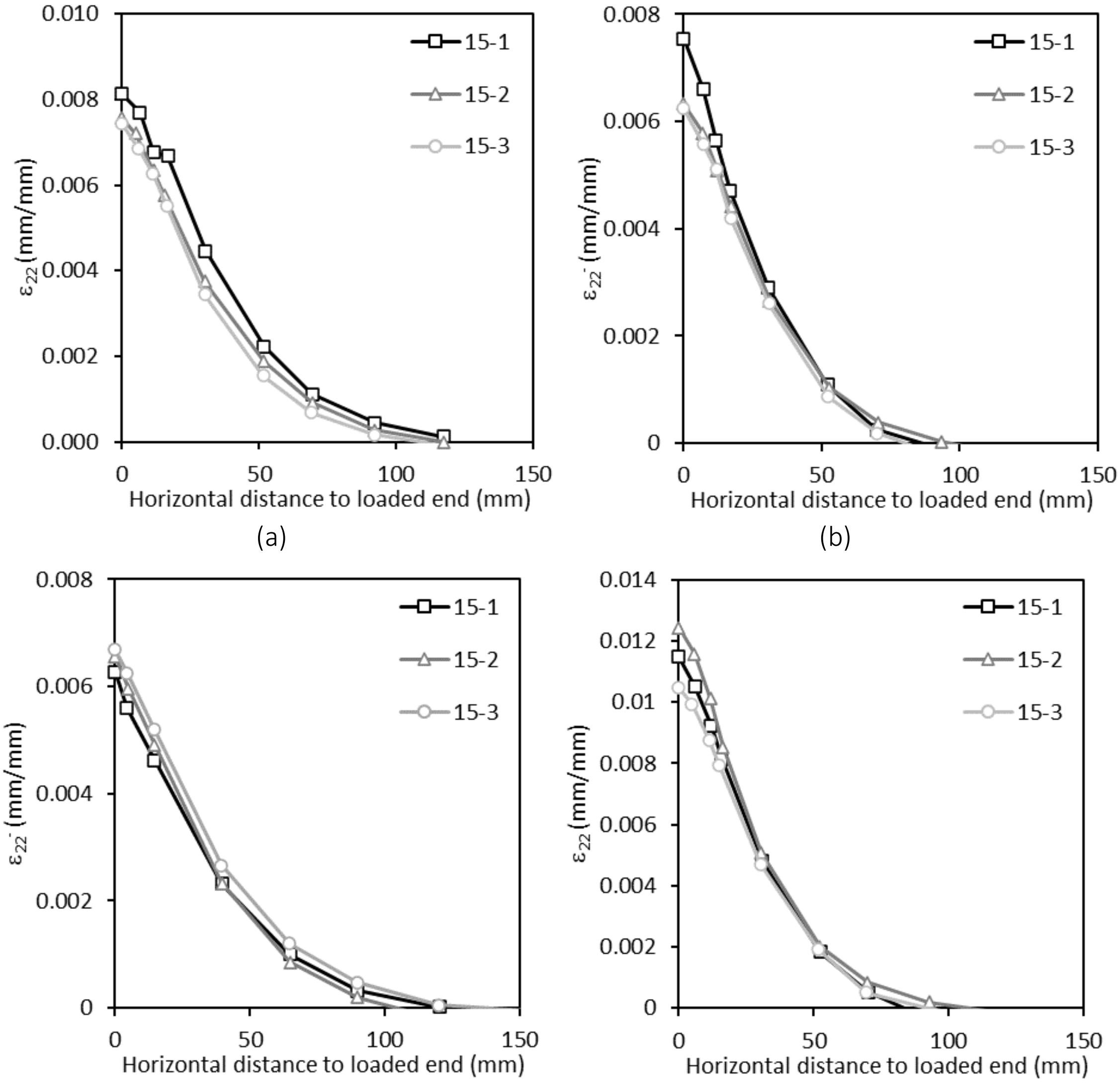

(a) (b)

(c) (d)

Figure 6.16: Transverse compressive strain distributions of ETF-15 test series:
(a) I150-A; (b) I152-C; (c) I200-F; (d) I150-S.

Figure 6.16 presents similar trends for all four I-section profiles, with a low variability between the specimens of each test series. The maximum strains ranged between 0.006 and 0.012, for I200-F and I150-S test series, respectively.

Figure 6.17 presents transverse compressive strain distributions of representative specimens for the ITF test series. As expected, the increase of bearing length led to significant increases in the compressed area of the web. However, all results show that significant transverse compressive strains occur within a 200 mm length, centred with the specimen symmetry axis. These strain distributions further validate the results of the parametric study (presented above), which indicated that specimens with a length of 1.5h should be a valid option for testing web-crippling under ETF and ITF configurations. Figure 6.17 shows that for an increasing bearing length, the distribution of strains across the length of the web become less sharp. Moreover, the lowest transverse compressive strains always correspond to the shortest bearing length of 15 mm. However, the effects of varying the bearing length from 50 mm to 100 mm in the maximum transverse compressive strains were not clear: in fact, the I150-A and I150-S ITF-50 tests presented a higher peak strain, when compared to specimens loaded with a longer bearing length of 100 mm; on the other hand, for I200-F specimens, the maximum transverse compressive strains occur for the longest bearing length of 100 mm.

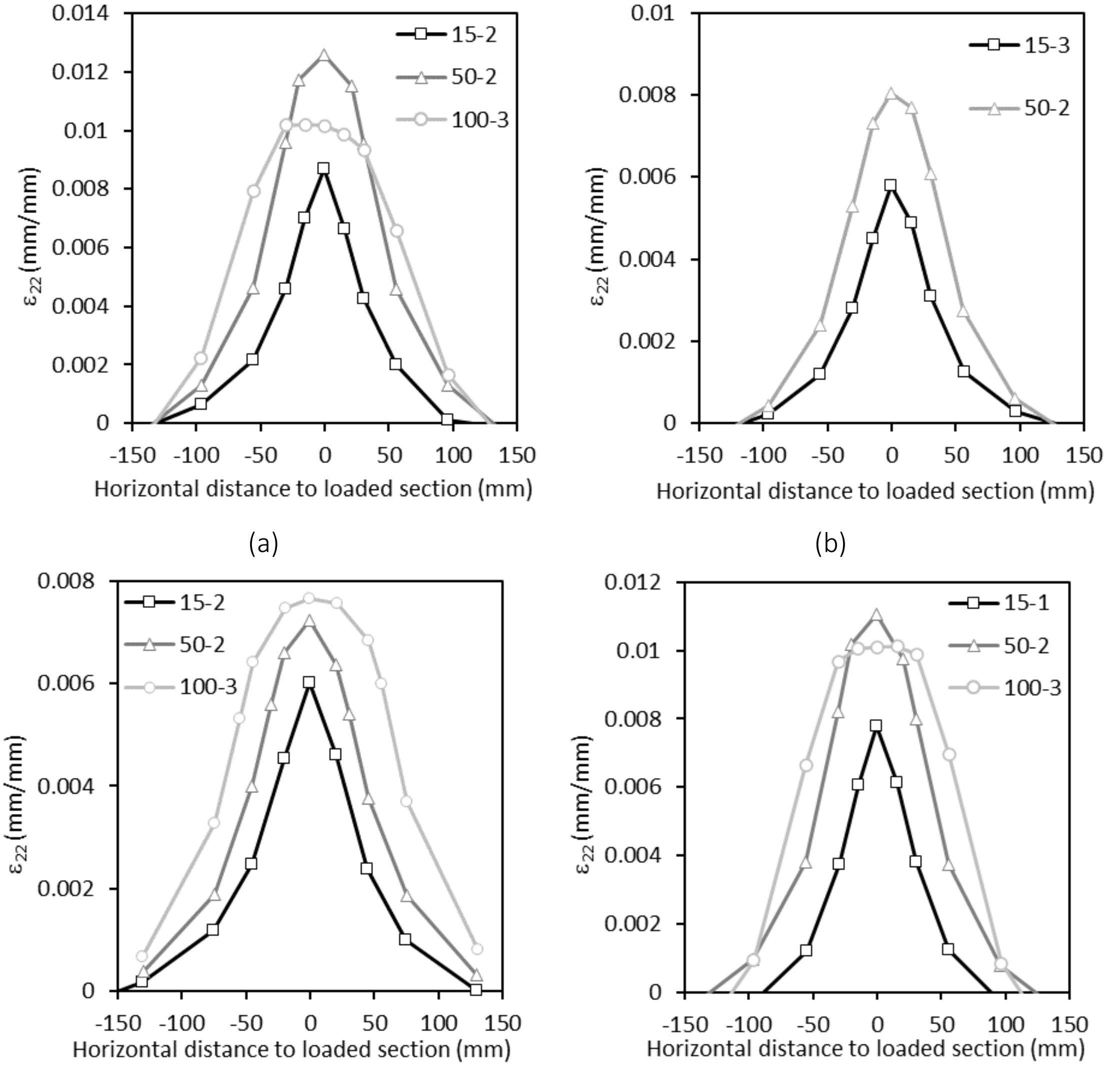

(a) (b)

(c) (d)

Figure 6.17: Transverse compressive strain distributions of ITF test series (one specimen per bearing length): (a) I150-A; (b) I152-C; (c) I200-F; (d) I150-S.

6.3.5. Out-of-plane displacements

Given the mixed failure mode presented by U150-S specimens, with out-of-plane displacements occurring early in the tests, a displacement transducer was used to measure these displacements. Figure 6.18 presents load *vs*. out-of-plane displacement curves for specimens loaded under different bearing lengths.

Figure 6.18 shows that significant out-of-plane displacements developed steadily from the beginning of each test, illustrating that web-buckling and web-crushing occur in parallel in these test series. A clear difference is also noticeable between ETF and ITF results, as ETF specimens present a significant load drop after the peak load is reached, whereas the ITF specimens seem to present a steady load plateau after an initial peak load is reached, as reported in section 3.2.

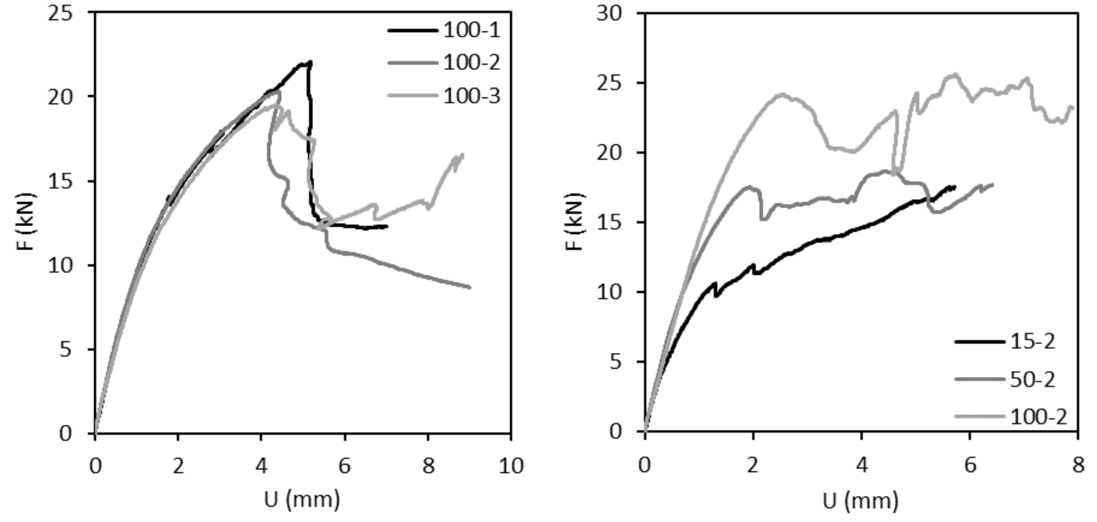

(a) (b)

Figure 6.18: Representative load *vs*. out-of-plane displacement curves of U-section profile tests: (a) ETF-100; (b) ITF (one specimen per bearing length).

6.4. Summary and discussion

This section presents experimental results as a function of the applied bearing length (l_b), in order to quantify the impact of this parameter on the stiffness, ultimate load and strain distributions for each GFRP profile. The analysis performed ahead has focused only in I-section profiles, as the video-extensometry technique was applied for a plane surface and all U-section tests showed early signs of out-of-plane displacements, thus influencing the readings.

6.4.1. Stiffness

The stiffness (K) of each test specimen was measured through the video-extensometry data, for the targets located at the loaded section. In particular, the (relative) displacement taken to compute K was determined as the difference of displacement between top and bottom targets (near each flange), as illustrated in Figure 6.3 (targets A). The crosshead displacement of the test machine could not be considered for this purpose due to the aforementioned reasons (*i.e.* it would provide higher estimates of displacement). Finally, the stiffness was determined from the slope of the load *vs*. displacement curve, for a load range between 10% and 20% of the ultimate load (for which the response was always linear). Figure 6.19 presents experimental stiffness results obtained for the different profiles, test configurations and bearing lengths.

Figure 6.19 shows two logical trends in the results: (i) ITF tests show significantly higher stiffness than their ETF counterparts; and (ii) ETF tests show a considerably higher relative increase of stiffness as a function of the bearing length. It is also noteworthy that, despite some significant variability in transverse elastic modulus (7.8 to 10.9 GPa) and web thickness (6.3 to 8.1 mm) among the various GFRP profiles tested, the stiffness of specimens with similar heights (I150-A, I150-S and I152-C) are very similar, indicating that varying both thickness and fibre layup had a reduced influence on stiffness for both ETF and ITF loading cases. It is worth referring, however, that the stiffness of the thickest profile, I200-F, is much higher than that obtained for the equivalent I150 series – this should be attributed to the higher web height of the former profile, which leads to higher effective bearing lengths in the web.

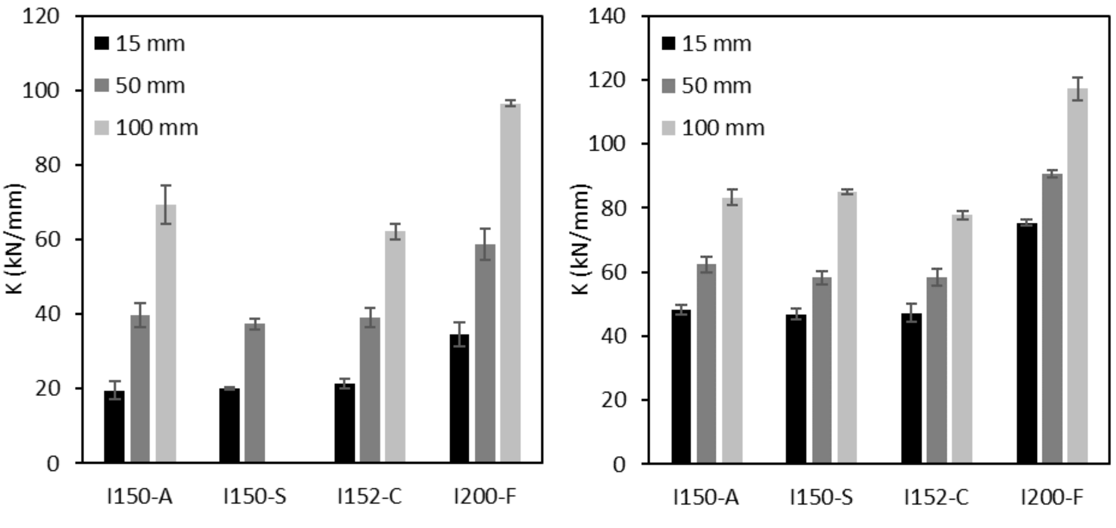

(a) (b)

Figure 6.19: Stiffness test results for different l_b – average ± standard deviation: (a) ETF test series; (b) ITF test series.

6.4.2. Ultimate load

Figure 6.20 presents a summary of the ultimate loads obtained for the different profiles, test configurations and bearing lengths. The results depicted in Figure 6.20 have some similar trends to the stiffness results: (i) the highest ultimate loads correspond to the ITF tests, and (ii) the ETF tests present the highest relative variation with the increase of bearing length. However, among specimens with similar heights, the ultimate loads are not as consistent as stiffness results.

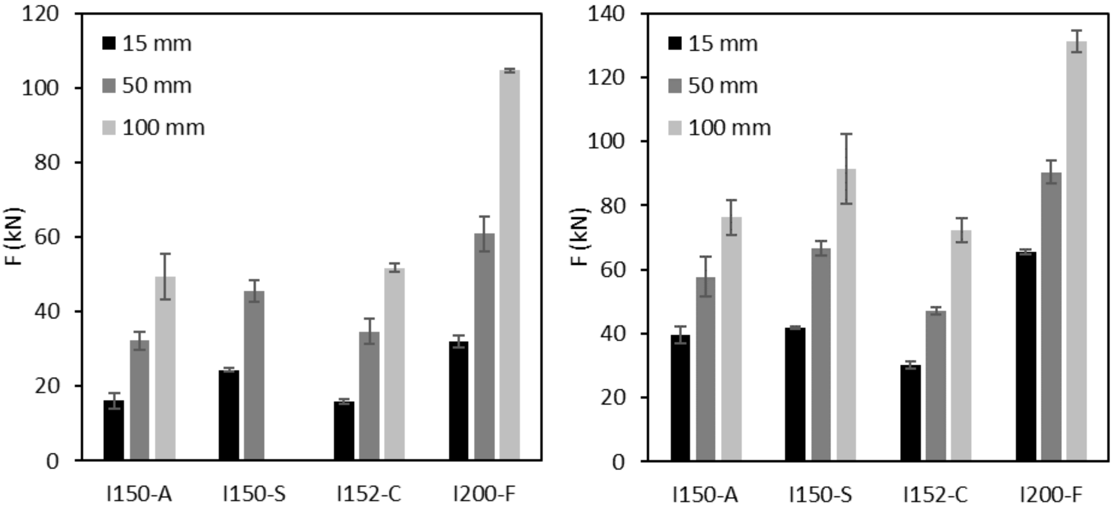

(a) (b)

Figure 6.20: Ultimate load results for different l_b – average ± standard deviation: (a) ETF test series; (b) ITF test series.

The similar ultimate loads presented by I150-A and I152-C specimens are an interesting albeit expectable result, which should be related to the fact that the higher thickness of I150-A specimens is balanced by the higher transverse compressive elastic modulus and ultimate stresses presented by I152-C specimens. On the other hand, Figure 6.20 indicates that the ultimate loads of I150-A and I150-S test series show noticeable but low relative differences; this was not expected *a priori* given their significant differences in material properties, namely in terms of their transverse compressive strengths, 60 MPa (I150-A) and 123 MPa (I150-S). These results are investigated in further depth in the numerical study presented in Chapter 7, where a better understanding is provided about the specific contributions of different geometrical and material properties to the ultimate load under ETF and ITF loading cases.

6.4.3. Local shear strains prior to damage onset

Figure 6.21 presents a summary of shear strain results, measured prior to significant damage propagation, for a load level corresponding to ≈95% of the ultimate load ($0.95F_u$), for all materials and test configurations. This load threshold was considered in order to avoid excessive damage propagation near the video-extensometry targets, which would naturally affect the results. For both ETF and ITF configurations, the results obtained for I150-S series stand out, corresponding to the highest maximum shear strains. It is also noticeable that the ETF results present a lower influence of the bearing length on the maximum shear strains, in contrast with previously summarized stiffness and ultimate load results. Finally, it is worth referring that the ITF test series present overall higher maximum shear strains, which is consistent with the also higher overall values of ultimate loads.

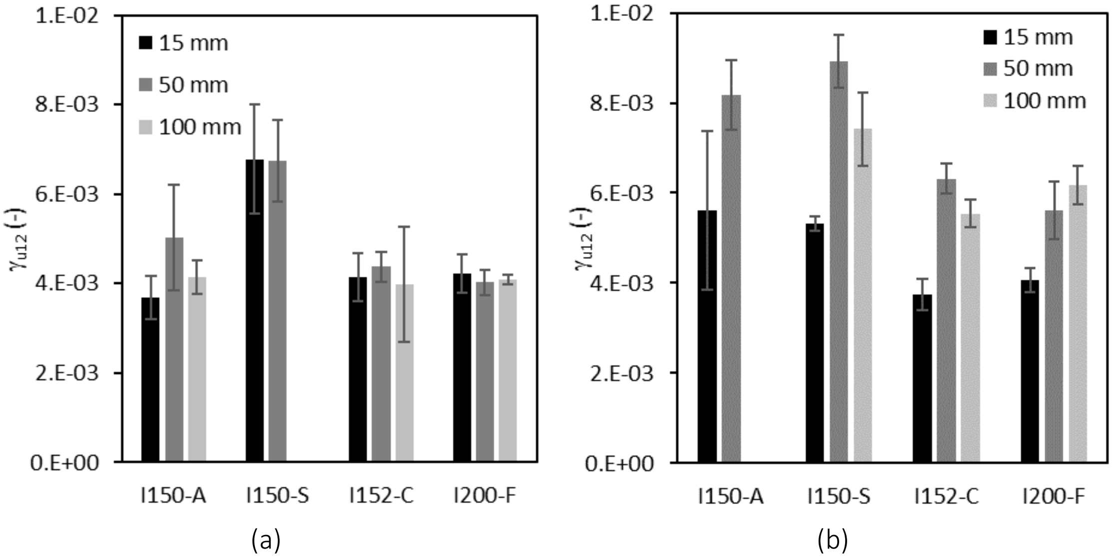

Figure 6.21: Shear strains for different l_b and an applied load of $0.95F_u$ – average ± standard deviation: (a) ETF test series; (b) ITF test series.

The shear strains were used to estimate the shear stresses in these regions near the bearing plate edges. To this end, the shear strain results of each material were multiplied by the respective shear modulus listed in Table 6.1. The average shear stresses prior to damage onset of each experimental series are summarized in Table 6.3.

Table 6.3 shows that overall specimens loaded with 50 mm bearing plates presented the highest maximum shear stresses, the exception being the I200-F results. The shear stresses measured in these areas for all materials are well below the ultimate shear stresses indicated in Table 6.1. As previously mentioned, these results should be considered as a lower bound to the peak shear stresses of each specimen, as the shear strains were monitored a few millimetres below the web-flange junction and the values listed in Table 6.1 correspond to 95% of the ultimate loads in each series.

Table 6.3: Average shear stresses [MPa] estimated near the bearing plate edges prior to damage onset.

Material	τ_{u12}	ETF			ITF		
		15	50	100	15	50	100
I150-A	48	11.5	15.7	12.9	17.5	25.5	-
I150-S	70	21.5	21.4	-	16.9	28.3	23.5
I152-C	65	17.5	18.5	16.9	15.9	26.8	23.5
I200-F	67	12.2	11.7	11.8	11.7	16.2	17.8
Average	-	15.7	16.8	13.9	15.5	24.2	21.6

6.4.4. Transverse compressive strains prior to damage onset

Figure 6.22 presents the transverse compressive strains measured through video-extensometry for a load level of ≈95% of the ultimate load, similarly to the shear strain results presented in the previous section. As mentioned, the transverse compressive strains were assessed through measurements of vertical displacements of targets positioned along the length of the specimen, near each flange (vertical distance between targets of 115 and 150 mm, for specimens with section heights of 150 and 200 mm, respectively). Therefore, unlike the shear strain measurements, the transverse compressive strains should not be considered as local strains, but rather as average strains throughout the depth of the web. Given the mixed failure modes observed in ETF-50 and 100 test series, as well as in I152-C-ITF-100 test series, these series were not considered in this part of the analysis.

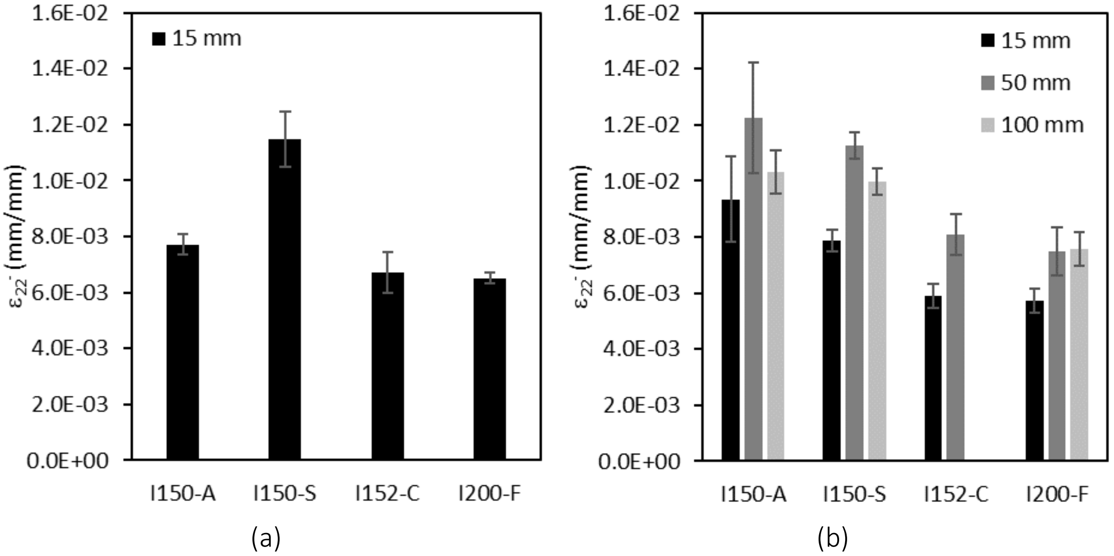

(a) (b)

Figure 6.22: Transverse compressive strains for different l_b and an applied load of $0.95F_u$ – average ± standard deviation: (a) ETF-15 test series; (b) ITF test series.

Figure 6.22 shows average transverse compressive strains that span from 0.006 to 0.012. The ETF-15 results are similar to ITF-15 results, except for I150-S specimens, where the ETF-15 transverse compressive strains are significantly higher than their ITF-15 counterparts. In line with previously shown shear strain results (Figure 6.21), the ITF specimens loaded with a 50 mm bearing plate present the overall highest values of transverse compressive strain. It is also noteworthy that the materials with highest web-thickness-to-height ratios (I150-A and I150-S) presented the overall highest transverse compressive strains, also in line with previous shear strain results.

The transverse compressive strains presented in Figure 6.22 can also be used to estimate the compressive stresses for the ultimate load stage, similarly to what was performed for shear stresses. These estimates are summarized in Table 6.4. In this case, the stress results should be considered as underestimations of the maximum compressive stresses, which are expected to occur near the bearing plate edges.

One major result should be highlighted in Table 6.4: the maximum transverse compressive stresses of the I150-A-ITF test series clearly exceeds the transverse compressive strength of the material. This indicates that the actual transverse compressive strength of this material may have been underestimated in the mechanical characterization tests. Furthermore, the stress values estimated for the I150-A-ITF test series are in line with those estimated for the remaining profiles, all of which present a significantly higher transverse compressive strength.

Table 6.4: Estimates of transverse compressive stresses prior to damage onset [MPa].

Material	σ_{u22}^{-}	ETF	ITF		
		15	15	50	100
I150-A	60	60.3	73.1	95.9	80.7
I150-S	123	106.8	73.4	105.0	93.1
I152-C	104	73.3	64.4	88.5	-
I200-F	122	70.3	61.1	81.0	81.8

6.4.5. Normalized transverse compressive strain fields

Figure 6.23 (a) presents the transverse compressive strain distributions of specimen I150-S-ETF-15-1 as a function of the horizontal distance to the loaded end, for different fractions of the failure load, F_u. Figure 6.23 (b) presents the same distributions, but with the strain values normalized to the maximum strain for each applied load ($\varepsilon_{22}/\varepsilon_{22(max)}$).

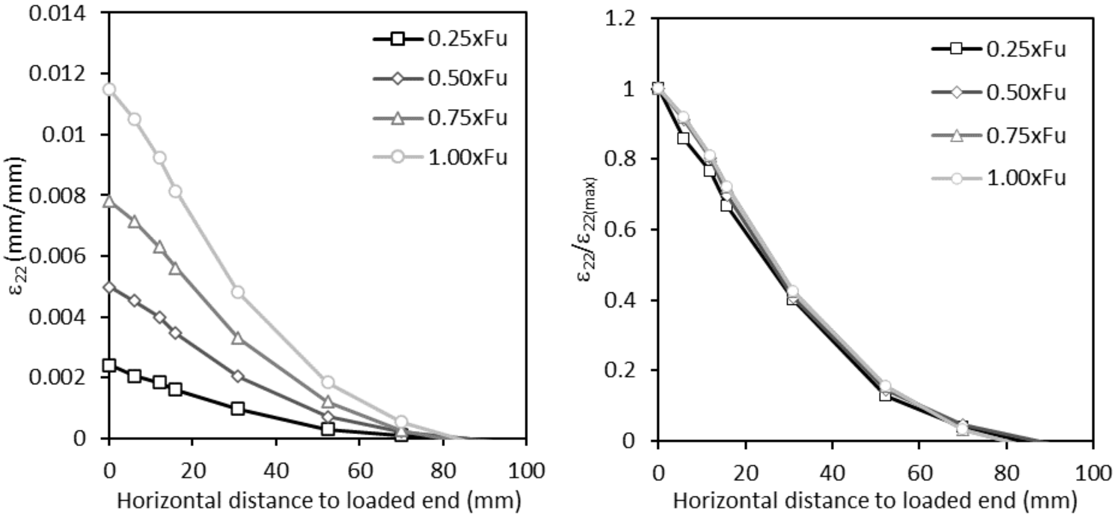

(a) (b)

Figure 6.23: Transverse compressive strain distributions of I150-S-ETF-15-1 test: (a) absolute values; (b) normalized results in respect to the maximum strain at each load level.

The results shown in Figure 6.23 clearly indicate that the transverse strain distributions affect a relatively constant area, regardless of the applied load. Results show a consistent trend in the transverse compressive strain fields of all specimens that failed due to web-crushing: when the strain values are normalized to the maximum strain for each applied load, the strain distributions remain constant for different load levels – this is attested in Figure 6.23 (b) for I150-S-ETF-15-1.

Figure 6.24 presents a comparison of normalized strain distributions, for the peak load stage, of test series that presented negligible out-of-plane displacements and clear web-crushing failure (ETF-15 test series and all ITF test series of I-section profiles). Figure 6.24 shows similar results for all materials, with a significantly low variability. These results seem to indicate that the fibre layup has a negligible influence on the effective bearing length of profiles under web-crippling. The results presented in Figure 6.24 have several potential applications, namely in the assessment of an effective bearing area, which can lead to more accurate design formulae, and in the validation of FE numerical models.

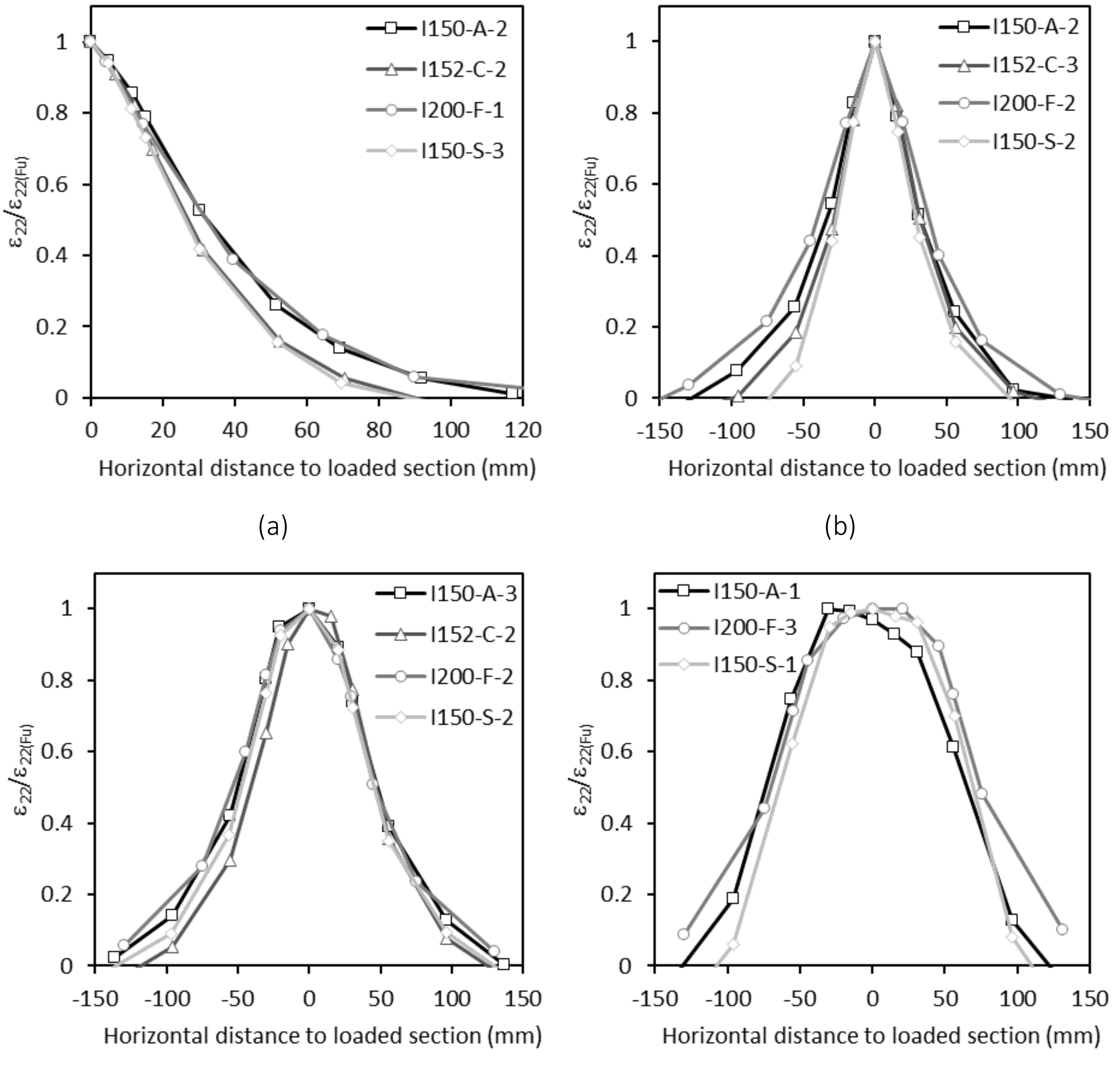

(a) (b)

(c) (d)

Figure 6.24: Normalized compressive strain distributions: (a) ETF-15; (b) ITF-15; (c); ITF-50; (d) ITF-100.

6.5. Conclusions

This chapter presented an experimental study about the web-crippling of pultruded GFRP profiles with three main goals: (i) to obtain a better understanding of the complex web-crippling phenomenon in GFRP profiles with different fibre layup; (ii) to help validating finite element numerical models, presented in Chapter 7; and (iii) to provide a wealth of test data for the development of design formulae, an effort presented in Chapter 8.

In accordance with the results of previous studies, the bearing length was found to present a significant and consistent impact in the ultimate load, stiffness and failure mode of all I-section profiles, for both ETF and ITF configurations. This impact was consistent for all I-section profiles, which is a significant result, given the wide variability of web thickness (6.3 to 9.9 mm), transverse compressive elastic modulus (7.8 to 10.9 GPa) and transverse compressive strength (60 to 123 MPa).

As expected, the highest values of stiffness and ultimate load were obtained for the ITF configuration. However, in the ETF tests the stiffness and ultimate load were more influenced by the increase of bearing length than in the ITF tests: when it increased from 15 mm to 100 mm, the ultimate loads increased between 207% (I150-A) and 227% (I200-F) in ETF tests, and between 93% (I150-A) and 139% (I152-C) in ITF tests. The U-section profile was considerably less affected by the bearing length: in ITF tests, when it increased from 15 mm and 100 mm the ultimate load increased 61%.

The failure modes observed in the experimental campaign were very consistent, clearly depending on the test configuration and bearing length. In all ITF tests and ETF-15 tests, failure involved clear web-crushing failure, the exception being the I152-C-ITF-100 tests. I152-C-ETF-50 and 100 tests showed clear signs of web-buckling. Other I-section ETF-50 and 100 tests showed a mixed failure mode, with damage initiation occurring due to web-crushing near the web-flange junction and final failure occurring due to web-buckling at the centre of the web. Finally, all U150-S tests also presented a mixed failure mode, with simultaneous and progressive web-crushing and web-buckling failure. This mixed failure mode involved higher values of vertical displacements, for relatively high (and non-decreasing) loads, in a quite different pattern to that of all I-section tests.

Shear strain and transverse compressive strain measurements were successfully performed for I-section specimens, providing additional data for numerical validation. U-section specimens were not assessed in this respect, as significant out-of-plane displacements developed throughout each test. The measurements of transverse compressive strains also showed that these strain fields affect a relatively constant area of the specimen throughout each test. Moreover, the development of normalized strains (with respect to the maximum transverse compressive strain) along the horizontal length was found to be nearly identical for all I-section profiles. This result highlights a major conclusion of this thesis: the significantly different fibre layups of the various profiles tested do not lead to different stress distributions along the length of the specimen. This result may be a significant starting point for the development of new design formulae for web-crippling failure.

6.6. References

[6.1] Borowicz, D. T., Bank, L. C., Behavior of Pultruded Fiber-Reinforced Polymer Beams Subjected to Concentrated Loads in the Plane of the Web*, Journal of Composites for Construction*, 15-2, pp. 2-9, 2011.

[6.2] Wu, C., Bai, Y., Web crippling behaviour of pultruded glass fibre reinforced polymer sections, *Composite Structures*, 108, pp. 789-800, 2014.

[6.3] Borowicz, D. T., Bank, L. C., Effect of web reinforcement on the behavior of pultruded fiber-reinforced polymer beams subjected to concentrated loads. *Construction and Building Materials*, 47, pp. 347-357, 2013.

[6.4] Wu, C., Bai, Y., & Zhao, X. L., Improved bearing capacities of pultruded glass fibre reinforced polymer square hollow sections strengthened by thin-walled steel or CFRP, *Thin-Walled Structures*, 89, pp. 67-75, 2014.

[6.5] Wu, C., Zhang, L., Bai, Y., Zhao, X. L., Web crippling behavior of pultruded GFRP channel sections under transverse bearing load, *Composite Structures*, 209, pp. 129-142, 2019.

[6.6] Almeida-Fernandes, L., Gonilha, J., Correia, J. R., Silvestre, N., Nunes, F., Web-crippling of GFRP pultruded profiles. Part 1: Experimental study. *Composite Structures*, 120, pp. 565-577, 2015.

[6.7] Almeida-Fernandes, L., Nunes, F., Silvestre, N., Correia, J. R., Gonilha, J., Web-crippling of GFRP pultruded profiles. Part 2: Numerical analysis and design. *Composite Structures*, 120, pp. 578-590, 2015.

[6.8] CNR-DT 205/2007, *Guide for the Design and Construction of Structures made of FRP Pultruded Elements*, National Research Council of Italy, Rome, 2008.

[6.9] *Pre-Standard for Load & Resistance Factor Design (LRFD) of Pultruded Fiber Reinforced Polymer Structures (FRP)*, American Society of Civil Engineers (ASCE), 2010.

[6.10] CEN/TC250 working Group 4, *Fibre reinforced polymer structures, scientific and technical report*, European Committee for Standardization, Brussels, 2016.

[6.11] Almeida-Fernandes, L., Silvestre, N., Correia, J. R., Fracture toughness-based models for web-crippling of pultruded GFRP profiles, *Composite Structures*, submitted, 2020.

[6.12] Almeida-Fernandes, L., Silvestre, N., Correia, J. R., Design guidelines for web-crippling of pultruded GFRP profiles, *Composites for Construction*, submitted, 2020.

[6.13] Almeida-Fernandes, L., Silvestre, N., Correia, J. R., Compressive transverse fracture behaviour of pultruded GFRP materials: experimental study and numerical calibration, *Composite Structures*, 247, 112453, 2020.

[6.14] Almeida-Fernandes, L., Correia, J. R., Silvestre, N., Transverse fracture behaviour of pultruded GFRP materials in tension: Effect of fibre layup, *Journal of Composites for Construction*, 24(4), 04020019, 2020.

[6.15] Hodgkinson J. M., *Mechanical Testing of Advanced Fibre Composites*, CRC Press, Cambridge, England, 2000.

Chapter 7. Fracture toughness-based numerical models for web-crippling failure

7.1. Introduction

The numerical simulation of damage in composite materials still remains a challenging topic and an unsolved problem [7.1]. Despite the typical brittle failure of composite materials, some structural cases exhibit significant damage propagation after initiation and before the ultimate failure. Typical examples of this behaviour are beam-to-column connections [7.2] and beams under localised loading, commonly known as web-crippling failure. While web-crippling of steel beams has been thoroughly investigated [7.3], the case for pultruded glass fibre reinforced polymer (GFRP) beams [7.3-7.10] is not yet understood. Because their transverse elastic modulus and compressive strength are much lower than their longitudinal counterparts, pultruded GFRP beams show a higher tendency for web-crippling failure than steel beams. Therefore, the experimental testing and numerical simulation of this phenomenon are deemed necessary and, ultimately, reliable design guidelines must be developed for engineering practice.

In a previous work [7.7, 7.8], the authors attempted to numerically predict the web-crippling ultimate loads of GFRP beams using the Tsai-Hill criterion [7.11]. It was concluded that stress-based criteria, such as the Tsai-Hill criterion, lead to excessively conservative predictions of ultimate loads – the numerical values were in average half of the experimentally ones. In a following study, Nunes *et al.* [7.9] showed that implementing the Hashin criterion [7.12] and the built-in damage evolution tools of Abaqus [7.13] led to significant improvements in the accuracy of ultimate load predictions. The fracture toughness parameters, required as input for the damage evolution criteria, were unknown and a parametric study was performed to better fit these parameters. Since then, a vast experimental campaign has been conducted to characterize the fracture behaviour of pultruded GFRP materials [7.14-7.16], namely their transverse compressive fracture toughness [7.16]. Therefore, the main objective of this study is to implement the previously determined fracture toughness parameters into numerical models, validate them against experimental web-crippling results reported in Chapter 6 and show that these simplified models are straightforward and reliable. These numerical analyses provided several outputs, including failure modes, stiffness and ultimate load values, as well as shear and compressive strain measurements.

7.2. Numerical modelling

7.2.1. Materials and damage criteria

The experimental programme included a total of five profiles, as detailed in Table 7.1. Four profiles present an I-section and one has a U-section. These materials were acquired from a total of four suppliers: (i) Alto Perfis pultrudidos (A); (ii) Creative Pultrusions (C); (iii) Fiberline Composites (F); (iv) STEP (S). Table 7.1 presents the geometry and mechanical properties determined for each profile, where E stands for the elastic modulus, G_{12} stands for the shear elastic modulus, σ_u stands for the ultimate stress, τ_{u12} stands for the shear ultimate stress, 1 and 2 indicate the longitudinal and in-plane transverse directions of the profile and + and - identify tensile and compressive properties. Table 7.1 also includes the transverse tensile (G_2^+) and compressive (G_2^-) fracture toughness of each material [7.14-7.16].

Table 7.1: Average geometric and mechanical properties of each pultruded GFRP profile.

Material	Height x Width [mm]	Wall thick., [mm]	E_{11}^- [GPa]	E_{22}^- [GPa]	G_{12} [GPa]	σ_{u11}^+ [MPa]	σ_{u22}^+ [MPa]	σ_{u22}^- [MPa]	τ_{u12} [MPa]	G_2^+ (N/mm) [7.14, 7.15]	G_2^- (N/mm) [7.16]
I150-A	150x 75	8.1	44.0	7.8	3.1	384	45	60	48	14	40
I152-C	152x 76	6.3	24.6	10.9	4.2	416	121	104	65	160	42
I200-F	200x 100	9.9	29.9	10.8	2.9	323	71	122	67	20	48
I150-S	150x 75	8.1	28.1	9.3	3.2	377	34	123	70	10	67
U150-S	150x 45	7.7	25.8	6.5	4.2	347	70	84	71	26	40

The I150-A material stands out with the lowest transverse compressive strength due to defects caused by insufficient levels of fibre/matrix bonding [7.16]. In addition, experimental and numerical studies based on compact compression (CCT) tests suggested that the transverse compressive strength can be affected by these defects and may be underestimated at the section level [7.16].

The material properties described in Table 7.1 were implemented through the Hashin criterion [7.12] to establish damage initiation. Abaqus built-in damage evolution tools were used for damage evolution, considering a linear cohesive law and the fracture toughness properties presented in Table 7.1. Regarding web-crippling failure, only transverse compressive failure is expected to be relevant, as no longitudinal loads are applied in these load cases and the longitudinal ultimate stresses of these materials are considerably higher than their transverse counterparts. Therefore, longitudinal fracture toughness properties were calibrated based on typical values on the literature, 100 N/mm [7.1], whereas transverse tensile fracture toughness input values were calibrated based on previous experimental results [7.14, 7.15].

7.2.2. Geometry, loading and measurements

Shell finite elements were used to model each specimen with the shape and dimensions shown in Table 7.1. The length of each specimen is equal to twice its height, in line with the experimental tests reported in Chapter 6. The bearing plates were modelled through solid finite elements (C3D8R), with a geometry that resembles the experimental tests, with a thickness of 10 mm and three different bearing lengths of 15, 50 and 100 mm. Figure 7.1 illustrates the geometry of an I150-S-ITF-15 model (Figure 7.1 (a)) and an U150-S-ITF-50 model (Figure 7.1 (b)).

Each bearing plate was modelled with the “Rigid body” constraint, with all nodes sharing the boundary conditions applied to the reference point, positioned at its geometrical centre. All boundary conditions were applied to the bearing plates, through this reference point. The displacements and rotations of the top bearing plate were fixed, whereas the bottom bearing plate was restricted in all displacements and rotations, with exception to the vertical displacement. Each model was loaded through displacement control, with vertical displacements imposed at the bottom bearing plates, thus simulating the experimental tests. Contact was implemented in two different procedures: (i) for damage analysis (D and DB), standard contact was defined for each set of bearing plate and flange surface; and (ii) for buckling analysis (B), the “general contact” tool was implemented, considering the same contact pairs as before – see labelling further ahead. The bearing plates were selected to present the master surfaces, whereas the flanges were defined as slave surfaces. Finally, the interaction properties were considered to avoid any interpenetration between surfaces and a friction coefficient of 0.4 was considered, in line with previous studies [7.8].

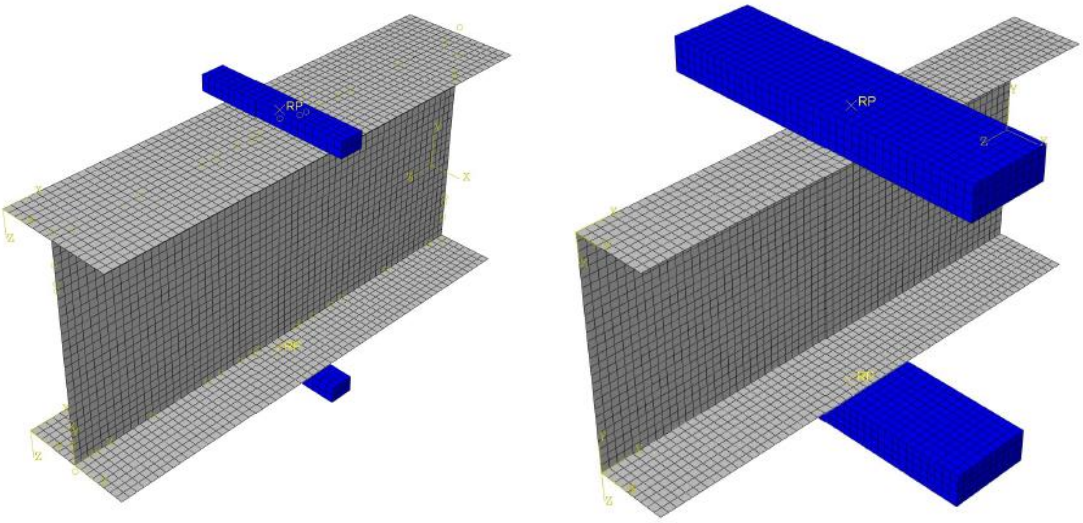

(a) (b)

Figure 7.1: Geometry and FE mesh of numerical models: (a) I150-S-ITF-15; (b) U150-S-ITF-50.

In order to have a direct validation between numerical and experimental strain measurements, the target grid considered for the experimental tests was reproduced in the numerical models, as displayed in Figure 7.2, including (i) targets for measurements along the height of the web (C), meant for determining vertical displacements and compressive strains; and (ii) targets positioned near the bearing plate edges, for shear strain measurements (S). These measurements were not considered for the U-section models because significant out-of-plane displacements occurred in the experimental tests, hindering such comparisons. Nevertheless, the out-of-plane displacement of the web centre of U-section models was monitored for comparison with the experimental values reported in Chapter 6.

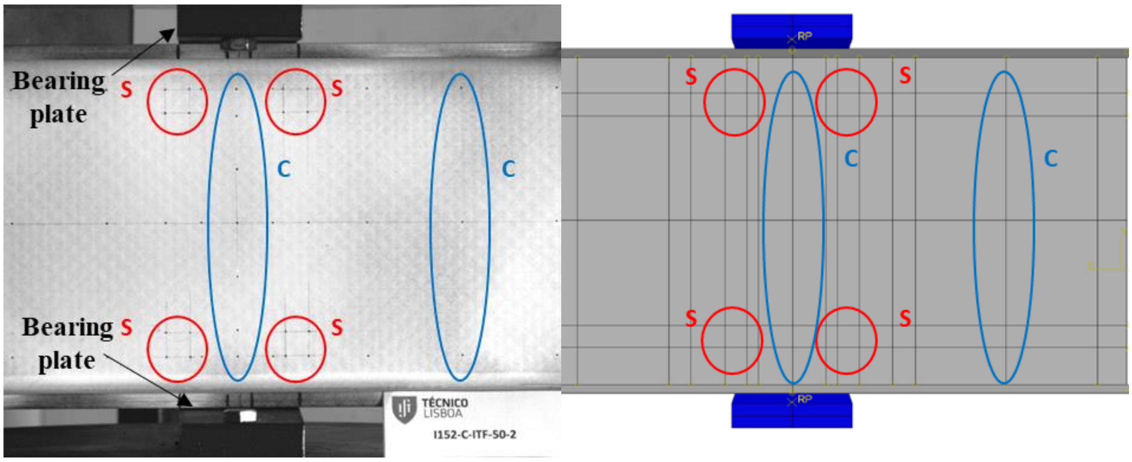

(a) (b)

Figure 7.2: Experimental and numerical targets for displacement measurements: (a) test specimen [7.10]; (b) FE model.

7.2.3. Damage analyses

The experimental tests reported in Chapter 6 were simulated through three different types of analysis: (i) D-analysis, where material failure is considered but buckling effects are disregarded; (ii) B-analysis, where material failure is not considered but buckling effects play a key role; and (iii) DB-analysis, which includes both material damage and buckling effects. Next, they are described in more detail:

D-analysis

These models should accurately predict web-crushing failure, but not web-buckling failure, when compared to experimental results. Damage initiation and evolution are implemented through Abaqus [7.13] built-in tools.

B-analysis

This numerical analysis consists of elastic predictions of web-buckling, ignoring material strength or fracture properties. This elastic buckling analysis was performed with the goal of comparing numerical critical buckling loads to the experimental ultimate loads and failure modes. In cases where the critical buckling loads are similar to the experimental failure loads, it would be expected to find clear signs of web-buckling failure in the experimental tests. This analysis is presented in Section 7.3.2.

DB-analysis

The deformed shapes of the first buckling mode were used as input for the geometrically non-linear models, which also considered the damage formulation implemented for D-analysis. Therefore, these models should be able to simulate both web-crushing and web-buckling failure, as well as their potential interaction. The first buckling mode was inserted in the analysis through the "Imperfection" option, with an amplitude of 0.01 mm, so that the imperfection would have minimal impact in the response of the model, aside from enabling a non-linear geometrical analysis. The numerical results of these non-linear models were compared to experimental failure modes and ultimate loads, in order to further establish the ability of this simplified approach to accurately simulate experimental tests.

7.2.4. Finite element mesh

A parametric study was performed, through D numerical models, in order to establish the mesh size and element for the numerical models. To this end, an analysis was performed for three different types of shell finite elements: (i) S4R; (ii) S4; and (iii) S8R. Figure 7.3 presents the results of this study, for a mesh size of 5 mm.

The S4R and S8R elements were found to present similar results, whereas S4 elements led to a higher ultimate load. This discrepancy was further clarified, as displayed in Figure 7.4, by performing parametric studies for the mesh sizes of S4R and S4 elements, varying from 1 to 5 mm. Figure 7.4 clearly shows that the S4R element results are nearly identical, whereas S4 results tend toward S4R results, as the mesh refinement increases. In face of the results shown in Figures 7.3 and 7.4, a mesh size of 5 mm was selected, as well as S4R elements.

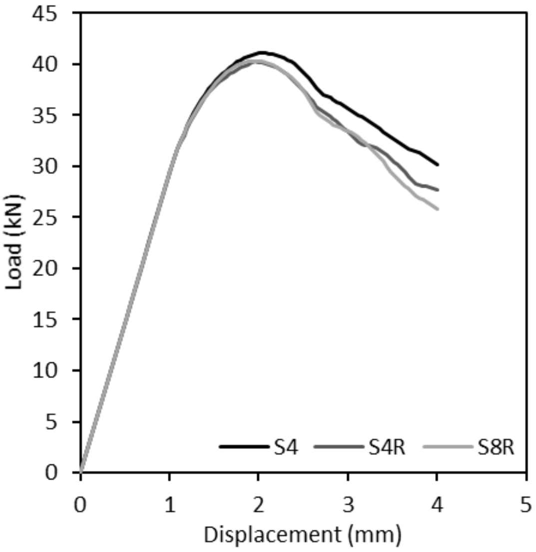

Figure 7.3: Influence of finite element type on load *vs*. displacement response of I150-S-ITF-15 model with 5 mm mesh size.

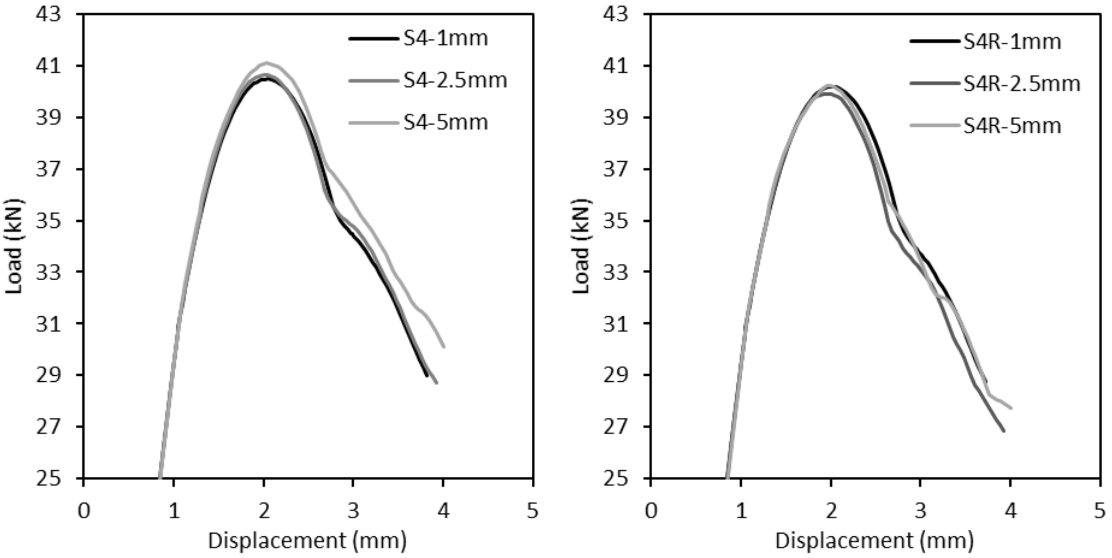

(a) (b)

Figure 7.4: Influence of finite element size on load *vs*. displacement response of I150-S-ITF-15 model: (a) S4 elements; (b) S4R elements.

7.3. Web-crippling of I-section beams

The numerical models of I-section beams, detailed in the previous section, are validated against experimental results in the following sub-sections, namely (i) stiffness results, determined through a video-extensometry system; (ii) failure modes; (iii) ultimate loads; (iv) localized shear strains; and (v) compressive strain distributions along the length of each specimen.

7.3.1. Stiffness results

The stiffness results compared in this section are based on measurements taken from similar points in both experimental tests and numerical models, as illustrated in Figure 7.2. Therefore, the displacement was measured as the difference between the target point near the bottom flange and the target point near the top flange, in the loaded section. In ETF tests, these measurements were taken from the edge of the specimen, whereas in ITF tests these measurements were taken from the centre of the specimen. Figure 7.5 presents a summary of experimental (average ± standard deviation) and numerical (DB) stiffness results.

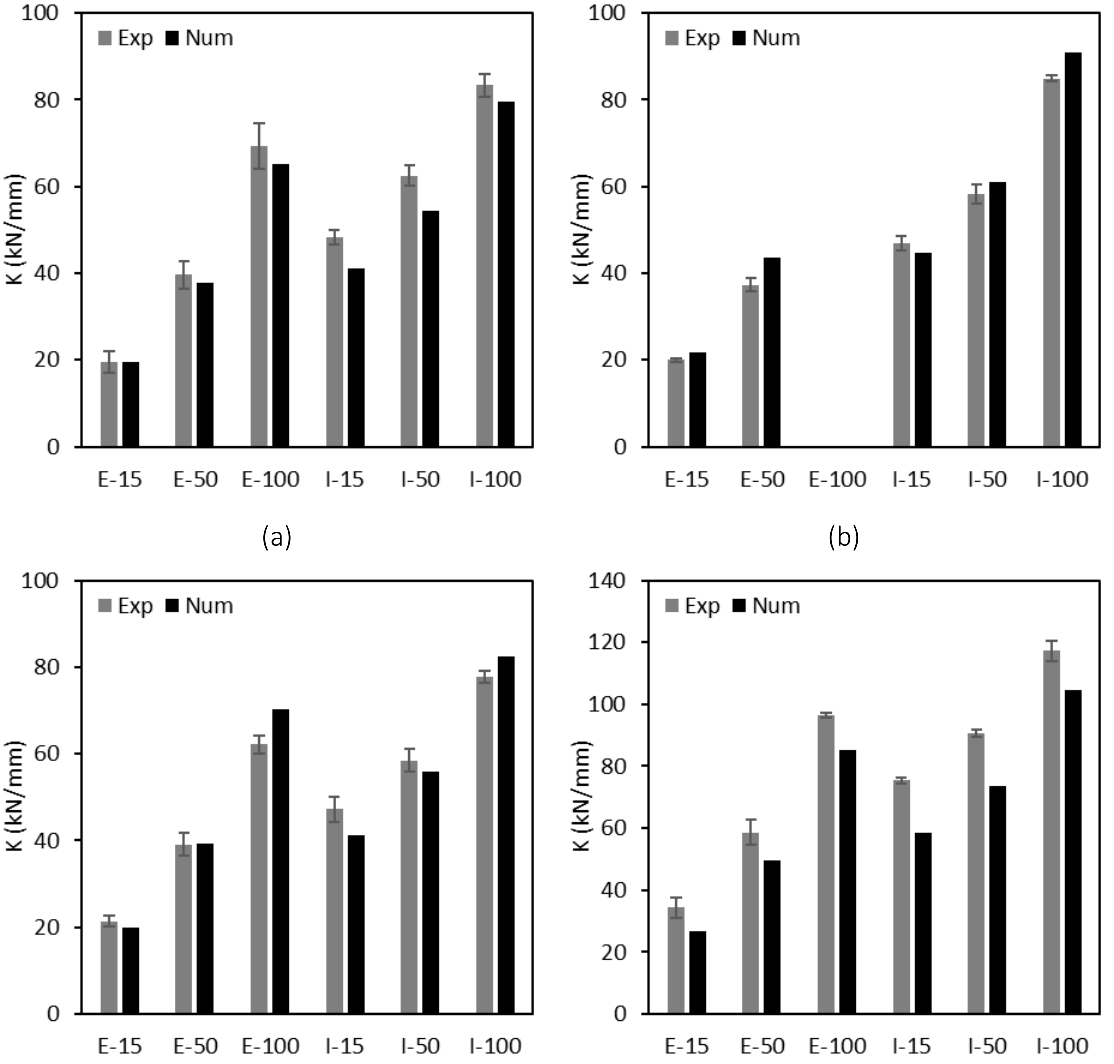

(a) (b)

(c) (d)

Figure 7.5: Experimental and numerical (DB) predictions of stiffness: (a) I150-A; (b) I150-S; (c) I152-C; (d) I200-F.

The results presented in Figure 7.5, show a similar trend between experimental and numerical predictions of stiffness. Only one material, I200-F, showed numerical results consistently lower than the experimental ones, however the differences were found to be acceptable considering the simplified approach taken for these models, which neglects the geometry of the web-flange junction and the through-the-thickness heterogeneity of the material.

7.3.2. Failure modes

The experimental failure modes were compared to the numerical results of B-analysis and DB-analysis. In a first stage, the critical loads of B-analysis were compared to experimental ultimate loads, in order to establish which experimental test series would be expected to present web-buckling failure. This analysis is particularly relevant for cases where the failure mode was less clear, as several ETF-50 and ETF-100 experimental tests.

Table 7.2 presents a summary of experimental test results and B-analysis results, as well as the ratio between a numerical critical buckling load and the respective experimental ultimate load. If this ratio is close to 1.0, it would be expected to find web-buckling failure modes in the experimental observations. On the contrary, if this ratio is significantly higher than 1.0, it would indicate that web-crushing would be expected in the experimental observations. The failure modes of web-crushing and web-buckling were labelled as “Cr” and “Bu”, respectively.

All ETF-50 and ETF-100 experimental tests (the exceptions being I152-C-ETF-50 and I152-C-ETF-100 specimens) were reported to present web-crushing failure, in spite of presenting a less clear failure mode, with damage initiation occurring near the web-flange junction, triggering subsequently web-buckling failure, at the centre of the web [7.10]. These specimens were considered to fail due to web-crushing as consistent signs of damage initiation were found near the web-flange junctions for these test series. This conclusion is supported by the numerical critical buckling loads presented in Table 7.2, which show that web-buckling should only occur for considerably higher applied loads. The failure modes of the experimental test series were also assessed through DB-analyses. Figure 7.6 presents experimental and numerical (DB) failure modes, where transverse compressive damage is highlighted. Figure 7.6 shows a good agreement between DB models and the experimental failure modes [7.10]. Web-crushing and web-buckling failure modes are clearly well-captured by the DB numerical models (Figures 7.6 (b) and (d)). The DB model also presents a mixed failure mode similar to that of the I200-F-ETF-100 test series (Figure 7.6 (f)). In this mixed failure mode, initial damage developed near the web-flange junction, followed by damage at the centre of the web. However, delamination phenomena are naturally outside the scope of these models, as occurred for the I200-F-ETF-100-1 specimen (Figure 7.6 (e)).

Table 7.2: Overview of experimental failure modes and numerical critical buckling load predictions (loads in kN).

Test Config.	ETF											
Material	I150-A			I150-S			I152-C			I200-F		
Bear. Length [mm]	15	50	100	15	50	100	15	50	100	15	50	100
Exp. Ult. Load	16.1	32.2	49.3	24.3	45.4	-	16.0	34.7	51.7	32.0	60.9	104.7
Buckling load	41.8	58.5	86.1	45.6	65.6	-	25.1	36.1	54.0	63.4	86.1	123.0
Buckl./Exp. ratio	2.61	1.82	1.74	1.88	1.44	-	1.57	1.04	1.04	1.98	1.41	1.17
Failure Mode	Cr	Cr	Cr	Cr	Cr	-	Cr	Bu	Bu	Cr	Cr	Cr
Test Config.	ITF											
Material	I150-A			I150-S			I152-C			I200-F		
Bear. Length [mm]	15	50	100	15	50	100	15	50	100	15	50	100
Exp. Ult. Load	39.4	57.7	76.2	41.8	66.5	91.4	30.2	47.1	72.3	65.4	90.4	131.2
Buckling load	100.9	112.6	133.8	109.8	124.2	149.8	60.6	68.6	81.9	161.3	175.8	204.1
Buckl./Exp. ratio	2.56	1.95	1.76	2.63	1.87	1.64	2.01	1.46	1.13	2.47	1.95	1.56
Failure Mode	Cr	Cr	Cr	Cr	Cr	Cr	Cr	Cr	Cr	Cr	Cr	Cr

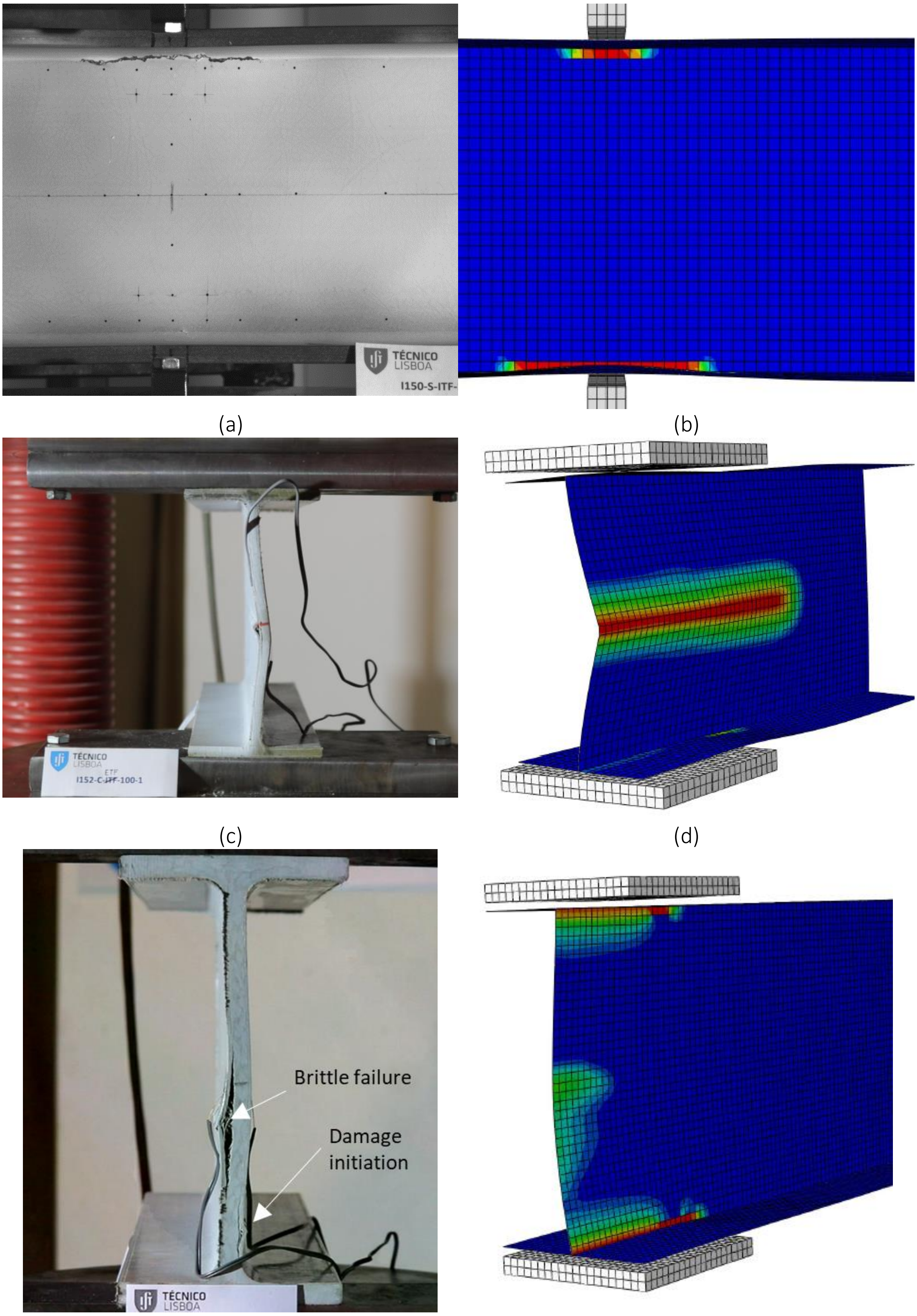

(a) (b)

(c) (d)

(e) (f)

Figure 7.6: Experimental [7.10] and numerical (DB) predictions of failure modes, including transverse compressive damage contours: (a) web-crushing of I150-S-ITF-15-2 specimen; (b) I150-S-ITF-15 FE model; (c) web-buckling of I152-C-ETF-100-1 specimen; (d) I152-C-ETF-100 FE model; (e) mixed failure mode of I200-F-ETF-100-1 specimen; (f) I200-F-ETF-100 FE model.

In a different perspective, the experimental failure mode of I150-A-ITF specimens, showing various longitudinal cracks along the web height [7.10], was further confirmed to be related to defects in the material, as all numerical models showed consistent web-crushing failure occurring near the web-flange junction. This discrepancy is illustrated in Figure 7.7.

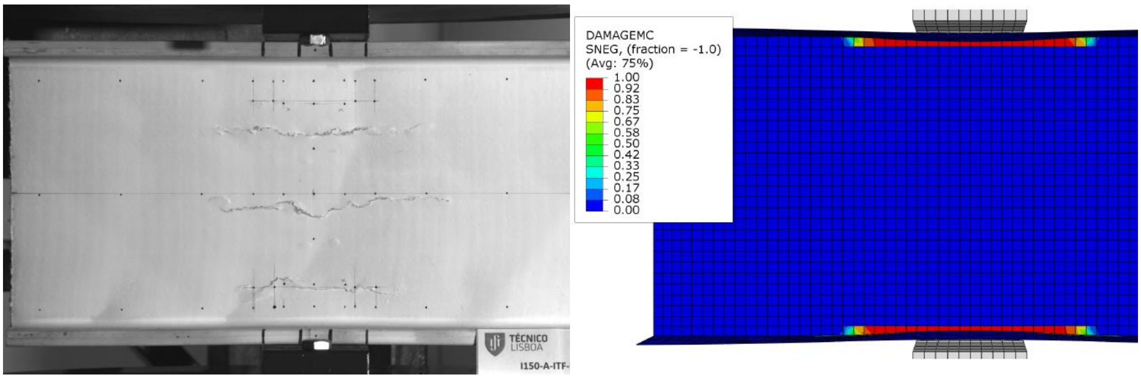

(a) (b)

Figure 7.7: I150-A-ITF web-crushing failure modes: (a) I150-A-ITF-50-2 specimen failure [7.10]; (b) FE model, including transverse compressive damage contours.

7.3.3. Ultimate loads

The experimental results were compared to results of both D and DB analyses, in order to assess the efficacy of these numerical models in estimating web-crippling failure. Figure 7.8 presents a summary of experimental (average ± standard deviation) and numerical results.

Figure 7.8 shows a generally good fit between numerical and experimental results, in particular for the DB model. The highest discrepancies were reported for D models, in test series where web-buckling occurred. As would be expected, the DB models were able to simulate this failure mode, providing more accurate estimates of ultimate loads. It is also noteworthy that, in some cases, the DB ultimate loads are slightly higher than their D counterparts, this was attributed to an artificial stiffening effect due to the initial imperfection.

Aside from the previous discrepancies, a few test series present relevant differences between experimental and numerical results, in particular the I150-A-ITF results. These results are of particular interest, as ETF series appear to be accurately modelled but ITF series present some discrepancies. At this time, this difference between I150-A-ETF and ITF results is attributed to the defects found in this material, which, when loaded in an end section (ETF), seem to promote failure for lower applied loads, similarly to what was found in mechanical characterization tests. In a different trend, ITF tests have a significant length to distribute the load, which may mitigate the impact of these defects.

Despite some relevant discrepancies between experimental and numerical results, the averaged ratios between DB and experimental ultimate loads ranged from 0.78 to 1.13 (averaging all test series within the same test configuration), these results are within typical variability ranges for these materials.

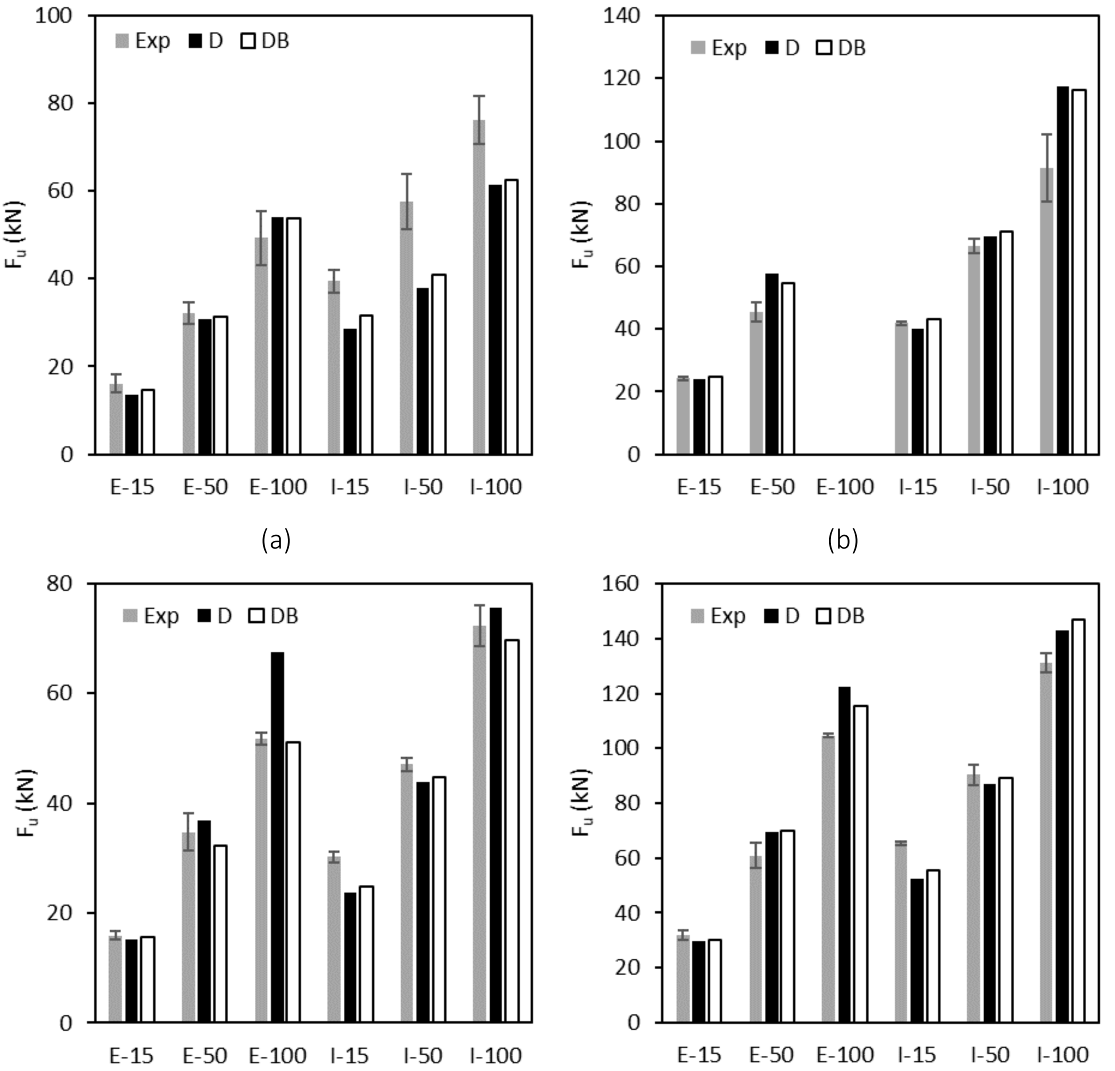

(a) (b)

(c) (d)

Figure 7.8: Experimental and numerical ultimate loads, including geometrically linear (D) and non-linear (DB) models: (a) I150-A; (b) I150-S; (c) I152-C; (d) I200-F.

7.3.4. Strain results

7.3.4.1. Shear strains

Aside from stiffness and ultimate load results, the strain fields were also considered as an important validation for these numerical models. The numerical shear strain results presented ahead were measured in nodes positioned as illustrated in Figure 7.2 (targets S). By measuring the position of these targets, the elongation of the diagonals was determined and thus, the shear strain was estimated. Figure 7.9 presents representative results for different test series.

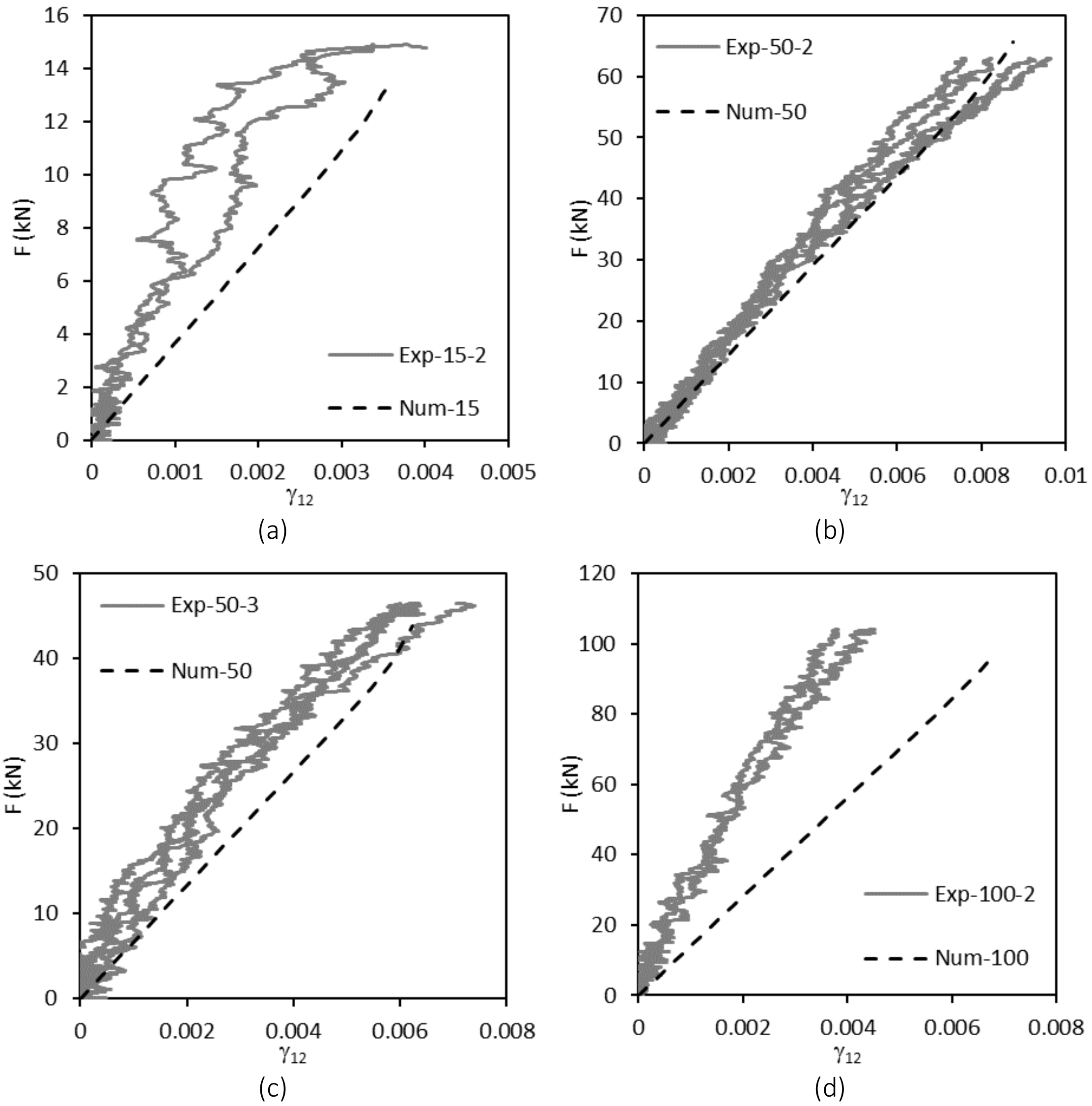

Figure 7.9: Experimental and numerical (DB) shear strain results: (a) I150-A-ETF-15; (b) I150-S-ITF-50; (c) I152-C-ITF-50; (d) I200-F-ETF-100.

The results presented in Figure 7.9 show significant variability in the results, as there are some test series where the numerical and experimental shear strain measurements are nearly identical (as illustrated in Figures 7.9 (b) and (c)) whereas in some test series, the numerical predictions of shear strains were significantly higher than the experimental measurements (Figures 7.9 (a) and (d)). At this time, as no clear trend was found across different materials and bearing lengths, these discrepancies were attributed to the simplification of the web-flange junction geometry (absence of rounded internal corners), which is expected to have a significant influence on the strain distribution between the bearing plate and the web.

7.3.4.2. Compressive strains

The transverse compressive strain fields measured throughout the length of each specimen were also used to validate the numerical models (see Figure 7.2, targets C). Additionally, these results may be used in establishing effective bearing lengths, which may be useful for the development of design formulae. These results were considered for the test series that presented clear signs of web-crushing failure (without relevant out-of-plane displacements), ETF-15 and all ITF test series.

Figure 7.10 presents compressive strain distributions for ETF-15 test series. Figure 7.10 shows a good agreement between numerical and experimental results, showing similar compressive strain profiles along the length of specimen. However, some differences can be found in the peak compressive strains.

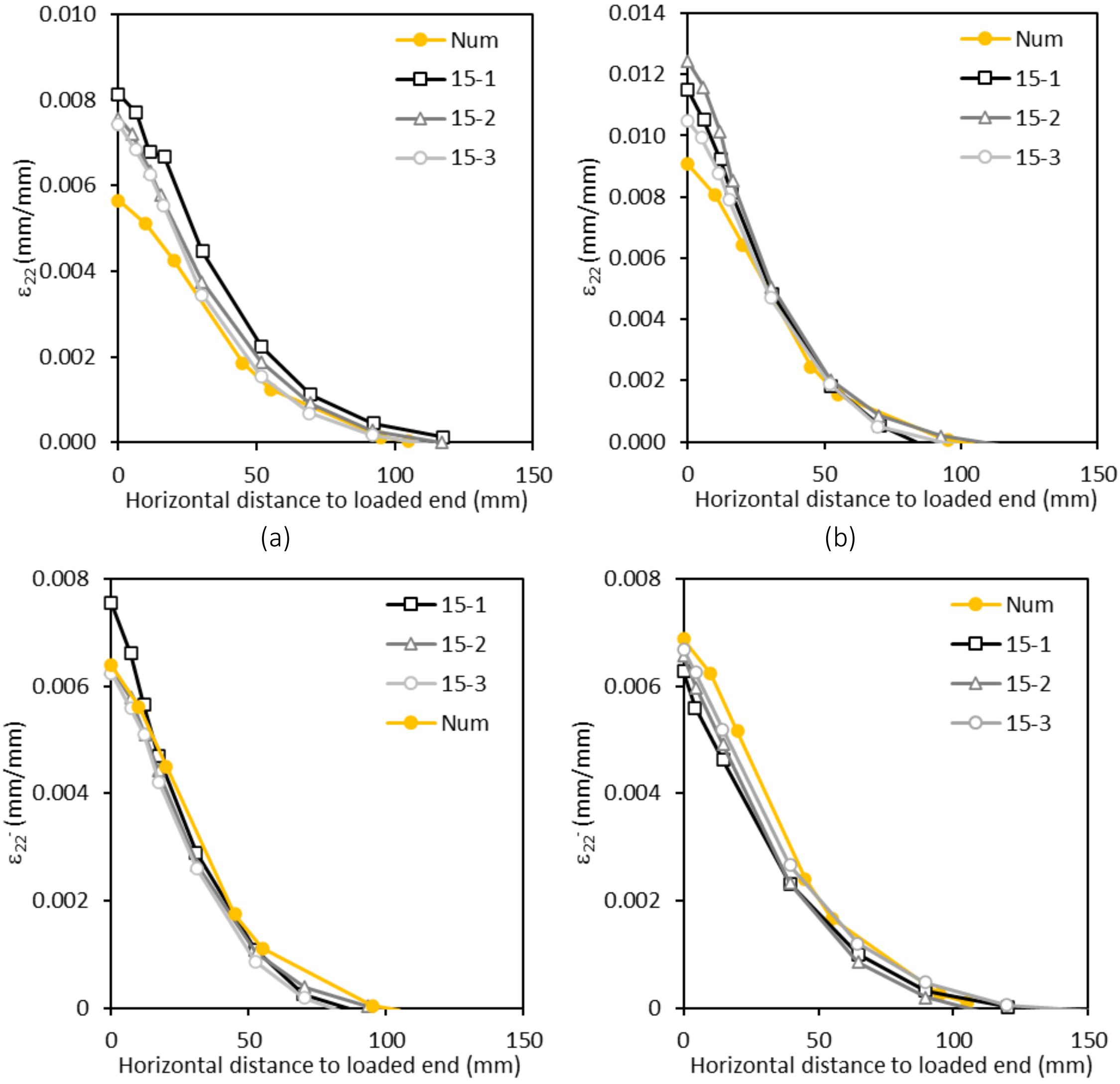

(a) (b)

(c) (d)

Figure 7.10: Experimental and numerical (DB) ETF-15 compressive strain results: (a) I150-A; (b) I150-S; (c) I152-C; (d) I200-F.

Figure 7.11 presents experimental and numerical compressive strain peak values. The numerical results were taken for an applied load of ≈95%, in line with the methodology applied for experimental results [7.10]. One material in particular, I150-A, presented some discrepancies between numerical and experimental results, for the ITF configuration. The remainder of the materials were found to present a satisfactory agreement. The differences found for I150-A materials were attributed to the aforementioned potential underestimation of the transverse compressive strength (60 MPa).

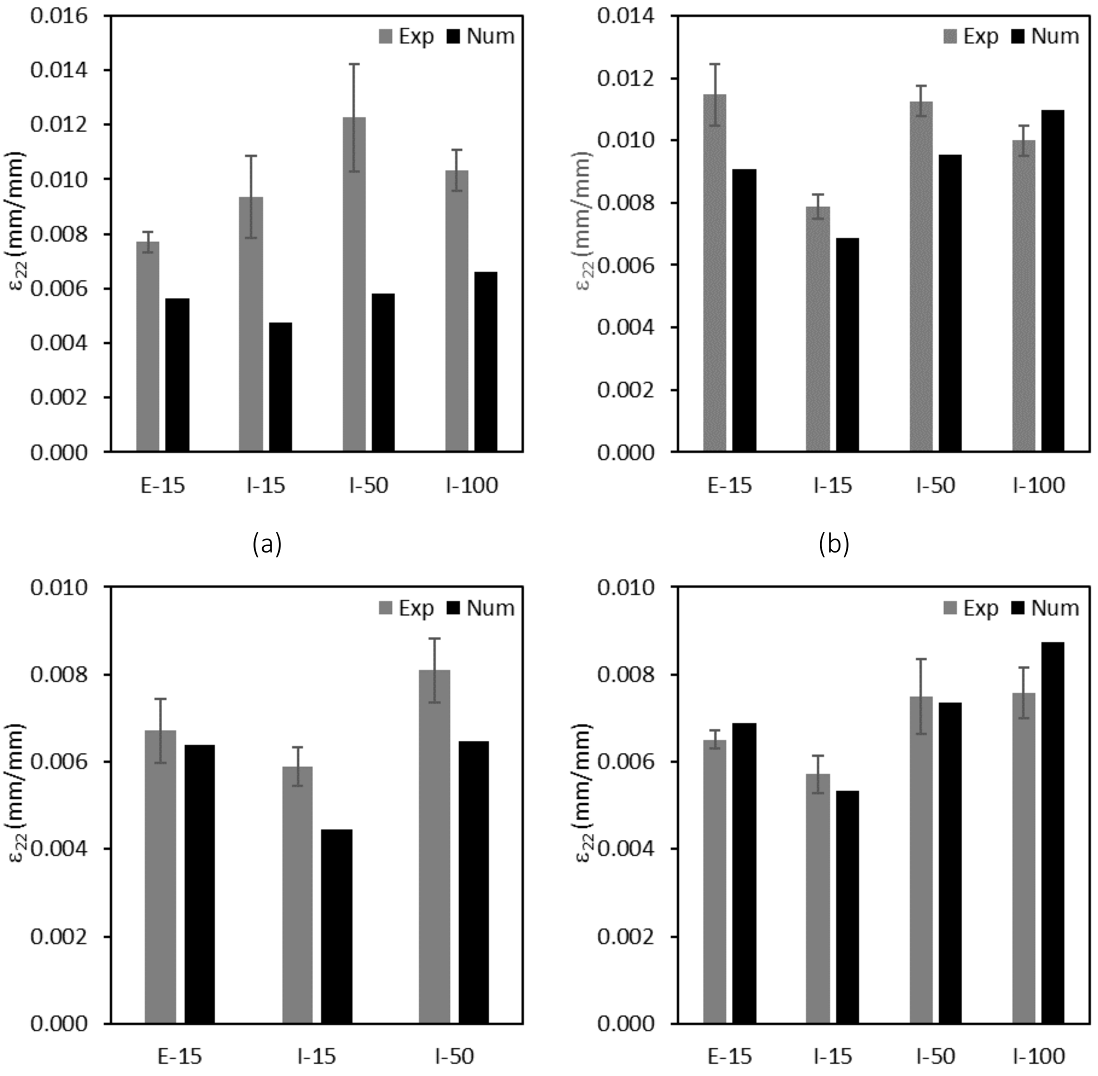

(a)

(b)

(c)

(d)

Figure 7.11: Experimental and numerical (DB) compressive strains at 95% of ultimate load: (a) I150-A; (b) I150-S; (c) I152-C; (d) I200-F.

Despite the differences found in peak compressive strains, it must be highlighted that the normalized compressive strain distributions of numerical models and experimental tests were found to be nearly identical across different materials and test configurations. This trend is illustrated in Figure 7.12, for various representative test series.

Figure 7.12 clearly shows that the models simulate well the experimental tests, in terms of an effective bearing length. These results show that this simplified approach may be a valid option to generate additional data for design purposes.

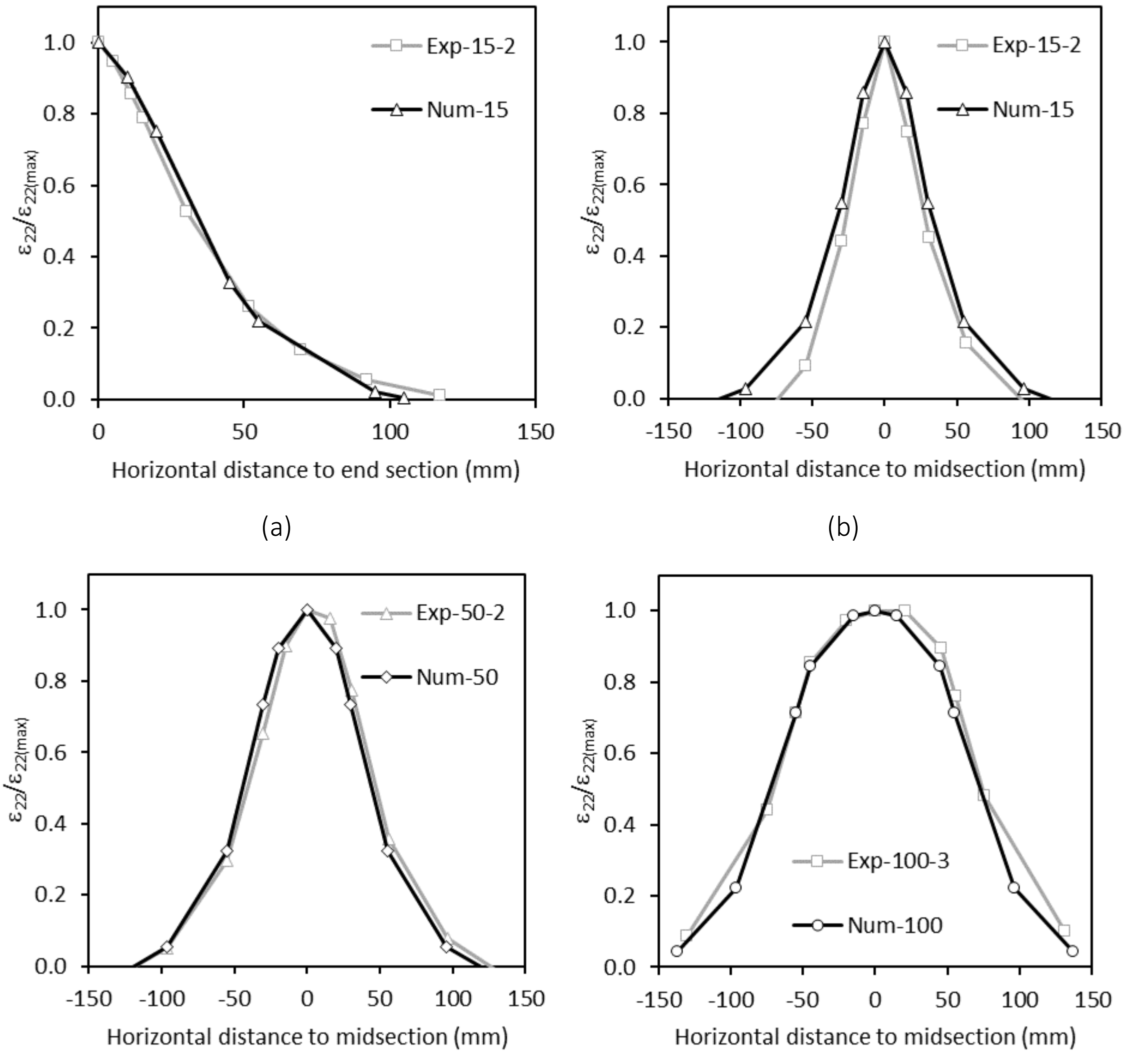

(a) (b)

(c) (d)

Figure 7.12: Experimental and numerical (DB) normalized compressive strain results: (a) I150-A-ETF-15; (b) I150-S-ITF-15; (c) I152-C-ITF-50; (d) I200-F-ITF-100.

7.3.5. Damage initiation analysis

7.3.5.1. Damage initiation *vs*. ultimate load

In this section, the loads that lead to damage initiation (F_i) in DB models, established by the Hashin criterion [7.12], are compared to the experimental ultimate loads, in order to measure the usefulness and impact of the inserted fracture properties on the numerical results. Figure 7.13 presents a summary of damage initiation (F_i) *vs*. experimental ultimate load (F_u) ratios. Damage initiation was reached for load ratios between 61% and 91%, showing that the load increase reached during the damage evolution stage is significant. These thresholds do not account for the I150-A numerical results, which range between 41% and 71%, a difference that highlights the underestimation of the actual strength of this material by the considered transverse compressive strength (60 MPa).

The damage initiation ratios shown in Figure 7.13 are considerably higher than those determined in a previous study [7.8], where damage initiation was predicted through the Tsai-Hill criterion [7.11], with results ranging from 33% to 66% of experimental ultimate loads. This rise can be attributed to two upgrades in the mechanical characterization of pultruded GFRP materials, regarding their shear and compressive properties. The use of the Iosipescu test setup [7.17] instead of the 10° off axis tension test [7.18], as well as the use of the combined load in compression (CLC) test [7.19] instead of the ASTM D 695-02 crushing test [7.20], led to higher and more accurate predictions of the shear and transverse compressive strength of these materials, leading to higher predictions for damage initiation. Despite these upgrades in the mechanical characterization, damage initiation still provides a conservative measure of experimental web-crippling failure.

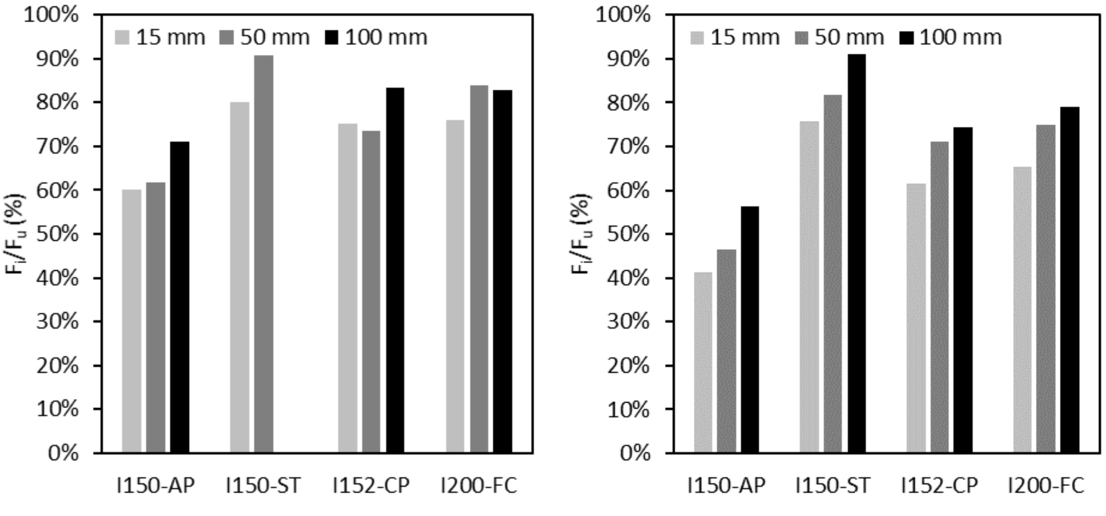

(a) (b)

Figure 7.13: Damage initiation load *vs*. experimental ultimate load ratios: (a) ETF test series; (b) ITF test series.

7.3.5.2. Stress component analysis at damage initiation

The stresses that led to damage initiation are analysed in this section, considering three different locations of the profile, illustrated in Figure 7.14: (i) the element with highest damage gradient, localized below the bearing plate, near its edge (1); (ii) the element adjacent to the bearing plate edge (2); and (iii) an element at the centre of the web, naturally more relevant for cases where web-buckling occurs (3).

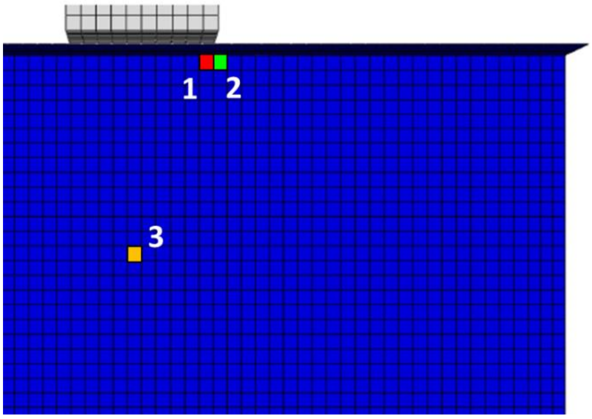

Figure 7.14: Elements selected for stress analysis: (1) below the bearing plate, near an edge; (2) adjacent to the bearing plate edge; (3) centre of the web.

This analysis was performed for the profiles with thinner and stockier webs (I152-C and I200-F), for the ETF-100 and ITF-15 test series, resulting in test cases prone to present web-buckling (I152-C-ETF-100) and web-crushing (I200-F-ITF-15) respectively. The stress component analyses are illustrated in Figures 7.15 and 7.16, for I152-C-ETF-100 and I200-F-ITF-15, respectively.

The stress components are normalized in respect to the corresponding material strength component, in line with the squared ratios of Hashin criterion ($s_{ij} = \sigma_{ij}^2/\sigma_{uij}^2$) [7.12], including longitudinal (s_{11}), transverse (s_{22}) and shear (s_{12}) stress ratios. Figures 7.15 and 7.16 also include the evolution of the Hashin criterion index for transverse compression (H_{mc}) and the transverse compressive damage variable (D_{mc}) with the imposed displacement U.

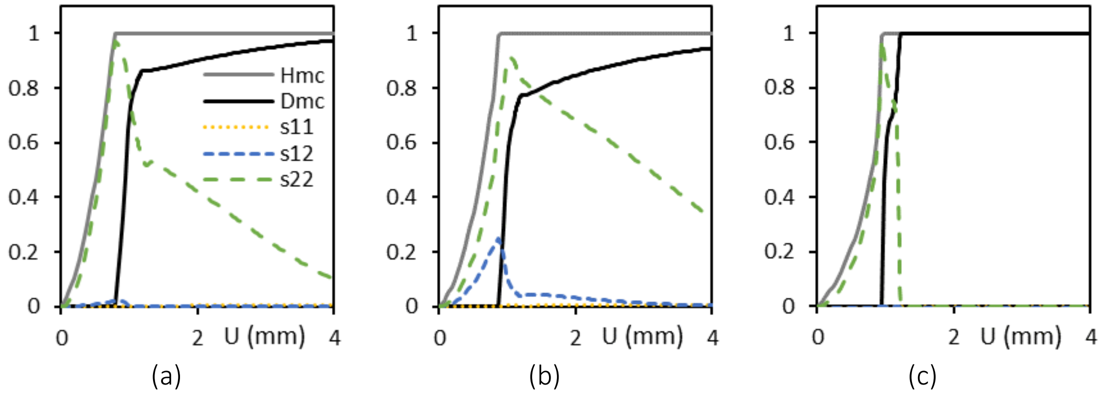

(a) (b) (c)

Figure 7.15: Stress component evolution with the imposed displacement of I152-C-ETF-100 model: (a) below the bearing plate (1); (b) adjacent to bearing plate edge (2); (c) centre of the web (3).

Figure 7.15 clearly shows that the transverse compressive stress governs both damage initiation and evolution as the ratio s_{22} achieves almost a unit value at failure. The shear stress squared ratio s_{12} reaches a maximum of 0.25, in Figure 7.15 (b), showing a relevant but lower contribution to damage initiation and evolution. This trend highlights that previous results [7.8], which indicated that shear stresses governed damage initiation, were significantly hindered by excessively conservative shear strength estimates. It is also noteworthy that global failure occurs due to damage at the centre of the web because the damage parameter suddenly reaches a unit value for an applied displacement of ≈1 mm (Figure 7.15 (c)), whereas Figures 7.15 (a) and (b) show a non-linear trend for the damage variable, which develops in a smoother rate after the centre of the web is fully damaged.

Figure 7.16 shows a different trend than that previously shown in Figure 7.15, as the centre of the web should not be damaged in web-crushing failure. Figure 7.16 (c) agrees with this pattern, showing no signs of damage initiation. Figures 7.16 (a) and (b) are similar to their counterparts in Figure 7.15, showing that transverse compressive stresses govern damage initiation and evolution. The shear stresses adjacent to the bearing plate edges (Figure 7.16 (b)) reach only a squared ratio of 0.15. These low contributions of shear stress to damage initiation are in line with the experimental results reported in [7.10], where shear strain measurements led to relatively low shear stress estimates, when compared to the shear strength of each material.

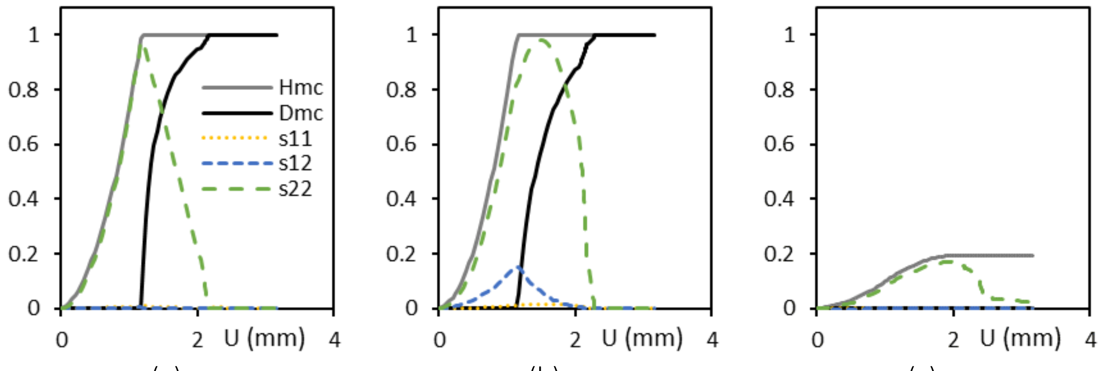

(a) (b) (c)

Figure 7.16: Stress component evolution *vs*. applied displacement of I200-F-ITF-15 model: (a) below the bearing plate (1); (b) adjacent to bearing plate edge (2); (c) centre of the web (3).

7.4. Web-crippling of U-section beams

The numerical models of U-section profiles were analysed in a narrower scope, when compared to the analysis performed for I-section profiles in the previous section. This more limited study is justified by the lower amount of experimental data reported in Chapter 6.

7.4.1. Failure modes

The experimental tests of all U-section specimens showed a mixed failure mode, with damage developing near the web-flange junction and significant out-of-plane displacements developing simultaneously at the centre of the web [7.10]. The D models consistently showed only web-crushing failure, near the web-flange junctions. These models should be disregarded in this analysis, as significant out-of-plane displacements have been reported in experimental tests [7.10].

In a different trend, the DB models showed a mixed failure mode for the U150-S-ITF-15 series, similarly to that of experimental tests, with damage developing near the web-flange junctions and significant out-of-plane displacements. All other DB models only presented damage at the centre of the web, showing a different trend to experimental results. Figure 7.17 compares experimental and numerical (DB) failure modes of U150-S-ITF-15 and U150-S-ETF-100 series.

This discrepancy between experimental and numerical failure modes is attributed to the simplification of the web-flange junction geometry. A round web-flange junction geometry was also considered, however, this option required using significantly finer meshes (<1 mm), in order to have a refined mesh in the round web-flange junction area. Furthermore, a simplified numerical round web-flange junction does not simulate the added thickness found on this region of the experimental specimens. As the scope of this study is the use of simplified numerical tools and to maintain a coherent numerical analysis for I-section and U-section profiles, this option was not pursued.

7.4.2. Load *vs*. displacement curves

This section presents a comparison of experimental and numerical load *vs*. out-of-plane displacement curves. The experimental tests were reported to present significant out-of-plane displacements, developing steadily throughout each test [7.10]. Figure 7.18 presents a summary of experimental and numerical load *vs*. out-of-plane displacement curves, for all U-section test series.

Figure 7.18 shows that the DB models present a relatively good fit to experimental results, whereas D models present an expectable considerably higher stiffness. The most significant discrepancies in the results of Figure 7.18 were reported for the U150-S-ITF-15 series (Figure 7.18 (b)), where even the DB models present a significantly stiffer behaviour, compared to experimental results. However, in all test series, the DB models seem to simulate accurately the overall trend of the experimental load *vs*. out-of-plane displacement curves.

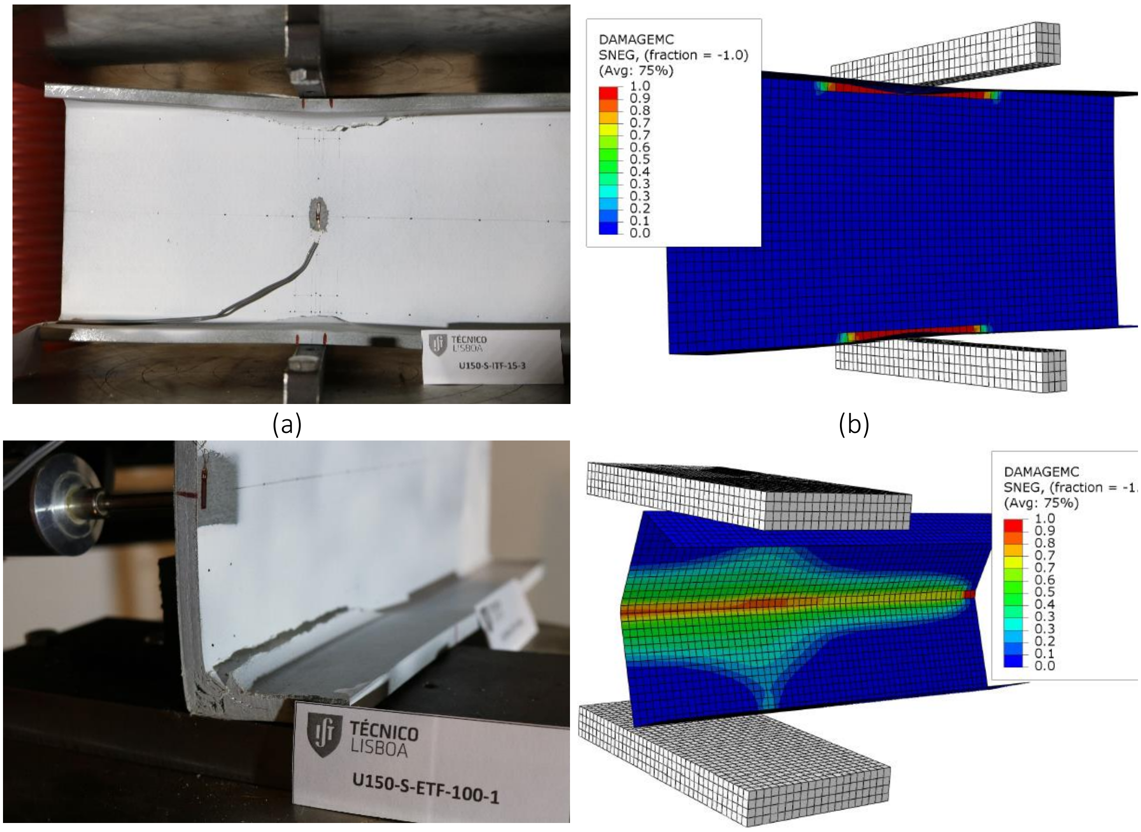

(a) (b)

(c) (d)

Figure 7.17: Experimental and numerical (DB) failure modes of U-section series: (a) U150-S-ITF-15-3 test; (b) U150-S-ITF-15 model; (c) U150-S-ETF-100-1 test; (d) U150-S-ETF-100 model.

7.4.3. Ultimate loads

Figure 7.19 presents a summary of experimental and numerical ultimate loads of U-section series. The numerical results were determined through DB models, which have been found to better fit the experimental results in the previous section.

The results presented in Figure 7.19 show a good agreement between experimental and numerical ultimate loads, showing that, despite the discrepancies found between experimental and numerical failure modes, the numerical models provided accurate failure predictions, within the known levels of mechanical variability shown by these materials.

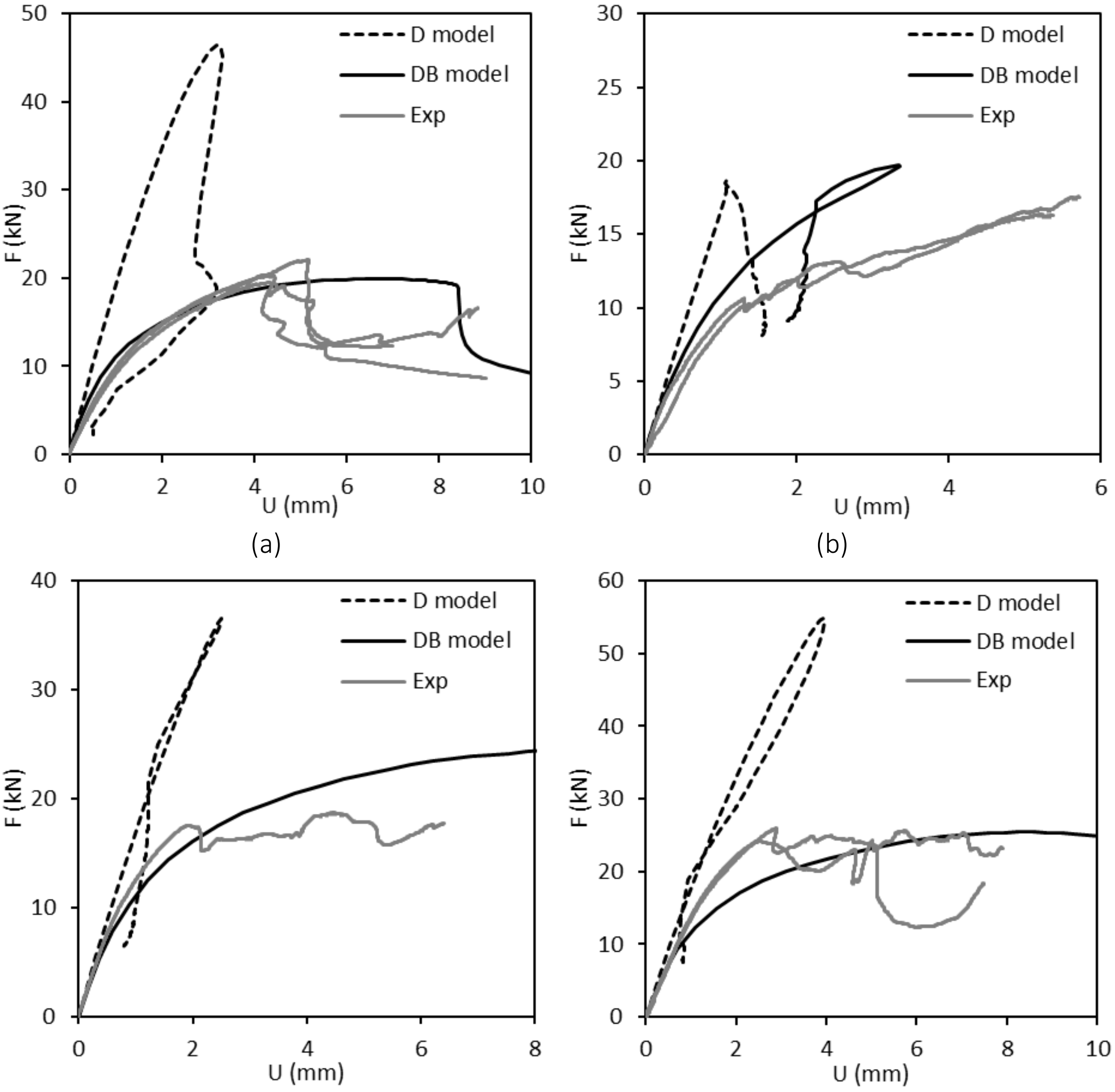

(a) (b)

(c) (d)

Figure 7.18: Experimental and numerical load *vs*. out-of-plane displacement curves of U-section series: (a) U150-S-ETF-100; (b) U150-S-ITF-15; (c) U150-S-ITF-50; (d) U150-S-ITF-100.

7.5. Conclusions

This chapter presented a numerical study on the web-crippling failure of GFRP profiles under external-two-flange (ETF) and internal-two-flange (ITF) configurations. The numerical study consisted of a simplified approach, implementing fracture toughness properties as damage evolution parameters, and its results were validated through experimental tests on four I-section profiles and one U-section profile. These models, with homogeneous properties through the thickness of the material and relatively coarse shell FE meshes, were successful in simulating complex web-crippling experimental tests. Therefore, they can easily be implemented in current commercial software, provided the mechanical characterization of the materials is available.

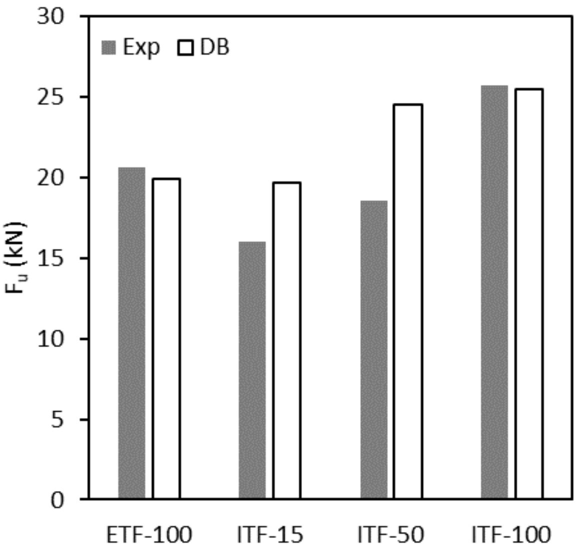

Figure 7.19: Experimental and numerical (DB)
ultimate loads of U-section series.

It was shown that models including only material damage (without web instability effects – D analysis) or web elastic buckling (without material damage effects – B analysis) were unable to provide an overall correct characterization of web-crippling. Only the analysis with both effects included (DB analysis) was able to tackle the problem in a consistent and rigorous way. This analysis was particularly important in understanding the failure modes reported for the experimental tests, shedding light on the interaction of damage initiation near the bearing plate edges and the ultimate web-buckling deformed shape of several test series. Aside from the failure modes, the DB models provided estimates of stiffness with average differences ranging from -17% to 13%, as well as estimates of ultimate load with differences that ranged from -22% and 13%, in respect to experimental tests. With the exception of one material (I150-A), the averaged differences between experimental and numerical ultimate loads per material ranged from -9% to 13%.

The numerical models were also validated against shear and compressive strain measurements. Relevant discrepancies were found between numerical and experimental shear strain results, which were attributed to the simplification of the web-flange junction. A good match was obtained between the compressive strain fields obtained in the numerical models and experimental tests. The differences found between numerical and experimental peak compressive strains ranged from -25% and 6%.

The values of damage initiation to ultimate load ratio varied between 61% and 91%, thus showing that stress-based criteria are inadequate to predicting web-crippling failure. In a different perspective, these results highlighted the impact of considering updated test methods for mechanical characterization, such as the combined load in compression test (CLC) [7.19] and the V-notched shear test [7.17], as previous research works have been hindered by significant underestimations of mechanical properties [7.8].

Finally, stress component analyses showed that damage initiation occurred below the bearing plate edges, with the largest contribution being attributed to transverse compressive stresses, while shear stress influence was found to be reduced. These results show that the transverse compressive strength and fracture toughness of a profile play a major role in its ultimate web-crippling failure in either ETF or ITF configurations.

7.6. References

[7.1] Girão Coelho, A. M., Toby Mottram, J., & Harries, K. A., Finite element guidelines for simulation of fibre-tension dominated failures in composite materials validated by case studies. Composite Structures, 126, pp. 299-313, 2015.

[7.2] Martins, D., Proença, M., Correia, J. R., Gonilha, J., Arruda, M., & Silvestre, N. (2017). Development of a novel beam-to-column connection system for pultruded GFRP tubular profiles. Composite Structures, 171, pp. 263-276.

[7.3] Borowicz, D. T., Bank, L. C., Behavior of Pultruded Fiber-Reinforced Polymer Beams Subjected to Concentrated Loads in the Plane of the Web*, Composites for Construction*, 15-2, pp. 2-9, 2011.

[7.4] Borowicz, D. T., Bank, L. C., Effect of web reinforcement on the behavior of pultruded fiber-reinforced polymer beams subjected to concentrated loads. *Construction and Building Materials*, 47, pp. 347-357, 2013.

[7.5] Wu, C., Bai, Y., & Zhao, X. L., Improved bearing capacities of pultruded glass fibre reinforced polymer square hollow sections strengthened by thin-walled steel or CFRP, *Thin-Walled Structures*, 89, pp. 67-75, 2014.

[7.6] Wu, C., Zhang, L., Bai, Y., Zhao, X. L., Web crippling behavior of pultruded GFRP channel sections under transverse bearing load, *Composite Structures*, 209, pp. 129-142, 2019.

[7.7] Almeida-Fernandes, L., Gonilha, J., Correia, J. R., Silvestre, N., Nunes, F., Web-crippling of GFRP pultruded profiles. Part 1: Experimental study. *Composite Structures*, 120, pp. 565-577, 2015.

[7.8] Almeida-Fernandes, L., Nunes, F., Silvestre, N., Correia, J. R., Gonilha, J., Web-crippling of GFRP pultruded profiles. Part 2: Numerical analysis and design. *Composite Structures*, 120, pp. 578-590, 2015.

[7.9] Nunes F., Silvestre N., Correia JR., Progressive damage analysis of web crippling of GFRP pultruded I-sections. *Composites for Construction*, 21(3), pp. 1-13, 2016.

[7.10] Almeida-Fernandes, L., Correia, J. R., Silvestre, N., Effect of fibre layup in web-crippling of pultruded GFRP profiles, *Composite Structures*, submitted, 2020.

[7.11] S. W. Tsai, Strength characterisation of composite materials, Tech. Rep. NASA CR-224, National Aeronautics and Space Agency (1965).

[7.12] Hashin, Z., and Rotem, A., A fatigue criterion for fiber-reinforced materials, *Journal of Composite Materials*, 7, pp. 448-464, 1973.

[7.13] Simulia, “Abaqus/CAE 2018”, 2018.

[7.14] Almeida-Fernandes, L., Silvestre, N., Correia, J. R., Characterization of transverse fracture properties of pultruded GFRP material in tension, *Composites Part B: Engineering*, 175, 107095, 2019.

[7.15] Almeida-Fernandes, L., Correia, J. R., Silvestre, N., Transverse fracture behaviour of pultruded GFRP materials in tension: Effect of fibre layup, *Composites for Construction*, 24(4), 04020019, 2020.

[7.16] Almeida-Fernandes, L., Silvestre, N., Correia, J. R., Arruda, M. R. T., Compressive transverse fracture behaviour of pultruded GFRP materials: experimental study and numerical calibration, *Composite Structures*, 247, 112453, 2020.

[7.17] ASTM D5379-05, Standard test method for shear properties of composite materials by the V-notched beam method. West Conshohocken, PA: ASTM, 2000.

[7.18] Hodgkinson J. M., *Mechanical Testing of Advanced Fibre Composites*, CRC Press, Cambridge, England, 2000.

[7.19] ASTM D6641 / D6641M – 09, Standard Test Method for Compressive Properties of Polymer Matrix Composite Materials Using a Combined Loading Compression (CLC) Test Fixture, ASTM International, West Conshohocken, Pennsylvania, 2009.

[7.20] ASTM D 695-02, “Standard Test Method for Compressive Properties of Rigid Plastics”, American Society for Testing and Materials (ASTM), West Conshohocken, PA, 2006.

Chapter 8. Design expressions for web-crippling of pultruded GFRP profiles

8.1. Introduction

8.1.1. Web-crippling in pultruded GFRP beams

Web-crippling is a failure mode where concentrated loads applied in the in-plane transverse direction of a beam's web lead to localized failure of the web [8.1]. This failure mode occurs typically when secondary beams unload on primary beams, or near support sections of beams. The web-crippling of steel beams has been extensively addressed through a significant amount of research, which has led to the development of well-established design guidelines for steel structures, such as the North American standard [8.2] and European standards [8.3, 8.4]. Conversely, and to the best of the authors' knowledge, only a few studies have been performed regarding web-crippling of pultruded GFRP beams [8.1, 8.5-8.11]. To some extent, this limited research is related to the fact that pultruded GFRP structures are typically limited by their serviceability limit states [8.12]; however, web-crippling may become a prevalent failure mode for these structures when the loads are applied in the weakest in-plane direction of the GFRP material. In fact, pultruded GFRP materials exhibit a markedly orthotropic behaviour, with the elastic moduli and ultimate stresses in the in-plane transverse direction being significantly lower than in the longitudinal direction [8.13], which presents the majority of fibre content.

Previous research [8.8, 8.10, 8.14-8.16] has shown that the bearing length considered in web-crippling loading configurations has a significant influence in the stiffness, failure mode and ultimate load of GFRP profiles; however, to date there are no well-established and broad-ranged design guidelines that relate the bearing length with the web-crippling bearing capacity of a pultruded GFRP beam. In fact, web-crippling is a difficult phenomenon to address due to its inherent three-dimensional nature and the significant number of related variables, such as the position of concentrated loads, web slenderness and bearing length. This inherent variability led to the definition of various web-crippling based test configurations, where loading is applied on one flange or two flanges. In addition, these test configurations vary in respect to the position of the loaded section, from interior sections to end sections. The web-crippling phenomenon is typically triggered by three main failure modes [8.9]: (i) web crushing, which consists of material failure near the web-flange junctions (typical of stocky webs and/or short bearing lengths); (ii) web buckling, consisting of local buckling of the web in the loaded area (typical of slender webs and/or long bearing lengths); and (iii) interaction between web crushing and web buckling, for intermediate cases.

8.1.2. Previous design expressions proposed for pultruded GFRP materials

This section outlines the most relevant contributions for design guidance concerning web-crippling of pultruded GFRP beams. Firstly, Bank [8.17] proposed separate design expressions to compute the ultimate loads for web crushing and web buckling. The ultimate load for web-crippling was then estimated as the minimum between these two, without any attempt to identify the interaction between the two. These formulae are similar to those presented in the earliest design guidelines for composite structures [8.18].

Borowicz and Bank [8.1] performed a significant number of IOF tests considering I-shaped and wide flange sections. Based on the experimental data, the authors presented a formula to predict the web-crippling bearing capacity of IOF cases, in which the length and thickness of the bearing plates were considered explicitly. Borowicz and Bank [8.1] considered the interlaminar shear strength to be the most influential property on IOF web-crippling failure.

Wu and Bai [8.6] performed a comprehensive study on ETF and ITF tests on tubular sections[3]. However, the bearing length was fixed for all tests and thus, limited information was reported on the influence of this parameter. Wu and Bai [8.6] also considered the interlaminar shear strength as the most influential property for their proposed design expressions. This trend was considered less clear in [8.14] for ETF and ITF tests, as significant transverse compressive stresses were found to occur between both bearing plates. As all specimens failed due to crushing near the web-flange junction, no web buckling considerations were made in respect to the proposed design expressions.

Previous research performed by the authors [8.14], based on ETF and ITF tests [8.8], led to the development of an expression which combined the analytical frameworks for steel structures provided by the North American standard [8.2] and Eurocode 3 - Part 1-5 [8.4]. The formula proposed in [8.14] combined the flexible format of the North American standard, based on four calibrated parameters, with the buckling formulations presented in Eurocode 3 - Part 1-5. Despite the good accuracy of this empirical approach to predict the experimental ultimate loads [8.8], the analytical expressions were mostly empirical, not being grounded on a rational mechanical basis.

In a more recent study, Wu *et al*. [8.9] investigated the web-crippling bearing capacity of pultruded GFRP channel section profiles. In this study the bearing length was also fixed for all tests. Wu *et al*. [8.9] reported different failure modes in this experimental study, as the slender specimens presented web buckling failure, with significant out-of-plane displacements and damage at the centre of the web. Considering these results, Wu *et al*. [8.9] proposed separate design expressions for web crushing and web buckling failure. Again, the interaction between web crushing and web buckling was not considered.

Very recently, Wu *et al*. [8.10] investigated the web-crippling behaviour of pultruded GFRP channel sections for various bearing lengths. The bearing length was found to have a significant impact on the ultimate loads and failure modes. Finally, these authors successfully implemented the previously developed formulae [8.9] to the additional experimental results, by addressing web crushing and web buckling separately.

From the summary of analytical studies presented above, it is clear that the interaction between web crushing and web buckling was never addressed by the proposed analytical solutions, with exception to the empirical formula previously proposed by the authors in [8.14].

8.1.3. Direct strength method

One of the most promising design methods for thin-walled steel structures is the direct strength method (DSM), as it accounts for the influence of several parameters in a rational way and grounded basis. DSM was initially proposed for steel beams by Schafer and Peköz [8.19] in 1998. Since then, it has been continuously improved [8.20, 8.21] and was included in the latest versions of the North American Specification for the design of cold-formed steel structures

---

[3] These authors also adopted test configurations for foundation structural elements, where one flange is continuously supported on the ground, which have not been considered for design standards.

AISI S100-16 [8.22] and the Australian/New Zealand Standards [8.23]. This method consists of establishing a design curve, based on the knowledge of (experimental) ultimate loads and both (theoretical) buckling and yield loads. The design curve is defined by plotting the variation of the ultimate-to-yield load ratio as a function of the slenderness, which is computed as the square root of the yield-to-buckling load ratio. This calibrated curve can then be implemented to any additional case, provided that the buckling and yield loads are known. The DSM design curve provides the ultimate load by multiplying the yield load to the fitted buckling reduction factor. Until 2016, the DSM was successfully applied to failure of columns (flexural buckling), beams (lateral-torsional buckling), beam-columns and also to shear buckling of steel beams. In 2016, the DSM was originally developed by Natário *et al*. [8.24, 8.25] for the design of steel beams against web-crippling. They reported a good agreement between DSM results and experimental results reported in the literature, including different section sizes and geometries. Besides the good overall performance of DSM, it was possible to consider the effect of interaction between yielding and buckling in a rational way.

Therefore, DSM is an interesting methodology to simultaneously take into account web buckling, web crushing, and the interaction between both phenomena when addressing the design of pultruded GFRP beams against web-crippling. The implementation of DSM for web-crippling of pultruded GFRP beams would essentially require replacing the yield load by the material crushing load. In Chapter 7, web crushing loads were determined through geometrically linear damage models performed in Abaqus [8.26], where damage initiation is determined by the Hashin criterion [8.27] and damage evolution is determined as a function of fracture toughness inputs. The transverse compressive stresses were found to have the most influential role on damage initiation and evolution, contrasting with findings reported by Wu *et al*. [8.9, 8.10], where the interlaminar shear strength was considered to predict web crushing. In this chapter, the results reported in Chapter 7 were considered and thus the ultimate transverse compressive strength was selected as the main property for the estimation of material crushing load.

In summary, the main objective of this study is to develop, for the first time, the DSM for the design of pultruded GFRP beams against web-crippling failure. Firstly, the specimens tested experimentally are briefly addressed, regarding the section geometries, material properties and ultimate loads. Then, a numerical study is presented and finite element (FE) models are used to determine the buckling loads, crushing loads and ultimate loads of the tested specimens, in order to assess the behaviour and trend of DSM curves for web-crippling. After that, the numerical models enable the calibration of approximate formulae to compute the buckling loads and crushing loads. Finally, a new DSM curve is developed based on the experimental ultimate loads and the approximate buckling and crushing loads.

8.2. Summary of experimental results

The experimental results comprise four I-section profiles, three described in Chapter 6 and one in [8.8], as detailed in Table 8.1. The profiles described in [8.15] were sourced from the following suppliers: (i) Creative Pultrusions (C); (ii) Fiberline Composites (F); and (iii) STEP (S). Table 8.1 presents the geometry and mechanical properties determined for each profile, where *E* stands for the elastic modulus, G_{12} stands for the shear modulus, σ_u stands for the ultimate stress, τ_{u12} stands for the ultimate shear stress, 1 and 2 indicate respectively the longitudinal and in-plane transverse directions of the profile, and + and - identify tensile and compressive properties. Table 8.1 also includes the transverse tensile (G_2^+) and compressive (G_2^-) fracture toughness of each material determined in previous studies [8.28-8.30], which are required for performing FE damage analyses.

Table 8.1: Average geometrical and mechanical properties of test materials [8.8, 8.15].

Material	Height x Width (mm)	Web thick., t_w (mm)	E_{11}^{+} (GPa)	E_{22}^{-} (GPa)	G_{12} (GPa)	σ_{u11}^{+} (MPa)	σ_{u22}^{-} (MPa)	τ_{u12} (MPa)	G_2^{+} (N/mm) [8.28, 8.29]	G_2^{-} (N/mm) [8.30]
I152-C [8.15]	152x76	6.3	28.8	10.9	4.2	416	104	65	160	42
I200-F [8.15]	200x100	9.9	29.6	10.8	2.9	323	122	67	20	48
I150-S [8.15]	150x75	8.1	30.0	9.3	3.2	377	123	70	10	67
I400-A [8.8]	400x150	14.5	27.8	7.7	3.8*	296	86	21*	NA	NA

* Determined through a 10° off-axis tensile test [8.31].

The I-section profile described in [8.8], with 400 mm of height, was manufactured by Alto Perfis Pultrudidos (I400-A). The geometry and material properties of this material are also summarized in Table 8.1. However, the experimental study performed in [8.8] did not include the characterization of its fracture properties, and therefore the I400-A material was not included in the numerical study presented herein, being included only in respect to its experimental web-crippling results. In addition, its shear properties were determined through a 10° off-axis tensile test [8.31], whereas the materials studied in [8.15] were characterized through the Iosipescu shear test (V-notched specimen) [8.32]. The 10° off-axis tensile test has been found to significantly underestimate the shear strength of the material [8.16].

Three other materials were tested in [8.8], however their mechanical characterization regarding transverse compression was based on a different test method, described in ASTM D 695-02 [8.33], whereas the results determined for I400-A and the materials reported in [8.15] were based on the combined load in compression (CLC) test method, standardized in ASTM D6641 [8.34]. Given this difference in mechanical characterization, the remainder of the materials tested in [8.8] were only considered for validation of the proposed expression, as detailed in Section 8.5.

In both these experimental studies [8.8, 8.15], the test setup implemented for ETF and ITF loading configurations was identical, consisting of bearing plates positioned at both flanges in an end and interior section, respectively (see Chapter 6). The bearing plates were composed of three sets, with bearing lengths of 15, 50 and 100 mm. Therefore, the test series were described as follows: (i) material; (ii) test configuration; and (iii) bearing length.

The experimental results showed a significant influence of the bearing length (l_b) on both stiffness and ultimate load. Table 8.2 summarizes experimental ultimate loads for the four materials considered in this study, including ETF and ITF tests. The I200-F profile stands out with the overall highest ultimate loads.

Most specimens failed due to web crushing, whereas specimens from the I152-C-ETF-50 and 100 series failed due to web buckling [8.15]. In addition, specimens from the I150-S-ETF-50 and the I200-F-ETF-50 and 100 series presented a mixed failure mode, consisting of damage initiation attributed to web crushing near the web-flange junctions leading to web buckling and damage at the centre of the web. This failure mode was labelled as web crushing failure, due to the consistent signs of damage initiation near the web-flange junctions. Finally, specimens from the I400-A-ETF-100 series were found to fail due to web-buckling phenomena, whereas those from the I400-A-ITF-100 series were reported to present web crushing failure [8.8]. Figure 8.1 presents illustrative examples of these failure modes. For additional information on these web-crippling tests, the reader is referred to [8.8, 8.15].

Table 8.2: Experimental web-crippling ultimate loads (kN).

Profile	Specimen	ETF			ITF		
		l_b=15 mm	l_b=50 mm	l_b=100 mm	l_b=15 mm	l_b=50 mm	l_b=100 mm
I152-C [8.15]	1	16.2	38.0	52.6	29.1	46.0	74.9
	2	15.2	34.9	52.1	30.5	48.4	69.7
	3	16.5	31.2	50.5	29.9	47.0	
	4				31.3		
I200-F [8.15]	1	33.8	65.5	105.1	64.5	89.0	135.2
	2	30.5	61.0	104.4	66.0	94.5	128.9
	3	31.7	56.2		65.7	87.6	129.6
I150-S [8.15]	1	24.8	45.3		41.4	67.9	99.8
	2	23.8	42.5		41.6	63.9	79.1
	3	24.2	48.5		42.4	67.8	95.3
I400-A [8.8]	1			71.5			119.6
	2			66.4			133.3
	3			84.1			128.9

8.3. Numerical study

8.3.1. Numerical modelling

The numerical study reported in this chapter used the same FE numerical models detailed in Chapter 7. These models considered (i) the material properties homogenized through the thickness of the material, instead of considering the fibre layup, and (ii) the web-flange junction with a sharp corner geometry, instead of a rounded one. The specimens were modelled with S4R shell FEs and the bearing plates were simulated through C3D8R solid FEs.

In addition to the simulation of the experimental tests that had been performed, the numerical models were also developed for a wider range of section geometries and bearing lengths. This step was necessary to generate extra numerical data for profiles with higher slenderness than the ones tested. Therefore, I152-C and I150-S profiles were also modelled with heights of 175 and 200 mm (instead of ~150 mm), whereas the I200-F profile was also simulated with heights of 150 mm (lowest web height-to-thickness ratio) and 250 mm (instead of 200 mm). Bearing lengths of 30, 75, 125 and 150 mm, other than those considered in the experimental tests, were also considered in the numerical study. In accordance with the DSM philosophy, three different types of analysis were performed [8.16]: (i) B-analysis to extract the buckling loads; (ii) D-analysis to compute the crushing loads; and (iii) DB-analysis to determine the ultimate loads. Next, these analyses are described in more detail.

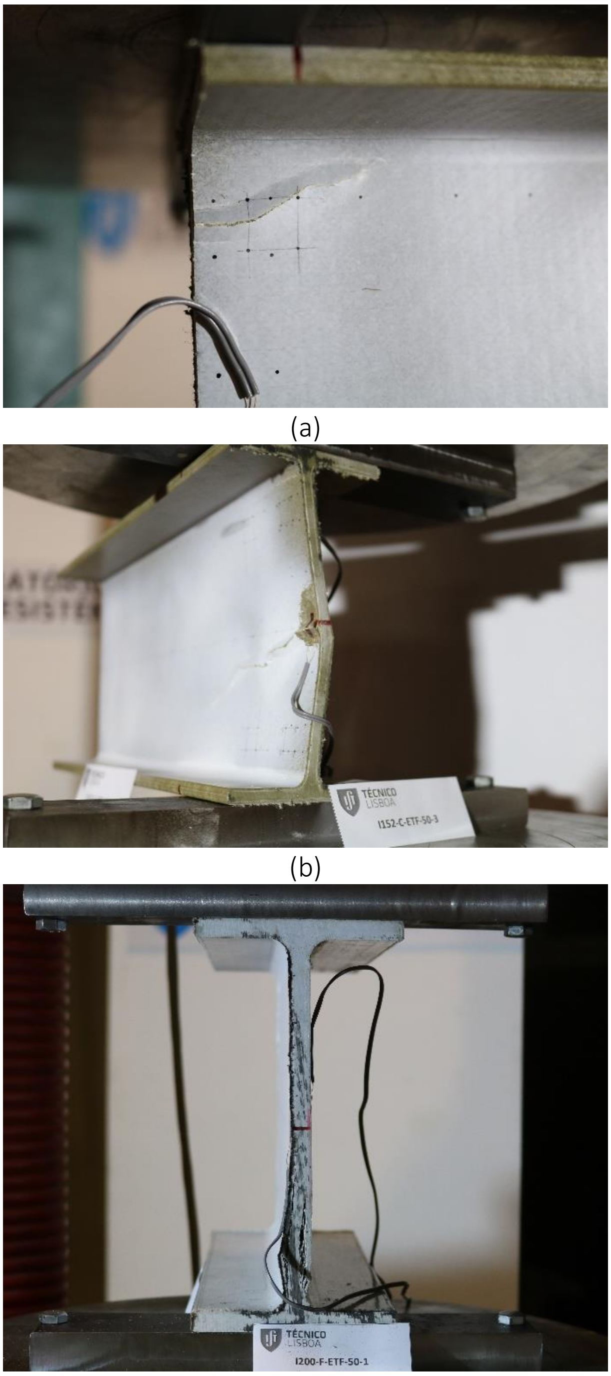

(a)

(b)

(c)

Figure 8.1: Experimental failure modes reported in [8.15]: (a) web crushing; (b) web buckling; (c) mixed failure mode.

8.3.1.1. B-analysis

This numerical analysis consists of obtaining elastic predictions of web buckling load (P_{buck}), ignoring material strength or fracture properties. This buckling analysis was performed with the goal of comparing numerical buckling loads to the experimental ultimate loads and failure modes.

8.3.1.2. D-analysis

These models should accurately predict web crushing load (P_{crush}), ignoring the detrimental buckling effects by adopting geometrically linear analysis. This analysis consisted of implementing built-in tools available in Abaqus [8.26] for damage analysis. Damage initiation was determined through the Hashin criterion [8.27], whereas damage evolution was simulated by implementing fracture toughness values as inputs. These fracture properties were characterized for transverse tension (G_2^+) and compression (G_2^-) in previous research performed by the authors [8.28-30]. The longitudinal fracture properties were sourced from the literature (100 N/mm, [8.35]) and are not expected to influence the results [8.16].

8.3.1.3. DB-analysis

These models should be able to compute the web-crippling ultimate loads (P_u), without ignoring any of the previous effects, as this analysis includes both material damage and buckling effects (materially and geometrically non-linear analysis). Note that the geometrical imperfections were not experimentally measured and thus a very small initial geometrical imperfection was considered, with the deformed shape of the first buckling mode and having a maximum amplitude of 0.01 mm. This small imperfection should have a minor influence on the numerical results, but enables the iterative solution to pass through the bifurcation point (increased convergence) if the buckling load is lower than the crushing load. The potential impact of imperfections on the experimental and numerical results is further discussed ahead.

8.3.2. Numerical results

8.3.2.1. B-analysis results

Figure 8.2 presents the variation of exact numerical (Ex) values of P_{buck} with l_b (solid lines), as well as approximate analytical results (Ap, dashed lines), which are discussed ahead. Both exact and approximate results show an almost perfect linear trend. In addition, the increase of web height for each source material leads to a decrease in the buckling load, as would be expected due to the increase of web slenderness.

8.3.2.2. D-analysis results

Figure 8.3 presents the variation of exact numerical (Ex) values of P_{crush} with l_b (solid lines) and approximate analytical estimates (Ap, dashed lines), which are discussed ahead. Similarly to the buckling loads, the crushing loads also present a quasi-linear trend with the bearing length. Another relevant aspect found in Figure 8.3 is that the height of the web has a negligible effect on the crushing load. This result is in sharp contrast with some design formulae, which compute the effective bearing length as a function of the web height [8.17, 8.18]. The variation of P_{crush} with l_b seems similar in ETF and ITF.

8.3.2.3. DB-analysis results

Figure 8.4 presents the variation of exact numerical (Ex) values of P_u with l_b. The non-linear trend found in most curves of Figure 8.4, reflecting two distinct l_b ranges with different $P_u(l_b)$ curve slopes, is attributed to cases where either crushing (low l_b, initial slope) or buckling (high l_b, final slope) predominates. As expected, the ETF configuration presents results that are more significantly affected by web buckling, whereas ITF results are nearly identical for a wider range of bearing lengths.

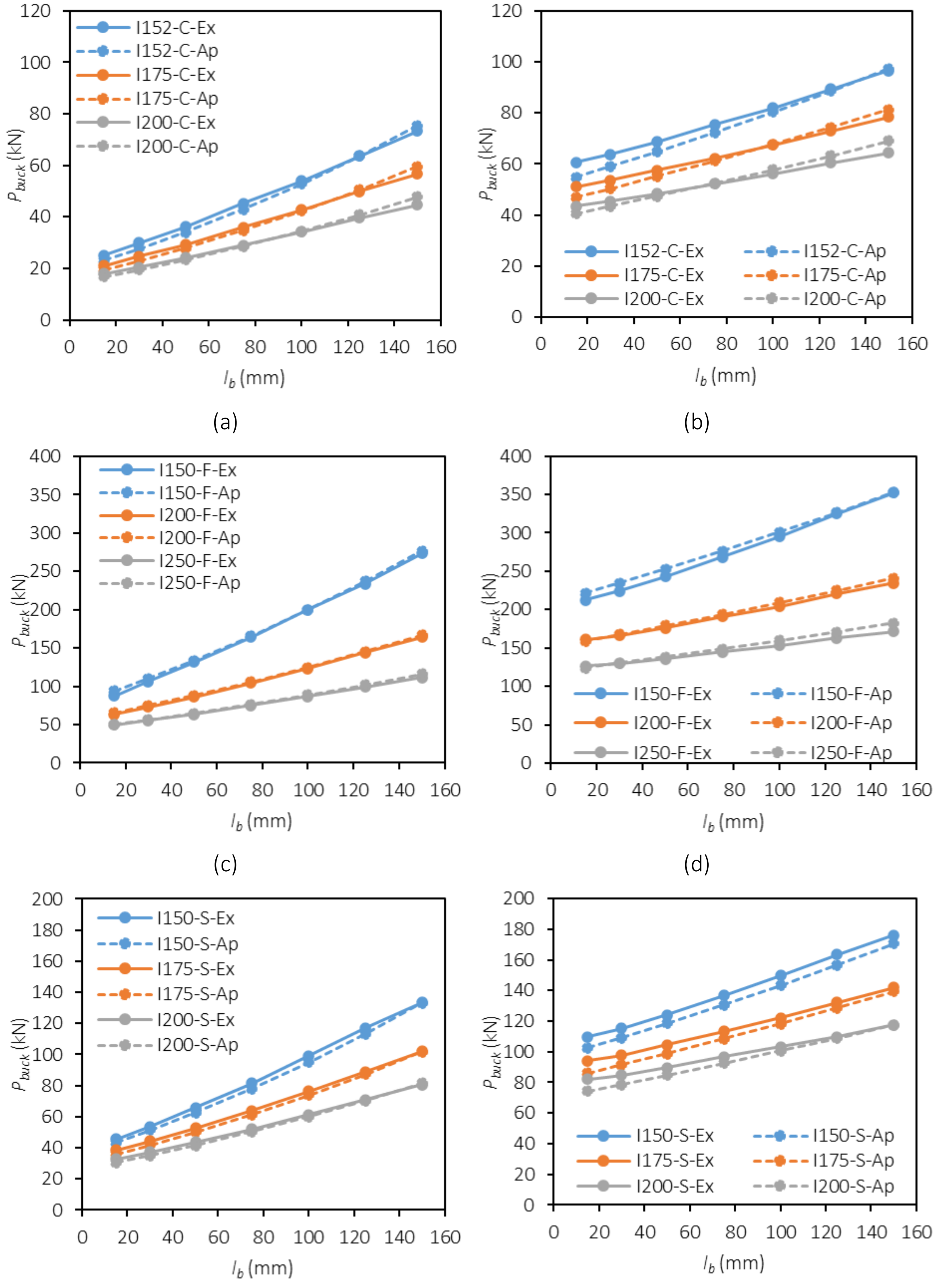

(a) (b)

(c) (d)

(e) (f)

Figure 8.2: Variation of exact (Ex) and approximated (Ap) buckling loads (P_{buck}) with the bearing length (l_b): (a) C-ETF; (b) C-ITF; (c) F-ETF; (d) F-ITF (e) S-ETF; (f) S-ITF.

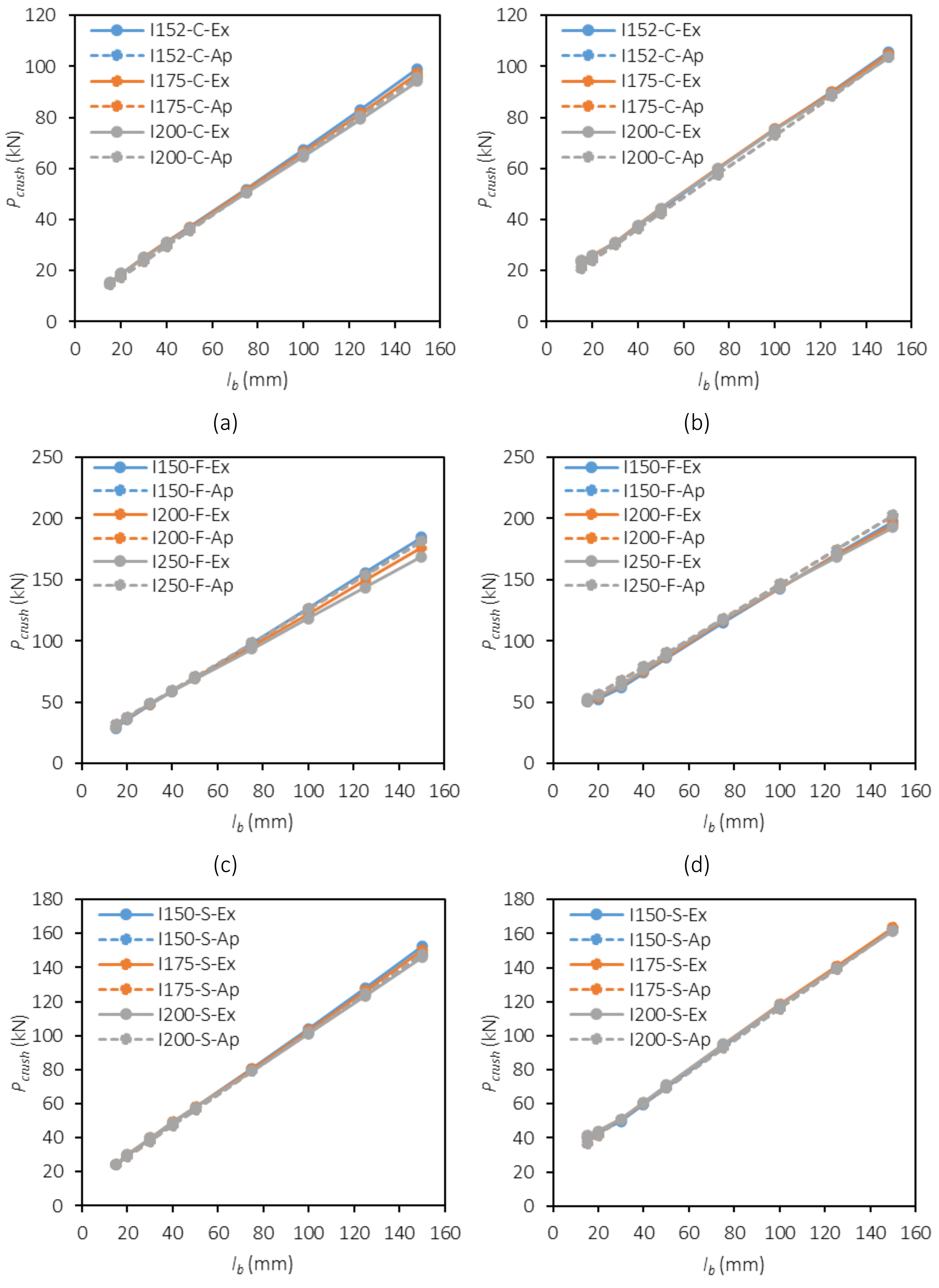

(a) (b)

(c) (d)

(e) (f)

Figure 8.3: Variation of exact (Ex) and approximated (Ap) crushing loads (P_{crush}) with the bearing length (l_b): (a) C-ETF; (b) C-ITF; (c) F-ETF; (d) F-ITF (e) S-ETF; (f) S-ITF.

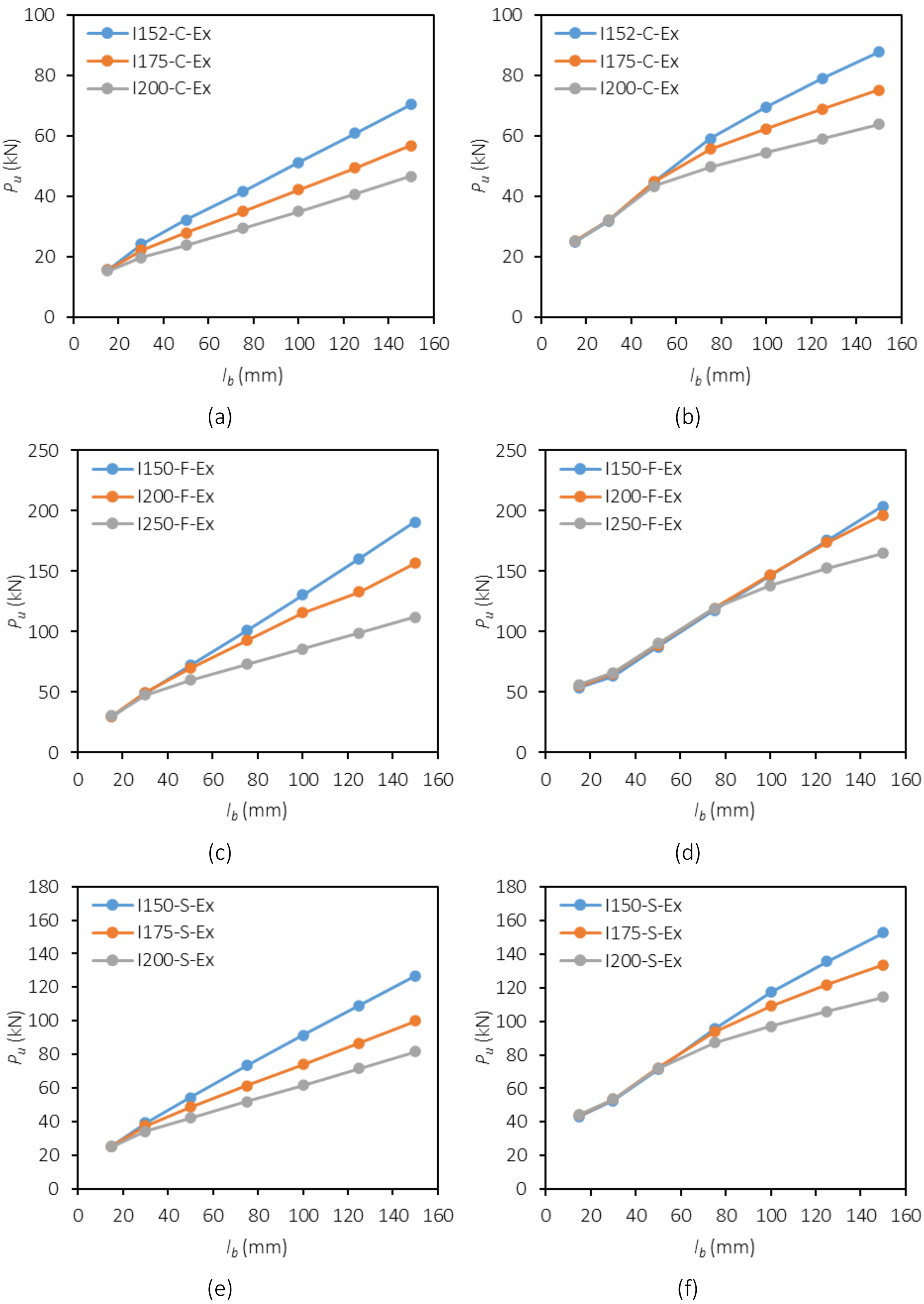

Figure 8.4: Variation of exact (Ex) ultimate loads (P_u) with the bearing length (l_b): (a) C-ETF; (b) C-ITF; (c) F-ETF; (d) F-ITF (e) S-ETF; (f) S-ITF.

8.4. Direct strength method

8.4.1. Numerically based DSM expressions

The first step towards the development of a DSM curve for web-crippling of GFRP profiles is to assess the overall trend and scatter of the variation of ultimate-to-crushing load ratio (P_u/P_{crush}) with the slenderness, given by,

$$\lambda = \sqrt{\frac{P_{crush}}{P_{buck}}} \tag{8.1}$$

To this end, all the loads (P_{buck}, P_{crush}, P_u) were determined numerically, either by B-analysis (P_{buck}), D-analysis (P_{crush}) or DB-analysis (P_u). Figure 8.5 presents the variation of the ratio P_u/P_{crush} with the slenderness λ for the three GFRP materials (C, F and S), as well as for both loading configurations (ETF and ITF).

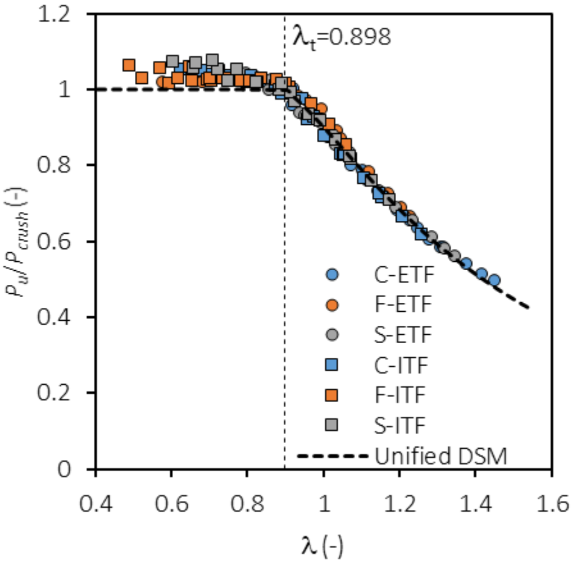

Figure 8.5: Numerical results and unified DSM curve.

Figure 8.5 shows a significantly coherent trend and excellent overall behaviour (low scatter) of the numerical results. In addition, Figure 8.5 shows a match between the results of ETF and ITF configurations, which was not anticipated *a priori*. The observation of Figure 8.5 also clearly shows two different zones: (i) one horizontal plateau, where the ratio P_u/P_{crush} does not vary much with λ and remains close to unit value, and (ii) a descending branch, where the ratio P_u/P_{crush} decreases steeply with λ. Therefore, these two distinct zones must be described by the DSM curve and the following analytical expression with the DSM format [8.19] should be considered,

$$\frac{P_u}{P_{crush}} = \begin{cases} 1, \ for\, \lambda < \lambda_t \\ k_a\left[1 - k_b\left(\frac{P_{buck}}{P_{crush}}\right)^{k_c}\right]\left(\frac{P_{buck}}{P_{crush}}\right)^{k_c}, for\, \lambda \geq \lambda_t \end{cases} \tag{8.2}$$

where, k_a, k_b and k_c are calibrated parameters, λ_t is the slenderness value for the transition between both zones, P_u is the ultimate (web-crippling) load, P_{crush} is the web crushing load and P_{buck} is the web buckling load. Natário *et al*. [8.24, 8.25] implemented a similar methodology to address web-crippling failure of cold-formed steel beams. Based on expression (8.2), the parameters were calibrated using the IBM SPSS software [8.36] by minimizing the sum of the squared errors. The obtained values of k_a, k_b and k_c are presented in Table 8.3. The transitional slenderness was determined to be λ_t=0.898 and the coefficient of determination (R^2) was found to be 0.999.

Table 8.3: Calibrated parameters for numerically based DSM curve.

k_a	k_b	k_c
1.337	0.326	1.186

Despite the low scatter of this curve, it cannot be considered for design because the calculation of both P_{buck} and P_{crush} values was based on FE models that would become impractical for design purposes. Therefore, the second step towards the development of a DSM-based expression is to derive simple and easy-to-use formulae to give approximate values of both P_{buck} and P_{crush}.

8.4.2. Approximate design formulae

8.4.2.1. Buckling failure

In this study, the approach proposed by Lagerqvist *et al*. [8.37] was considered, who developed expressions to determine the critical buckling loads of steel profiles under patch loading (a particular case of web-crippling). These were later implemented in a more simplified version in the Eurocode 3 - Part 1-5 [8.4]. The original expression proposed by Lagerqvist *et al*. [8.37] is given by,

$$P_{buck} = k_F \frac{\pi^2 E}{12(1-\upsilon^2)} \frac{{t_w}^3}{h_w} \tag{8.3}$$

where, k_F is a buckling coefficient dependent on the loading configuration and geometrical parameters, E is the elastic modulus, ν is the Poisson coefficient, h_w is the web height and t_w is the web thickness. In the current study, expression (8.3) was implemented by substituting the isotropic elastic modulus (E) by the transverse compressive elastic modulus (E_{22}^-), and the squared isotropic Poisson ratio (υ^2) by the cross product between orthotropic Poisson ratios ($\nu_{12}.\nu_{21}$) – typical values for pultruded GFRP profiles of 0.3 and 0.1, respectively, were considered.

For the calibration of the k_F parameter, Lagerqvist *et al*. [8.37] considered the influence of the flange geometry and the positioning of web stiffeners. These parameters were not considered at this initial stage, as they were not addressed in the experimental studies that support this analysis [8.8, 8.15]. Instead, a similar formula to those presented in the Eurocode 3 - Part 1-5 [8.4] was proposed for the ETF and ITF configurations, as detailed below,

$$k_F = \left(k_1 + \frac{l_b}{k_2 t_w}\right)\left(k_3 + \frac{l_b}{k_4 h_w}\right) \tag{8.4}$$

where, k_1, k_2, k_3 and k_4 are parameters to calibrate separately for the ETF and ITF configurations. The optimized values, determined by minimising the sum of the squared errors, are presented in Table 8.4.

Table 8.4: Calibrated parameters for web buckling expression.

Configuration	k_1	k_2	k_3	k_4
ETF	5.758	6.261	0.200	3.892
ITF	5.014	8.448	0.611	7.771

In order to show the accuracy of the calibrated formula, the approximated values of P_{buck} are presented in Figure 8.2 and their variation with l_b is given by the dashed curves (Ap). The fitting between exact numerical (Ex) and approximated (Ap) values of web buckling load is very good. The averaged ratio and standard deviation between approximated and exact results are 0.987 ± 0.039 (ETF) and 0.986 ± 0.042 (ITF). It should be added that the highest relative differences were observed for the lowest bearing lengths, which are less prone to web-crippling triggered by buckling [8.8, 8.15].

8.4.2.2. Crushing failure

In a similar process to the calibration performed for web buckling, an analytical expression was developed and calibrated to fit numerical results for web crushing. Instead of using the interlaminar shear strength (like other authors did), the transverse compressive strength (σ_{u22}^-) was selected as the governing material property for web crushing [8.16]. Therefore, the web crushing load (P_{crush}) is related to an effective bearing length ($l_{b,eff}$) through the transverse compressive strength (σ_{u22}^-), as given by,

$$P_{crush} = l_{b,eff} t_w \sigma_{u22}^- \tag{8.5}$$

The numerical values of $l_{b,eff}$ were thus determined by dividing the numerical crushing loads (P_{crush}) by the product between the transverse compressive strength (σ_{u22}^-) and the web thickness (t_w). The analytical $l_{b,eff}$ was then calibrated to match these numerical results, as detailed ahead.

Figure 8.6 illustrates for both loading conditions the relation between the numerical values obtained for the effective bearing length ($l_{b,eff}$) and the bearing lengths (l_b) used in the experiments of the different profile sections. It shows a linear trend between $l_{b,eff}$ and l_b, with reduced offsets between the three materials. In Figure 8.6 it is noticeable that the ITF configuration leads to higher $l_{b,eff}$ values; however, the relative difference between ETF and ITF configurations decreases for higher l_b values, as the curve slopes for both configurations are nearly parallel.

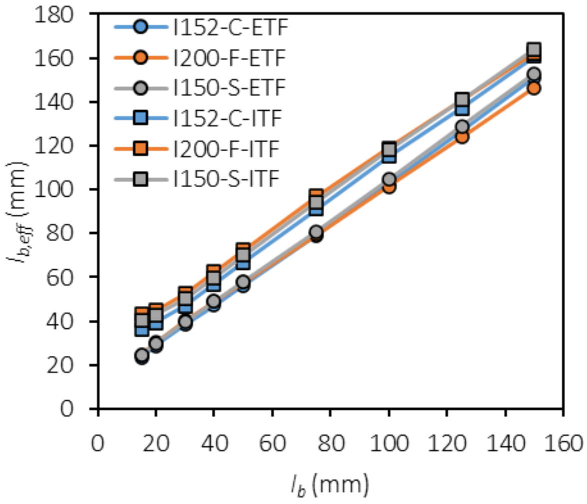

Figure 8.6: Numerical $l_{b,eff}$ *vs*. experimental l_b values.

In Figure 8.6 it is also noticeable that for lower values of l_b the highest values of $l_{b,eff}$ are presented by the profiles with thickest webs (particularly for ITF results). Therefore, the thickness of the web was also considered in the formula to take into account this apparent offset between the different profiles, and a linear relation was considered between $l_{b,eff}$ and l_b. Therefore, the proposed formula to approximate the effective bearing length is given by,

$$l_{b,eff} = k_5 t_w + k_6 l_b \tag{8.6}$$

where, k_5 and k_6 are parameters to calibrate separately for ETF and ITF configurations. Table 8.5 presents a summary of the optimized k_5 and k_6 values, determined by minimising the sum of squared errors.

Table 8.5: Calibrated parameters for web crushing expression.

Configuration	k_5	k_6
ETF	1.312	0.918
ITF	2.859	0.933

In order to show the accuracy of the calibrated formula, the approximated values of P_{crush} are shown in Figure 8.3 and their variation with l_b is given by the dashed curves (Ap). A good fitting exists between the exact numerical (Ex) and approximated (Ap) values of crushing loads. The averaged ratio and standard deviation between approximated and exact results are 0.992 ± 0.039 (ETF) and 0.989 ± 0.044 (ITF).

8.4.3. Experimentally based DSM expressions

After having developed design formulae to determine approximately the values of P_{buck} and P_{crush}, the DSM expressions can now be derived based on the experimental values of ultimate (web-crippling) loads P_u. This is a significant step, as experimental results are an essential requirement for the establishment of reliable design guidelines.

8.4.3.1. ETF results

Figure 8.7 presents the variation of P_u/P_{crush} ratio with λ for the ETF configuration. The P_{buck} and P_{crush} values were determined through the approximate formulae (8.4) and (8.6), respectively, while P_u values correspond to experimental results reported in [8.8, 8.15].

As expected, the scatter of results observed in Figure 8.7 (which include the experimental scatter) is much higher than that observed for the numerical results (*cf.* Figure 8.5). The DSM parameters (k_a, k_b, k_c) were calibrated for these results - their values are summarized in Table 8.6 - and the DSM curve is plotted in Figure 8.7 (dotted line). In this case, the transitional slenderness is λ_t=0.844 and the coefficient of determination is R^2=0.940. As expected, the R^2 determined for experimental results is lower than that found for numerical results, a difference that is attributed to the inherent variability of experimental results.

The I400-A results [8.8] clearly contributed to expand the slenderness range. It is also noteworthy that this profile presents the lowest ratio between experimental ultimate load and web crushing load. The variability found in these results naturally takes into account the geometrical imperfections of each profile or specimen; however, such imperfections were not measured. In this respect, the influence of material imperfections in the web-flange junction may also play a relevant role, as the material properties determined for these profiles were based on coupons taken from their web. The results presented in Figure 8.7 seem to indicate that the geometrical imperfections of the I152-C profile present the lowest magnitude among the profiles tested. The influence of these imperfections is further assessed in Section 8.5.

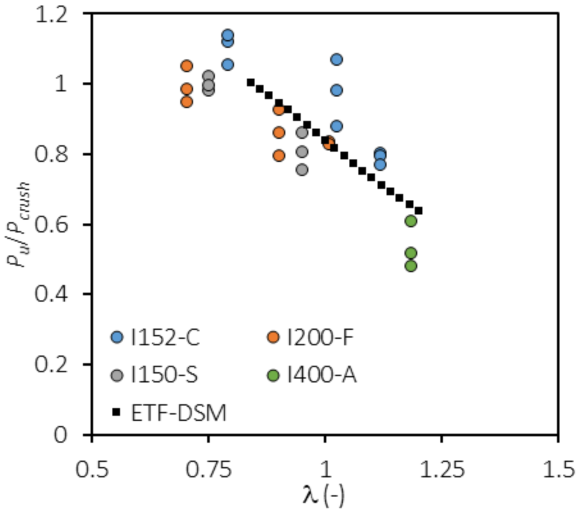

Figure 8.7: ETF experimental results and DSM curve.

Table 8.6: Calibrated parameters for ETF-DSM expression.

k_a	k_b	k_c
1.168	0.282	1.084

8.4.3.2. ITF results

Figure 8.8 is similar to Figure 8.7, but now for the ITF configuration. It is noteworthy that the ITF results present a narrower slenderness range, because the ITF configuration is considerably less prone to instability issues than the ETF configuration. In Figure 8.8 it is also noteworthy that the I400-A results do not stand out as significantly in the ITF configuration when compared to the ETF configuration, but they are still amongst the highest slenderness ratios. The calibrated DSM parameters are summarized in Table 8.7 and the DSM curve is plotted in Figure 8.8 (dotted line). In this case, the transitional slenderness is λ_t=0.762, which indicates that the ITF results lead to a slightly more conservative design curve than previously reported for the ETF results. This assessment is further detailed in Section 8.5. The coefficient of determination was found to be R^2=0.870, a lower value than that reported for the ETF results.

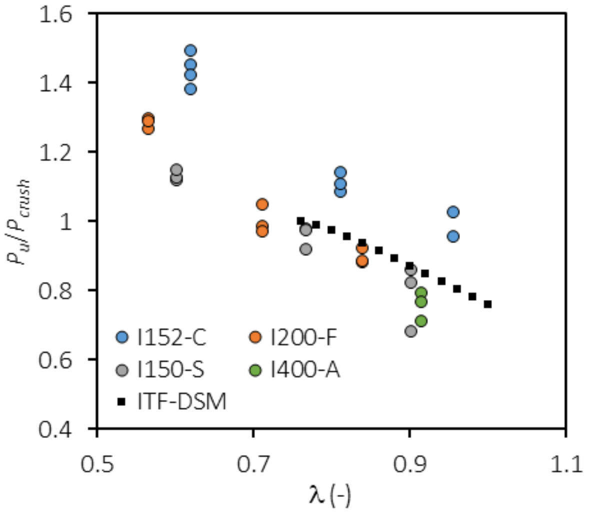

Figure 8.8: ITF experimental results and DSM curve.

Table 8.7: Calibrated parameters for ITF-DSM expression.

k_a	k_b	k_c
1.016	0.252	1.079

The experimental results depicted in Figure 8.8 show a similar trend to those reported for the ETF configuration in Figure 8.7, with the I152-C results presenting higher P_u/P_{crush} ratios than the other profiles, which seems to confirm that the imperfections in this profile presented a lower magnitude.

It is noteworthy that the test series with lowest slenderness present P_u values higher than P_{crush} values. This result is attributed to a poorer fit between approximated and exact (numerical) results for the lowest bearing lengths. In addition, the experimental ultimate loads are higher than the numerical crushing loads for these bearing lengths. It should be highlighted that these discrepancies occur for a bearing length of 15 mm, which is naturally a lower bound of bearing lengths likely to be found in construction.

8.4.3.3. Unified ETF and ITF results

Given the trend found in the numerical results, where ETF and ITF results appear to be well fitted by a single DSM curve, as well as the similar calibrated parameters presented in Tables 8.6 and 8.7, the DSM was applied simultaneously to ETF and ITF experimental results. Figure 8.9 presents the combined ETF and ITF experimental results, as well as the resulting DSM curve. The calibrated parameters for this global DSM curve are detailed in Table 8.8, which are applicable for $\lambda \geq 0.776$. The coefficient of determination was found to be $R^2=0.932$, showing that the unified DSM expression fits well both test configurations.

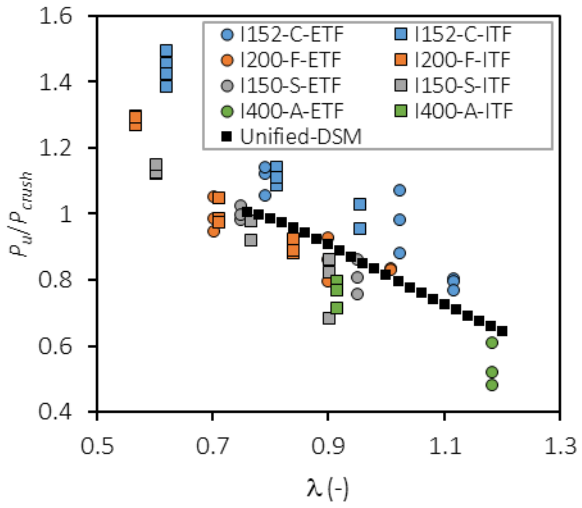

Figure 8.9: ETF and ITF experimental results and unified DSM curve.

Table 8.8: Calibrated parameters for Unified-DSM expression.

k_a	k_b	k_c
1.132	0.280	0.930

The DSM curve presented in Figure 8.9 shows a good fit to both ETF and ITF results. The I150-S and I200-F results present the best fit to the proposed design expression, whereas the I400-A results are overestimated and the I152-C results are underestimated. As future development, it will be important to attempt to correlate experimental measurements of imperfections with these discrepancies.

8.5. Discussion

8.5.1. Experimental vs. numerical DSM curves

Figure 8.10 enables the comparison between the four previously presented DSM curves: (i) Unified numerical (Unif-Num), (ii) ETF-experimental (ETF-Exp), (iii) ITF-experimental (ITF-Exp), and (iv) Unified experimental (Unif-Exp). It is worth mentioning that the unified numerical curve provides unconservative results in comparison to the unified experimental curve. This is due to the low magnitude of imperfections considered in the DB-analysis, which had a maximum amplitude of 0.01 mm.

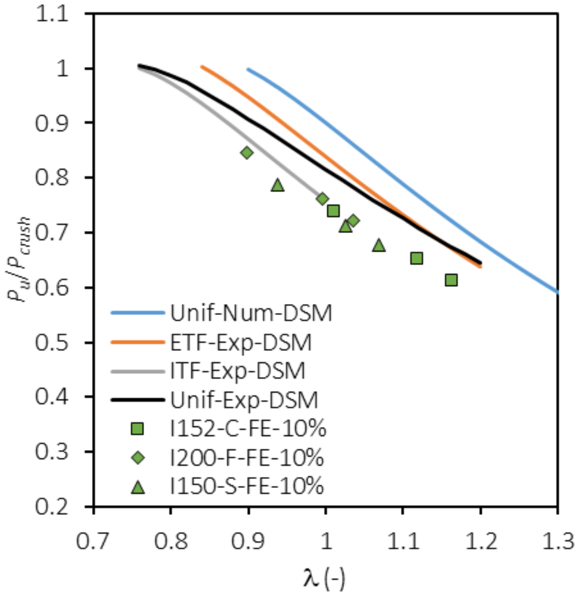

Figure 8.10: DSM curves for experimental (Exp) ETF, ITF and unified results, with numerical (Num) unified results, including additional numerical results with 10% imperfections.

To assess the sensitivity of numerical models to geometrical imperfections, a specific study was conducted for the I152-C-ETF-100 series by considering several imperfection amplitudes in DB-analysis. Figure 8.11 presents load *vs*. displacement curves for different levels of imperfection, showing that the magnitude of the imperfection has a significant influence on the ultimate load P_u. These results further highlight the need to measure the initial imperfections of test specimens in future experimental studies.

Given the potential impact of different imperfections in the numerical results, a complementary study was performed to assess which imperfection magnitude would improve the accuracy of numerical results. This study was performed for the ETF series with normalized imperfections, in respect to the thickness of the profile. Figure 8.10 presents numerical results with imperfection amplitudes of 10% of the web thickness, showing a good agreement to the most conservative experimental results, determined for the ITF load configuration. Therefore, an imperfection range up to $0.1t_w$ seems to provide accurate numerical FE simulations of web-crippling of pultruded GFRP profiles. These imperfections were also compared to the web height of the profiles. The imperfection amplitudes varied between 0.5% and 0.7% of the web height.

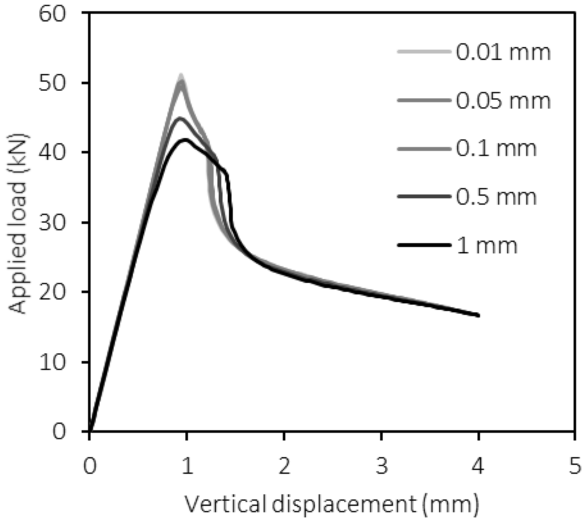

Figure 8.11: Numerical DB results for I152-C-ETF-100 test series with several imperfection amplitudes.

Figure 8.10 also shows that the unified DSM curve determined by combining ETF and ITF experimental results presents a good fit to both individual test configurations, showing a better agreement to ITF results for lower λ values, and a better fit to ETF results for higher λ values. However, given the low difference between these curves, the unified DSM expression was considered to accurately fit the experimental results, eliminating the need of different DSM expressions for ETF and ITF configurations. This trend was also found in the numerical results, as highlighted in Figure 8.5.

Finally, it is also very important to note that the descending branch of this unified curve (Figure 8.10) begins for $\lambda \geq 0.776$. Noting also that a unit slenderness ($\lambda=1$) corresponds to the case where the buckling load equals the crushing load ($P_{buck}=P_{crush}$, see expression 8.1), we may immediately define three different ranges:

- For $\lambda<0.776$, the web-crippling load is triggered only by web crushing and one has $P_u=P_{crush}$.
- For $\lambda>1.0$, the web-crippling load is triggered by web buckling and one has $P_u=\chi P_{crush}$.
- For $0.776\leq\lambda\leq1.0$, the web-crippling load is triggered by the interaction between web buckling and web crushing and one has $P_u=\chi P_{crush}$.

The parameter χ is known as the buckling reduction factor ($\chi<1$), as it reduces the crushing load (P_{crush}) to take into account the buckling effects on web-crippling. This is done in a moderate way for $0.776\leq\lambda\leq1.0$ (interactive crushing-buckling) and a severe way for $\lambda>1.0$ (buckling). The expression of χ is that shown in expression 8.2 and Table 8.8. This is a significant advantage of the DSM, when compared to all the existing design methodologies.

8.5.2. Assessment and validation

This section presents a study on the accuracy of the proposed DSM formulation determined for the unified experimental ETF and ITF results (expression 8.2 and Table 8.8), as it was found to present a good fit to both test configurations. In summary, the proposed DSM formulation is detailed below, as well as the approximate expressions for web buckling and web crushing,

Web buckling:

$$P_{buck} = k_F \frac{\pi^2 E_{22}^{-}}{12(1-\upsilon_{12}\upsilon_{21})} \frac{{t_w}^3}{h_w} \tag{8.7}$$

$$k_F = \begin{cases} \left(5.758 + \dfrac{l_b}{6.261 t_w}\right)\left(0.200 + \dfrac{l_b}{3.892 h_w}\right), for\ ETF \\ \left(5.014 + \dfrac{l_b}{8.448 t_w}\right)\left(0.611 + \dfrac{l_b}{7.771 h_w}\right), for\ ITF \end{cases} \tag{8.8}$$

Web crushing:

$$P_{crush} = l_{b,eff} t_w \sigma_{u22}^{-} \tag{8.9}$$

$$l_{b,eff} = \begin{cases} 1.312 t_w + 0.918 l_b, for\ ETF \\ 2.859 t_w + 0.933 l_b, for\ ITF \end{cases} \tag{8.10}$$

DSM:

$$P_u = \begin{cases} P_{crush},\ \ for\ \lambda < 0.776 \\ 1.132 P_{crush} \left[1 - 0.280 \left(\dfrac{P_{buck}}{P_{crush}}\right)^{0.930}\right] \left(\dfrac{P_{buck}}{P_{crush}}\right)^{0.930} , for\ \lambda \geq 0.776 \end{cases}$$

$$\lambda = \sqrt{\frac{P_{crush}}{P_{buck}}} \tag{8.11}$$

Usually, when applying DSM for the design of steel structures, the definition of a set of pre-qualified sections and steel classes is required [8.24] to know the conditions for which the method was calibrated, *i.e.* its applicability range. In the present case, the implemented DSM formulations were developed based on a relatively wide range of geometrical and material properties, as summarized in Table 8.9.

Table 8.9: Geometrical and material boundaries of the pultruded GFRP materials implemented to calibrate the DSM.

Geometry (mm)	Min.	Max.	Material	Min.	Max.
h	150	400	E_{11}^{+} (GPa)	27.8	30.0
t_w	6.3	14.5	E_{22}^{-} (GPa)	7.7	10.9
t_f	6.3	14.5	G_{12} (GPa)	2.9	4.2
b_f	75	150	σ_{u11}^{+} (MPa)	296	416
			σ_{u22}^{-} (MPa)	86	123
			τ_{u12} (MPa)	65*	70
			G_{2}^{-} (N/mm)	42	67

* The I400-A result (21 MPa) was not considered, as it was determined by a different test method [8.8, 8.15].

In an initial stage, the results of the proposed DSM expression were compared to the experimental results of web-crippling tests previously used to calibrate it. Figure 8.12 presents DSM *vs*. experimental web-crippling ultimate loads, for both ETF and ITF configurations. The results illustrated in Figure 8.12 show an overall good agreement between DSM predictions (P_{u_DSM}) and experimental results (P_{u_Exp}), with some minor discrepancies. The results for the I400-A profile are overestimated by the proposed expression due to its considerably higher slenderness and potential higher imperfection magnitudes, in comparison to other specimens.

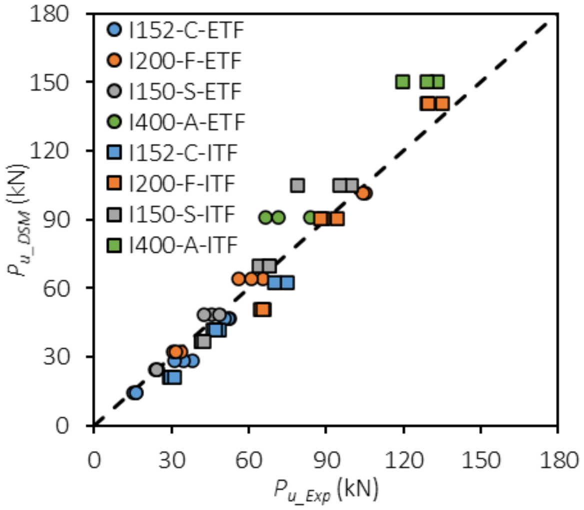

Figure 8.12: DSM (P_{u_DSM}) *vs*. experimental (P_{u_Exp}) ultimate loads.

Figure 8.13 presents analytical *vs*. numerical DB ultimate load results. As expected, Figure 8.13 presents a good agreement between numerical and analytical results, as the analytical expressions for web crushing and web buckling were calibrated based on numerical results. The analytical results slightly underestimate the numerical ultimate loads, as would be expected by the offset between experimental and numerical DSM curves displayed in Figure 8.10. The most significant discrepancies occur for the highest loads; however, they are well within the typical scatter found for pultruded GFRP materials.

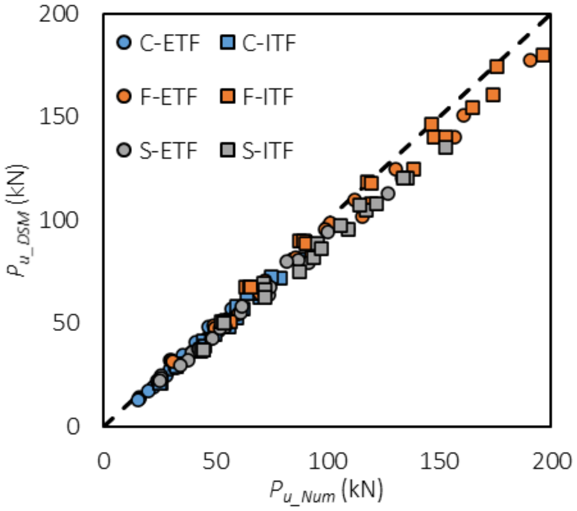

Figure 8.13: DSM (P_{u_DSM}) *vs*. numerical DB (P_{u_Num}) ultimate loads.

For additional validation, the experimental results reported in [8.8] were compared to those obtained by using DSM. This comparison is deemed important because this sample of experimental results was not considered for the calibration of the proposed DSM expression. Two I-section profiles were considered for this analysis: (i) a profile with 100 mm of height manufactured by Alto Perfis Pultrudidos, and (ii) a profile with 120 mm of height manufactured by Fiberline Composites. The geometric details and mechanical properties of these profiles are detailed in Table 8.10 [8.8].

Table 8.10: I100-A and I120-F geometry and mechanical properties [8.8].

Material	Height x Width (mm)	Web thick., t_w (mm)	E_{11}^{+} (GPa)	E_{22}^{-} (GPa)	G_{12} (GPa)	σ_{u11}^{+} (MPa)	σ_{u22}^{-} (MPa)	τ_{u12} (MPa)
I100-A	100x50	8	18.5	4.5	4.1*	426	73	20*
I120-F	120x60	6	28.9	8.5	3.9*	309	121	31*

* Determined through the 10° angled tensile test [8.31].

The DSM results of these materials should be considered with care, as their compressive mechanical properties were characterized through a different method, the one defined in ASTM D 695-02 [8.33], which may underestimate the ultimate strength [8.8, 8.16]. Figure 8.14 presents DSM *vs*. experimental [8.8] results, showing a good overall agreement, with some expectable discrepancies (either due to differences in material characterization or deviations to the proposed DSM expression). This good agreement is a significant result, as the I100-A and I120-F profiles present geometrical and material properties that fall outside the range of pre-qualified sections summarized in Table 8.9.

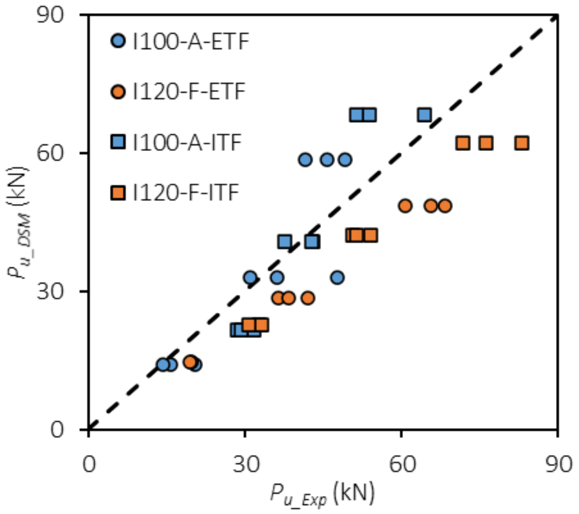

Figure 8.14: DSM (P_{u_DSM}) *vs*. experimental [8.8] (P_{u_Exp}) ultimate loads for data not used in calibration.

8.6. Conclusions

This chapter presented a novel methodology for the design of pultruded GFRP profiles against web-crippling failure, by implementing an approach based on the direct strength method (DSM). The results of the proposed design formula, developed for beams under end two flange (ETF) and interior two flange (ITF) loading cases, presented a very good agreement with the ultimate loads obtained experimentally [8.8, 8.15] and numerically (FE) [8.16], for a wide range of profiles and materials. The following main concluding remarks are made:

- The developed FE models were crucial to identify the excellent trend and behaviour of the DSM curve, thus paving the way for the DSM calibration.
- The results of FE analyses (B- and D-analysis) were fundamental to derive approximate formulae to estimate the values of web buckling loads and web crushing loads, a crucial step towards the use of DSM.
- The proposed DSM expression may be implemented for both ETF and ITF loading cases in a unified fashion, as the difference to these individual cases was found to be negligible.
- Besides the calculation of web-crippling ultimate loads, the proposed DSM expression is able to identify the origin of failure, either from web crushing, web buckling or the interaction thereof.
- The proposed DSM expression may be used for a wide set of prequalified I-sections and materials, as it is usually stated in the DSM philosophy. Despite these pre-qualified geometrical and property ranges, the proposed DSM still seems to behave very well for sections and materials outside those ranges.

The absence of widely accepted guidelines for web-crippling failure of FRP composite beams in current structural design standards may now be partially overcome. To that end, the expressions presented herein should be assessed in respect to additional variables, such as flange geometry and positioning of web stiffeners. In addition, the reliability of the proposed DSM expressions should be assessed, by implementing this approach to additional materials, section geometries and loading configurations. This step is further highlighted as there are currently various design guidelines under development regarding the use of pultruded GFRP profiles in construction [8.38, 8.39].

8.6. References

[8.1] Borowicz, D. T., Bank, L. C., Behavior of Pultruded Fiber-Reinforced Polymer Beams Subjected to Concentrated Loads in the Plane of the Web*, Composites for Construction*, 15-2, 2-9, 2011.

[8.2] NAS – North American specification for the design of cold-formed steel structural members, American iron and steel institute (AISI), Washington DC, 2007.

[8.3] EN 1993-1-3. Eurocode 3 – Part 1–3: general rules – supplementary rules for cold-formed members and sheeting. European committee for standardization (CEN), Brussels; 2006.

[8.4] EN 1993-1-5. Eurocode 3 – Part 1–5: plated structural elements. European committee for standardization (CEN), Brussels; 2006.

[8.5] Borowicz, D. T., Bank, L. C., Effect of web reinforcement on the behavior of pultruded fiber-reinforced polymer beams subjected to concentrated loads. *Construction and Building Materials*, 47, 347-357, 2013.

[8.6] Wu, C., Bai, Y., Web-crippling behaviour of pultruded glass fibre reinforced polymer sections, *Composite Structures*, 108, 789-800, 2014.

[8.7] Wu, C., Bai, Y., & Zhao, X. L., Improved bearing capacities of pultruded glass fibre reinforced polymer square hollow sections strengthened by thin-walled steel or CFRP, *Thin-Walled Structures*, 89, 67-75, 2014.

[8.8] Almeida-Fernandes, L., Gonilha, J., Correia, J. R., Silvestre, N., Nunes, F., Web-crippling of GFRP pultruded profiles. Part 1: Experimental study. *Composite Structures*, 120, 565-577, 2015.

[8.9] Wu, C., Zhang, L., Bai, Y., Zhao, X. L., Web-crippling behavior of pultruded GFRP channel sections under transverse bearing load, *Composite Structures*, 209, 129-142, 2019.

[8.10] Wu, C., Zhang, L.-T., Tam, L., Yan, L., He, L., Effect of Bearing Length on Web-crippling Behavior of Pultruded GFRP Channel Section, *Composite Structures*, 112810, 2020.

[8.11] Almeida-Fernandes, L., Correia, J. R., Silvestre, N., Effect of fibre layup in web-crippling of pultruded GFRP profiles, *Engineering Structures*, submitted, 2020.

[8.12] A. Gonilha, J., R. Correia, J., A. Branco, F., Sena-Cruz, J., Durability of GFRP-concrete adhesively bonded connections: Experimental and numerical studies. *Engineering Structures*, 168, 784-798, 2018.

[8.13] Almeida-Fernandes, L., *Structural behaviour of GFRP beams subjected to concentrated loads: experimental tests, numerical modeling and analytical study*, MSc dissertation in Civil Engineering, Instituto Superior Técnico, Lisbon, Portugal, 2014 [In Portuguese].

[8.14] Almeida-Fernandes, L., Nunes, F., Silvestre, N., Correia, J. R., Gonilha, J., Web-crippling of GFRP pultruded profiles. Part 2: Numerical analysis and design. *Composite Structures*, 120, 578–590, 2015.

[8.15] Almeida-Fernandes, L., Correia, J. R., Silvestre, N., Effect of fibre layup in web-crippling of pultruded GFRP profiles, *Engineering Structures*, submitted, 2020.

[8.16] Almeida-Fernandes, L., Silvestre, N., Correia, J. R., Fracture toughness-based models for web-crippling of pultruded GFRP profiles, *Composites Part B: Engineering*, submitted, 2020.

[8.17] Bank, L.C., *Composites for construction: structural design with FRP materials*, New Jersey: John Wiley & Sons Inc; 2006.

[8.18] Clarke J.L., editor. *Structural design of polymer composites – EuroComp design code and handbook*, London: E&FN Spon, 1996.

[8.19] Schafer, B. W., Peköz, T., *Direct strength prediction of cold-formed steel members using numerical elastic buckling solutions*, Fourteenth International Specialty Conference on Cold-Formed Steel Structures, St. Louis, Missouri, October 15-16, 1998.

[8.20] Schafer, B. W., The direct strength method of cold-formed steel member design, *Journal of constructional steel research*, 64 (7-8), 766-778, 2008.

[8.21] Schafer, B. W., Advances in the Direct Strength Method of cold-formed steel design, *Thin-Walled Structures*, 140, 533-541, 2019.

[8.22] AISI S100-16, North American Specification for the Design of Cold-Formed Steel Structural Members, American Iron and Steel Institute (AISI), Washington DC, 2016.

[8.23] DR AS/NZS 4600:2018, Cold-formed steel structures, Standards Australia, Sydney, 2018.

[8.24] Natário, P., Silvestre, N., Camotim, D., Direct strength prediction of web-crippling failure of beams under ETF loading. *Thin-Walled Structures*, 98, 360-374, 2016.

[8.25] Natário, P., Silvestre, N., & Camotim, D., Web-crippling of beams under ITF loading: A novel DSM-based design approach, *Journal of Constructional Steel Research*, 128, 812–824, 2017.

[8.26] Simulia, "Abaqus/CAE 2018", 2018.

[8.27] Hashin, Z., and Rotem, A., A fatigue criterion for fiber-reinforced materials, *Journal of Composite Materials*, 7, 448-464, 1973.

[8.28] Almeida-Fernandes, L., Silvestre, N., Correia, J. R., Characterization of transverse fracture properties of pultruded GFRP material in tension, *Composites Part B: Engineering*, 175, 107095, 2019.

[8.29] Almeida-Fernandes, L., Correia, J. R., Silvestre, N., Transverse fracture behaviour of pultruded GFRP materials in tension: Effect of fibre layup, *Composites for Construction*, 24(4), 04020019, 2020.

[8.30] Almeida-Fernandes, L., Silvestre, N., Correia, J. R., Arruda, M. R. T., Compressive transverse fracture behaviour of pultruded GFRP materials: experimental study and numerical calibration, *Composite Structures*, 247, 112453, 2020.

[8.31] Hodgkinson J. M., *Mechanical Testing of Advanced Fibre Composites*, CRC Press, Cambridge, England, 2000.

[8.32] ASTM D5379-05, Standard test method for shear properties of composite materials by the V-notched beam method, American Society for Testing and Materials (ASTM), West Conshohocken, PA, 2000.

[8.33] ASTM D 695-02, Standard Test Method for Compressive Properties of Rigid Plastics, American Society for Testing and Materials (ASTM), West Conshohocken, PA, 2006.

[8.34] ASTM D6641 / D6641M – 09, Standard Test Method for Compressive Properties of Polymer Matrix Composite Materials Using a Combined Loading Compression (CLC) Test Fixture, ASTM International, West Conshohocken, Pennsylvania, 2009.

[8.35] Girão Coelho, A. M., Toby Mottram, J., & Harries, K. A., Finite element guidelines for simulation of fibre-tension dominated failures in composite materials validated by case studies. *Composite Structures*, 126, 299–313, 2015.

[8.36] IBM, "SPSS statistics", version 24, 2016.

[8.37] Lagerqvist, O., Johansson, B., Resistance of I-girders to Concentrated Loads, *Journal of Constructional Steel Research*, 39(2), 87-119, 1996.

[8.38] ACMA, Pre-Standard for Load & Resistance Factor Design (LRFD) of Pultruded Fiber Reinforced Polymer (FRP) Structures. American Composites Manufacturers Association, 2010.

[8.39] CEN/TC250 working Group 4, *Fibre reinforced polymer structures, scientific and technical report*, European Committee for Standardization (CEN), Brussels (2016).

Part IV

Conclusions and future developments

Preamble

This thesis presented a comprehensive study, combining (i) the experimental characterization and numerical implementation of fracture toughness, with (ii) the numerical simulation of web-crippling experimental tests. This comprehensive study enabled the development of novel codifiable design expressions for web-crippling.

Part IV details the most relevant conclusions drawn throughout each chapter of this thesis, organized into the topics of fracture toughness and web-crippling. In addition, future developments are also proposed for these topics.

Chapter 9. Conclusions and future developments

9.1. Conclusions

This chapter addresses the main conclusions and results reported in this thesis, as well as the major future developments that were identified, decomposed by the two main topics of this thesis: (i) experimental characterization of fracture toughness of pultruded GFRP materials; and (ii) web-crippling of pultruded GFRP profiles. These two topics are addressed separately regarding both the conclusions and future developments.

The conclusions drawn regarding the experimental characterization of the fracture toughness are based on the results reported in Part II of this thesis. These results and conclusions have been submitted through four papers, published in international journals [9.1-9.4]. The conclusions drawn regarding web-crippling are based on the results reported in Part III of this thesis, which are based on three papers submitted to international journals [9.5-9.7].

9.1.1. Fracture toughness of pultruded GFRP materials

9.1.1.1. Research background

A significant amount of research has been conducted on the experimental characterization of fracture toughness in composite materials; however, very little research has been found regarding intralaminar and translaminar fracture of pultruded GFRP materials. Most research on fracture toughness of composite materials has focused on CFRP laminates, typically designed for the automotive and aerospace industries.

Several test configurations have been successfully implemented to characterize intralaminar and translaminar tensile fracture toughness of composite materials. Of these configurations, the Compact Tension (CT) test configuration stands out, as it has been implemented in a greater number of experimental studies, addressing a wider range of materials and has been used with several data reduction methods. This test configuration has the added benefit of being versatile, as can be perceived by the large number of successful CT-based test configurations that have been implemented in the past, as the extended (ECT), over-height (OCT) and Wide (WCT) compact tension tests.

To the best of the author’s knowledge, in addition to the present thesis, only two experimental studies have been reported regarding the experimental characterization of translaminar/intralaminar fracture toughness: (i) El-Hajjar and Haj-Ali [9.8] developed ECT tests for the longitudinal and transverse directions; and (ii) Liu *et al.* [9.9] developed three-point bending tests to characterize the transverse fracture toughness of a pultruded GFRP material.

The determination of compressive fracture properties poses an added challenge, due to the complexity of the damage propagation mechanisms. Some test configurations have been proposed in the past, as the compact compression test (CCT) and four-point bending configurations; however, there are significant doubts at present, regarding the data reduction methodology that can be implemented in parallel with these tests. These doubts stem from the complexity of the compressive fracture process, which includes several damage propagation phenomena, such as fibre kinking, delamination and local buckling of the layers.

9.1.1.2. Material characterization

The mechanical characterization study provided insights into the tensile, compressive and shear mechanical properties of the test materials to be experimentally tested and numerically simulated in this thesis. In addition, the fibre layups of these materials were characterized, and the fibre content attributed to each material in-plane direction was also determined.

It is noteworthy that materials acquired from different manufacturers presented significant differences in terms of fibre layup, as (i) one material presented only randomly oriented fibres as transverse reinforcement (I150-S); (ii) three materials presented woven [0/90] layers (I150-A, P300-A and I200-F); and (iii) two materials presented a quasi-isotropic transverse reinforcement, with mats oriented at ±45° and 90° (I152-C and U150-S). This variability provided an important basis for analysing the influence of fibre layup on transverse fracture properties.

The mechanical characterization programme showed that the various test materials present similar longitudinal mechanical properties, but significantly different transverse mechanical properties. These differences in transverse mechanical properties were found to be in good agreement with the fibre layups that were characterized for each material. In further detail, the I150-S material, which only presented continuous filament mats as transverse reinforcement, was found to present the lowest transverse tensile strength (34 MPa). In the same trend, the material that presented the highest percentage of fibre content applied to transverse reinforcement, I152-C, also presented the highest transverse tensile strength (121 MPa).

In an opposite trend to transverse tensile properties, the mechanical characterization tests showed that the transverse compressive properties were not proportional to the transverse reinforcement percentages. In fact, the I150-S material, with its aforementioned lowest levels of transverse reinforcement, presented the highest transverse compressive strength (123 MPa).

9.1.1.3. Transverse tensile fracture toughness (G_2^+) characterization

In an initial stage, the CT test configuration was implemented. However, the CT tests were found to present significant specimen geometry dependency, providing overestimations of transverse tensile fracture toughness (G_2^+). These results led to the development of WCT tests for a second experimental stage, which present a significantly higher width, therefore enabling more room for crack propagation.

The WCT test configuration was found to provide accurate fracture toughness results, when coupled with visually based data reduction methods, such as FE-based J-integral and standard compliance calibration. Significant variations of initial notch lengths provided similar G_2^+ results, validating this test configuration.

Considering the lower initial notch length and the FE-based J-integral method, WCT tests led to fracture toughness results that ranged from 10 N/mm, for a material with low levels of transverse reinforcement (I150-S), to 26 N/mm for a material with quasi-isotropic layup (U150-S). Materials presenting woven [0/90] layers (I150-A, P300-A and I200-F) presented intermediate results, spanning from 14 to 21 N/mm.

Visually based data reduction methods presented similar G_2^+ results; however, modified compliance calibration was found to be unsuitable to be performed with loading/unloading cycles, having led to significant underestimations of fracture toughness.

The WCT tests were unsuccessful in reaching a stable propagation stage for one material, I152-C, as bearing failure occurred before significant damage propagation occurred. Therefore, a scaled-up CT test configuration was developed for this material. The scaled-up CT test provided higher fracture toughness estimates than the baseline CT test, however, a stable propagation stage was also not achieved. A conservative value of 160 N/mm was considered for this material, which clearly stands out from previous results determined through the WCT tests for other materials.

The results of all six test materials highlighted an exponential trend between G_2^+ and the transverse fibre reinforcement percentage, as materials with reinforcement percentages between ≈0% and ≈20% presented G_2^+ results between 10 and 26 N/mm, whereas a material with ≈30% (I152-C) presented considerably higher results, with 160 N/mm.

The WCT tests also led to the determination of estimates for the cohesive law shape and maximum cohesive stress of each material. All materials showed an exponential trend regarding their cohesive laws and the maximum cohesive stress was found to be higher than the transverse tensile strength for most materials. It was also noteworthy that the thinner materials presented the most significant differences between the maximum cohesive stress and transverse tensile strength, ranging from 50% to 86% (I152-C and P300-A), whereas for thicker materials this difference ranged from 13% to 26%.

Simplified numerical models, based on commercial FE software and with homogenized mechanical properties through the thickness, were found to present a good agreement to experimental load *vs*. displacement curves, for all three test configurations. These results clearly validated the experimentally based fracture properties.

In addition, a user-material subroutine (UMAT) was implemented in order to compare numerical results based on a linear and an exponential cohesive law. This step showed that numerical models calibrated with an exponential cohesive law and the cohesive stress presented a better fit to experimental tests in regard to damage propagation, when compared to models calibrated with a linear cohesive law and the material strength.

9.1.1.4. Transverse compressive fracture toughness (G_2^-) characterization

The previously reported methodology for WCT tests, of implementing a data reduction method based on experimental fracture tests, was tested for compact compression tests (CCT). This methodology led to non-stabilizing results of energy release rate for all materials, in agreement with results found in the literature. This trend in the results was attributed to contact stresses acting behind the damage front.

As an alternative methodology, the experimental tests were implemented to calibrate FE numerical models. To this end, the experimental load *vs*. displacement curves were fitted with numerical load *vs*. displacement curves. The numerical curves were calibrated in respect to two main parameters: (i) transverse compressive fracture toughness (G_2^-); and (ii) residual transverse compressive stress (σ_r). Firstly, G_2^- defined the ultimate load reached by the numerical curve, whereas the residual stress defined the softening slope.

Through this methodology, G_2^- was found to range between 36 and 67 N/mm, for all six tested materials. Most materials presented therefore higher G_2^- estimates than previously reported values for G_2^+ (the exception being I152-C). It was also noteworthy that G_2^- does not share the exponential trend found between G_2^+ and transverse fibre reinforcements, as the material with lowest transverse fibre reinforcement percentages, I150-S, was found to present the highest G_2^- value (67 N/mm).

The optimal residual stresses could only be assessed for four materials, as two materials (I150-A and I150-S) presented early signs of tensile failure in the posterior face. For the remaining four materials, a narrow range of results was determined for the optimal residual stress, ranging from

9% to 16% of the material transverse compressive strength, corresponding to a range between 8 and 17 MPa in absolute values.

The CCT numerical models were also used to assess the transverse tensile properties of these materials, by comparing the experimental and numerical stages where tensile damage initiated. This analysis showed that models calibrated with the cohesive stress measured through WCT tests, instead of the transverse tensile strength, presented a better fit to experimental failure modes.

9.1.2. Web-crippling of pultruded GFRP materials

9.1.2.1. Research background

Little research has been performed so far on the experimental characterization of web-crippling in pultruded GFRP materials [9.10-9.16]. Furthermore, the research performed to date has been dispersed into different and narrow experimental ranges, focused on limited test configurations and profile cross-sections. This limited experimental basis, together with the complexity of the phenomena involved, has led to even fewer numerical studies performed on this topic [9.17, 9.18]; moreover such simulations lacked input data on relevant material properties, namely fracture toughness. Some design expressions have been developed for web-crippling of pultruded GFRP materials [9.10, 9.12, 9.14, 9.16], however, their range of applicability is narrow and their experimental background is also limited.

Considering these shortcomings in previous experimental, numerical and analytical studies on web-crippling, a comprehensive test programme was conducted in this thesis, to fulfil some of the gaps identified, together with numerical modelling, supported by the necessary material properties to simulate the main phenomena involved in web crippling. Moreover, a broad analytical study was also performed, through the direct strength method (DSM), which can be easily applicable to additional section geometries and test configurations; therefore, the DSM is considered a promising lead for a broad design methodology against web-crippling of pultruded GFRP profiles.

9.1.2.2. Experimental study

The experimental study presented in this thesis departed from previous studies [9.16, 9.17], considering a sample of materials with a relatively narrow range of geometries but a broad range in terms of mechanical properties. The ETF and ITF test configurations were also addressed herein, applied to four I-section and one U-section profiles. In accordance with the results of previous studies, the bearing length was found to present a significant and consistent impact in the ultimate load, stiffness and failure mode of all I-section profiles, for both ETF and ITF configurations. As expected, the highest values of stiffness and ultimate load were obtained for the ITF configuration. However, in the ETF tests the stiffness and ultimate load were more influenced by the increase of bearing length than in the ITF tests: when it increased from 15 mm to 100 mm, the ultimate loads increased between 207% (I150-A) and 227% (I200-F) in ETF tests, and between 93% (I150-A) and 139% (I152-C) in ITF tests. The U-section profile was considerably less affected by the bearing length: in ITF tests, when it increased from 15 mm and 100 mm, the ultimate load increased 61%.

The failure modes observed in the experimental campaign were very consistent, clearly depending on the test configuration and bearing length. In all ITF tests and ETF-15 tests, failure involved clear web-crushing failure, the exception being the I152-C-ITF-100 tests. I152-C-ETF-50 and 100 tests showed clear signs of web-buckling. Other I-section ETF-50 and 100 tests showed a mixed failure mode, with damage initiation occurring due to web-crushing near the web-flange junction and final failure occurring due to web-buckling at the centre of the web. Finally, all U150-S tests also presented a mixed failure mode, with simultaneous and progressive web-crushing and web-buckling failure. This mixed failure mode involved higher values of vertical displacements, for relatively high (and non-decreasing) loads, in a quite different pattern to that of all I-section tests.

Shear strain and transverse compressive strain measurements were successfully obtained for I-section specimens, providing additional data for numerical validation. U-section specimens were not assessed in this respect, as significant out-of-plane displacements developed throughout each test. The measurements of transverse compressive strains also showed that these strain fields affect a relatively constant area of the specimen throughout each test. Moreover, the distribution of normalized strains (with respect to the maximum transverse compressive strain) along the horizontal length was found to be nearly identical for all I-section profiles. This result highlights a major conclusion of this thesis: the different fibre layups of the various profiles tested did not lead to significantly different stress distributions along the length of the specimens. This result is a relevant starting point for the development of new design formulae for web-crippling failure.

9.1.2.3. Numerical study

The numerical study on web-crippling developed in this thesis consisted of a simplified approach, implementing fracture toughness properties as damage evolution parameters. This can be easily applicable in current commercial software, if the mechanical characterization of the materials is available. These simplified numerical models, with homogeneous properties through the thickness of the material and computationally inexpensive meshes of shell elements, were successful in simulating complex web-crippling experimental tests.

The geometrically non-linear damage analysis (DB) was particularly important in understanding the failure modes observed in the experimental tests, shedding light on the interaction of damage initiation near the bearing plate edges and the ultimate web-buckling deformed shape of several test series. Aside from the failure modes, the DB models provided estimates of stiffness with average differences ranging from -17% to 13%, as well as estimates of ultimate load with differences that ranged from -22% and 13%, in respect to experimental tests.

The numerical models were also validated against shear and compressive strain measurements. Relevant discrepancies were found between numerical and experimental shear strain results, which are attributed at this time to the simplification of the web-flange junction. The numerical compressive strain fields measured in the numerical models presented a good agreement to experimental results, however, some discrepancies were still found between numerical and experimental peak compressive strain results, which ranged from -25% and 6%.

Damage initiation loads were found to correspond to ratios between 61% and 91% of numerical ultimate loads, thus confirming that stress-based criteria are inadequate in predicting web-crippling failure. In a different perspective, these results are significantly higher than estimates of damage initiation determined in a previous study [9.17] (numerical damage initiation loads ranged between 34% and 70% of the experimental ultimate loads), highlighting the impact that different mechanical characterization test methods can have in numerical simulation.

A stress component analysis was performed, showing that damage initiation occurred below the bearing plate edges, with the largest contribution being attributed to transverse compressive stresses, whereas shear stresses were found to be nearly negligible. In the elements adjacent to the bearing plate edges, the shear stresses presented a higher contribution to damage initiation; however, damage initiation was still dominated by transverse compressive stresses. These results show that for ETF and ITF tests configurations, the transverse compressive strength and fracture toughness of a profile play a major role in the ultimate failure of each test.

9.1.2.4. Analytical study

The data generated through web-crippling experimental tests and numerical models (FE) were used to develop new design guidelines. A novel approach was proposed for the design of pultruded GFRP profiles against web-crippling failure, by implementing the direct strength method (DSM). The results of the proposed design formula, developed for I-section beams under end two flange (ETF) and interior two flange (ITF) loading cases, presented an excellent agreement with the ultimate loads obtained experimentally and numerically, for a wide range of profiles and materials. Furthermore, the proposed DSM expression was found to fit both ETF and ITF loading cases in a unified fashion, as the difference to these individual cases was found to be negligible.

The developed FE models were crucial to identify the trend of the DSM curve, by fitting the numerical buckling, crushing and ultimate loads and thus, paving the way for the DSM calibration. In addition, the results of FE analyses (B- and D-analysis) were crucial to derive approximate expressions to determine estimates of web buckling loads and web crushing loads. This is an essential step towards a widespread use of DSM.

The proposed design formula also presented a good fit to pultruded GFRP materials that were not considered in its calibration and that presented geometrical and material properties outside the pre-qualified section range. Finally, it should be highlighted that, aside from accurately predicting experimental ultimate loads, the proposed DSM expression can identify the failure mode for any given case, either from web crushing, web buckling or an interaction between these two.

9.2. Future developments

9.2.1. Characterization and implementation of fracture properties

9.2.1.1. Tensile fracture tests

The experimental results showed an exponential trend between transverse reinforcement fibre content and transverse tensile fracture toughness. This trend should be further analysed by testing pultruded GFRP materials with other fibre layups and different levels of transverse reinforcement. This step will be important to establish if the fracture toughness may be reasonably predicted based on fibre layup characterization. In a different trend, materials with different resin materials and similar fibre layups should be tested, in order to establish the impact of this constituent in tensile fracture properties of composite materials.

As pultruded GFRP materials are known to present a significant sensitivity to increased temperatures, a future development should also assess the impact of temperature on the fracture behaviour of these materials.

WCT tests were found to accurately characterize the transverse tensile fracture toughness of pultruded GFRP materials. However, it will be important to compare this methodology with other test configurations, in order to further validate these results. Moreover, the WCT test configuration was not successful in testing the material with higher transverse reinforcement percentages. This issue must be further assessed, to establish a range of application for the WCT test configuration.

In a different perspective, WCT tests led to estimates of maximum cohesive stresses that were higher than the material strength, for most materials. This should be attributed to the different failure modes exhibited by mechanical characterization tests, with sudden failure and significant delamination, and fracture tests, with stable damage propagation and negligible signs of delamination. The implementation of fracture tests as complementary mechanical characterization tests should be further assessed in the future, in order to better characterize the complex structural behaviour of pultruded GFRP materials.

9.2.1.2. Compressive fracture tests

This thesis presented an inverse methodology applied to CCT specimens, based on calibrating fracture properties based on experimental load *vs*. displacement curves, which is a cumbersome approach. It would be important to develop a purely experimental methodology, similarly to that performed for tensile fracture tests, so that compressive fracture properties may be experimentally characterized instead of numerically calibrated.

The transverse compressive fracture toughness results were found to be independent of the fibre layups. This result highlights the need to study materials with similar fibre layups but different resin materials. This will be an important step to better understand the contribution of the resin material to the transverse compressive fracture behaviour of pultruded GFRP materials.

The numerical models were not fully able to simulate two of the materials (I150-A and U150-S), which was attributed to an underestimation of their mechanical properties. This result shows that these fracture tests may also be useful complementary tools for mechanical characterization of composite materials. This trend should be considered in the future, regarding a more complete mechanical characterization of pultruded GFRP materials.

9.2.1.3. Numerical simulation of damage evolution

Despite the promising numerical results reported in this thesis, there were also some relevant questions raised that require further research: (i) the numerical results show a different fit to the softening stage of baseline CT and WCT load *vs.* displacement curves, which may indicate some level of geometry dependency of the experimentally determined fracture toughness; (ii) the applicability of models with an exponential cohesive law and calibrated with the maximum cohesive stress should be tested for other experimental tests, namely mechanical characterization tests, which should yield overestimations of the failure loads, as the cohesive stress was found to be significantly higher than the material strength for some materials.

In order to simulate more generalized and complex cases, these two topics should be addressed in the future, (i) analytically, through a more complex damage formulation, in particular regarding different failure modes involving transverse tension, such as matrix cracking, delamination or fibre bridging; and (ii) experimentally, by applying this methodology to a wider experimental program in terms of test configurations and geometry ranges.

Regarding the numerical simulations of compressive fracture tests, a relevant future development would be to integrate delamination into the damage initiation and evolution formulations, as all CCT tests showed relevant signs of delamination throughout compressive damage propagation.

9.2.2. Web-crippling failure

9.2.2.1. Web-crippling experimental tests

This topic has a significant need for future developments. The experimental studies performed to date still cover a narrow research scope, as web-crippling must be analysed for (i) a wide variety of profile sections and geometries; (ii) a significant number of test configurations; (iii) different bearing lengths and bearing materials; and (iv) several strengthening methodologies.

As reported in Chapter 2 and Section 9.1.2.1, only a fraction of the above variables has been analysed to date. Therefore, the experimental assessment of these various components is crucial, so that subsequent numerical analyses may be performed and, ultimately, design expressions may be proposed and validated.

In a different perspective, the implementation of digital image correlation (DIC), as performed by Wu *et al.* [9.14] for a fixed bearing length, should be further developed in future experimental studies, with the objective of establishing effective bearing lengths in the web of the profile, as a function of different applied bearing lengths. Defining the effective bearing lengths for several web-crippling cases should lead to broader and more simplified design expressions.

9.2.2.2. Web-crippling numerical models

Web-crippling tests were accurately simulated with Abaqus built-in tools, calibrated with experimentally based fracture toughness results. This simplified methodology provided a good agreement for stiffness, ultimate load and failure mode for I-section profiles. However, it would be important to further develop these numerical models, by including more complex damage evolution tools. In particular, it would be important to include delamination into the damage formulations, as several specimens showed signs of delamination, occurring particularly when damage developed at the centre of the web.

Another complementary research development that should be considered is the experimental characterization of the mechanical properties in the web-flange junction area. This area of the profile is expected to present weaker mechanical properties, due to higher resin content. Furthermore, web-crushing has been found to occur in the web-flange junction area for most of the specimens.

9.2.2.3. Web-crippling design guidelines

The analytical approximate expressions proposed for web buckling and web crushing will require continuous updating, in order to extend their range of applicability. To that end, the expressions presented herein should be assessed (and, if needed, updated) in respect to additional variables, such as flange thickness and width, other section geometries and positioning of web stiffeners. As an alternative, analytical studies should also be pursued to derive the exact solutions for these failure modes.

Given the accuracy of the proposed DSM expressions, the absence of widely accepted guidelines for web-crippling failure of FRP composite beams may now be partially overcome. In addition, the reliability of the proposed DSM expressions should be assessed, by implementing this approach to additional materials, section geometries and loading configurations. This step is further highlighted as there are currently various design guidelines under development regarding the use of pultruded GFRP profiles in construction [9.19, 9.20].

9.3. References

[9.1] Almeida-Fernandes, L., Silvestre, N., Correia, J. R., Characterization of transverse fracture properties of pultruded GFRP material in tension, *Composites Part B: Engineering*, 175, 107095, 2019.

[9.2] Almeida-Fernandes, L., Correia, J. R., Silvestre, N., Transverse fracture behaviour of pultruded GFRP materials in tension: Effect of fibre layup, *Journal of Composites for Construction*, 24(4), 04020019, 2020.

[9.3] Almeida-Fernandes, L., Silvestre, N., Correia, J. R., Arruda, M. R. T., Fracture toughness-based models for damage simulation of pultruded GFRP materials, *Composites Part B: Engineering*, 186, 107818, 2020.

[9.4] Almeida-Fernandes, L., Silvestre, N., Correia, J. R., Arruda, M. R. T., Compressive transverse fracture behaviour of pultruded GFRP materials: experimental study and numerical calibration, *Composite Structures*, 247, 112453, 2020.

[9.5] Almeida-Fernandes, L., Correia, J. R., Silvestre, N., Effect of fibre layup in web-crippling of pultruded GFRP profiles, *Engineering Structures*, submitted, 2020.

[9.6] Almeida-Fernandes, L., Silvestre, N., Correia, J. R., Fracture toughness-based models for web-crippling of pultruded GFRP profiles, *Composites Part B: Engineering*, submitted, 2020.

[9.7] Almeida-Fernandes, L., Silvestre, N., Correia, J. R., Direct strength method for web-crippling design of pultruded GFRP beams, *Journal of Composite for Construction*, submitted, 2020.

[9.8] El-Hajjar R., Haj-Ali R., Mode-I fracture toughness testing of thick section FRP composites using the ESE(T) specimen, *Engineering Fracture Mechanics*, 72, pp. 631-643, 2005.

[9.9] Liu W., Feng P., Huang J., Bilinear softening model and double K fracture criterion for quasi-brittle fracture of pultruded FRP composites, *Composite Structures*, 160, pp. 1119-1125, 2016.

[9.10] Borowicz, D.T., Bank, L.C., Behavior of Pultruded Fiber-Reinforced Polymer Beams Subjected to Concentrated Loads in the Plane of the Web, *Journal of Composites for Construction*, 15, pp. 2-9, 2011.

[9.11] Borowicz, D.T., Bank, L.C., Effect of web reinforcement on the behavior of pultruded fiber-reinforced polymer beams subjected to concentrated loads. *Construction and Building Materials*, 47, pp. 347-357, 2013.

[9.12] Wu, C., Bai, Y., Web crippling behaviour of pultruded glass fibre reinforced polymer sections, *Composite Structures*, 108, pp. 789-800, 2014.

[9.13] Wu, C., Bai, Y., Zhao, X.L., Improved bearing capacities of pultruded glass fibre reinforced polymer square hollow sections strengthened by thin-walled steel or CFRP, *Thin-Walled Structures*, 89, pp. 67-75, 2014.

[9.14] Wu, C., Zhang, L., Bai, Y., Zhao, X. L., Web crippling behavior of pultruded GFRP channel sections under transverse bearing load, *Composite Structures*, 209, pp. 129-142, 2019.

[9.15] Wu, C., Zhang, L.-T., Tam, L., Yan, L., He, L., Effect of Bearing Length on Web-crippling Behavior of Pultruded GFRP Channel Section, *Composite Structures*, 112810, 2020.

[9.16] Almeida-Fernandes, L., Gonilha, J., Correia, J. R., Silvestre, N., Nunes, F., Web-crippling of GFRP pultruded profiles. Part 1: Experimental study. *Composite Structures*, 120, pp. 565-577, 2015.

[9.17] Almeida-Fernandes, L., Nunes, F., Silvestre, N., Correia, J.R., Gonilha, J., Web-crippling of GFRP pultruded profiles. Part 2: Numerical analysis and design, *Composite Structures*, 120, pp. 578-590, 2015.

[9.18] Nunes F., Silvestre N., Correia JR., Progressive damage analysis of web crippling of GFRP pultruded I-sections, *Composites for Construction*, 21(3), pp. 1-13, 2016.

[9.19] ACMA, Pre-Standard for Load & Resistance Factor Design (LRFD) of Pultruded Fiber Reinforced Polymer (FRP) Structures. American Composites Manufacturers Association, 2010.

[9.20] CEN/TC250 working Group 4, *Fibre reinforced polymer structures, scientific and technical report*, European Committee for Standardization (CEN), Brussels (2016).